

1 2 9 0



UNIVERSIDADE D
COIMBRA

Giusi Piccirillo

DEVELOPMENT OF SOLID MATERIALS FOR
ENVIRONMENTAL REMEDIATION

Tese no âmbito do doutoramento em Química,
ramo de Catálise e Sustentabilidade orientada pelo
Professor Doutor Mário José Ferreira Calvete, co-orientada
pela Professora Doutora Maria Ermelinda da Silva Eusébio e pelo
Professor Doutor João Paulo Costa Tomé e apresentada ao
Departamento de Química da Faculdade de Ciências e Tecnologia
da Universidade de Coimbra

Dezembro de 2022

Faculdade de Ciências e Tecnologia da Universidade de Coimbra

Development of Solid Materials for Environmental Remediation

Giusi Piccirillo

Tese no âmbito do doutoramento em Química, ramo de Catálise e Sustentabilidade orientada pelo
Professor Doutor Mário José Ferreira Calvete, co-orientada pela
Professora Doutora Maria Ermelinda da Silva Eusébio e pelo Professor Doutor João Paulo Costa
Tomé e apresentada ao Departamento de Química da Faculdade de Ciências e Tecnologia da
Universidade de Coimbra

Dezembro de 2022



UNIVERSIDADE D
COIMBRA

“Voli, sempre voli, fortissimamente voli”

V. Alfieri, 1783

Agradecimentos

Com o tempo, aprendi que nenhum objetivo na vida se alcança sozinho e a conclusão desta etapa importante e significativa para mim, não teria sido possível sem a presença e o apoio de um grupo de pessoas. Por isso, gostaria de expressar a minha gratidão a todas as pessoas que, ao longo destes anos, tiveram um papel fundamental e que me enriqueceram a nível profissional e pessoal.

Em primeiro lugar, gostaria de agradecer à Professora Doutora Mariette Pereira que, apesar de não ser a minha orientadora “no papel”, teve sempre um papel ativo na minha orientação ao longo destes anos e sempre se demonstrou disponível para esclarecer as minhas dúvidas. Agradeço a oportunidade que me deu e o conhecimento científico que me transmitiu. Muito obrigada também pela sua ajuda, não só a nível profissional mas sobretudo a nível pessoal, em particular neste último ano muito difícil para mim.

Ao meu orientador, Professor Doutor Mário Calvete, agradeço toda a orientação ao longo deste percurso, a enorme ajuda e os ensinamentos. Por todo o acompanhamento, assim como a disponibilidade para esclarecer todas as minhas questões. Também gostaria de agradecer por todas as conversas e a costante paciência comigo.

À minha co-orientadora, Professora Doutora Maria Ermelinda Eusébio, um grande obrigada por acreditar em mim, mesmo sabendo, desde o início, que a sua área científica seria um desafio. Obrigada por ser um exemplo, pelo incansável trabalho que teve comigo neste último período e por me impulsionar, desde o primeiro momento, a lidar com várias situações e a perceber que um resultado negativo é sempre um resultado.

Ao meu co-orientador, Professor Doutor João Tomé, infelizmente a pandemia não me permitiu vir ao seu laboratório, mas obrigada pela pronta disponibilidade, apoio e pela colaboração.

Ao Professor Doutor Armando Pombeiro e a toda a comissão avaliadora do programa doutoral CATSUS – Catálise e Sustentabilidade, pela seleção e atribuição da bolsa de doutoramento. Também, agradeço o apoio financeiro da Fundação para a Ciência e Tecnologia (FCT) através da cedência da bolsa PD/BD/135532/2018 e da prorrogação COVID/BD/152523/2022.

Também tenho de agradecer ao Professor Doutor João Canotilho e ao Professor Doutor Ricardo Castro pela ajuda na utilização dos aparelhos de caracterização de estado

sólido, assim como na interpretação dos resultados e no esclarecimento das dúvidas, mas sobretudo por terem sempre sorriso, boa disposição e pelo constante apoio. À Professora Teresa Roseiro pela constante colaboração na análise de TG-DSC.

À Doutora Matilde Moreira-Santos do Centro de Ecologia Funcional (CFE) do Departamento de Ciências da Vida da Universidade de Coimbra, pela colaboração e ajuda nos estudos de toxicidade em microrganismos aquáticos e também pelas conversas e boa disposição.

À Professora Doutora Gabriela Jorge da Silva por me ter permitido realizar os meus estudos com bactérias no seu laboratório de microbiologia, tornando a minha tese ainda mais multidisciplinar. Um particular agradecimento ao Tiago e à Sandra, que tive a oportunidade de conhecer durante os meus dias no laboratório de microbiologia, pela ajuda e pelas risadas.

Ao Professor Doutor Arthur Silva e a Doutora Mónica Válega da Universidade de Aveiro pela colaboração na identificação dos produtos de degradação nos processos de catálise oxidativa.

Ao Doutor Rui Manadas do laboratório de galénica e tecnologia farmacêutica da Faculdade de Farmácia pela colaboração e ajuda nos ensaios de dissolução.

À Doutora Sílvia Gramacho pelos conselhos, mas sobretudo pelas explicações, pelo apoio e pelo esclarecimento de todas as minhas dúvidas sobre o funcionamento do Hplc. Se hoje consigo ser autónoma, é, também, por seu mérito.

Ao Professor Doutor Sérgio Seixas de Melo e à Carla Cunha pela disponibilidade em fornecer a água Milli-Q e o aparelho do UV-Vis de estado sólido.

Ao Professor Doutor Rui Brito e ao Pedro Cruz pelo serviço de Ressonância Magnética Nuclear do Centro de Química de Coimbra, agradeço a disponibilidade na obtenção dos espectros de RMN.

A todos os funcionários do Departamento de Química, Sr. Jorge, à D^a Lurdes e ao Sr. António Manuel, muito obrigada pelos bons momentos e incansável apoio que dão a todos nós da investigação.

A todos os membros do grupo de Termodinâmica e Química do estado sólido, particularmente ao João Baptista, ao João Santos e à Joana da Silva, pelo acolhimento, companheirismo e partilha de conhecimento.

A todos os membros do grupo de Catálise e Química Fina, antigos e atuais, com quem tive a sorte de partilhar bons momentos que guardarei comigo no futuro: César Henriques, Lucas Dias, Liliana Damas, Vanessa Tomé, Carolina Vinagreiro, Diana Gomes, Nídia Maldonado-Carmona, Rui Carrilho, Sara Pinto, Inês Fonseca, Alexandre Felgueiras, Vitaliy Masliy, Zoé Arnaut, Madalena Silva, Iúri Tavares, Carolina Neto, Inês Cruz, Diana Marques, Carolina Domingos, Daniela Teixeira, Andreia Gonzalez, Fábio Rodrigues e Rafael Aroso. Queria agradecer-vos pelo companheirismo no laboratório, pelo convívio diário, pelas partilhas e pela solidariedade nos momentos bons e maus. Contudo, gostaria de agradecer, em especial, algumas pessoas porque cada uma delas contribuiu para o meu crescimento como profissional e como ser humano.

À Carolina, um mix de ansiedade e energia que consegue compreender os meus “momentos”, agradeço todas as nossas conversas que terminam em risadas e os grandes abraços. À Daniela, tive a oportunidade de conhecer-te melhor nos últimos tempos e só consigo pensar “Ainda bem!”, um enorme obrigada não chega para agradecer toda a ajuda que me deste ao longo da escrita desta tese. Obrigada por confiares em mim, pelas longas conversas, por ficar sentada ao meu lado “simplesmente” a fazer companhia, nunca irei esquecer. À minha Diana, a minha querida tutoranda, mas foste mais que isso, foste o meu desafio. Obrigada por me desafiares a ser uma pessoa melhor para poder responder às tuas “infinitas” questões e tentar encontrar soluções aos vários problemas que iam surgindo. Obrigada por acreditares nas minhas capacidades como tua tutora, pelo apoio, disponibilidade e amizade nos momentos mais impensáveis (nunca irei esquecer a nossa videochamada quando estava em New York com covid).

Ao longo destes anos, tive a oportunidade de cultivar grandes amizades com pessoas que tenho certeza que estarão na minha vida tal como estiveram até hoje.

À Carolina, obrigada por dar-me força em todos os momentos, pelos conselhos, pelos numerosos abraços, por compreender e respeitar os meus silêncios, por acreditar em mim quando eu estava pronta a largar tudo. Obrigada por estar sempre presente mesmo com todos estes quilômetros que nos separam.

Ao Fábio, por ter sido a pessoa que mais se esforçou desde o início para que me sentisse incluída no grupo, mesmo quando só falava em inglês, para sentir saudades de casa. Obrigada pelas imensas e longas conversas inspiradoras desde o primeiro dia até hoje, pelos conselhos, pela tua amizade e pelo altruísmo.

À Andreia, simplesmente por seres tu mesma. Nós as duas não acertamos imediatamente devido ao nosso mau feitio, mas tenho certeza que a tua amizade teve e tem um impacto importante no meu percurso até hoje. Obrigada pelos desabafos nos momentos difíceis que deixavam o coração mais leve, por me dares energia positiva, pelas palavras de incentivo e apoio diário.

Ao Rafael, por ter sido um amigo incansável no momento mais escuro da minha vida e por não me ter deixado sozinha nem por um momento, por ter feito o impossível para eu estar bem, vou lembrar-me desses momentos para o resto da minha vida. Obrigada por teres sido imensuravelmente chato, ao longo destes anos e também pelas intermináveis conversas diárias. Pelas risadas e pelas picardias, pelo teu companherismo e altruísmo dentro e fora do laboratório, pela revisão desta tese (mesmo os teus comentários sendo um grande pesadelo). Um enorme obrigada por tudo!

Alle mie amiche di una vita, Federica e Ilaria, per aver creduto fin dall'inizio che ce l'avrei potuta fare, per le telefonate e le videochiamate, soprattutto durante il primo anno, per non farmi sentire la solitudine, per esserci sempre state e per aver gioito con me delle mie conquiste.

Alla mia famiglia, nonna e zia Tittina, mia sorella e mio cognato, mio nipote, scusate la mia assenza e se mi sono persa tanti momenti durante questi anni. Grazie per non aver mai smesso di credere in me e per cercare di alleggerire questa distanza che ci separa. A mio nonno, ti ho "portato con me" in ogni viaggio. In particolare, a mia sorella, grazie per avermi sostenuto incondizionatamente fin dall'inizio e per gioire dei miei successi e grazie per farti carico di "fardelli", a volte troppo grandi, a causa della mia lontananza.

Un ringraziamento speciale va ai miei genitori che sono il pilastro della mia vita! Grazie per tutto quello che mi avete insegnato, per i valori che mi avete trasmesso e che mi hanno fatto diventare la persona che sono oggi. Grazie per la vostra dedizione, il vostro aiuto e supporto, per le ore passate al telefono, per le risate e per i pianti, per avermi sopportato durante questi anni che non sono stati facili, per il vostro amore incondizionato. A mia madre, grazie per sempre presente, per prendere il primo aereo ogni volta che ho avuto e che ho bisogno di te, per tutti gli incoraggiamenti e per sostenere le mie scelte. A mio padre, per avermi sempre ripetuto di non arrendermi e per aver sempre creduto in me...ti porto nel mio cuore! Questa tesi la dedico a voi due perché non sarei qui se non fosse stato per voi.

Por último, só porque em último vem o melhor, um agradecimento muito especial ao Marcos, o meu marido, que tive a grande sorte de encontrar durante este percurso. Obrigada por seres o meu porto de abrigo, por todo o teu amor e carinho, pela compreensão e pela infinita paciência, por seres o meu grande apoio nos momentos de tristeza e por celebrar comigo as conquistas. Infinitamente grata por fazeres o impossível para ver-me feliz e por ter mudado e melhorado a minha vida!

Muito Obrigada a todos!

Table of contents

Abstract	i
Resumo	iii
Abbreviations and Symbols	vii
Nomenclature	xv
Chapter 1 - Introduction	1
1.1 Antibiotics: from being a solution to a big problem	1
1.2 Fate of antibiotics in water	5
1.3 Aqueous antibiotics remediation processes: downstream approach	7
1.4 Porphyrins as catalysts in antibiotic AOPs	16
1.4.1 Antibiotics oxidative porphyrin-based catalytic degradation	16
1.4.2 Antibiotics photocatalytic degradation	20
1.5 Development of new pharmaceutical multicomponent solid forms: upstream approach	24
1.6 Work proposal	29
1.7 References	31
Chapter 2 - Synthesis, characterization and applications of porphyrin-based catalysts in the degradation of antibiotics	51
2.1 Trimethoprim and sulfamethoxazole as target antibiotics	51
2.2 Synthesis of metalloporphyrins for homogeneous catalytic systems	53
2.3 Homogeneous catalytic degradation of TMP	59
2.4 Synthesis and characterization of hybrid materials for heterogeneous catalysis	65
2.4.1 Synthesis, functionalization, and characterization of MNPs	65
2.4.2 Synthesis of MnTDCPPS-NH@MNPs	69
2.4.3 Synthesis of MnTDCPP-based 3-aminopropyl functionalized silica, MnTDCPPS@SiO ₂	71

2.5 Heterogeneous catalytic oxidative degradation of TMP	76
2.6 Product analysis and possible degradation pathway	82
2.7 Ecotoxicity studies	85
2.8 Photocatalytic homogeneous degradation of TMP	89
2.9 Development of porphyrin-based lignin heterogeneous photocatalyst	94
2.10 Antibiotics photodegradation by Por@AcL photocatalyst	98
2.10.1 Photodegradation of trimethoprim	99
2.10.2 Photodegradation of sulfamethoxazole	103
2.11 Photocatalyst reutilization studies	105
2.12 Photodegradation of cotrimoxazole	109
2.13 TOC analysis	112
2.14 Degradation products analysis	113
2.15 <i>E. coli</i> resistance assay	117
2.16 Conclusion	120
2.17 References	123
Chapter 3 - Development, characterization and evaluation of TMP-based multicomponent solid forms	137
3.1 Introduction	137
3.2 Screening, preparation and characterization of TMP-based multicomponent solid forms	141
3.2.1 Development of TMP-based multicomponent forms using GRAS compounds.	143
3.2.2 Development of TMP-based multicomponent forms using co-API molecules	157
3.3 Dissolution rate tests	166
3.4 Antibacterial activity	171
3.5 Conclusions	177
3.6 References	180
Chapter 4 - Experimental Section	193

4.1 General information	193
4.1.1 Chemicals and solvents	193
4.1.2 Instrumentation and methodology	193
4.1.3 Solvent drying	200
4.2 Experimental of Chapter 2	200
4.2.1 Synthesis of porphyrins	200
4.2.2 Chlorosulfonation of porphyrins	203
4.2.3 Hydrolysis of porphyrins	204
4.2.4 Synthesis of metalloporphyrins	206
4.2.5 Synthesis, coating and functionalization of magnetic nanoparticles (MNPs)	208
4.2.6 Synthesis of MnTDCPPS-NH@MNPs	209
4.2.7 Synthesis of hybrid catalyst MnTDCPPS@SiO ₂	210
4.2.8 Trimethoprim homogeneous degradation	211
4.2.9 Trimethoprim heterogeneous degradation	212
4.2.10 Catalyst reutilization studies	212
4.2.11 Ecotoxicity assay	212
4.2.12 Synthesis of zinc (II) 5,10,15,20-tetrakis(2,6-dichloro-3-sulfonatophenyl)porphyrin	214
4.2.13 Synthesis of acetylated lignin (AcL)	214
4.2.14 Encapsulation of porphyrins inside acetylated lignin nanoparticles (Por@AcL)	215
4.2.15 Trimethoprim photodegradation under homogeneous conditions	216
4.2.16 Antibiotics photodegradation using TDCPP@AcL	216
4.2.17 TDCPP@AcL reutilization studies	217
4.3 Experimental of Chapter 3	217
4.3.1 Development of new multicomponent solid-forms	218
4.3.2 Intrinsic dissolution rate tests	218
4.3.3 Trimethoprim MIC determination	219
4.4 References	221

Abstract

The research presented in this PhD thesis aims to contribute with two strategies for the remediation and/or prevention of antibiotics' environmental accumulation. The first, "*a posteriori*", was focused on the development of new catalytic materials for aqueous catalytic and photocatalytic antibiotics oxidation, while the second, "*a priori*", was centred on finding new pharmaceutical multicomponent solid-forms with lower antibiotic loads, for potential reduction in human intake.

In Chapter 1, the problem is outlined, particularly on the use of antibiotics, their accumulation in water and development of antimicrobial resistance. Emphasis on Advanced Oxidation Processes (AOPs), particularly with a critical state of the art review on the use of porphyrins as valid alternatives in the catalyzed antibiotics' oxidation is given. Finally, the development of new pharmaceutical multicomponent solid forms that may be key to improve the existing active pharmaceutical ingredients' properties is also presented.

After contextualization on the studied antibiotics, Chapter 2 is divided in two main parts: the first begins with a preliminary evaluation of metalloporphyrin catalytic properties in which the Mn(III) *meso*-tetra(2,6-dichloro-3-sulfonyl-phenyl)porphyrin (**7**) showed the best catalytic performance, reaching 95% of TMP oxidation in 150 min at room temperature. Hence, this catalyst was covalently immobilized onto MNPs (**14**) and 3-aminopropyl functionalized silica (**16**) and fully characterized by standard solid-state techniques. Then, after the implementation in TMP degradation using H₂O₂ as oxidant, **16** showed a 95% of TMP degradation and 24% of total organic carbon (TOC) release in 150 min at room temperature using a TMP:Cat ratio = 500:1. Additionally, 7 degradation products were identified, a possible degradation pathway was proposed and the catalyst was recovered and reutilized in 5 cycles with no loss of activity and no leaching. Finally, the ecotoxicity of the initial TMP and the resulting products' solutions was evaluated, both showing similar toxicity.

The second part of Chapter 2 describes TMP photodegradation, performed in a photoreactor (400 W medium pressure Hg lamp). A new hybrid photo-nanomaterial was developed by incorporating *meso*-tetra(2,6-dichlorophenyl)porphyrin (**6**) into acetylated lignin, characterized by UV-Vis and TEM and then, applied in the TMP, sulfamethoxazole and cotrimoxazole photodegradation. A complete photooxidation of

each substrate was obtained using a 500:1 AB:Cat ratio and after 4 h, 20 min and 2h, respectively, achieved 75%, 83% and 79% of TOC removal. No loss of activity or photocatalyst leaching was found after 10 reutilization cycles in both cases. Only two photodegradation products (PPs) were identified for the TMP degradation. Finally, the *E. coli* resistance to TMP was determined after 10 days, resulting in a 1000-fold increase in the TMP minimum inhibitory concentration (MIC) while, after the exposure to PPs solution, no development of resistance was observed, validating the efficiency of the developed photodegradation process.

Chapter 3 was focused on the upstream approach, involving the development of new TMP-based multicomponent solid-forms to improve TMP performance. Acceptable co-formers and other active pharmaceutical ingredients were selected, with potential to improve either TMP aqueous solubility/dissolution rate or its antibacterial properties. Screening/development of the TMP-based multicomponent solid-forms was performed using a green mechanochemical approach, assisted by ethanol. Four new (1:1) TMP salts were identified, with picolinic, salicylic, nicotinic (NIC) and ibuprofen acids, and eutectic forming systems with paracetamol (PARA), curcumin (CURC) and ciprofloxacin (CIP), which with eutectic compositions were determined. Dissolution rate tests were carried out, showing 25% enhancement of TMP dissolution rate when using TMP-NIC and a statistically significant 5% increase with the TMP-PARA eutectic mixture, always against pure TMP. Then, the *E. coli* and *S. aureus* susceptibility was evaluated against selected multicomponent solid-forms. The association with CURC in the eutectic composition exhibited a statistically significant decrease in the TMP MIC value (from 0.98 to $\sim 0.36 \mu\text{g mL}^{-1}$) for *E. coli*, whereas an increase (from ~ 2.54 to $\sim 5.73 \mu\text{g mL}^{-1}$) was found when tested against *S. aureus*. Finally, the *E. coli* susceptibility was also evaluated for TMP and CIP, individually, for an equimolar mixture and for the estimated eutectic composition, $x_{\text{TMP}} = 0.85$. A decrease in MIC was observed in both cases, demonstrating the benefits of associating two antibiotics with different mechanism of action, representing a possible clinical solution for antibacterial activity improvement.

In Chapter 4, the instrumentation, the experimental procedures and the full characterization of synthesized compounds and materials as well as the biological assays are described.

Keywords: antibiotic degradation, trimethoprim, homo/heterogeneous catalysis, metal-pyrrolic macrocycles, magnetic nanohybrids, multicomponent solid-forms.

Resumo

Esta dissertação de doutoramento centra-se em duas estratégias para a remediação e prevenção da acumulação de antibióticos (AB) no meio ambiente. A primeira, “*a posteriori*”, baseia-se no desenvolvimento de novos catalisadores, para a oxidação catalítica e fotocatalítica de antibióticos em água, enquanto que a segunda, “*a priori*”, centra-se na descoberta de novas formas sólidas farmacêuticas multicomponente com quantidade menores do antibiótico, de forma a reduzir a quantidade mássica do mesmo (dose).

No Capítulo 1 apresenta-se o problema dos antibióticos, da sua acumulação ambiental e o desenvolvimento da resistência antimicrobiana. Enfatizam-se os Processos de Oxidação Avançada, com uma análise crítica da literatura relativa ao uso de porfirinas como uma alternativa na oxidação catalítica de antibióticos. Por fim, é apresentado o desenvolvimento de novas formas sólidas farmacêuticas multicomponente como chave para melhorar as propriedades dos ativos farmacêuticos (API) existentes.

Após contextualização dos antibióticos selecionados, o Capítulo 2 é dividido em duas partes: primeiro avaliaram-se as propriedades catalíticas de metaloporfirinas, sendo a porfirina de manganês tetra-diclorofenil sulfonada (**7**) a mais eficaz, alcançando 95% de TMP oxidado em 150 min, à temperatura ambiente. Assim, este catalisador foi covalentemente imobilizado em nanopartículas magnéticas (**14**) e sílica funcionalizada (**16**), e os materiais resultantes caracterizados por técnicas de estado sólido. Após implementação na degradação de TMP usando H₂O₂ como oxidante, **16** permitiu obter 95% de degradação do TMP e 24% de libertação de carbono orgânico total (TOC) em 150 min à temperatura ambiente com TMP:Cat=500:1. Sete produtos de degradação foram identificados, uma possível via de degradação foi proposta e o catalisador foi recuperado e reutilizado em 5 ciclos sem perda significativa de atividade nem lixiviação. Por fim, a ecotoxicidade da solução do TMP inicial e dos produtos resultantes foi avaliada apresentando estes toxicidade semelhante.

A segunda parte do Capítulo 2 descreve a fotooxidação do TMP, utilizando um fotoreator (lâmpada de Hg de média pressão 400 W). Um novo fotomaterial híbrido foi sintetizado incorporando a porfirina *meso*-tetra(2,6-diclorofenil) (**6**) na lignina acetilada e caracterizado através UV-Vis e TEM, sendo implementado na fotodegradação de TMP, sulfametoxazol and cotrimoxazol. A fotodegradação de cada substrato foi obtida

utilizando uma relação AB:catalisador de 500:1 após 4 h, 20 min e 2 h, respetivamente, com 75%, 83% e 79% de remoção de TOC. Nenhuma perda significativa nem lixiviação foi detectada após 10 ciclos de reutilização em ambos os casos. Além disso, apenas dois produtos de fotodegradação (PPs) foram detetados para o TMP. Foi então avaliada a resistência de *E.coli* ao TMP ao longo de 10 dias, resultando num aumento da concentração mínima inibitória (MIC) do TMP em 1000 vezes. Após exposição à solução de PPs, não foi desenvolvida resistência, validando a eficiência do processo de fotodegradação.

No Capítulo 3 é descrita a abordagem “*a priori*”, envolvendo o desenvolvimento de novas formas sólidas multicomponente baseadas em TMP para melhorar o desempenho do mesmo. Co-formadores apropriados e outros API foram selecionados com potencial para aumentar a solubilidade aquosa/velocidade de dissolução (VD) do TMP ou as suas propriedades antibacterianas. A triagem/desenvolvimento das formas sólidas multicomponente foi realizada usando uma abordagem mecanoquímica verde, assistida por etanol. Foram identificados 4 novos sais de TMP (1:1), com ácidos picolínico, salicílico, nicotínico (NIC) e ibuprofeno e sistemas com formação de eutéticos com paracetamol (PARA), curcumina (CURC) e ciprofloxacina (CIP), para os quais foram determinadas as composições eutéticas. Foi determinada a VD, verificando-se um aumento de 25% na VD do TMP ao usar o TMP-NIC e um aumento estatisticamente significativo de 5% com a mistura eutética TMP-PARA, ambos em comparação com o TMP. De seguida, a suscetibilidade da *E. coli* e *S. aureus* foi avaliada usando formas sólidas multicomponente selecionadas. Para a mistura TMP-CURC, uma diminuição estatisticamente significativa do valor da MIC do TMP (de 0.98 a ~ 0.36 $\mu\text{g mL}^{-1}$) foi determinada em *E. coli*, enquanto para *S. aureus* este valor aumentou de 3.54 a ~ 5.73 $\mu\text{g mL}^{-1}$. Por fim, foi avaliada a suscetibilidade de *E. coli* ao TMP e à CIP individualmente, numa mistura equimolar e usando a composição estimada para o eutético, $x_{\text{TMP}} = 0,85$. Uma diminuição na MIC para ambos os casos foi observada, demonstrando os benefícios da associação de dois antibióticos com mecanismos de ação diferentes, sendo esta uma possível solução clínica para uma melhoria da atividade antibacteriana.

No Capítulo 4, encontram-se descritas as técnicas, instrumentação e procedimentos experimentais seguidos e a completa caracterização de todos os materiais e produtos, assim como os respetivos estudos microbiológicos efetuados.

Palavras-chave: Degradação de antibióticos, catálise homogénea/heterogénea, anohídros magnéticos, macrociclos metalo-pirrólicos, sólidos multicomponente.

Abbreviations and Symbols

$[M]^+$	Molecular ion
$[M+H]^+$	Protonated molecular ion
% w/v	Weight by volume percent
% w/w	Weight by weight percent
β	Heating rate
2θ	Angle between the incident and reflected ray
δ	Chemical shift
ΔH^{ex}	Excess enthalpy of an undercooled melt made up of the components
$\Delta_{fus}H$	Enthalpy of fusion
$\Delta_{fus}H^*$	Experimental enthalpy of fusion of the pure compound
ΔpK_a	Difference between the negative base-10 logarithm of the base dissociation constant (K_b) and the acid dissociation constant (K_a)
ϵ	Molar absorption coefficient
λ	Wavelength
μg	Micrograms
ν	Stretching frequency
Φ_F	Fluorescence quantum yield
1H -NMR	Proton nuclear magnetic resonance
^{13}C -NMR	Carbon 13 nuclear magnetic resonance
1O_2	Singlet oxygen
$\cdot O_2^-$	Superoxide anion
$\cdot OH$	Hydroxyl radical
AB	Antibiotic
Abs	Absorbance
AB _{Smix}	Antibiotics' mixture
AcL	Acetylated lignin
AMR	Antimicrobial resistance
AMX	Amoxicillin
AOPs	Advanced oxidation processes
API	Active pharmaceutical ingredient
APTES	3-Aminopropyltriethoxysilane

aq	Aqueous
ATCC	American Type Culture Collection
BCS	Biopharmaceutical Classification System
C ₀	Concentration at time zero
CAF	Caffeine
Cat	Catalyst
CB	Conduction band
CCDC	Cambridge Crystallographic Data Centre
CFU	Colony forming units
CIP	Ciprofloxacin
CL	Confidence limits
CNT	Carbon nanotube
CoTDCPPS	Cobalt(III) 5,10,15,20- <i>tetrakis</i> (2,6-dichloro-3-sulphophenyl)-porphyrin
C _t	Concentration at time t
CURC	Curcumin
d	Doublet
dd	Doublet of doublets
dQ/dt	Heat flow
DCF	Diclofenac
DCS	Developability Classification System
DMA	<i>N,N</i> -Dimethylacetamide
DMF	<i>N,N</i> -Dimethylformamide
DMSO	Dimethyl sulfoxide
DNA	Deoxyribonucleic acid
DP	Degradation product
DPD	5,5-diphenylhydantoin
DSC	Differential scanning calorimetry
DTGS	Deuterated triglycine sulfate
e ⁻	Electron
EAFUS	Everything Added to Food in the United States
EbC	Total cell density
EC	European Commission
EC ₂₀	20% Effective concentration
EC ₅₀	Half maximal effective concentration

EPR	Electron Paramagnetic Resonance
Eq	Equation
Er	Percentage of growth inhibition
ErC	Specific growth rate
ERY	Erythromycin
ESI	Electrospray ionization
EUCAST	European Committee on Antimicrobial Susceptibility Testing
eV	Electronvolt
f_{fit}	Molecular flexibility
FAAS	Flame Atomic Absorption Spectroscopy
FDA	United States Food Drug and Administration
FDC	Fixed dose combination
FFA	Flufenamic acid
FTIR	Fourier-transform infrared spectroscopy
g	g -Force
GO	Graphene oxide
GRAS	Generally Recognized as Safe
h	Hours
h^+	Hole
HPLC	High-performance liquid chromatography
IBU	Ibuprofen
ICP-OES	Inductively coupled plasma - optical emission spectrometry
Igepal CO-520®	Polyoxyethylene (5) nonylphenylether (branched)
INM	Isonicotinamide
IR	Infrared spectroscopy
I.S.	Internal standard
IUPAC	Internal Union of Pure and Applied Chemistry
J	Coupling constant
k	Reaction rate constant
K	Adsorption coefficient of the reactant
k_{app}	Apparent first-order rate constant
l	Optical path length
L-H	Langmuir-Hinshelwood kinetic model
LAG	Liquid assisted grinding
LC-MS	Liquid chromatography – mass spectrometry

LDH	Layered double hydroxide
LEU	Leucine
LEV	Levofloxacin
LMCT	Ligand to metal charge transfer
m	Multiplet
m/z	Mass-to-charge ratio
m-CPBA	3-Chloroperoxybenzoic acid
MAN	Mannitol
MDR	Multidrug Resistance
MeOH	Methanol
MFA	Mefenamic acid
MH	Mueller-Hinton
MIC	Minimum inhibitory concentration
min	Minutes
MLCT	Metal to ligand charge transfer
Mn(Br ₈ T4CMPP)Cl	Manganese(III) 2,3,7,8,12,13,17,18-(octabromo)-5,10,15,20- <i>tetrakis</i> (4-carbomethoxyphenyl)porphyrin chloride
Mn(Br ₈ T4CPP)Cl	Manganese(III) 2,3,7,8,12,13,17,18-(octabromo)- 5,10,15,20- <i>tetrakis</i> (4-carboxyphenyl)porphyrin chloride
Mn(T4CPP)Cl	Manganese(III) 5,10,15,20- <i>tetrakis</i> (4-carboxyphenyl)porphyrin chloride
Mn(T4CMPP)Cl	Manganese(III) 5,10,15,20- <i>tetrakis</i> (4-carbomethoxyphenyl)porphyrin chloride
Mn(T2,3DCPP)Cl	Manganese(III) 5,10,15,20- <i>tetrakis</i> (2,3-dichlorophenyl)porphyrin chloride
Mn(T2,6CFPP)Cl	Manganese(III) 5,10,15,20- <i>tetrakis</i> (2-chloro-6-fluorophenyl)porphyrin chloride
MnTDCPP	Manganese (III) 5,10,15,20- <i>tetrakis</i> (2,6-dichlorophenyl)porphyrin acetate
MnTDCPPS	Manganese (III) 5,10,15,20- <i>tetrakis</i> (2,6-dichloro-3-sulfonatophenyl)porphyrin acetate
Mn(TPP)Cl	Manganese (III) 5,10,15,20-tetraphenylporphyrin chloride
MnTPPS	Manganese(III) 5,10,15,20- <i>tetrakis</i> (4-chlorosulfonylphenyl)porphyrin acetate
MNP	Magnetic nanoparticle
MOF	Metal Organic Framework
MS	Mass spectrometry
MTR	Metroxazole

MW	Microwave
N	Normality
NaY	Zeolite Y, sodium
NF	Nitrofurantoin
NG	Neat grinding
NIC	Nicotinic acid
ng	Nanograms
nm	Nanometers
NMR	Nuclear magnetic resonance
NOR	Norfloxacin
NSAID	Non-steroidal anti-inflammatory drug
OAc	Acetate
OECD	Organisation for Economic Cooperation and Development
OXA	Oxolinic acid
OTC	Oxytetracycline
PABA	4-Aminobenzoic acid
PARA	Acetaminophen/Paracetamol
PhIO	Iodosylbenzene
pH	Potential of hydrogen
PhI(OAc) ₂	(Diacetoxyiodo)benzene
PIC	Picolinic acid
pKa	The negative base-10 logarithm of the acid dissociation constant (Ka)
Por@AcL	Porphyrin encapsulated into acetylated lignin
PP	Photoproduct
ppm	Parts per million
ppb	Parts per billion
PCS	Photocatalyst surface
PTFE	Poly(tetrafluoroethene)
PVD	Physical vapor deposition
QUE	Quercetin
R	Ideal gas constant
RIB	Riboflavin
RNA	Ribonucleic acid
ROS	Oxygen reactive species

RP	Reverse phase
rpm	Rotations per minute
RT	Room temperature
s	Singlet
S/C	Substrate/Catalyst ratio
SAL	Salicylic acid
SEM	Scanning electron microscopy
SMPD	Sulfamethoxypyridazine
SMX	Sulfamethoxazole
SnTCPP	Tin (II) 5,10,15,20- <i>tetrakis</i> (4-carboxyphenyl)porphyrin
STP	Sewage treatment plant
t	Time
<i>t</i>	Triplet
t.t.	Thermal treatment
T_{fus}	Melting temperature
T_{fus}^*	Experimental melting temperature of pure compound
$T_{\text{fus}}^{\text{ex}}$	Melting temperature of the excess component
t_r	Retention time
TBR	Theobromine dihydrate
TC	Tetracycline
TCPP	5,10,15,20- <i>tetrakis</i> (4-carboxyphenyl)porphyrin
TDI	Toluene diisocyanate
TDCPP	5,10,15,20- <i>tetrakis</i> (2,6-dichlorophenyl)porphyrin
TDCPPS	5,10,15,20- <i>tetrakis</i> (2,6-dichloro-3-sulfonatophenyl)porphyrin
TDCPPSO ₂ Cl	5,10,15,20- <i>tetrakis</i> (2,6-dichloro-3-chlorosulfonylphenyl)porphyrin
TEM	Transmission electron microscopy
TEOS	Tetraethoxysilane
TFA	Tolfenamic acid
TG	Thermogravimetry
THF	Tetrahydrofuran
THPP	5,10,15,20- <i>tetrakis</i> (3-hydroxyphenyl)porphyrin
TIC	Total ion chromatogram
TLC	Thin-layer chromatography
TOC	Total Organic Carbon

TMP	Trimethoprim
TMPyP	5,10,15,20- <i>tetrakis</i> (1-methylpyridin-1-ium-4-yl)porphyrin chloride
TMS	Tetramethylsilane
TPP	5,10,15,20-tetraphenylporphyrin
TPPS	5,10,15,20- <i>tetrakis</i> (4-sulfonatophenyl)porphyrin
TPPSO ₂ Cl	5,10,15,20- <i>tetrakis</i> (4-chlorosulfonylphenyl)porphyrin
UPLC-MS	Ultra Performance Liquid Chromatography – Mass Spectrometer
URA	Uracil
USP	United States Pharmacopeia
UV-Vis	Ultraviolet-visible
UV	Ultraviolet
V	Volt
v/v	Volume by volume
VB	Valence band
V _{total}	Total volume
W	Watt
WHO	World Health Organization
WWTPs	Wastewater treatment plants
x_N	Molar fraction of compound N
x_{TMP}	Trimethoprim molar fraction
XRPD	X-ray powder diffraction
ZnTDCPPS	Zinc (II) 5,10,15,20- <i>tetrakis</i> (2,6-dichloro-3-sulfonatophenyl) porphyrin
ZnTHPP	Zinc (II) 5,10,15,20- <i>tetrakis</i> (3-hydroxyphenyl)porphyrin

Nomenclature

In this thesis, the IUPAC recommendations were followed for compounds naming and numbering, with exceptions for pharmaceuticals' names and porphyrins' nomenclature and numbering that will be described below.

Pharmaceuticals

For the nomenclature of pharmaceutical compounds was used the International Nonproprietary Name (INN) which is also reported in the abbreviations section. As an example, we select the following:

Pharmaceutical trivial name	IUPAC name	Abbreviation name
Trimethoprim	5-(3,4,5-Trimethoxybenzyl)pyrimidine-2,4-diamine	TMP
Sulfamethoxazole	4-Amino-N-(5-methylisoxazol-3-yl)-benzenesulfonamide	SMX
Ciprofloxacin	1-cyclopropyl-6-fluoro-4-oxo-7-piperazin-1-ylquinoline-3-carboxylic acid	CIP

Porphyrins

The porphyrins' name is attributing followed the Fischer [1] nomenclature, however the IUPAC [2] numbering system was used in the experimental chapter. Therefore, according to the IUPAC numbering system, all macrocycle carbon atoms are successively numbered from 1 to 20 and the internal nitrogen atoms from 21 to 24, as showed in **Figure I-a**. As reported by Fischer, porphyrin shows the *meso* positions (methylene bridge) reported as α , β , γ and δ , whereas the β -pyrrolic positions (external positions) are numbered from 1 to 8, as showed in **Figure I-b**.

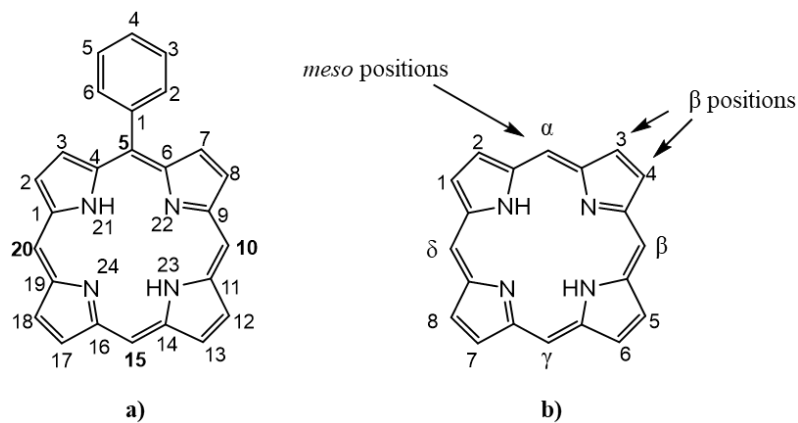


Figure I. Numbering system for tetrapyrrolic macrocycles: **a)** IUPAC and **b)** Fischer.

For the metallic tetrapyrrolic macrocycles the IUPAC nomenclature system is followed.

References

- [1] H. Fischer, H. Orth, Die Chemie des Pyrrols, Akademische Verlagsges, Germany 1934.
- [2] G.P. Moss, Nomenclature of tetrapyrroles, Pure and Applied Chemistry, 59 (1987) 779. <http://dx.doi.org/10.1351/pac198759060779>

Chapter 1

Introduction

1.1 Antibiotics: from being a solution to a big problem

The word “antibiotic” derives from Greek $\alpha\nu\tau\iota'$ + $\beta\iota\omicron\varsigma$, which literally means “against life” [1]. It arises from “antibiosis”, a term used for the first time by Vuillemin to define a process in which a life could destroy another [2]. Antibiotics (ABs) are in most cases, substances produced by bacteria and fungi which can kill or inhibit other microbial species [3]. Thus, they may be of natural origin, if generated by microorganisms, semisynthetic or synthetic, if obtained entirely in a laboratory. The first synthetic antibiotic was developed only in 1910 by Ehrlich and was named *Salvarsan*. This was an arsenic-based drug used to treat *Treponema pallidum*, a syphilis bacterium [4, 5]. Unfortunately, its application in clinical practise was short-lived, due to several side effects such as rashes, liver damage and even coma. These effects led to its clinical suspension and later it was supplanted by a sulfonamide drug, *Prontosil*, discovered by Domagk [4]. Due to their broad spectrum of action, sulfonamides were widely used in clinic, but their consumption was restricted until the discovery of penicillin by Fleming in 1928. The advent of penicillin represented the beginning of the “golden age” for antibiotics [6, 7]. Since then, antibiotics were massively used particularly in surgery (organ transplantation or open-chest surgery) avoiding numerous deaths due to bacterial infections. [4, 8, 9].

Nowadays, it exists a huge variety of antibiotics and they can be divided in several classes, according to their mechanism of action and their structure [10]: β -lactams (e.g. penicillin, cephalosporin) [11, 12], quinolones (e.g. ciprofloxacin, norfloxacin, levofloxacin) [13-15], tetracyclines (e.g. tetracyclin, doxycyclin) [16], antifolates (e.g. trimethoprim, sulfamethoxazole) [17, 18], aminoglycosides (e.g. streptomycin and gentamicin) [19, 20] and macrolides (azithromycin, erythromycin) [21-23] (**Figure 1.1**).

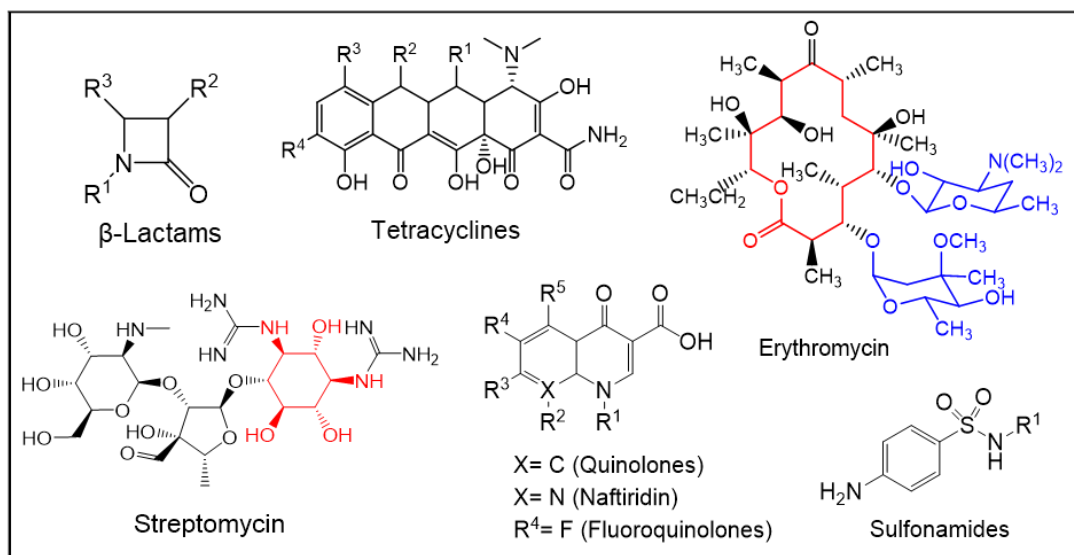


Figure 1.1 Examples of the six main ABs' classes.

Antibiotics may act in several ways and these mechanisms can be generally divided in [24]: i) inhibition of cell wall synthesis; ii) inhibition of protein synthesis; iii) inhibition of nucleic acid synthesis; iv) alteration of cell membranes and v) inhibition of metabolic pathways (**Figure 1.2**).

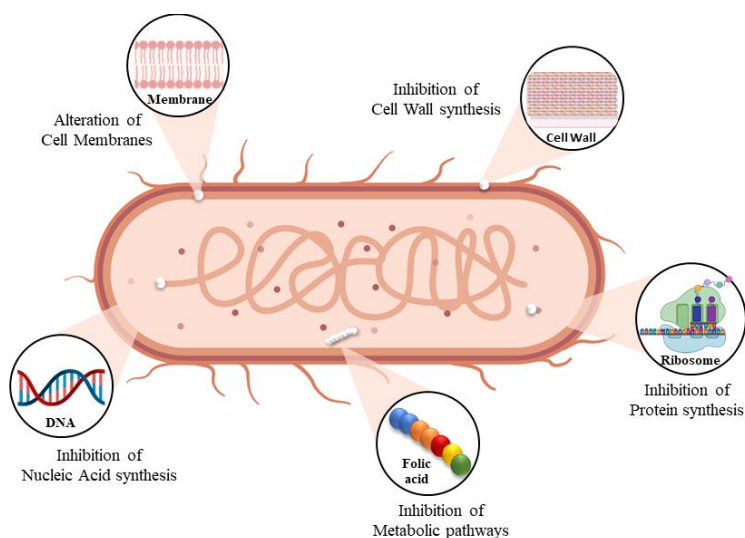


Figure 1.2 The five main ABs' mechanisms of action.

Over the years, if on the one hand, antibiotics have played an important role in the decrease of mortality, on the other hand their abuse has represented a huge concern. This is well portrayed in a study, reporting that, between the 2000 and 2015, antibiotics consumption increased about 65% worldwide [25, 26]. For instance, the Center for

Disease Control and Prevention (CDC), in USA, reported that around 47 million antibiotics therapies are incorrectly prescribed each year, intended to treat infections that do not require the use of antibiotic therapy. This number means that around 30% of antibiotics' prescriptions are unnecessary or, when necessary, may suffer from wrong prescription, dosage and treatment duration [27]. Furthermore, in 2018, the European Centre for Disease Prevention and Control reported that, in 29 European countries, 4264 tons of antibiotics were used in human, while 6358 tons were used in animal husbandry [28].

This massive consumption caused the development of resistant bacteria, which consequently led to the problem of Antimicrobial Resistance (AMR). AMR is the ability of infection causing microorganisms (e.g. bacteria) to be resistant to an antimicrobial agent (e.g. antibiotic) that could normally kill them or inhibit their growth. This phenomenon of resistance is the result of bacteria's high propensity for genetic mutations. If, in a given population of bacteria, a few antibiotic-resistant species are present among susceptible bacteria, they may survive when exposed to sub-therapeutic doses of antibiotics. In these conditions, the antibiotic susceptible bacteria will be preferentially eliminated, leaving room for the proliferation and spread of the antibiotic-resistant bacteria (**Figure 1.3**).

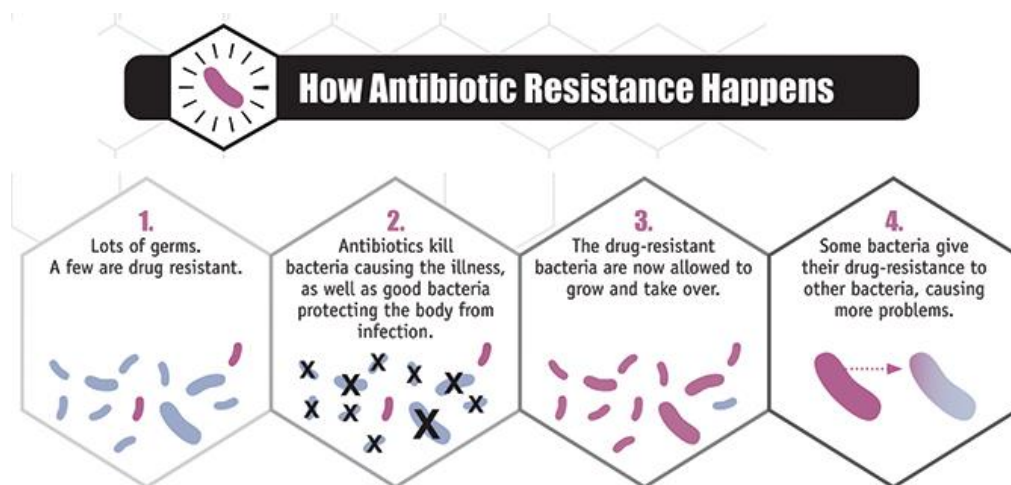


Figure 1.3 How antibiotic resistance happens. (Copyright Ref [29])

Furthermore, several microorganisms can possess resistance mechanisms against more than one antimicrobial agent, which led to the emergence of multidrug resistant bacteria, colloquially called “superbugs” [24]. Their surviving mechanisms against

stressful environmental factors to gain resistance is divided in (**Figure 1.4**) [24, 30, 31]: 1) Limiting access to the target, 2) drug modification, 3) target-site modification *via* genetic mutations and 4) activation of efflux pumps. Bluntly, the consequences of AMR are the increase in the number of deaths and treatment failures, as well as increased costs of care and long hospitalizations [32].

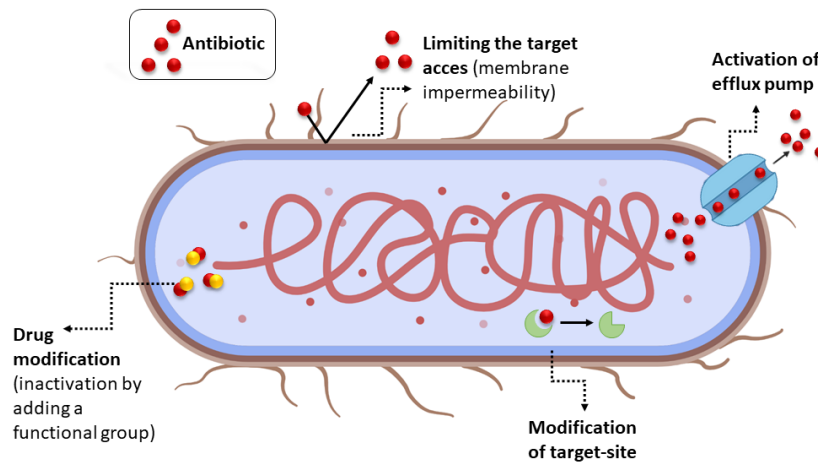


Figure 1.4 Four main antibiotic resistance mechanisms.

Considering the aforementioned aspects, it is straightforward to understand that AMR can spread easily in animal farming, in the community, in healthcare facilities and even through traveling [33]. Particularly, two main transmission chains have been identified: the first one involving the use of antibiotics in animal farming for treatment and prevention of infections and the second one attributed to the direct antibiotics' intake in the community. Regarding the first pathway, after the animals' antibiotics digestion, vegetables may be contaminated with AB-resistant bacteria from animal manure used as fertilizer and these can spread to humans through food or direct contact with animals. The second transmission pathway concerns direct antibiotic consumption by humans, following incorrect prescriptions or by incorrect drugs administration leading to a development of resistance as natural adaptive reaction. At the same time, whether in the community or at hospitals, resistant bacteria can spread either directly within people (*e.g.* hospital staff, patients and/or visitors) or indirectly, through poor hygiene and unclean surfaces and devices [34].

1.2 Fate of antibiotics in water

Expectedly, another relevant consequence of the massification of the antibiotics use in humans and animal husbandry is their spread into the environment due to the significant amount of antibiotics excreted as faeces and urine (from 30% up to 90%) [35]. Additionally, since animals' manure is very often reutilized as fertilizer, pharmaceutical residues can easily spread into groundwater. In this way, antibiotics contaminate aquatic ecosystems through surface runoff toward surface water and/or leaching to groundwater [36, 37]. Certainly, these are not the only two pathways how antibiotics can reach the environment, as improper waste disposal, including of medical waste, aquaculture, plant production and sewage treatment plant (STP) effluents represent a considerable percentage of ABs source [38] (**Figure 1.5**).

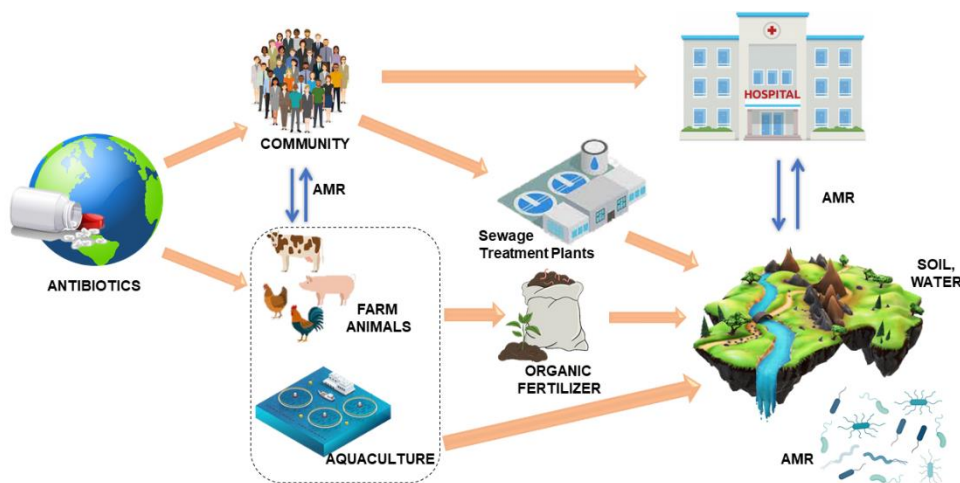


Figure 1.5 The main chains of antibiotics' spread in the environment.

As previously mentioned, ABs consumption is increasing worldwide, and their presence is commonly registered in soil [39, 40], sludge [41], municipal sewage [41], and particularly in water at different domains such as groundwater [42-44], surface water [45-47] and drinking water [48, 49]. For instance, in 2021, Gros *et al.* led a study about the detection of antibiotics, evaluating eleven different sites in three different seasons in Barcelona province, Spain. He reported the presence of tetracyclines (TC) and sulfonamides in concentrations of ng L^{-1} but the consequence of their persistence was visible in values of nitrates with a concentrations exceeding the 50 mg L^{-1} , in several water springs [44]. Besides, among all ABs the ciprofloxacin (CIP) displayed the highest concentration of 28-31 mg L^{-1} found in surface waters [38].

Antibiotics' concentrations detected in wastewater treatment plants (WWTPs) appear in the range of ng L^{-1} to $\mu\text{g L}^{-1}$, but their persistence and recalcitrant nature, as well as their by-products, causes much concern. The WWTPs plants are mainly based on activated sludge and can reduce pollutants in wastewater before discharging the treated water into watercourses. The problem is that these plants are not designed to treat and remove micropollutants such as pharmaceuticals and this obviously means that drugs, including antibiotics, “escape” without receiving any treatment. To this respect, Zhang *et al.* reported in 2015 that China, one of the main antibiotics' global producer and consumer, released 46% of antibiotics consumed into rivers through sewage effluents, whereas the remaining part was released into the soil through manure and sludge [50]. Furthermore, in the same year, Xu *et al.* revealed the presence of TC, sulfonamides and quinolones in secondary effluent at higher concentration values than those detected in the receiving river water [51]. Regarding the Europe, particularly the Mediterranean region, due to prolonged drought periods, the contaminated water flowing from WWTPs is mainly re-used for irrigation and aquifers replenishment [52].

Nevertheless, even if medicines are detected in low concentrations and therefore may not represent a direct risk to the human health, their presence in drinking water will always be one of the main focuses of concern. Hence, several studies have been reported on the presence of antibiotics in drinking water, to reveal potentially dangerous situations. In 2003, Schwartz *et al.* found resistant bacteria in both drinking water and wastewater in Germany [53]. This data could indicate the possibility of a bacteria direct transfer from wastewater to water network for human consumption. More recently, Sun *et al.* found resistant *E. coli* in drinking water from wells in rural China, considering this a possible source of human acquisition [54].

Additionally, another important aspect should be mentioned concerning antibiotics' excretion, as they can enter in the environment as unmetabolized antibiotics or as transformation/degradation products resulting from natural, biotic and/or abiotic processes. These degraded products represent another problem due to their different physicochemical and pharmacological properties, which could change their bioaccumulation. To that respect, during the last years, several authors reported the presence of trimethoprim (TMP) and its residues in Europe at different environmental domains [55]. This has been considered a pseudo-persistent drug since its transformation products remain continuously in the aquatic environment. It was detected in all influent

wastewater samples in a range of 100-6000 ng L⁻¹ [56] and in WWTPs effluent in range of 60-3000 ng L⁻¹. Indeed, higher concentrations were detected in hospital effluents, > 3 µg L⁻¹, confirming TMP frequent administration [57]. A relevant consequence of their persistence and bioaccumulation in water resides in the possible ecotoxicological effects that can interrupt life cycles of organisms living in the aquatic ecosystems, such as bacteria, algae, and invertebrates.

Development of effective strategies to avoid and prevent the accumulation of antibiotics in the environment and concomitant AMR spread is urgent. To answer to this global matter, in this thesis we consider two general strategies that can be followed: “downstream” and “upstream” approaches. The first one consists of the antibiotics destruction after their utilization by humans, developing new sustainable and catalytic systems such as Advanced Oxidation Processes (AOPs) to degrade and preferentially mineralize the antibiotics present in wastewaters. It is crucial to reduce the amount of degradation products and to ensure its reduced ecotoxicity and AMR spreading capability. The second strategy, an upstream approach, proposes the discovery of new pharmaceutical multicomponent solid forms involving the use of lower antibiotic loads to prevent the drugs accumulation in the environment. These discovered new solid-state forms should lead to an increase in Active Pharmaceutical Ingredient (API) bioavailability and/or to improvement in the antimicrobial activity. Bearing this in mind, we present the literature review referring to each of these topics in the next sections.

1.3 Aqueous antibiotics remediation processes: downstream approach

As previously mentioned, WWTPs plants cannot efficiently remove pharmaceuticals from water, so nowadays, new strategies for their removal/destruction were developed. In literature, several methodologies have been described and can be divided in: *in situ* techniques [58-60], membrane separation processes [61, 62], traditional and alternative processes.

Traditional treatments are divided in three main groups: physical and biological (e.g. filtration, coagulation–flocculation, sedimentation, and biological treatments) and chemical [63-65]. Table 1.1 presents general methodologies adopted to remove/destroy antibiotics, including their advantages and disadvantages.

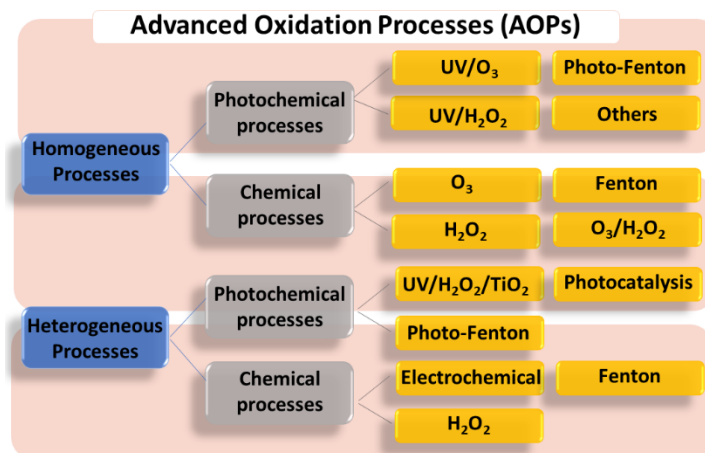
Table 1.1 General processes used to remove antibiotics.

Treatment	Method	Advantages	Disadvantages
Physical (non-destructive methods)	- Filtration - Adsorption - Extraction - Flocculation/Sedimentation - Air flotation	- Low cost - Safe and easy operational conditions	- High energy cost - Volatile emissions - Low removal rates
Biological (destructive methods)	- Aerobic - Anaerobic - Activated sludge	- Simple maintenance - Safe and easy operational conditions	- Volatile emissions - Necessity to remove sludge - Sensitive to antibiotics
Chemical (destructive methods)	- Chemical oxidation - Chemical precipitation - Combustion - Ion exchange	- High efficiency - Elimination of the dissolved pollutant	- High costs - Hard operational conditions

Unfortunately, these methods are quite inefficient in antibiotics treatment, due to their complex structure and their high chemical stability. In fact, physical processes usually show low pollutant removal rates, due to sludge formation [66]; whereas the biological procedures are quite interesting in terms of sustainability but strictly depend on the organic contaminants recalcitrant nature [67, 68]. Moreover, these techniques can be applied only when wastewater contains low concentrations of contaminants [69].

The Advanced Oxidation Processes (AOPs) are the most accredited strategies to mitigate the environmental drug accumulation, due to their ability to oxidize and degrade pollutants, including drugs, usually in less harmful products, promoting their destruction [70, 71]. During these processes, Reactive Oxygen Species (ROS) are generated *in situ*, especially hydroxyl radicals ($\bullet\text{OH}$), superoxide anions ($\bullet\text{O}_2^-$) and singlet oxygen ($^1\text{O}_2$). The excellent applicability of AOPs depends on the efficiency of $\bullet\text{OH}$ radicals, this being the second species with the highest oxidation potential (+2.8 V) after fluorine (+3.5 V), which rapidly react with numerous organic species with rate constants on the order of $10^8 - 10^{10} \text{ M}^{-1} \text{ s}^{-1}$. Furthermore, since $\bullet\text{OH}$ radicals have a short lifetime, approximately 10^{-9} s , they are generated *in situ* using oxidizing agents (such as H_2O_2 , O_2 or O_3), by irradiation (using ultraviolet light or ultrasound) or by catalyst utilization (such as photocatalysis, Fenton/photo-Fenton or metal complex catalysed oxidation). These processes could ideally degrade drugs until complete mineralization forming CO_2 , H_2O and inorganic ions [72, 73].

Since AOPs include several oxidation methods, they can be categorized in two main groups, the photochemical and the chemical processes (Scheme 1.1).



Scheme 1.1 Main types of AOPs used to remove organic pollutants from water.

The chemical methods do not need photonic energy to generate $\bullet\text{OH}$ radicals and include ozonation, alone or in combination with other agents (such as oxidation agents or catalysts), Fenton oxidation, persulfate methods, alone or in combination with iron catalysts. Some examples of each of these applications are described below. The most applied in the wastewater treatment are the ozonation and the Fenton processes. Regarding the ozonation, this method has been applied to remove many antibiotics dissolved in water in recent years. As an example, Garoma *et al.* conducted a study in which it was possible to remove 4 antibiotics of the sulfonamide class, including sulfamethoxazole (SMX), employing O_3 at different concentrations. The study revealed that a 99% degradation was observed at basic pH values in deionized water [74]. More recently, Östman *et al.* used a pilot scale ozonation system in a spiked sewage treatment plant (STP) effluent, to efficiently remove ($> 94\%$) four antibiotics, namely CIP, erythromycin (ERY), TMP and metronidazole (MTR) [75]. These results were possible due to the strong oxidant nature of O_3 , which forms high amounts of $\bullet\text{OH}$ radicals that react with organic pollutants. On the one hand, this methodology has several advantages, such as: no sludge production; easy elimination of non-reacted O_3 by decomposition into $\bullet\text{O}_2$; requirement of simple and small-scale installations. On the other hand, big limitations include the high cost of energy supplied to carry out the process and the consequent high cost of equipment maintenance. Additionally, if high levels of halogen atoms are dissolved in water, then ozonation leads to the generation of halogenated

species, which are carcinogenic [76]. Therefore, the use of O₃ has been improved through the combination with H₂O₂. As it is well known, by-products are usually formed during the degradation pathway, which may be recalcitrant toward the ozone oxidation. At this point, the simultaneous action of H₂O₂ may be crucial to achieve high mineralization degrees [77]. Gomes *et al.* reported, in 2017, a study in which a secondary effluent from municipal WWTP were spiked with diclofenac (DCF) and SMX and treated with O₃/H₂O₂. Degradation of SMX and DCF was observed after 45 min and 60 min, respectively, using values of concentration of 0.42 mM and 5 mM for O₃ and H₂O₂, respectively. After the oxidation, some inorganic salts and low molecular weight organic compound were detected [78].

Another highly used methodology is the Fenton process, which involves the use of iron salts (Fe²⁺/Fe³⁺) concomitantly with H₂O₂. Regardless of its cost, as large amounts of iron salt are required producing huge quantities of metal sludge, it has been applied in many industrial sectors [79]. To reduce the amount of these salts in the medium, efficient and stable solid catalysts have been developed originating the class of “heterogeneous Fenton-processes”. The most relevant aspects associated to this procedure are the high abundance and non-toxic nature of Fe²⁺, the non-toxicity and easy-handle of H₂O₂, the non-formation of chlorinated compounds which are carcinogenic and the operative simplicity [69, 80]. For instance, Gupta *et al.* applied the classical Fenton process to remove CIP from synthetic wastewater. After establishing operational optimized conditions of [H₂O₂]:[Fe²⁺] = 10, peroxide agent concentration of 14.2 mM and a pH value of 3, 70% of CIP degradation was obtained in 15 min with 55% of total organic carbon (TOC) removal and five degradation products (DPs) were identified [81]. Additionally, Wang *et al.* studied the application of two processes, the Fenton and Fe(II)-activated persulfate one, to degrade TMP in spiked deionized water. When the concentrations of H₂O₂ and Fe(II) were 1 mM and 0.05 mM, respectively, 55% of mineralization was achieved. On the contrary, applying Fe(II)-activated persulfate process, ~ 73% of TMP degradation, with a 40% of mineralization, were reported using concentration of both [persulfate] and [Fe(II)] = 4 mM. Transposing these systems for wastewater with spiked TMP, 36% and 45% of oxidation were observed for Fenton and Fe(II)-activated persulfate method [82]. Furthermore, an example of heterogeneous Fenton-like process is a recent work led by Xu *et al.*, in which the catalytic activity of a hybrid catalyst to remove MTR was evaluated. Designing a three-dimensional

macroporous graphene-wrapped zero-valent Cu nanoparticles synthesized by self-assembly process, 92% of MTR degradation was observed with the addition of H₂O₂ ([H₂O₂] = 2mM) [83]. It is worth noting that several drawbacks are associated with these methodologies, for instance the regeneration of Fe²⁺ during the oxidation meaning that the •OH radicals formation continues until the H₂O₂ disappearance; the formation of sludge at pH > 3.5 due to iron hydroxide precipitation and the possibility of complexation between Fe²⁺ or Fe³⁺ and organic ligands.

The other family of processes are designated as photochemical AOPs, which need the UV/Vis irradiation to destroy antibiotics. Ozonation coupled with H₂O₂ and UV radiation, ozonation only with UV, photo-Fenton processes and photocatalysis are the main ones yet implemented in water treatment [73, 84].

O₃ alone cannot generate •OH radicals and thus high concentrations are required to oxidize pollutants with acceptable mineralization values. This is overcome by combining O₃ with UV radiation, as large concentrations of radicals may be rapidly generated. Additionally, this method is applied to degrade acids, alcohols and organochlorines since organic compounds are excited by UV radiation, •OH radicals attacks are favoured. Although this technique seems to have a great potential, it shows two important drawbacks: the high cost to produce O₃ and UV light use. For instance, Pancan *et al.* performed a study in which the efficiency of O₃/UV process was evaluated on 38 pharmaceuticals and personal care products. The experiments were carried out in a system supplied with two flow reactors connected in series, both equipped with three 65 W lamps. The study was conducted by varying the ozone dosage and the hydraulic retention time. Finally, 31 compounds were degraded using [O₃] = 6 mg L⁻¹ in 10 min, whereas seven of them were still present in water due to their recalcitrant nature [85].

Using the ternary system O₃/H₂O₂/UV allows a more rapid O₃ decomposition due to the presence of both H₂O₂ and UV light, nevertheless still exhibiting the same limitations. For this reason, few works in the literature reported the application of this system in water treatment. Morandi *et al.* investigated the degradation of SMX using a UV photo-reactor ternary system equipped with a low-pressure mercury vapour lamp (5.7 W). Nevertheless, a full SMX degradation was achieved in 10 min at pH 7, with a [O₃] = 0.03 mM, at room temperature. Prolonging the irradiation for 30 min, 98% TOC mineralization was also obtained [86].

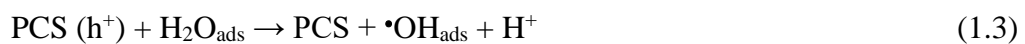
Among all these methods, the photo-Fenton system has been the most considered for water decontamination, as UV radiation accelerates the degradation of organic compounds and high concentration of $\bullet\text{OH}$ radicals are constantly produced during the entire process, avoiding the formation of secondary chlorinated oxidation products. Thus, many examples have been already reported in literature. For example, Guerra *et al.* studied the application of solar photo-Fenton on amoxicillin (AMX) and paracetamol (PARA) degradation. The study was conducted under natural light and using $\text{Fe}_2(\text{SO}_4)_3$ as iron source. The 90% of degradation was achieved for AMX in only 9 min, at pH value between 7-8 and using $[\text{H}_2\text{O}_2] = 0.08 \text{ mM}$ and $[\text{Fe}^{3+}] = 0.05 \text{ mM}$, with negligible mineralization [87].

Another process involves the use of photocatalysts, activated upon the absorption of radiation with energy above its bandgap. The main photocatalysts applied in the antibiotics photooxidation are hybrid materials based on semiconductors and based on organic photosensitizers (PS) immobilized on solid supports. Indeed, the most widely used photocatalytic materials are titanium dioxide (TiO_2)-based heterogeneous semiconductors [73, 88]. The oxidation mechanism starts when the semiconductor photocatalyst is irradiated and absorbs a radiation with an energy greater or equal to its band gap energy. At this point an electron (e^-)/hole (h^+) pair is formed in the valence band (VB) (Eq. 1.1).



When absorbed photons have higher energy than the semiconductor band gap energy, e^- will be excited and promoted from VB to conduction band (CB), leaving h^+ in the VB. These excited e^- and associated h^+ reduce and oxidize organic compounds adsorbed on the photocatalyst's surface (PCS) (**Figure 1.6**) [73].

The h^+ , due to the high oxidation potential, can promote oxidation reactions of organic contaminants or generate ROS species from water (especially $\bullet\text{OH}$ radicals) (Eqs. 1.2-1.3).



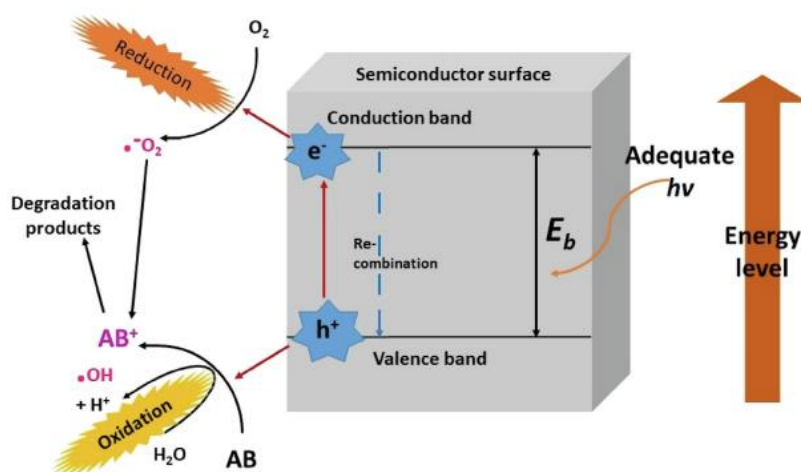
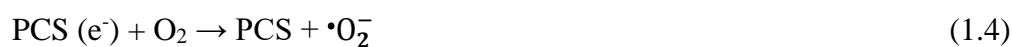


Figure 1.6 Schematic representation of antibiotic (AB) degradation using semiconductor-based heterogeneous catalyst. (Reproduced from [73]. Copyright 2021 Coordination Chemistry Reviews, Elsevier.)

Meanwhile, e^- located in CB, on the one hand can generate superoxide radical ion ($\bullet\text{O}_2^-$) reducing the oxygen dissolved in water which is subsequently converted in H_2O_2 (Eqs. 1.4-1.6) and on the other hand can reduce H_2O_2 in $\bullet\text{OH}$ species.



However, as we previously mentioned, an ideal oxidation mechanism should lead to the complete contaminant mineralization (Eqs. 1.7-1.8).



Many authors reported the application of TiO_2 -based photocatalysts modified with organic and inorganic moieties to extend their application also under solar irradiation conditions and avoid the fast recombination of e^- and h^+ in bulk and on photocatalyst surface. It is well known that the solar light is composed by only 3-5% of UV component, meaning that TiO_2 -based photocatalysis is less sustainable on industrial scale since it cannot be implemented under visible light conditions [89, 90]. Hence, many modifications have been proposed including heterojunctions involving the combination of TiO_2 with other semiconductors such as ZnO , SiO_2 , CdS permitting a better separation

of charge carriers and enhancing the visible light utilization [69, 91]. This improvement is also achieved when TiO₂ is doped with other metal ions, such as transition and noble metals, and non-metals, such as carbon, fluorine, nitrogen. In this way, the photocatalyst band gap is reduced and the surface area is enhanced. Furthermore, the photocatalyst immobilization on inorganic solid support improves the cost-effectiveness of the process increasing the catalytic performance and favouring the material recycling and reutilization [92].

In recent years, these photocatalytic systems have been particularly applied in the photooxidation of quinolones, with CIP commonly used as model AB [83]. For instance, Manasa *et al.* studied the performance of four boron and cerium doped TiO₂ photocatalysts on the CIP photodegradation under natural sunlight. Several experiments were carried out varying the catalyst composition, where the best photocatalysts contained 1% Ce-TiO₂ and 1% B-TiO₂, both favouring ~ 93% of CIP photodegradation in 180 min at neutral pH and 33 °C. Under these conditions, a remarkable mineralization (92% and 93%, respectively) was observed, concomitantly with high pseudo first-order kinetic constants. In both cases, the photocatalysts showed high stability after three reutilization cycles [93]. In another report, a series of TiO₂ and maghematite (γ -Fe₂O₃) co-doped graphene oxide (GO) nanosheets were designed and tested in the degradation of CIP. The heterogeneous material was prepared by self-assembly varying the TiO₂ concentration. A 99% of degradation was achieved in 140 min at pH of 6.6 and under visible light irradiation using a 300 W Xe lamp. The authors also performed reutilization tests for the photocatalyst, which maintained its activity for four cycles with pseudo first-order kinetics [94].

Other researchers studied the degradation pathways of sulfonamides using heterogenous TiO₂ and non-TiO₂-based materials. Regarding the SMX photodegradation using TiO₂-based photocatalyst, Jahdi *et al.* developed new nanocomposites doping TiO₂ with fluorine (F) and palladium (Pd) through microwave-assisted thermal synthesis. This new photocatalyst was tested using both solar simulator and direct sunlight irradiation, using 10% of Pd as a dopant, and up to 98% of SMX was eliminated within 40 min, with a consequent mineralization of 93% [95]. Furthermore, another example of nanocomposites developed for this purpose, was reported by Mourid *et al.*, who designed a calcined layered double hydroxide (LDH) impregnated by TiO₂ via coprecipitation method in alkaline medium (pH 10). A complete SMX photodegradation was observed

using a 10% of TiO₂ in the nanocomposite at basic pH and a high-pressure UV-A lamp (300 W). The process also revealed a 100% of mineralization after 144 h, probably due to the formation of •OH radicals, which were responsible for the oxidation. The authors also studied the photocatalyst reusability which, after five cycles, still showed ~ 90% of degradation [96].

In another study, Zhu *et al.* developed two semiconducting WO₃ based photocatalysts, containing graphitic carbon nitride (g-C₃N₄-WO₃) and carbon nanotubes (CNT-WO₃), prepared by hydrothermal method. Both were implemented in the SMX photooxidation using a 300 W visible light Xe lamp irradiation. In the first case a full removal was achieved after 90 min using the lamp and 95% was degraded in 2 h under natural sunlight conditions [97]. A 65% was obtained after 180 min with CNT-WO₃ and no loss of activity was detected after four reutilization cycles [98].

Samy *et al.* studied the photodegradation of TMP antibiotic using two photocatalysts (S-TiO₂ and Ru/WO₃/ZrO₂), both immobilized on circular aluminium plates by polysiloxane. The experiments were carried out using a 400 W metal halide lamp as light source and both photocatalysts were immobilized and both could completely degrade TMP in 240 min at pH 7. Furthermore, authors also performed catalytic reutilization tests for testing them both for four cycles revealing some loss in degradation efficiencies. The mechanism was also proposed and superoxide radicals, holes and hydroxyl radicals were found to be the main effectors [99]. Additionally, Villanueva *et al.* tested the efficiency of keratin–TiO₂ nanocomposite developed by keratin hydrogel with immersed TiO₂ nanoparticles on TMP removal from wastewater. These hydrogel nanocomposites absorbed and degraded the antibiotic in 30 min under simulated solar light produced by Xe lamp. They also studied the photocatalyst removal performance for four cycles with no loss in activity [100]. Furthermore, Wang *et al.* investigated the application of this technology in TMP degradation. The experiments were carried out in a photoreactor supplied with a high-pressure Hg lamp, varying the [H₂O₂] between 0.03 and 5 mM, the [Fe²⁺] between 0.03 and 2 mM and the range of pH between 2.5 and 4.5. A 99% of TMP oxidation was observed after 6 min at room temperature and under optimized conditions of [H₂O₂] = 0.09 mM, [Fe²⁺] = 0.09 mM and pH value of 4.5 [102].

1.4 Porphyrins as catalysts in antibiotic AOPs

Porphyrins have emerged as valid alternatives in AOPs, due to their multifunctional properties, which arise from their amenable modulability and capability to coordinate with more than 70 metals from the Periodic Table. Porphyrins are tetrapyrrole derivatives, composed by four pyrrole subunits interconnected *via* –CH= bridges and contain an inner core formed by 18 π electrons. They are involved in key vital processes, for instance the heme group (protoporphyrin IX – Fe(II) complex) which is responsible for xenobiotics metabolism [101]. Free-base porphyrins can absorb visible light, particularly in the regions of 400-450 nm and 500-660 nm [102-104]. Therefore, considering the main goal of this thesis, as well as the recent interest for this topic in both catalytic and photocatalytic applications, we present the state of art in the next sections.

1.4.1 Antibiotics oxidative porphyrin-based catalytic degradation

Owing to their widespread applicability, there has been a growing use of biomimetic synthetic metalloporphyrins as catalysts for oxidation reactions [105-112]. Nevertheless, their use as catalysts for oxidative degradation of pollutants has been less reported [1, 113-121], and even less for degradation of antibiotics [1]. Their implementation, particularly in pollutants abatement, has reached a rapid and massive interest during the last decades, due to the rising need for the development of sustainable oxidative catalytic processes involving the use of benign oxidant agents (*e.g.* H₂O₂ and O₂) [108, 122], in detriment of other hazardous oxidants that are commonly used [123], as well as the use of less toxic metals such as manganese (Mn) and iron (Fe), given their particular stability in multiple oxidation states.

Several studies have been reported about the combination of metalloporphyrins and H₂O₂ in pollutants degradation. The general mechanism showing the biomimetic action of metalloporphyrins in environmental remediation, involving water as medium and H₂O₂ as oxidant, is schematically represented in **Figure 1.7** [1, 106, 124].

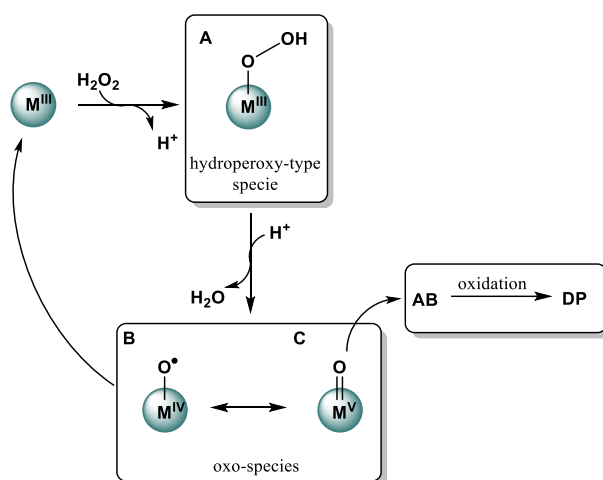


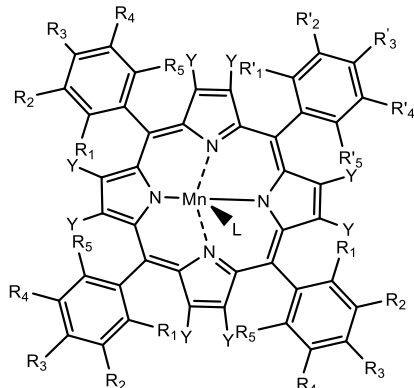
Figure 1.7 Schematic representation of general antibiotic oxidation mechanism using H₂O₂ and metalloporphyrin as catalyst.

First, the central metal can coordinate with the peroxide, forming hydroperoxy-species, A. Then, the oxidation of metal with consequent water elimination allows to form oxo-species, B and C. It is well accepted that several factors may influence the formation of these species, involving heterolytic or homolytic cleavage of O-O bond, such as metal ions, solvents, functional groups in the porphyrin structure and the peroxide agent. So, when the porphyrin is substituted by electron-withdrawing groups, in presence of a highly protic solvent such water, the heterolytic cleavage inducing the formation of the oxo species B and C is preferred [109, 125]. Meunier *et al.* studied the metalloporphyrin structural influence and divided them in first-generation catalysts, based on *meso*-tetraphenyl porphyrin (TPP) and their *p*-substituted analogues, which lacked stability when coordinated with H₂O₂. Second-generation catalysts were constituted by *meso*-TPP bearing halogen atoms in *ortho*-positions at phenyl rings, which improved the robustness, activity, and selectivity of the catalysts prepared thereof [126, 127]. Finally, the third-generation catalysts were known for the introduction of withdrawing group in *beta*- or *meso*-positions of the macrocycles, which has, unquestionably, delivered even more active and selective catalysts; however, with much diminished stability towards the reaction conditions [128].

Concerning the application of metalloporphyrin based catalysts for the oxidative degradation of antibiotics, there are only a very few literature examples reported, which are summarized in Table 1.2.

Table 1.2 State of art regarding antibiotics oxidative degradation catalysed by homogeneous metalloporphyrins.

#/Ref	Catalyst	AB	Experimental Conditions	Comments
1[129]	Mn(TPP)Cl Mn(T4CMPP)Cl Mn(Br ₈ T4CMPP)Cl	CIP	- Matrix: Distilled water/ CH ₃ CN - [Mn(TPP)Cl]= 0.02 g L ⁻¹ [Mn(T4CMPP)Cl] = 0.03 g L ⁻¹ [Mn(Br ₈ T4CMPP)Cl] = 0.04 g L ⁻¹ - oxidant: H ₂ O ₂ , PhIO, <i>m</i> -CPBA -pH = N/A; T = 25 °C	- 76% CIP removal (24 h) with Mn(T4CMPP)Cl and PhIO -Mechanism by •OH -Oxidation pathway proposed
2[123]	Mn(T4CPP) Mn(Br ₈ T4CPP)	CIP LEV	- Matrix: phosphate:CH ₃ CN buffer, CH ₃ CN -[Mn(T4CPP)] = 0.03 g L ⁻¹ [Mn(Br ₈ T4CPP)] = 0.04 g L ⁻¹ - oxidant: H ₂ O ₂ , PhIO, <i>m</i> -CPBA, PhI(OAc) ₂ -pH = N/A; T = 25 °C	- 100% CIP removal (24 h) in phosphate:CH ₃ CN buffer with Mn(Br ₈ T4CPP) and PhIO - 98% LEV removal (24 h) in CH ₃ CN with Mn(T4CPP) and <i>m</i> -CPBA -Mechanism by •OH -LEV oxidation pathway proposed
3[125]	Mn(TPP)Cl Mn(T2,3DCPP)Cl Mn(T2,6CFPP)Cl	NOR	- Matrix: H ₂ O (dist.)/ CH ₃ CN -[Mn(TPP)Cl]= [Mn(T2,3DCPP)Cl] = [Mn(T2,6CFPP)Cl] = 0.04 g L ⁻¹ - oxidant: H ₂ O ₂ , <i>t</i> -BuOOH, Oxone® -pH <6; T = 25 °C	- 58% NOR removal (24 h) with Mn(T2,3DCPP)Cl and Oxone® -Mechanism by •OH, •SO ₄ ⁻ -Oxidation pathway proposed



Mn(TPP)Cl	R ₁ ,R ₂ ,R ₃ ,R ₄ ,R ₅ ,R' ₁ ,R' ₂ ,R' ₃ ,R' ₄ ,R' ₅ =H; Y=H; L=Cl
Mn(T4CMPP)Cl	R ₃ =R' ₃ =COOCH ₃ ; R ₁ ,R ₂ ,R ₄ ,R ₅ ,R' ₁ ,R' ₂ ,R' ₄ ,R' ₅ =H; Y=H; L=Cl
Mn(Br₈T4CMPP)Cl	R ₃ =R' ₃ =COOCH ₃ ; R ₁ ,R ₂ ,R ₄ ,R ₅ ,R' ₁ ,R' ₂ ,R' ₄ ,R' ₅ =H; Y=Br; L=Cl
Mn(T4CPP)	R ₃ =COOH; R' ₃ =COO ⁻ ; R ₁ ,R ₂ ,R ₄ ,R ₅ ,R' ₁ ,R' ₂ ,R' ₄ ,R' ₅ =H; Y=H; L=none
Mn(Br₈T4CPP)	R ₃ =COOH; R' ₃ =COO ⁻ ; R ₁ ,R ₂ ,R ₄ ,R ₅ ,R' ₁ ,R' ₂ ,R' ₄ ,R' ₅ =H; Y=Br; L=none
Mn(T2,3DCPP)Cl	R ₁ ,R ₂ ,R' ₁ ,R' ₂ =Cl; R ₃ ,R ₄ ,R ₅ ,R' ₃ ,R' ₄ ,R' ₅ =H; Y=H; L=Cl
Mn(T2,6CFPP)Cl	R ₁ ,R' ₁ =Cl; R ₅ ,R' ₅ =F; R ₂ ,R ₃ ,R ₄ ,R' ₂ ,R' ₃ ,R' ₄ =H; Y=H; L=Cl

These reports used homogeneous conditions, the metalloporphyrins were complexed with Mn and used to oxidize quinolone-type antibiotics. Lage *et al.* tested first-, second- and third-generation Mn-porphyrins as catalysts to oxidize CIP in four different media (methanol, water, ethanol and acetonitrile) and using three oxidants (H₂O₂, PhIO, *m*-CPBA) (Table 1.2, entry 1) [129]. The best result achieved was 76% of CIP degradation in CH₃CN, using the 2nd-generation Mn(T4CMPP)Cl as catalyst and iodosylbenzene (PhIO) as oxidant. Indeed, authors explained that although the PhIO high toxicity it permitted the formation of no toxic degradation products eliminating the CIP antibacterial activity due to the alteration of the pharmacophore of fluoroquinolone. When using H₂O₂ and *m*-CPBA, the fluoroquinolone moiety remained intact. The same group later discriminated the catalytic performance between water-soluble 2nd- and 3rd-generation Mn-porphyrins in CIP and LEV homogeneous degradation, using several oxidant agents (H₂O₂, PhIO, *m*-CPBA and PhI(OAc)₂) (Table 1.2, entry 2) [123]. The catalytic experiments were performed in CH₃CN and phosphate:CH₃CN buffer as media. The authors were able to degrade CIP using both generations of catalyst and with each oxidant but the high degree of CIP oxidation was achieved with the system Mn(Br₈T4CPP)/PhIO, in buffer condition. This system was also the most selective one allowing the formation of only one product. On the other hand, levofloxacin (LEV) showed 98% degradation in CH₃CN, using Mn(Br₈T4CPP) as catalyst and *m*-CPBA as oxidant, favouring the formation of only one oxidized product. In this work, they underlined that the presence of electron-withdrawing substituents at β-pyrrolic positions led to the formation of the high-valence active species. The last example is reported by Meireles *et al.*, who evaluated the efficiency of several Mn-porphyrins in norfloxacin (NOR) homogeneous oxidation (Table 1.2, entry 3) [125]. The authors performed the catalytic experiments using several oxidant agents (H₂O₂, *t*-BuOOH and Oxone®). The Mn(T2,3DCPP)Cl exhibited the best performance reaching ~ 58 %, NOR degradation, using Oxone® (KHSO₅) as oxidant. Authors attributed this result to: i) presence of a total of eight chlorine atoms in the aryl-groups at the *meso*-positions of the macrocycle, allowing the formation of Mn(V)-oxo species; ii) absence of halogen atoms in one of the *ortho*-positions of the *meso*-aryl groups which facilitate the NOR approach to these more reactive Mn species.

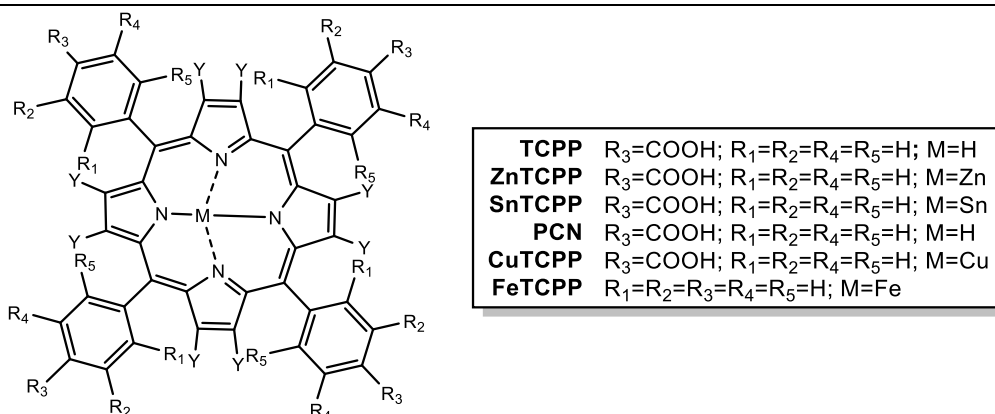
It should be mentioned that, to the best of our knowledge, AOPs using metalloporphyrins as catalysts have been exclusively reported under homogeneous

conditions for antibiotics degradation. To date, no reports on the use of immobilized porphyrins had been delivered and therefore this is one of the main goals of our work. Indeed, to transform metalloporphyrins into suitable real-world application catalysts, it is crucial to promote their immobilization onto solid supports to improve their stability and allow their reutilization. For this reason, the immobilization of metalloporphyrins on inorganic supports may overcome these shortcomings, being that a major goal of the studies described in Chapter 2 [130, 131].

1.4.2 Antibiotics photocatalytic degradation

Besides the use of metalloporphyrins as catalysts in chemical oxidative degradation processes, they can also be used as efficient photocatalysts due to their high absorption in UV-Vis region. Furthermore, they have high quantum yields of triplet state, which may be improved through metal complexation or halogen atom incorporation [132, 133]. When a photocatalyst is in its triplet excited state, after absorbing visible irradiation at a suitable wavelength, its interaction with O₂ can occur through two mechanisms, defined as Type I and II. A type I mechanism involves the direct or indirect electron transfer between the photocatalyst and O₂ promoting the formation of •OH and •O₂ radicals; whereas the type II occurs by energy transfer involving the formation of singlet oxygen (¹O₂) [134-136]. These reactive species will promote the contaminants degradation.

Thus, there are several review papers in recent literature describing the use of tetrapyrrolic macrocycles (phthalocyanines and porphyrins) as homogeneous or heterogeneous photocatalysts for photodegradation of organic pollutants including antibiotics [1, 134, 137]. In line with our goals of developing hybrid materials for aqueous antibiotics photodegradation, we critically selected relevant reports on the field, which are presented in Table 1.3.

Table 1.3. State of art regarding antibiotics photodegradation using porphyrin-based heterogeneous catalysts.

#/Ref	Catalyst	AB	Experimental Conditions	Comments
1[138]	TCPP@rGO-Bi ₂ WO ₆	TC	- Matrix: Distilled water - Visible light (300 W Xenon lamp) -[TCPP@rGO-Bi ₂ WO ₆] = 0.3 g L ⁻¹ -pH = 7; T = N/A	- 84% TC removal (60 min) -Mechanism by •O ₂ and h ⁺ -Reutilization cycles: 5 -Oxidation pathway: N/A
2[139]	10%ZnTCPP@g-C ₃ N ₄	TC	- Matrix: Distilled water - Visible light (300 W Xenon lamp) -[ZnTCPP@g-C ₃ N ₄] = 0.15 g L ⁻¹ -pH = 7; T = N/A	- 80% TC removal (120 min) -Mechanism by •OH -Reutilization cycles: 5 -Oxidation pathway proposed
3[140]	12%SnTCPP/30% Bi ₂ WO ₆ /g-C ₃ N ₄	LEV	- Matrix: Distilled water - Visible light (250 W Xenon lamp) -[12%SnTCPP/30% Bi ₂ WO ₆ /g-C ₃ N ₄] = 1 g L ⁻¹ -pH = 7; T = N/A	- 86% LEV removal (150 min) -59% TOC release (10 h) -Mechanism by •OH -Reutilization cycles: N/A -Oxidation pathway proposed
4[141]	PCN-224 (300nm)	TC CIP	- Matrix: Distilled water - Visible light (500 W Xenon lamp) -[PCN-224] = 0.25 g L ⁻¹ -pH = 7; T = N/A	- 92% TC removal (180 min) -82% CIP removal (180 min) -Mechanism: N/A -Reutilization cycles: 5 -Oxidation pathway: N/A

5[142]	CuTCPP MOF	TC NOR	- Matrix: Distilled water - Visible light (300 W Xenon lamp) -[CuTCPP MOF] = 0.05 g L ⁻¹ -pH = 5-9; T = 25 °C	- 72% TC removal (360 min; pH 5) -44% NOR removal (360 min; pH 9) - Mechanism by •O ₂ and h ⁺ -Reutilization cycles: N/A -Oxidation pathway: N/A
6[143]	CuTCPP@TiO ₂	OXA OTC	- Matrix: Distilled water - Solar simulator (300 W) -[CuTCPP@TiO ₂] = 0.02 g L ⁻¹ -pH = 7; T = N/A	- 68% OXA removal (40 min) - 63% OTC removal (40 min) - Mechanism: N/A -Reutilization cycles: N/A -Oxidation pathway: N/A
7[144]	FeTPP–TDI–TiO ₂	TC NOR	- Matrix: Distilled water - Visible light (150 W Xenon lamp) -[FeTCPP–TDI–TiO ₂] = 1 g L ⁻¹ -pH = N/A; T = N/A	- 99% TC removal (120 min) - 99% NOR removal (120 min) - Mechanism: N/A -Reutilization cycles (TC): 5 -Oxidation pathway proposed

The literature regarding the photodegradation of antibiotics is very prolific in the use of heterogenized photocatalysts. The tetracycline family has been one of the most studied over the last few years and several groups described the TC degradation fate incorporating porphyrins onto semiconducting photocatalysts. For instance, Hu *et al.* developed a ternary Z-scheme heterojunction incorporating bismuth tungstate (Bi₂WO₆) with reduced graphene oxide (rGO) and *meso*-tetra(4-carboxyphenyl)porphyrin (TCPP) (Table 1.3, entry 1). Under visible light irradiation (300W Xe lamp), 84% of TC degradation was achieved in just 60 min. Authors also demonstrated that the mechanism took place by •O₂ and h⁺ species and the photocatalyst was reused along 5 irradiation cycles [138]. Ma *et al.* developed a heterogeneous photocatalyst constituted by the Zn(II) TCPP and the polymeric graphitic carbon nitride (g-C₃N₄) and applied into the TC photooxidation (Table 1.3, entry 2) [139]. The g-C₃N₄ is a metal-free semiconductor with a moderate band gap (~ 2.7 eV), low toxic and high chemical stability. It can be easily synthesized by thermal condensation from its precursor

(*e.g.* thiourea or melamine). When used in combination with ZnTCPP, it allowed to achieve a 80% of TC degradation in 120 min, as a result of the favourable electrostatic linkage formation between the porphyrin's carboxyl groups and the polymer's amino groups [139]. Meanwhile, the same authors designed a cascade system, by coupling Sn(II) TCPP with g-C₃N₄ and Bi₂WO₆ (Table 1.3, entry 3) [140]. Particularly, a 12% SnTCPP/30% Bi₂WO₆/g-C₃N₄ exhibited the best photocatalytic performance, degrading 85% of LEV in aqueous medium, reaching 59% of TOC release, after 10 hours of visible light irradiation with a 250 W Xe lamp. They also tested the material reutilization and along 5 reutilization cycles no loss of activity was observed [140]. More recently, Zong *et al.* developed a porphyrin-based zirconium metal organic framework (MOF) material, PCN-224, for the photodegradation of TC and CIP (Table 1.3, entry 4) [141]. Under visible light irradiation with a 500 W Xe lamp, a 92% and 82% of TC and CIP were reached in 180 min, respectively. Authors also performed five reutilization cycles without loss of catalytic efficiency. Another example of porphyrin-based MOF photocatalyst was given by Zhao *et al.* (Table 1.3, entry 5) [142]. The author prepared a Cu(II) TCPP-based MOF material to photodegrade 72% of TC and 44% of NOR in 360 min, upon irradiation with a 300 W Xe lamp. The photooxidation pathway occurred following a 2nd order kinetic rate involving h⁺ and •O₂ species.

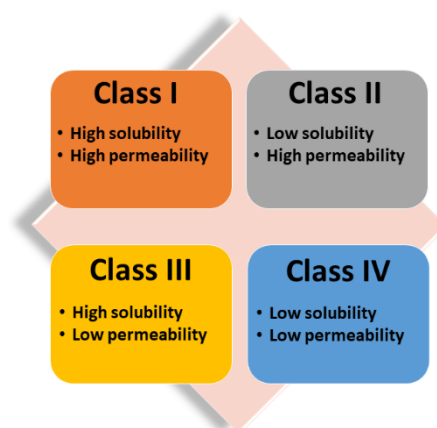
Furthermore, Gaeta *et al.* developed a TiO₂ nanomaterial based on CuTCPP, ZnTCPP and TCPP to photodegrade oxolinic acid (OXA) and oxytetracycline (OTC) (Table 1.3, entry 6) [143]. The CuTCPP@TiO₂, prepared by adsorption of CuTCPP on the TiO₂ surface, favoured by strong interactions between the carboxylic acid groups and the surface, exhibited the highest catalytic efficiency and under simulated solar irradiation, degrading 70% and 60% of OXA and OTC, respectively [143]. Following this study, Yao *et al.* developed a new photocatalyst combining the TiO₂ with Fe(II)-TCPP bonded through toluene diisocyanate (TDI), used as a bridging molecule, FeTCPP–TDI–TiO₂ (Table 1.3, entry 7). This hybrid material was able to fully degrade TC in 2 h of visible light irradiation, using a 150 W Xe lamp. The authors additionally performed five cycles of photocatalyst reutilization. The study was further extended to the complete photodegradation of NOR [144].

The works herein discussed reveal the topicality of this field and converge to our goals of promoting the immobilization of porphyrins to implement a heterogeneous photodegradation processes to degrade antibiotics, directly in aqueous medium.

1.5 Development of new pharmaceutical multicomponent solid forms: upstream approach

As mentioned above, the development of effective AOPs for the degradation of antibiotics may be a highly pursued goal, but it is not the only way to mitigate their presence in the environment, especially in water domains, and to prevent AMR proliferation. In our perspective, it is also reasonable to invert the thinking, by finding novel protocols to reduce the impact of pharmaceutical drug administration, in an upstream approach. Thus, bearing that in mind, we also directed our focus towards this issue, and propose developing new pharmaceutical solid forms with a lower antibiotic load, aiming to diminish antibiotics needs. These new solid forms should impact on the API aqueous solubility/dissolution rate and therefore on its oral bioavailability, and/or use co-formers that can contribute to an enhanced antibiotic activity.

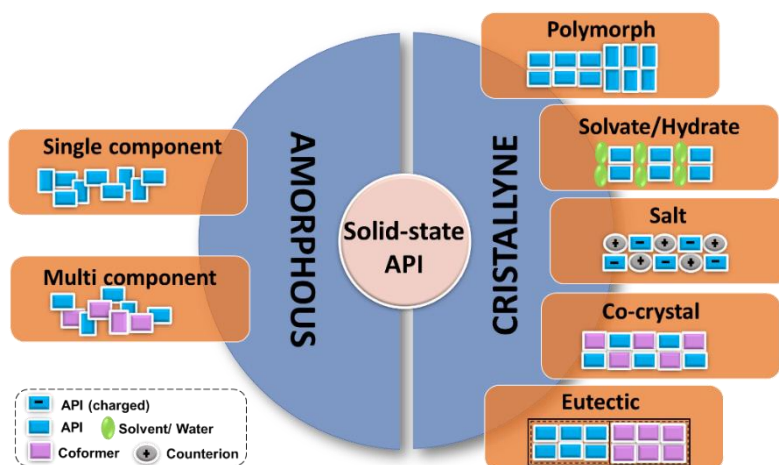
The majority of pharmaceuticals are given to patients in solid-state forms, such as powders, tablets or capsules, as these are cheaper, more stable and easier to administrate. During the early 21st century, both academia and industry increased their interest on active pharmaceutical ingredient (API) solid forms, due to their potential to impact on the performance of drugs orally taken [145-147]. For instance, many APIs are characterized by their poor aqueous solubility, being included in the Biopharmaceutical Classification System (BCS) classes II and IV [148], Scheme 1.2, meaning hard consequences in terms of low absorption and oral bioavailability [149-151].



Scheme 1.2 Schematic representation of Drugs BCS classification.

The physicochemical properties of solid forms depend on their composition, on the packing, and relevant properties such as stability, aqueous solubility, dissolution rate, antibacterial activity may be eventually tuned by screening the most effective solid form.

Active pharmaceutical ingredients solid forms can be divided into amorphous and crystalline (Scheme 1.3).



Scheme 1.3 Schematic classification of the main solid-state pharmaceutical forms.

Amorphous solids are metastable phases characterized by the absence of long-range order. They can be single component and may be kinetically stabilized by dispersion in a solid matrix, usually a polymeric one [152]. Co-amorphous are multicomponent amorphous materials made up of the API and of low molecular weight co-formers, that contribute to kinetic stabilization due to mixing effects and intermolecular interactions [153, 154].

Crystalline forms can also be subdivided in single-component and multi-component solids. The first class is limited to polymorphs, suggesting a narrow possibility to tune the physicochemical properties [155]. Multicomponent crystalline solids include salts, solvates/hydrates, co-crystals, ionic co-crystals, salt solvates, co-crystal solvates, eutectic mixtures [156-158] (Scheme 1.3).

The use of salts has been the most common approach to modulate the APIs' physical properties, and more than half of the commercialized drugs are administrated as salt forms [159]. Salt formation is predicted to occur when the $\Delta pK_a = pK_{a_{base}} - pK_{a_{acid}} > 3$ [160] and are preferred, as they significantly increase the

solubility of drug molecules. As an example, a study was performed, where three salts were prepared combining norfloxacin, BCS class IV [161], with succinic, malonic and maleic acids, as well as a co-crystal of norfloxacin and isonicotinamide [162]. After equilibrating for 72 h, the apparent aqueous solubility was measured: 0.21 mg/mL for NOR, whereas for the co-crystal it was 0.59 mg/mL and 3.9 mg/mL and 9.8 mg/mL for the malonate and the maleate salts, respectively. These results demonstrated the ability of salts (and of co-crystals) to increase the API solubility. Salt formation is limited, of course, to APIs that have acidic or basic groups. There is also a limited number of counterions that are pharmaceutically acceptable [163].

Co-crystals are formed by the API and one or more pharmaceutically acceptable co-formers. The United States Food Drug and Administration (FDA) published a guidance to regulate the classification of pharmaceutical co-crystals in 2018, in which co-crystal was defined as “crystalline material composed of two or more different molecules, typically API and co-formers, in the same crystal lattice” [164]. The components do not interact to form a salt, and all of them are solids, when pure at ambient conditions (which distinguishes co-crystals from solvate/hydrates [165]). In the co-crystal structure, supramolecular synthons are the smallest structural units within the “supermolecules”, which can be assembled *via* intermolecular interactions [166]. Supramolecular synthons can be divided in two main groups (**Figure 1.8**): homosynthons, for instance carboxylic acid dimer (**Figure 1.8 A**) and amide dimer (**Figure 1.8 B**), and heterosynthons, such as carboxylic acid-amide (**Figure 1.8 D**) and carboxylic acid-aromatic nitrogen (**Figure 1.8 C**).

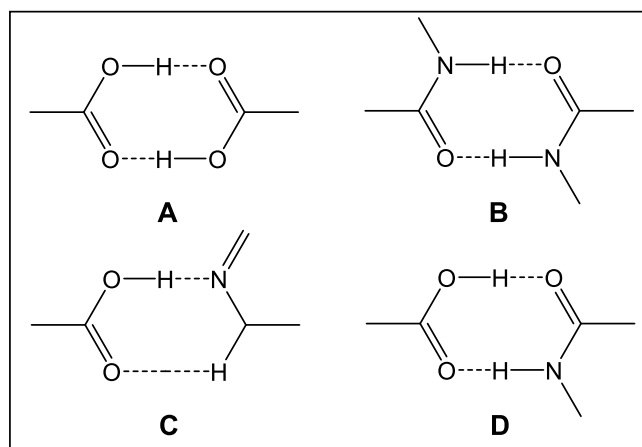


Figure 1.8 Some common supramolecular synthons found in co-crystals.

The intermolecular forces involved in the synthon's connections are mostly hydrogen bonds, due to their directionality and its natural abundance. Among all, van der Waal forces, halogen bonds and π - π interactions in aromatic structure also contribute to co-crystal formation [167]. When the heterosynthon is formed between an acid group and a basic one, the distinction between a co-crystal and a salt is sometimes not straightforward, as it depends on the relative position of the hydrogen atom between the donor and the acceptor groups [168].

The co-former choice is the key step in pharmaceutical co-crystal development. A large number of potential co-formers can be chosen, such as compounds from FDA's Everything Added to Food in the United States (EAFUS) or Generally Recognized as Safe (GRAS) lists: any excipient, neutral, acid or basic substance could be considered as long as it is pharmaceutically acceptable. The co-former needs to hold certain features, such as complementary functional groups which can, *a priori*, interact with the API forming supramolecular synthons [169]. This is a starting guideline, however, despite some attempts to try to predict co-crystal formation [170-174], this is still largely a trial-and-error task. Furthermore, an additional API could be used as co-former, forming multi-API co-crystals, in order to enhance properties and biological activity of one or both APIs in the new solid form [175]. For instance, the meloxicam-aspirin co-crystal compared with meloxicam, decreased the time required to reach the human therapeutic concentration [176]. Among the limited reports presented in literature, amoxicillin-clavulanate co-crystal is also another relevant example, since this combination improved the antibiotic activity against non-*beta* lactamase bacterial, *Sarcina lutea* [177]. Co-crystal formation may also be preferred when one of the API presents polymorphism. The new co-crystal form can also improve the stability of each component, avoiding undesired alterations in the drug's performance due to a change between polymorphs [178]. Other substances that have been used as co-formers are nutraceuticals, such as flavonoids and vitamins, which are molecules found in food, with medical and health benefits [175, 179]. Despite their poor bioavailability, these compounds provide cost-effective synergic combinations, when in co-crystal form, improving physicochemical properties, in combination with the API [180].

Several reports are available in literature concerning the determination of the dissolution rate of co-crystals of poorly water-soluble APIs with reference to increase in this parameter when using the co-crystal with respect to their pure components [181]. For

instance, for indomethacin, which is a non-steroidal anti-inflammatory drug (NSAID) and a BCS class II, an higher dissolution rate in phosphate buffer (pH = 7.4) has been described for its co-crystal with saccharin than that of δ -indomethacin [182]. A fenofibrate, (BCS class II), co-crystal with nicotinamide exhibits a higher dissolution rate than the raw API [183]. Curcumin shows similar results when in combination with hydroxyquinol [157]. In this case, curcumin may form two co-crystals with stoichiometric ratios of 1:1 and 1:2 in which the 1:2 co-crystal exhibited enhanced dissolution rate compared to the 1:1 one and raw curcumin. Solvated/hydrated co-crystals are characterized by the presence of solvent or water molecules in the crystal structure. In several cases, these molecules are essential to preserve the crystalline structure, as the structure may collapse after these molecules' removal.

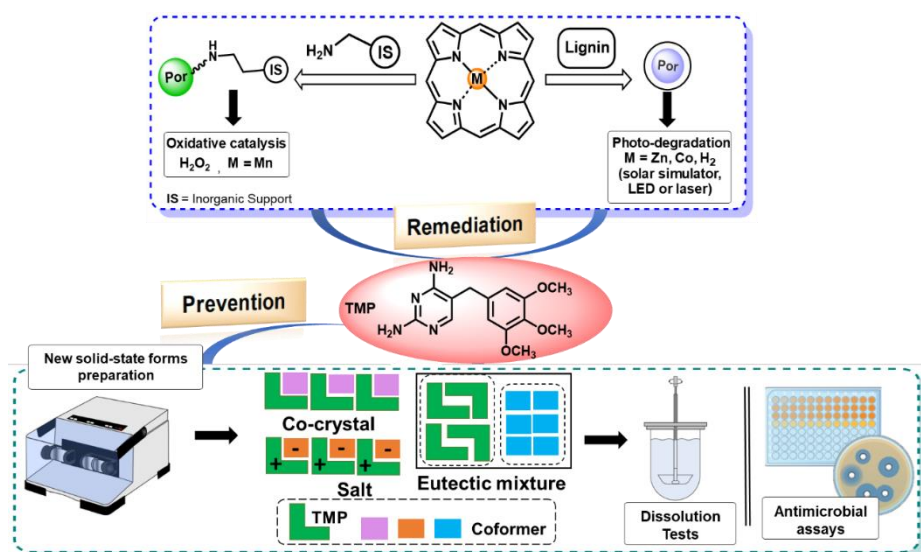
In addition, binary eutectic mixtures are multicomponent solid dispersions that may be obtained for components that are immiscible in the solid state (or only residually miscible) and miscible in the liquid phase. They correspond to the composition of the invariant point in a binary solid-liquid phase diagram, at constant pressure. Cherukuvada and Nangia recently defined them as “conglomerates” in which molecules with similar structure are held together by strong interactions while those ones with different structure are stabilized by weaker adhesive interactions. These forms are characterized by lower melting points if compared to the single components [184, 185]. For instance, some authors developed several binary eutectic mixtures combining curcumin, with reported antitumoral, antimalarial and antibacterial properties, with nicotinamide, hydroxyquinone, *p*-hydroxybenzoic acid, tartaric acid, ferulic acid and salicylic acid with different mole fractions of coformers (0.67, 0.5, 0.5, 0.5, 0.5 and 0.67 respectively) [186]. All the obtained eutectic mixtures revealed an enhanced dissolution rate of curcumin when compared with raw curcumin.

A wide range of different experimental multicomponent solid forms screening methods have been developed, based on conventional solvent-based methods, besides those that do not require the use of solvents. These methods can be divided into: i) solid-state methods including grinding, contact formation and extrusion; ii) solution-based methods, consisting of solvent and slow cooling evaporation and vapour diffusion; iii) supercritical fluid methods such as supercritical CO₂-assisted spray drying and crystallization with supercritical solvent and iv) miscellaneous co-crystal preparation for instance by freeze and spray drying and electrospray technology [187].

Since one of the goals of this thesis is to avoid the antibiotics accumulation in the environment, as we mentioned previously, our primary intent was to develop new multicomponent solid forms, using TMP as API and co-formers, directing our methodology to the use of solid-state methods such as mechanochemistry, dry or liquid-assisted grinding techniques [166]. To that respect, mechanochemistry is, currently, one of the green and sustainable methods to develop multicomponent solid forms, due to its advantageous properties such as easy, cheap and eco-friendly operational conditions and fast reaction rates.

1.6 Work proposal

The main goals of this thesis were designed to evidence our perspective on the development of effective strategies to prevent the accumulation of antibiotics in the environment and concomitant AMR spread. We will consider two main strategies to deal with this global matter: a “downstream” approach and an “upstream” approach. The first is an “*a posteriori*” viewpoint, focusing on the destruction of antibiotics after their utilization by humans, *i.e.*, present in the environment, particularly in wastewaters, using AOPs based on heterogenized porphyrin (photo)catalysts and benign oxidants, *e.g.* H_2O_2 and O_2 (Chapter 2). The second strategy, an “*a priori*” methodology, proposes the discovery of new pharmaceutical multicomponent solid forms using lower antibiotic loads that could, ideally, reduce antibiotic human intake and, consequently, lower the environmental fate of antibiotics and its accumulation (Chapter 3) (**Scheme 1.4**).



Scheme 1.4 Thesis graphical abstract.

In Chapter 2, our intent is to go beyond the state of the art and develop sustainable highly efficient catalytic systems based on hybrid materials incorporating porphyrins and metalloporphyrins, as this type of compounds is quite promising and still underexplored in antibiotic oxidation. The first part of Chapter 2 is focused on heterogeneous metal complex catalysed oxidative degradation of antibiotic TMP, in presence of hydrogen peroxide as benign oxidant. Its specific goals include preliminary evaluation of ideal metalloporphyrin properties, such as stability and catalytic activity. Then its covalent immobilization onto inorganic supports, *e.g.* functionalized silica gel and magnetic nanoparticles, will be pursued in order to fully evaluate the heterogeneous catalysts in the aqueous TMP degradation.

In the second part of Chapter 2, an hybrid photocatalyst will be developed, by encapsulating porphyrin into acetylated lignin, chosen as suitably sustainable support. This novel hybrid material will be implemented in the heterogenized photocatalytic degradation of TMP, using a 400 W mercury UV-Vis lamp as irradiation source. Then, this system is extended to other antibiotics' photodegradation.

Additionally, concerning the “*a priori*” perspective, Chapter 3 focuses on the development of new solid state-forms, using TMP as API. Pharmaceutically acceptable co-formers were chosen from the GRAS and EAFUS lists, aiming to improve TMP performance, with a lower loading within the formulations, in order to prevent the antibiotics accumulation in water by human use/excretion. The inhibitory activity of the new TMP solid-forms obtained will be evaluated against *E. coli* and *S. aureus* and dissolution tests will be also performed.

1.7 References

- [1] G. Piccirillo, R.T. Aroso, F.M.S. Rodrigues, R.M.B. Carrilho, S.M.A. Pinto, M.J.F. Calvete, M.M. Pereira, Oxidative degradation of pharmaceuticals: the role of tetrapyrrole-based catalysts, *Catalysts*, 11 (2021) 1335. <https://doi.org/10.3390/catal11111335>
- [2] M. Patait, N. Urvashi, M. Rajderkar, S. Kedar, K. Shah, R. Patait, Antibiotic prescription: an oral physician's point of view, *Journal of Pharmacy & Bioallied Sciences*, 7 (2015) 116. <https://doi.org/10.4103/0975-7406.154434>
- [3] K. Iskandar, J. Murugaiyan, D. Hammoudi Halat, S.E. Hage, V. Chibabhai, S. Adukkadukkam, C. Roques, L. Molinier, P. Salameh, M. Van Dongen, Antibiotic discovery and resistance: the chase and the race, *Antibiotics-Basel*, 11 (2022) 182. <https://doi.org/10.3390/antibiotics11020182>
- [4] M.I. Hutchings, A.W. Truman, B. Wilkinson, Antibiotics: past, present and future, *Current Opinion in Microbiology*, 51 (2019) 72. <https://doi.org/10.1016/j.mib.2019.10.008>
- [5] A. Gelpi, A. Gilbertson, J.D. Tucker, Magic bullet: Paul Ehrlich, Salvarsan and the birth of venereology, *Sexually Transmitted Infections*, 91 (2015) 68. <https://doi.org/10.1136/sextrans-2014-051779>
- [6] G.A. Durand, D. Raoult, G. Dubourg, Antibiotic discovery: history, methods and perspectives, *International Journal of Antimicrobial Agents*, 53 (2019) 371. <https://doi.org/10.1016/j.ijantimicag.2018.11.010>
- [7] S. Dhingra, N.A.A. Rahman, E. Peile, M. Rahman, M. Sartelli, M.A. Hassali, T. Islam, S. Islam, M. Haque, Microbial resistance movements: an overview of global public health threats posed by antimicrobial resistance, and how best to counter, *Frontiers in Public Health*, 8 (2020) 22. <https://doi.org/10.3389/fpubh.2020.535668>
- [8] E. Etebu, I. Arikekpar, Antibiotics: classification and mechanisms of action with emphasis on molecular perspectives, 2016, pp. 90.
- [9] M.A. Kohanski, D.J. Dwyer, J.J. Collins, How antibiotics kill bacteria: from targets to networks, *Nature Reviews Microbiology*, 8 (2010) 423. <https://doi.org/10.1038/nrmicro2333>
- [10] C. Walsh, Antibiotics: actions, origins, resistance, American Society for Microbiology (ASM), Washington, DC, 2003.
- [11] R.N. Iyer, β -Lactam Antibiotics, *Comprehensive Pharmacology*, Elsevier, 2022.
- [12] N. Pandey, M. Cascella, Beta Lactam Antibiotics, StatPearls Publishing

Copyright © 2022, StatPearls Publishing LLC, Treasure Island (FL), 2022.

- [13] V.T. Andriole, The quinolones: past, present, and future, *Clinical Infectious Diseases*, 41 (2005) S113. <https://doi.org/10.1086/428051>
- [14] A. Fàbrega, S. Madurga, E. Giralt, J. Vila, Mechanism of action of and resistance to quinolones, *Microbial Biotechnology*, 2 (2009) 40. <https://doi.org/10.1111/j.1751-7915.2008.00063.x>
- [15] A. Rusu, I.-A. Lungu, O.-L. Moldovan, C. Tanase, G. Hancu, Structural characterization of the millennial antibacterial (fluoro)quinolones—Shaping the fifth generation, *Pharmaceutics*, 13 (2021) 1289. <https://doi.org/10.3390/pharmaceutics13081289>
- [16] M.L. Nelson, S.B. Levy, The history of the tetracyclines, *Annals of the New York Academy of Sciences*, 1241 (2011) 17. <https://doi.org/10.1111/j.1749-6632.2011.06354.x>
- [17] E. Scholar, Sulfonamides, in: S.J. Enna, D.B. Bylund (Eds.) *xPharm: the comprehensive pharmacology reference*, Elsevier, New York, 2007, pp. 1.
- [18] F. van Bambeke, M.-P. Mingeot-Leclercq, Y. Glupczynski, P.M. Tulkens, Mechanisms of action, in: J. Cohen, W.G. Powderly, S.M. Opal (Eds.) *Infectious Diseases (Fourth Edition)*, Elsevier 2017, pp. 1162.
- [19] K.M. Krause, A.W. Serio, T.R. Kane, L.E. Connolly, Aminoglycosides: an overview, *Cold Spring Harbor perspectives in medicine*, 6 (2016) a027029. <https://doi.org/10.1101/cshperspect.a027029>
- [20] J.E. Leggett, 143 - Aminoglycosides, in: J. Cohen, W.G. Powderly, S.M. Opal (Eds.) *Infectious Diseases (Fourth Edition)*, Elsevier 2017, pp. 1233.
- [21] A. Khondker, R.-C. Bider, I. Passos-Gastaldo, G.D. Wright, M.C. Rheinstädter, Membrane interactions of non-membrane targeting antibiotics: the case of aminoglycosides, macrolides, and fluoroquinolones, *Biochimica et Biophysica Acta (BBA) - Biomembranes*, 1863 (2021) 183448. <https://doi.org/10.1016/j.bbamem.2020.183448>
- [22] P.H. Patel, M.F. Hashmi, Macrolides, StatPearls, StatPearls Publishing Copyright © 2022, StatPearls Publishing LLC., Treasure Island (FL), 2022.
- [23] N. Vázquez-Laslop, A.S. Mankin, How macrolide antibiotics work, *Trends in Biochemical Sciences*, 43 (2018) 668. <https://doi.org/10.1016/j.tibs.2018.06.011>

- [24] W.C. Reygaert, An overview of the antimicrobial resistance mechanisms of bacteria, *AIMS microbiology*, 4 (2018) 482. <https://doi.org/10.3934/microbiol.2018.3.482>
- [25] Center For Disease Dynamics, Economics & Policy (CDDEP). The State of the World's Antibiotics in 2021. 2021. <https://cddep.org/publications/the-state-of-the-worlds-antibiotic-in-2021/#:~:text=Researchers%20at%20CDDEP%20have%20released,www.resistancemap.org%2C>. (last accessed on 03/10/2022)
- [26] E.Y. Klein, M. Milkowska-Shibata, K.K. Tseng, M. Sharland, S. Gandra, C. Pulcini, R. Laxminarayan, Assessment of WHO antibiotic consumption and access targets in 76 countries, 2000–15: an analysis of pharmaceutical sales data, *The Lancet Infectious Diseases*, 21 (2021) 107. [https://doi.org/10.1016/S1473-3099\(20\)30332-7](https://doi.org/10.1016/S1473-3099(20)30332-7)
- [27] Centers for Disease Control and Prevention (CDC). U.S. Department of health and human services. Antibiotic use in the United States progress and opportunities 2018 UPDATE. <https://www.cdc.gov/antibiotic-use/stewardship-report/pdf/stewardship-report-2018-508.pdf>. (last accessed on 03/10/2022)
- [28] European Centre for Disease Prevention and Control (ECDC). Antimicrobial resistance in the EU/EEA- A one health response 2022. <https://www.ecdc.europa.eu/sites/default/files/documents/antimicrobial-resistance-policy-brief-2022.pdf>. (last accessed on 03/10/2022)
- [29] Centers of Disease Control and Prevention (CDC)-National antimicrobial resistance monitoring system for Enteric bacteria (NARMS). <https://www.cdc.gov/narms/faq.html>. (last accessed on 01/10/2022)
- [30] J.M. Munita, C.A. Arias, Mechanisms of antibiotic resistance, *Microbiology spectrum*, 4 (2016). <https://doi.org/10.1128/microbiolspec.VMBF-0016-2015>
- [31] J.M. Blair, M.A. Webber, A.J. Baylay, D.O. Ogbolu, L.J. Piddock, Molecular mechanisms of antibiotic resistance, *Nature Reviews Microbiology*, 13 (2015) 42. <https://doi.org/10.1038/nrmicro3380>
- [32] N.D. Friedman, E. Temkin, Y. Carmeli, The negative impact of antibiotic resistance, *Clinical Microbiology and Infection*, 22 (2016) 416. <https://doi.org/10.1016/j.cmi.2015.12.002>
- [33] R. Rajendran, Superbug infection, *Journal of Drug Metabolism & Toxicology*, 9 (2018) 1000238. <https://doi.org/10.4172/2157-7609.1000238>
- [34] European court of auditors. EU action to fight antimicrobial resistance. February 2019. https://www.eca.europa.eu/Lists/ECADocuments/AP19_03/AP_AMR_EN.pdf (last accessed on 03/10/2022)

- [35] S.I. Polianciuc, A.E. Gurzău, B. Kiss, M.G. Ștefan, F. Loghin, Antibiotics in the environment: causes and consequences, *Medicine and Pharmacy Reports*, 93 (2020) 231. <https://doi.org/10.15386/mpr-1742>
- [36] I.T. Carvalho, L. Santos, Antibiotics in the aquatic environments: a review of the european scenario, *Environment International*, 94 (2016) 736. <https://doi.org/10.1016/j.envint.2016.06.025>
- [37] N. Sasakova, G. Gregova, D. Takacova, J. Mojziso, I. Papajova, J. Venglovsky, T. Szaboova, S. Kovacova, Pollution of surface and ground water by sources related to agricultural activities, 2 (2018) 1. <https://doi.org/10.3389/fsufs.2018.00042>
- [38] C. Bhagat, M. Kumar, V.K. Tyagi, P.K. Mohapatra, Proclivities for prevalence and treatment of antibiotics in the ambient water: a review, *Clean Water*, 3 (2020) 42. <https://doi.org/10.1038/s41545-020-00087-x>
- [39] X.-W. Li, Y.-F. Xie, C.-L. Li, H.-N. Zhao, H. Zhao, N. Wang, J.-F. Wang, Investigation of residual fluoroquinolones in a soil–vegetable system in an intensive vegetable cultivation area in northern China, *Science of the Total Environment*, 468 (2014) 258. <https://doi.org/10.1016/j.scitotenv.2013.08.057>
- [40] M. D'Alessio, L.M. Durso, D.N. Miller, B. Woodbury, C. Ray, D.D. Snow, Environmental fate and microbial effects of monensin, lincomycin, and sulfamethazine residues in soil, *Environmental Pollution*, 246 (2019) 60. <https://doi.org/10.1016/j.envpol.2018.11.093>
- [41] R.H. Lindberg, J. Fick, M. Tysklind, Screening of antimycotics in swedish sewage treatment plants – Waters and sludge, *Water Research*, 44 (2010) 649. <https://doi.org/10.1016/j.watres.2009.10.034>
- [42] R. López-Serna, A. Jurado, E. Vázquez-Suñé, J. Carrera, M. Petrović, D. Barceló, Occurrence of 95 pharmaceuticals and transformation products in urban groundwaters underlying the metropolis of Barcelona, Spain, *Environmental Pollution*, 174 (2013) 305. <https://doi.org/10.1016/j.envpol.2012.11.022>
- [43] K.K. Barnes, D.W. Kolpin, E.T. Furlong, S.D. Zaugg, M.T. Meyer, L.B. Barber, A national reconnaissance of pharmaceuticals and other organic wastewater contaminants in the United States - I) Groundwater, *Science of the Total Environment*, 402 (2008) 192. <https://doi.org/10.1016/j.scitotenv.2008.04.028>
- [44] M. Gros, N. Catalán, J. Mas-Pla, M. Čelić, M. Petrović, M.J. Farré, Groundwater antibiotic pollution and its relationship with dissolved organic matter: Identification and

- environmental implications, *Environmental Pollution*, 289 (2021) 117927. <https://doi.org/10.1016/j.envpol.2021.117927>
- [45] D. Zhang, L. Lin, Z. Luo, C. Yan, X. Zhang, Occurrence of selected antibiotics in Jiulongjiang river in various seasons, south China, *Journal of Environmental Monitoring*, 13 (2011) 1953. <https://doi.org/10.1039/C0EM00765J>
- [46] C. Yan, Y. Yang, J. Zhou, M. Liu, M. Nie, H. Shi, L. Gu, Antibiotics in the surface water of the Yangtze estuary: occurrence, distribution and risk assessment, *Environmental Pollution*, 175 (2013) 22. <https://doi.org/10.1016/j.envpol.2012.12.008>
- [47] H.Q. Anh, T.P.Q. Le, N. Da Le, X.X. Lu, T.T. Duong, J. Garnier, E. Rochelle-Newall, S. Zhang, N.-H. Oh, C. Oeurng, C. Ekkawatpanit, T.D. Nguyen, Q.T. Nguyen, T.D. Nguyen, T.N. Nguyen, T.L. Tran, T. Kunisue, R. Tanoue, S. Takahashi, T.B. Minh, H.T. Le, T.N.M. Pham, T.A.H. Nguyen, Antibiotics in surface water of east and southeast asian countries: a focused review on contamination status, pollution sources, potential risks, and future perspectives, *Science of the Total Environment*, 764 (2021) 142865. <https://doi.org/10.1016/j.scitotenv.2020.142865>
- [48] Y. Ben, M. Hu, X. Zhang, S. Wu, M.H. Wong, M. Wang, C.B. Andrews, C. Zheng, Efficient detection and assessment of human exposure to trace antibiotic residues in drinking water, *Water Research*, 175 (2020) 115699. <https://doi.org/10.1016/j.watres.2020.115699>
- [49] T. Meng, W. Cheng, T. Wan, M. Wang, J. Ren, Y. Li, C. Huang, Occurrence of antibiotics in rural drinking water and related human health risk assessment, *Environmental Technology & Innovation*, 42 (2021) 671. <https://doi.org/10.1080/09593330.2019.1642390>
- [50] Q.-Q. Zhang, G.-G. Ying, C.-G. Pan, Y.-S. Liu, J.-L. Zhao, Comprehensive evaluation of antibiotics emission and fate in the river basins of China: source analysis, multimedia modeling, and linkage to bacterial resistance, *Environmental Science & Technology*, 49 (2015) 6772. <https://doi.org/10.1021/acs.est.5b00729>
- [51] J. Xu, Y. Xu, H. Wang, C. Guo, H. Qiu, Y. He, Y. Zhang, X. Li, W. Meng, Occurrence of antibiotics and antibiotic resistance genes in a sewage treatment plant and its effluent-receiving river, *Chemosphere*, 119 (2015) 1379. <https://doi.org/10.1016/j.chemosphere.2014.02.040>
- [52] A. de Santiago-Martín, R. Meffe, G. Teijón, V. Martínez Hernández, I. López-Heras, C. Alonso Alonso, M. Arenas Romasanta, I. de Bustamante, Pharmaceuticals and trace metals in the surface water used for crop irrigation: Risk to health or natural attenuation,

Science of the Total Environment, 705 (2020) 135825.
<https://doi.org/10.1016/j.scitotenv.2019.135825>

[53] T. Schwartz, W. Kohnen, B. Jansen, U. Obst, Detection of antibiotic-resistant bacteria and their resistance genes in wastewater, surface water, and drinking water biofilms, *FEMS Microbiology Ecology*, 43 (2003) 325. [https://doi.org/10.1016/S0168-6496\(02\)00444-0](https://doi.org/10.1016/S0168-6496(02)00444-0)

[54] P. Sun, Z. Bi, M. Nilsson, B. Zheng, B. Berglund, C.S. Lundborg, S. Börjesson, X. Li, B. Chen, H. Yin, L.E. Nilsson, Occurrence of blaKPC-2, blaCTX-M, and mcr-1 in Enterobacteriaceae from well water in rural China, *Antimicrobial Agents and Chemotherapy*, 61 (2017) e02569. <https://doi.org/10.1128/AAC.02569-16>

[55] F.M. Mpatani, A.A. Aryee, A.N. Kani, R. Han, Z. Li, E. Dovi, L. Qu, A review of treatment techniques applied for selective removal of emerging pollutant-trimethoprim from aqueous systems, *Journal of Cleaner Production*, 308 (2021) 127359. <https://doi.org/10.1016/j.jclepro.2021.127359>

[56] A. Mendoza, J. Aceña, S. Pérez, M. López de Alda, D. Barceló, A. Gil, Y. Valcárcel, Pharmaceuticals and iodinated contrast media in a hospital wastewater: a case study to analyse their presence and characterise their environmental risk and hazard, *Environmental Research*, 140 (2015) 225. <https://doi.org/10.1016/j.envres.2015.04.003>

[57] L.H.M.L.M. Santos, M. Gros, S. Rodriguez-Mozaz, C. Delerue-Matos, A. Pena, D. Barceló, M.C.B.S.M. Montenegro, Contribution of hospital effluents to the load of pharmaceuticals in urban wastewaters: Identification of ecologically relevant pharmaceuticals, *Science of the Total Environment*, 461 (2013) 302. <https://doi.org/10.1016/j.scitotenv.2013.04.077>

[58] Y. Chen, T. Lan, L. Duan, F. Wang, B. Zhao, S. Zhang, W. Wei, Adsorptive removal and adsorption kinetics of fluoroquinolone by nano-hydroxyapatite, *PLOS ONE*, 10 (2015) e0145025. <https://doi.org/10.1371/journal.pone.0145025>

[59] C. Chen, J. Li, P. Chen, R. Ding, P. Zhang, X. Li, Occurrence of antibiotics and antibiotic resistances in soils from wastewater irrigation areas in Beijing and Tianjin, China, *Environmental Pollution*, 193 (2014) 94. <https://doi.org/10.1016/j.envpol.2014.06.005>

[60] L. Shao, Z. Wu, L. Zeng, Z.M. Chen, Y. Zhou, G.Q. Chen, Embodied energy assessment for ecological wastewater treatment by a constructed wetland, *Ecological Modelling*, 252 (2013) 63. <https://doi.org/10.1016/j.ecolmodel.2012.09.004>

- [61] J.L. Acero, F.J. Benitez, F.J. Real, F. Teva, Removal of emerging contaminants from secondary effluents by micellar-enhanced ultrafiltration, *Separation and Purification Technology*, 181 (2017) 123. <https://doi.org/10.1016/j.seppur.2017.03.021>
- [62] M.-K. Liu, Y.-Y. Liu, D.-D. Bao, G. Zhu, G.-H. Yang, J.-F. Geng, H.-T. Li, Effective removal of tetracycline antibiotics from water using hybrid carbon membranes, *Scientific Reports*, 7 (2017) 43717. <https://doi.org/10.1038/srep43717>
- [63] D.G. Larsson, C. de Pedro, N. Paxeus, Effluent from drug manufactures contains extremely high levels of pharmaceuticals, *Journal of Hazardous Materials*, 148 (2007) 751. <https://doi.org/10.1016/j.jhazmat.2007.07.008>
- [64] B. Subedi, K. Balakrishna, R.K. Sinha, N. Yamashita, V.G. Balasubramanian, K. Kannan, Mass loading and removal of pharmaceuticals and personal care products, including psychoactive and illicit drugs and artificial sweeteners, in five sewage treatment plants in India, *Journal of Environmental Chemical Engineering*, 3 (2015) 2882. <https://doi.org/10.1016/j.jece.2015.09.031>
- [65] O.A. Arikan, Degradation and metabolization of chlortetracycline during the anaerobic digestion of manure from medicated calves, *Journal of Hazardous Materials*, 158 (2008) 485. <https://doi.org/10.1016/j.jhazmat.2008.01.096>
- [66] M.T. Amin, A.A. Alazba, U. Manzoor, A review of removal of pollutants from water/wastewater using different types of nanomaterials, *Advances in Materials Science and Engineering*, 2014 (2014) 825910. <https://doi.org/10.1155/2014/825910>
- [67] R. Gothwal, T. Shashidhar, Antibiotic pollution in the environment: a review, *Clean-Soil Air Water*, 43 (2015) 479. <https://doi.org/10.1002/clen.201300989>
- [68] A. Barra Caracciolo, E. Topp, P. Grenni, Pharmaceuticals in the environment: biodegradation and effects on natural microbial communities. A review, *Journal of Pharmaceutical and Biomedical Analysis*, 106 (2015) 25. <https://doi.org/10.1016/j.jpba.2014.11.040>
- [69] E.M. Cuerda-Correa, M.F. Alexandre-Franco, C. Fernández-González, Advanced Oxidation processes for the removal of antibiotics from water. An overview, *Water*, 12 (2020) 102. <https://doi.org/10.3390/w12010102>
- [70] D.B. Miklos, C. Remy, M. Jekel, K.G. Linden, J.E. Drewes, U. Hübner, Evaluation of advanced oxidation processes for water and wastewater treatment – a critical review, *Water Research*, 139 (2018) 118. <https://doi.org/10.1016/j.watres.2018.03.042>
- [71] M. Sillanpää, M.C. Ncibi, A. Matilainen, Advanced oxidation processes for the removal of natural organic matter from drinking water sources: a comprehensive review,

- Journal of Environmental Management, 208 (2018) 56.
<https://doi.org/10.1016/j.jenvman.2017.12.009>
- [72] Y. Deng, R. Zhao, Advanced oxidation processes (AOPs) in wastewater treatment, *Current Pollution Reports*, 1 (2015) 167. <https://doi.org/10.1007/s40726-015-0015-z>
- [73] M.J.F. Calvete, G. Piccirillo, C.S. Vinagreiro, M.M. Pereira, Hybrid materials for heterogeneous photocatalytic degradation of antibiotics, *Coordination Chemistry Reviews*, 395 (2019) 63. <https://doi.org/10.1016/j.ccr.2019.05.004>
- [74] T. Garoma, S.K. Umamaheshwar, A. Mumper, Removal of sulfadiazine, sulfamethizole, sulfamethoxazole, and sulfathiazole from aqueous solution by ozonation, *Chemosphere*, 79 (2010) 814. <https://doi.org/10.1016/j.chemosphere.2010.02.060>
- [75] M. Östman, B. Björleinius, J. Fick, M. Tysklind, Effect of full-scale ozonation and pilot-scale granular activated carbon on the removal of biocides, antimycotics and antibiotics in a sewage treatment plant, *Science of the Total Environment*, 649 (2019) 1117. <https://doi.org/10.1016/j.scitotenv.2018.08.382>
- [76] S.K. Stylianou, I.A. Katsoyiannis, M. Mitrakas, A.I. Zouboulis, Application of a ceramic membrane contacting process for ozone and peroxone treatment of micropollutant contaminated surface water, *Journal of Hazardous Materials*, 358 (2018) 129. <https://doi.org/10.1016/j.jhazmat.2018.06.060>
- [77] R.F. Dantas, S. Contreras, C. Sans, S. Esplugas, Sulfamethoxazole abatement by means of ozonation, *Journal of Hazardous Materials*, 150 (2008) 790. <https://doi.org/10.1016/j.jhazmat.2007.05.034>
- [78] D.S. Gomes, L.M. Gando-Ferreira, R.M. Quinta-Ferreira, R.C. Martins, Removal of sulfamethoxazole and diclofenac from water: strategies involving O₃ and H₂O₂, *Environmental Technology*, 39 (2018) 1658. <https://doi.org/10.1080/09593330.2017.1335351>
- [79] J.P. Ribeiro, M.I. Nunes, Recent trends and developments in Fenton processes for industrial wastewater treatment – a critical review, *Environmental Research*, 197 (2021) 110957. <https://doi.org/10.1016/j.envres.2021.110957>
- [80] B. Jain, A.K. Singh, H. Kim, E. Lichtfouse, V.K. Sharma, Treatment of organic pollutants by homogeneous and heterogeneous Fenton reaction processes, *Environmental Chemistry Letters*, 16 (2018) 947. <https://doi.org/10.1007/s10311-018-0738-3>
- [81] A. Gupta, A. Garg, Degradation of ciprofloxacin using Fenton's oxidation: effect of operating parameters, identification of oxidized by-products and toxicity assessment, *Chemosphere*, 193 (2018) 1181. <https://doi.org/10.1016/j.chemosphere.2017.11.046>

- [82] S. Wang, J. Wang, Trimethoprim degradation by Fenton and Fe(II)-activated persulfate processes, *Chemosphere*, 191 (2018) 97. <https://doi.org/10.1016/j.chemosphere.2017.10.040>
- [83] L. Xu, Y. Yang, W. Li, Y. Tao, Z. Sui, S. Song, J. Yang, Three-dimensional macroporous graphene-wrapped zero-valent copper nanoparticles as efficient micro-electrolysis-promoted Fenton-like catalysts for metronidazole removal, *Science of the Total Environment*, 658 (2019) 219. <https://doi.org/10.1016/j.scitotenv.2018.12.040>
- [84] H.-Y. Ma, L. Zhao, L.-H. Guo, H. Zhang, F.-J. Chen, W.-C. Yu, Roles of reactive oxygen species (ROS) in the photocatalytic degradation of pentachlorophenol and its main toxic intermediates by TiO₂/UV, *Journal of Hazardous Materials*, 369 (2019) 719. <https://doi.org/10.1016/j.jhazmat.2019.02.080>
- [85] N.E. Paucar, I. Kim, H. Tanaka, C. Sato, Effect of O₃ dose on the O₃/UV treatment process for the removal of pharmaceuticals and personal care products in secondary effluent, *Chemical Engineering Journal*, 3 (2019) 53. <https://doi.org/10.3390/chemengineering3020053>
- [86] M. Moradi, G. Moussavi, Investigation of chemical-less UVC/VUV process for advanced oxidation of sulfamethoxazole in aqueous solutions: evaluation of operational variables and degradation mechanism, *Separation and Purification Technology*, 190 (2018) 90. <https://doi.org/10.1016/j.seppur.2017.08.006>
- [87] M.M. Hinojosa Guerra, I. Oller Alberola, S. Malato Rodriguez, A. Agüera López, A. Acevedo Merino, J.M. Quiroga Alonso, Oxidation mechanisms of amoxicillin and paracetamol in the photo-Fenton solar process, *Water Research*, 156 (2019) 232. <https://doi.org/10.1016/j.watres.2019.02.055>
- [88] D. Kanakaraju, B.D. Glass, M. Oelgemöller, Titanium dioxide photocatalysis for pharmaceutical wastewater treatment, *Environmental Chemistry Letters*, 12 (2014) 27. <https://doi.org/10.1007/s10311-013-0428-0>
- [89] Y. Ma, X. Wang, Y. Jia, X. Chen, H. Han, C. Li, Titanium dioxide-based nanomaterials for photocatalytic fuel generations, *Chemical Reviews*, 114 (2014) 9987. <https://doi.org/10.1021/cr500008u>
- [90] L. Gomathi Devi, R. Kavitha, Review on modified N-TiO₂ for green energy applications under UV/visible light: selected results and reaction mechanisms, *RSC Advances*, 4 (2014) 28265. <https://doi.org/10.1039/C4RA03291H>

- [91] F. Zhang, X. Wang, H. Liu, C. Liu, Y. Wan, Y. Long, Z. Cai, Recent advances and applications of semiconductor photocatalytic technology, *Applied Science*, 9 (2019) 2489. <https://doi.org/10.3390/app9122489>
- [92] A. Kutuzova, T. Dontsova, W. Kwapinski, Application of TiO₂-based photocatalysts to antibiotics degradation: cases of sulfamethoxazole, trimethoprim and ciprofloxacin, *Catalysts*, 11 (2021) 728. <https://doi.org/10.3390/catal11060728>
- [93] M. Manasa, P.R. Chandewar, H. Mahalingam, Photocatalytic degradation of ciprofloxacin & norfloxacin and disinfection studies under solar light using boron & cerium doped TiO₂ catalysts synthesized by green EDTA-citrate method, *Catalysis Today*, 375 (2021) 522. <https://doi.org/10.1016/j.cattod.2020.03.018>
- [94] F. Wang, X. Yu, M. Ge, S. Wu, One-step synthesis of TiO₂/γ-Fe₂O₃/GO nanocomposites for visible light-driven degradation of ciprofloxacin, *Chemical Engineering Journal*, 384 (2020) 123381. <https://doi.org/10.1016/j.cej.2019.123381>
- [95] M. Jahdi, S.B. Mishra, E.N. Nxumalo, S.D. Mhlanga, A.K. Mishra, Smart pathways for the photocatalytic degradation of sulfamethoxazole drug using F-Pd co-doped TiO₂ nanocomposites, *Applied Catalysis B: Environmental*, 267 (2020) 118716. <https://doi.org/10.1016/j.apcatb.2020.118716>
- [96] E.H. Mourid, E.M. El Mouchtari, L. El Mersly, L. Benaziz, S. Rafqah, M. Lakraimi, Development of a new recyclable nanocomposite LDH-TiO₂ for the degradation of antibiotic sulfamethoxazole under UVA radiation: An approach towards sunlight, *Journal of Photochemistry and Photobiology A: Chemistry*, 396 (2020) 112530. <https://doi.org/10.1016/j.jphotochem.2020.112530>
- [97] W. Zhu, F. Sun, R. Goei, Y. Zhou, Construction of WO₃-g-C₃N₄ composites as efficient photocatalysts for pharmaceutical degradation under visible light, *Catalysis Science & Technology*, 7 (2017) 2591. <https://doi.org/10.1039/C7CY00529F>
- [98] W. Zhu, Z. Li, C. He, S. Faqian, Y. Zhou, Enhanced photodegradation of sulfamethoxazole by a novel WO₃-CNT composite under visible light irradiation, *Journal of Alloys and Compounds*, 754 (2018) 153. <https://doi.org/10.1016/j.jallcom.2018.04.286>
- [99] M. Samy, M.G. Ibrahim, M. Gar Alalm, M. Fujii, S. Ookawara, T. Ohno, Photocatalytic degradation of trimethoprim using S-TiO₂ and Ru/WO₃/ZrO₂ immobilized on reusable fixed plates, *Journal of Water Process Engineering*, 33 (2020) 101023. <https://doi.org/10.1016/j.jwpe.2019.101023>

- [100] M.E. Villanueva, M. Puca, J. Pérez Bravo, J. Bafico, V. Campo Dall Orto, G.J. Copello, Dual adsorbent-photocatalytic keratin–TiO₂ nanocomposite for trimethoprim removal from wastewater, *New Journal of Chemistry*, 44 (2020) 10964. <https://doi.org/10.1039/D0NJ02784G>
- [101] T.L. Poulos, Heme enzyme structure and function, *Chemical Reviews*, 114 (2014) 3919. <https://doi.org/10.1021/cr400415k>
- [102] S. Hiroto, Y. Miyake, H. Shinokubo, Synthesis and functionalization of porphyrins through organometallic methodologies, *Chemical Reviews*, 117 (2017) 2910. <https://doi.org/10.1021/acs.chemrev.6b00427>
- [103] S.M.A. Pinto, C.A. Henriques, V.A. Tomé, C.S. Vinagreiro, M.J.F. Calvete, J.M. Dąbrowski, M. Piñeiro, L.G. Arnaut, M.M. Pereira, Synthesis of meso-substituted porphyrins using sustainable chemical processes, *Journal of Porphyrins and Phthalocyanines*, 20 (2016) 45. <https://doi.org/10.1142/s1088424616300020>
- [104] J.M. Dąbrowski, B. Pucelik, M.M. Pereira, L.G. Arnaut, W. Macyk, G. Stochel, New hybrid materials based on halogenated metalloporphyrins for enhanced visible light photocatalysis, *RSC Advances*, 5 (2015) 93252. <https://doi.org/10.1039/C5RA19742B>
- [105] M.M. Pereira, L.D. Dias, M.J.F. Calvete, Metalloporphyrins: bioinspired oxidation catalysts, *ACS Catalysis*, 8 (2018) 10784. <https://doi.org/10.1021/acscatal.8b01871>
- [106] M.J.F. Calvete, M. Piñeiro, L.D. Dias, M.M. Pereira, Hydrogen peroxide and metalloporphyrins in oxidation catalysis: old dogs with some new tricks, *ChemCatChem*, 10 (2018) 3615. <https://doi.org/10.1002/cctc.201800587>
- [107] M.J.F. Calvete, M. Silva, M.M. Pereira, H.D. Burrows, Inorganic helping organic: recent advances in catalytic heterogeneous oxidations by immobilised tetrapyrrolic macrocycles in micro and mesoporous supports, *RSC Advances*, 3 (2013) 22774. <https://doi.org/10.1039/C3RA44038A>
- [108] S.L.H. Rebelo, M.M. Pereira, P.V. Monsanto, H.D. Burrows, Catalytic oxidative degradation of s-triazine and phenoxyalkanoic acid based herbicides with metalloporphyrins and hydrogen peroxide: identification of two distinct reaction schemes, *Journal of Molecular Catalysis A: Chemical*, 297 (2009) 35. <https://doi.org/10.1016/j.molcata.2008.09.005>
- [109] R.A. Baglia, J.P.T. Zaragoza, D.P. Goldberg, Biomimetic reactivity of oxygen-derived manganese and iron porphyrinoid complexes, *Chemical Reviews*, 117 (2017) 13320. <https://doi.org/10.1021/acs.chemrev.7b00180>

- [110] S.L.H. Rebelo, S.M.G. Pires, M.M.Q. Simões, B. de Castro, M.G.P.M.S. Neves, C.J. Medforth, Biomimetic oxidation of benzofurans with hydrogen peroxide catalyzed by Mn(III) porphyrins, *Catalysts*, 10 (2020) 62. <https://doi.org/10.3390/catal10010062>
- [111] C.F. Pereira, M.M.Q. Simões, J.P.C. Tomé, F.A. Almeida Paz, Porphyrin-based metal-organic frameworks as heterogeneous catalysts in oxidation reactions, *Molecules*, 21 (2016) 1348. <https://doi.org/10.3390/molecules21101348>
- [112] S.M.G. Pires, M.M.Q. Simões, I.C.M.S. Santos, S.L.H. Rebelo, F.A.A. Paz, M.G.P.M.S. Neves, J.A.S. Cavaleiro, Oxidation of organosulfur compounds using an iron(III) porphyrin complex: an environmentally safe and efficient approach, *Applied Catalysis B: Environmental*, 160 (2014) 80. <https://doi.org/10.1016/j.apcatb.2014.05.003>
- [113] P. Zhang, J. Hu, B. Liu, J. Yang, H. Hou, Recent advances in metalloporphyrins for environmental and energy applications, *Chemosphere*, 219 (2019) 617. <https://doi.org/10.1016/j.chemosphere.2018.12.024>
- [114] L. Fernandez, V.I. Esteves, A. Cunha, R.J. Schneider, J.P.C. Tome, Photodegradation of organic pollutants in water by immobilized porphyrins and phthalocyanines, *Journal of Porphyrins and Phthalocyanines*, 20 (2016) 150. <https://doi.org/10.1142/s108842461630007x>
- [115] M. Silva, M.E. Azenha, M.M. Pereira, H.D. Burrows, M. Sarakha, C. Forano, M.F. Ribeiro, A. Fernandes, Immobilization of halogenated porphyrins and their copper complexes in MCM-41: environmentally friendly photocatalysts for the degradation of pesticides, *Applied Catalysis B: Environmental*, 100 (2010) 1. <https://doi.org/10.1016/j.apcatb.2010.07.033>
- [116] M. Silva, M.J.F. Calvete, N.P.F. Gonçalves, H.D. Burrows, M. Sarakha, A. Fernandes, M.F. Ribeiro, M.E. Azenha, M.M. Pereira, Zinc(II) phthalocyanines immobilized in mesoporous silica Al-MCM-41 and their applications in photocatalytic degradation of pesticides, *Journal of Hazardous Materials*, 233 (2012) 79. <https://doi.org/10.1016/j.jhazmat.2012.06.059>
- [117] S.L.H. Rebelo, A. Melo, R. Coimbra, M.E. Azenha, M.M. Pereira, H.D. Burrows, M. Sarakha, Photodegradation of atrazine and ametryn with visible light using water soluble porphyrins as sensitizers, *Environmental Chemistry Letters*, 5 (2007) 29. <https://doi.org/10.1007/s10311-006-0072-z>
- [118] K.A.D.F. Castro, J.M.M. Rodrigues, M.A.F. Faustino, J.P.C. Tomé, J.A.S. Cavaleiro, M.d.G.P.M.S. Neves, M.M.Q. Simões, Photocatalytic degradation of methyl orange mediated by a silica coated nanomagnet porphyrin hybrid, *Journal of*

- Organometallic Chemistry, 938 (2021) 121751.
<https://doi.org/10.1016/j.jorganchem.2021.121751>
- [119] C.M.B. Neves, O.M.S. Filipe, N. Mota, S.A.O. Santos, A.J.D. Silvestre, E.B.H. Santos, M. Neves, M.M.Q. Simões, Photodegradation of metoprolol using a porphyrin as photosensitizer under homogeneous and heterogeneous conditions, *Journal of Hazardous Materials*, 370 (2019) 13. <https://doi.org/10.1016/j.jhazmat.2018.11.055>
- [120] C.M.B. Neves, M.M.Q. Simões, M.R.M. Domínguez, I.C.M.S. Santos, M.G.P.M.S. Neves, F.A.A. Paz, A.M.S. Silva, J.A.S. Cavaleiro, Oxidation of diclofenac catalyzed by manganese porphyrins: synthesis of novel diclofenac derivatives, *RSC Advances*, 2 (2012) 7427. <https://doi.org/10.1039/C2RA20801F>
- [121] C.M.B. Neves, M.M.Q. Simões, I.C.M.S. Santos, F.M.J. Domingues, M.G.P.M.S. Neves, F.A. Almeida Paz, A.M.S. Silva, J.A.S. Cavaleiro, Oxidation of caffeine with hydrogen peroxide catalyzed by metalloporphyrins, *Tetrahedron Letters*, 52 (2011) 2898. <https://doi.org/10.1016/j.tetlet.2011.03.139>
- [122] S.M.G. Pires, M.M.Q. Simões, I.C.M.S. Santos, S.L.H. Rebelo, M.M. Pereira, M.G.P.M.S. Neves, J.A.S. Cavaleiro, Biomimetic oxidation of organosulfur compounds with hydrogen peroxide catalyzed by manganese porphyrins, *Applied Catalysis A: General*, 439 (2012) 51. <https://doi.org/10.1016/j.apcata.2012.06.044>
- [123] A.L.A. Lage, A.C. Marciano, M.F. Venâncio, M.A.N. da Silva, D. Martins, Water-soluble manganese porphyrins as good catalysts for cipro- and levofloxacin degradation: solvent effect, degradation products and DFT insights, *Chemosphere*, 268 (2021) 129334. <https://doi.org/10.1016/j.chemosphere.2020.129334>
- [124] S.L.H. Rebelo, M.M. Pereira, M.M.Q. Simoes, M.G.P.M.S. Neves, J.A.S. Cavaleiro, Mechanistic studies on metalloporphyrin epoxidation reactions with hydrogen peroxide: evidence for two active oxidative species, *Journal of Catalysis*, 234 (2005) 76. <https://doi.org/10.1016/j.jcat.2005.05.026>
- [125] A.M. Meireles, A.L.A. Lage, J.M. Ribeiro, M.A.N. da Silva, E.M. de Souza-Fagundes, D.C.D. Martins, Synthetic Mn(III) porphyrins as biomimetic catalysts of CYP450: degradation of antibiotic norfloxacin in aqueous medium, *Environmental Research*, 177 (2019) 108615. <https://doi.org/10.1016/j.envres.2019.108615>
- [126] B. Meunier, Metalloporphyrins as versatile catalysts for oxidation reactions and oxidative DNA cleavage, *Chemical Reviews*, 92 (1992) 1411. <https://doi.org/10.1021/cr00014a008>

- [127] A.M.D.R. Gonsalves, M.M. Pereira, A.C. Serra, R.A.W. Johnstone, M.L.P.G. Nunes, 5,10,15,20-tetrakisaryl and 2,3,7,8,12,13,17,18-octahalogeno-5,10,15,20-tetrakisarylporphyrins and their metal-complexes as catalysts in hypochlorite epoxidations, *Journal of the Chemical Society-Perkin Transactions 1*, (1994) 2053. <https://doi.org/10.1039/P19940002053>
- [128] A.M.D.R. Gonsalves, M.M. Pereira, State of the art in the development of biomimetic oxidation catalysts, *Journal of Molecular Catalysis a-Chemical*, 113 (1996) 209. [https://doi.org/10.1016/S1381-1169\(96\)00050-7](https://doi.org/10.1016/S1381-1169(96)00050-7)
- [129] A.L.A. Lage, A.M. Meireles, A.C. Marciano, J.M. Ribeiro, E.M. de Souza-Fagundes, D.C.S. Martins, Ciprofloxacin degradation by first-, second-, and third-generation manganese porphyrins, *Journal of Hazardous Materials*, 360 (2018) 445. <https://doi.org/10.1016/j.jhazmat.2018.08.036>
- [130] S. Nakagaki, G. K.B. Ferreira, A. L. Marcalb, K. J. Ciuffi, Metalloporphyrins immobilized on silica and modified silica as catalysts in heterogeneous processes, *Current Organic Synthesis*, 11 (2014) 67. <https://doi.org/10.2174/15701794113106660087>
- [131] A. Erigoni, U. Diaz, Porous silica-based organic-inorganic hybrid catalysts: a review, *Catalysts*, 11 (2021) 79. <https://doi.org/10.3390/catal11010079>
- [132] İ. Gürol, M. Durmuş, V. Ahsen, Photophysical and photochemical properties of fluorinated and nonfluorinated n-propanol-substituted zinc phthalocyanines, *European Journal of Inorganic Chemistry*, 2010 (2010) 1220. <https://doi.org/10.1002/ejic.200901096>
- [133] E.G. Azenha, A.C. Serra, M. Pineiro, M.M. Pereira, J.S. de Melo, L.G. Arnaut, S.J. Formosinho, A.M.D.R. Gonsalves, Heavy-atom effects on metalloporphyrins and polyhalogenated porphyrins, *Chemical Physics*, 280 (2002) 177. [https://doi.org/10.1016/S0301-0104\(02\)00485-8](https://doi.org/10.1016/S0301-0104(02)00485-8)
- [134] L. Fernández, V.I. Esteves, Â. Cunha, R.J. Schneider, J.P.C. Tomé, Photodegradation of organic pollutants in water by immobilized porphyrins and phthalocyanines, *Journal of Porphyrins and Phthalocyanines*, 20 (2016) 150. <https://doi.org/10.1142/s108842461630007x>
- [135] S. Nonell, C. Flors, Singlet oxygen: applications in biosciences and nanosciences, *Comprehensive Series in Photochemical & Photobiological Sciences*, RSC books, Cambridge, 2016.

- [136] M.S. Baptista, J. Cadet, P. Di Mascio, A.A. Ghogare, A. Greer, M.R. Hamblin, C. Lorente, S.C. Nunez, M.S. Ribeiro, A.H. Thomas, M. Vignoni, T.M. Yoshimura, Type I and type II photosensitized oxidation reactions: guidelines and mechanistic pathways, *Photochemical & Photobiological Sciences*, 93 (2017) 912. <https://doi.org/10.1111/php.12716>
- [137] S. Silvestri, A.R. Fajardo, B.A. Iglesias, Supported porphyrins for the photocatalytic degradation of organic contaminants in water: a review, *Environmental Chemistry Letters*, 20 (2022) 731. <https://doi.org/10.1007/s10311-021-01344-2>
- [138] K. Hu, C. Chen, Y. Zhu, G. Zeng, B. Huang, W. Chen, S. Liu, C. Lei, B. Li, Y. Yang, Ternary Z-scheme heterojunction of Bi₂WO₆ with reduced graphene oxide (rGO) and meso-tetra (4-carboxyphenyl) porphyrin (TCPP) for enhanced visible-light photocatalysis, *Journal of Colloid and Interface Science*, 540 (2019) 115. <https://doi.org/10.1016/j.jcis.2019.01.013>
- [139] Z. Ma, C. Zeng, L. Hu, Q. Zhao, Q. Yang, J. Niu, B. Yao, Y. He, A high-performance photocatalyst of ZnTCPP sensitized porous graphitic carbon nitride for antibiotic degradation under visible light irradiation, *Applied Surface Science*, 484 (2019) 489. <https://doi.org/10.1016/j.apsusc.2019.04.117>
- [140] Y. He, H. Lv, Y. Daili, Q. Yang, L.B. Junior, D. Liu, H. Liu, Z. Ma, Construction of a new cascade photogenerated charge transfer system for the efficient removal of bio-toxic levofloxacin and rhodamine B from aqueous solution: mechanism, degradation pathways and intermediates study, *Environmental Research*, 187 (2020) 109647. <https://doi.org/10.1016/j.envres.2020.109647>
- [141] Y. Zong, S. Ma, J. Gao, M. Xu, J. Xue, M. Wang, Synthesis of porphyrin Zr-MOFs for the adsorption and photodegradation of antibiotics under visible light, *ACS Omega*, 6 (2021) 17228. <https://doi.org/10.1021/acsomega.1c00919>
- [142] S. Zhao, S. Li, Z. Zhao, Y. Su, Y. Long, Z. Zheng, D. Cui, Y. Liu, C. Wang, X. Zhang, Z. Zhang, Microwave-assisted hydrothermal assembly of 2D copper-porphyrin metal-organic frameworks for the removal of dyes and antibiotics from water, *Environmental Science and Pollution Research International*, 27 (2020) 39186. <https://doi.org/10.1007/s11356-020-09865-z>
- [143] M. Gaeta, G. Sanfilippo, A. Fraix, G. Sortino, M. Barcellona, G. Oliveri Conti, M.E. Fragalà, M. Ferrante, R. Purrello, A. D'Urso, Photodegradation of antibiotics by noncovalent porphyrin-functionalized TiO₂ in water for the bacterial antibiotic resistance

- risk management, *International Journal of Molecular Sciences*, 21 (2020) 3775. <https://doi.org/10.3390/ijms21113775>
- [144] B. Yao, C. Peng, Y. He, W. Zhang, Q. Zhang, T. Zhang, Conjugated microspheres FeTCPP–TDI–TiO₂ with enhanced photocatalytic performance for antibiotics degradation under visible light irradiation, *Catalysis Letters*, 146 (2016) 2543. <https://doi.org/10.1007/s10562-016-1888-1>
- [145] C.R. Gardner, C.T. Walsh, O. Almarsson, Drugs as materials: valuing physical form in drug discovery, *Nature Reviews Drug Discovery*, 3 (2004) 926. <https://doi.org/10.1038/nrd1550>
- [146] N. A. Meanwell, in *Annual reports in medicinal chemistry*, Ed. E. M. John, Academic Press, 2008, 43, 373. <https://vdoc.pub/download/annual-reports-in-medicinal-chemistry-54uq2ig47c50> (last accessed on 04/10/2022)
- [147] O. Almarsson, M.J. Zaworotko, Crystal engineering of the composition of pharmaceutical phases. Do pharmaceutical co-crystals represent a new path to improved medicines?, *Chemical Communications*, 17 (2004) 1889. <https://doi.org/10.1039/b402150a>
- [148] T. Takagi, C. Ramachandran, M. Bermejo, S. Yamashita, L.X. Yu, G.L. Amidon, A provisional biopharmaceutical classification of the top 200 oral drug products in the United States, Great Britain, Spain, and Japan, *Molecular Pharmaceutics*, 3 (2006) 631. <https://doi.org/10.1021/mp0600182>
- [149] A. Portell, R. Barbas, M. Font-Bardia, P. Dalmases, R. Prohens, C. Puigjaner, Ziprasidone malate, a new trimorphic salt with improved aqueous solubility, *Crystal Engineering Communications*, 11 (2009) 791. <https://doi.org/10.1039/B813401D>
- [150] A.R. Duarte, A.S. Ferreira, S. Barreiros, E. Cabrita, R.L. Reis, A. Paiva, A comparison between pure active pharmaceutical ingredients and therapeutic deep eutectic solvents: solubility and permeability studies, *European Journal of Pharmaceutics and Biopharmaceutics*, 114 (2017) 296. <https://doi.org/10.1016/j.ejpb.2017.02.003>
- [151] K.T. Savjani, A.K. Gajjar, J.K. Savjani, Drug solubility: importance and enhancement techniques, *ISRN pharmaceutics*, 2012 (2012) 195727. <https://doi.org/10.5402/2012/195727>
- [152] S. Huang, C. Mao, R.O. Williams, III, C.-Y. Yang, Solubility advantage (and disadvantage) of pharmaceutical amorphous solid dispersions, *Journal of Pharmaceutical Sciences*, 105 (2016) 3549. <https://doi.org/10.1016/j.xphs.2016.08.017>

- [153] J.M. Skieneh, I. Sathisaran, S.V. Dalvi, S. Rohani, Co-amorphous form of curcumin–folic acid dihydrate with increased dissolution rate, *Crystal Growth & Design*, 17 (2017) 6273. <https://doi.org/10.1021/acs.cgd.7b00947>
- [154] J. Haneef, R. Chadha, Drug-drug multicomponent solid forms: cocrystal, coamorphous and eutectic of three poorly soluble antihypertensive drugs using mechanochemical approach, *American Association of Pharmaceutical Scientists*, 18 (2017) 2279. <https://doi.org/10.1208/s12249-016-0701-1>
- [155] ANDAs: pharmaceutical solid polymorphism. Available online: <https://www.fda.gov/downloads/Drugs/Guidances/UCM072866.pdf> (last accessed on 30/05/2022)
- [156] S. Cherukuvada, A. Nangia, Fast dissolving eutectic compositions of two anti-tubercular drugs, *Crystal Engineering Communications*, 14 (2012) 2579. <https://doi.org/10.1039/C2CE06391C>
- [157] I. Sathisaran, S.V. Dalvi, Crystal engineering of curcumin with salicylic acid and hydroxyquinol as coformers, *Crystal Growth & Design*, 17 (2017) 3974. <https://doi.org/10.1021/acs.cgd.7b00599>
- [158] S. Aitipamula, R. Banerjee, A.K. Bansal, K. Biradha, M.L. Cheney, A.R. Choudhury, G.R. Desiraju, A.G. Dikundwar, R. Dubey, N. Duggirala, P.P. Ghogale, S. Ghosh, P.K. Goswami, N.R. Goud, R.R.K.R. Jetti, P. Karpinski, P. Kaushik, D. Kumar, V. Kumar, B. Moulton, A. Mukherjee, G. Mukherjee, A.S. Myerson, V. Puri, A. Ramanan, T. Rajamannar, C.M. Reddy, N. Rodriguez-Hornedo, R.D. Rogers, T.N.G. Row, P. Sanphui, N. Shan, G. Shete, A. Singh, C.C. Sun, J.A. Swift, R. Thaimattam, T.S. Thakur, R. Kumar Thaper, S.P. Thomas, S. Tothadi, V.R. Vangala, N. Variankaval, P. Vishweshwar, D.R. Weyna, M.J. Zaworotko, Polymorphs, salts, and cocrystals: what's in a name?, *Crystal Growth & Design*, 12 (2012) 2147. <https://doi.org/10.1021/cg3002948>
- [159] C. Saal, A. Becker, Pharmaceutical salts: a summary on doses of salt formers from the orange book, *European Journal of Pharmaceutical Sciences*, 49 (2013) 614. <https://doi.org/10.1016/j.ejps.2013.05.026>
- [160] S.L. Childs, G.P. Stahly, A. Park, The salt–cocrystal continuum: the influence of crystal structure on ionization state, *Molecular Pharmaceutics*, 4 (2007) 323. <https://doi.org/10.1021/mp0601345>
- [161] S.A. Breda, A.F. Jimenez-Kairuz, R.H. Manzo, M.E. Olivera, Solubility behavior and biopharmaceutical classification of novel high-solubility ciprofloxacin and

- norfloxacin pharmaceutical derivatives, *International Journal of Pharmaceutics*, 371 (2009) 106. <https://doi.org/10.1016/j.ijpharm.2008.12.026>
- [162] S. Basavoju, D. Boström, S.P. Velaga, Pharmaceutical cocrystal and salts of norfloxacin, *Crystal Growth & Design*, 6 (2006) 2699. <https://doi.org/10.1021/cg060327x>
- [163] P.H. Stahl, C.G. Wermuth, *Handbook of pharmaceutical salts: properties, selection and use*, Wiley-VCH, Weinheim, Germany 2011.
- [164] Guidance for industry: regulatory classification of pharmaceutical co-crystals, 2018. <https://www.fda.gov/downloads/Drugs/Guidances/UCM281764> (last accessed on 9/05/2022)
- [165] E. Grothe, H. Meekes, E. Vlieg, J.H. ter Horst, R. de Gelder, Solvates, salts, and cocrystals: a proposal for a feasible classification system, *Crystal Growth & Design*, 16 (2016) 3237. <https://doi.org/10.1021/acs.cgd.6b00200>
- [166] R. Shaikh, R. Singh, G.M. Walker, D.M. Croker, Pharmaceutical cocrystal drug products: an outlook on product development, *Trends in Pharmacological Sciences*, 39 (2018) 1033. <https://doi.org/10.1016/j.tips.2018.10.006>
- [167] C.B. Aakeröy, A.S. Sinha, Chapter 1-Co-crystals: introduction and scope, co-crystals: preparation, characterization and applications, *The Royal Society of Chemistry* 2018, pp. 1.
- [168] C.B. Aakeröy, M.E. Fasulo, J. Desper, Cocrystal or salt: does it really matter?, *Molecular Pharmaceutics*, 4 (2007) 317. <https://doi.org/10.1021/mp060126o>
- [169] S.R. Fukte, M.P. Wagh, S. Rawat, Coformer selection: an important tool in cocrystal formation, *International Journal of Pharmacy and Pharmaceutical Sciences*, 6 (2014) 9. <https://innovareacademics.in/journals/index.php/ijpps/article/view/1733>
- [170] C.R. Taylor, G.M. Day, Evaluating the energetic driving force for cocrystal formation, *Crystal Growth & Design*, 18 (2018) 892. <https://doi.org/10.1021/acs.cgd.7b01375>
- [171] T. Grecu, C.A. Hunter, E.J. Gardiner, J.F. McCabe, Validation of a computational Cocrystal prediction tool: comparison of virtual and experimental cocrystal screening results, *Crystal Growth & Design*, 14 (2014) 165. <https://doi.org/10.1021/cg401339v>
- [172] Y.A. Abramov, C. Loschen, A. Klant, Rational coformer or solvent selection for pharmaceutical cocrystallization or desolvation, *Journal of Pharmaceutical Sciences*, 101 (2012) 3687. <https://doi.org/10.1002/jps.23227>

- [173] C. Loschen, A. Klamt, Solubility prediction, solvate and cocrystal screening as tools for rational crystal engineering, *Journal of Pharmacy and Pharmacology*, 67 (2015) 803. <https://doi.org/10.1111/jphp.12376>
- [174] C.R. Groom, I.J. Bruno, M.P. Lightfoot, S.C. Ward, The cambridge structural database, *Acta crystallographica. Section B, Structural science, crystal engineering and materials*, 72 (2016) 171. <https://doi.org/10.1107/S2052520616003954>
- [175] B.S. Sekhon, Drug-drug co-crystals, *DARU Journal of Pharmaceutical Sciences*, 20 (2012) 45. <https://doi.org/10.1186/2008-2231-20-45>
- [176] M.L. Cheney, D.R. Weyna, N. Shan, M. Hanna, L. Wojtas, M.J. Zaworotko, Coformer selection in pharmaceutical cocrystal development: a case study of a meloxicam aspirin cocrystal that exhibits enhanced solubility and pharmacokinetics, *Journal of Pharmaceutical Sciences*, 100 (2011) 2172. <https://doi.org/10.1002/jps.22434>
- [177] I. Nugrahani, S. Asyarie, S.N. Soewandhi, S.J.I.J.P. Ibrahim, The antibiotic potency of amoxicillin-clavulanate co-crystal, *International Journal of Pharmacology*, 3 (2007) 475. <https://doi.org/10.3923/ijp.2007.475.481>
- [178] S. Aitipamula, P.S. Chow, R.B.H. Tan, Trimorphs of a pharmaceutical cocrystal involving two active pharmaceutical ingredients: potential relevance to combination drugs, *Crystal Engineering Communications*, 11 (2009) 1823. <https://doi.org/10.1039/B904616J>
- [179] I.G. Télessy, Chapter 24 - Nutraceuticals, in: R.B. Singh, R.R. Watson, T. Takahashi (Eds.) *The role of functional food security in global health*, Academic Press 2019, pp. 409-421.
- [180] A.S. Sinha, A.R. Maguire, S.E. Lawrence, Cocrystallization of ntraceuticals, *Crystal Growth & Design*, 15 (2015) 984. <https://doi.org/10.1021/cg501009c>
- [181] A.O.L. Évora, R.A.E. Castro, T.M.R. Maria, M.R. Silva, J.H. ter Horst, J. Canotilho, M.E.S. Eusébio, A thermodynamic based approach on the investigation of a diflunisal pharmaceutical co-crystal with improved intrinsic dissolution rate, *International Journal of Pharmaceutics*, 466 (2014) 68. <https://doi.org/10.1016/j.ijpharm.2014.02.048>
- [182] H.G. Moradiya, M.T. Islam, N. Scoutaris, S.A. Halsey, B.Z. Chowdhry, D. Douroumis, Continuous manufacturing of high auality pharmaceutical cocrystals integrated with process analytical tools for in-line process control, *Crystal Growth & Design*, 16 (2016) 3425. <https://doi.org/10.1021/acs.cgd.6b00402>

- [183] S. Shewale, A.S. Shete, R.C. Doijad, S.S. Kadam, V.A. Patil, A.V. Yadav, Formulation and solid state characterization of nicotinamide-based co-crystals of fenofibrate, *Indian journal of pharmaceutical sciences*, 77 (2015) 328. <https://doi.org/10.4103/0250-474x.159669>
- [184] S. Cherukuvada, A. Nangia, Eutectics as improved pharmaceutical materials: design, properties and characterization, *Journal of Chemical Communications*, 50 (2014) 906. <https://doi.org/10.1039/C3CC47521B>
- [185] S. Cherukuvada, T.N. Guru Row, Comprehending the formation of eutectics and cocrystals in terms of design and their structural interrelationships, *Crystal Growth & Design*, 14 (2014) 4187. <https://doi.org/10.1021/cg500790q>
- [186] N.R. Goud, K. Suresh, P. Sanphui, A. Nangia, Fast dissolving eutectic compositions of curcumin, *International Journal of Pharmaceutics*, 439 (2012) 63. <https://doi.org/10.1016/j.ijpharm.2012.09.045>
- [187] M. Karimi-Jafari, L. Padrela, G.M. Walker, D.M. Croker, Creating cocrystals: a review of pharmaceutical cocrystal preparation routes and applications, *Crystal Growth & Design*, 18 (2018) 6370. <https://doi.org/10.1021/acs.cgd.8b00933>

Chapter 2

Synthesis, characterization and applications of porphyrin-based catalysts in the degradation of antibiotics

2.1 Trimethoprim and sulfamethoxazole as target antibiotics

As mentioned in the introduction, trimethoprim and sulfamethoxazole (TMP and SMX) are currently among the most prescribed antibiotics, showing high persistency, due to recalcitrant nature for the former and sufficient hydrophilicity of the latter [1-7]. They are usually used in a 1:5 fixed dose combination (FDC), having the common name of cotrimoxazole, commercially known as Bactrim [8]. They may be administered as two single entity products or combined in a “finished pharmaceutical product” [9]. These FDC drugs have been implemented for their advantages, particularly on improvement of treatment responses, when compared to monotherapies, due to synergistic mechanisms [9, 10]. Actually, TMP and SMX are synergistically used to treat and prevent a wide range of bacterial infections [11]. The World Health Organization (WHO) has listed them as some of the essential drugs required in a basic health system [12]. Sulfonamides began to be considered antimicrobial chemotherapeutic agents when, in 1932, the German scientist Domagk discovered the protective activity of sulfachrysoidine against streptococcal infections [13]. In the late 1930s, the simplest sulfonamide was studied and modified to reduce side effects and improve the activity, for example in urinary infections. However, only in the late 60s, Bushby and Hitchings reported the ability of TMP to enhance the effect of sulfonamide and, in 1974, TMP-SMX became a prescribed medication [14] (Figure 2.1).

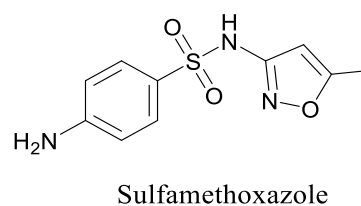
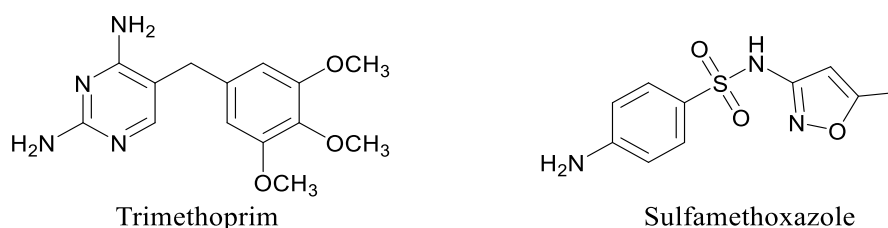


Figure 2.1 Chemical structures of TMP and SMX.

The FDA approved the use of TMP-SMX for many types of illnesses, such as urinary tract infections [15, 16], respiratory tract infections and cholera, methicillin-resistant *Staphylococcus aureus* skin infection [17-19], otitis in children and acute exacerbations of chronic obstructive pulmonary disease [20-22]. Moreover, it is also used to cure and prevent pneumocystis pneumonia and toxoplasmosis in people with HIV/AIDS and other causes of immunosuppression [8, 23]. Taking this into account, it is conceivable and well documented that the use of SMX-TMP is one of the highest in the world [24]. In fact, after leading a survey on the global consumption of antibiotics between 2000 and 2010, Van Boeckel revealed that the use of trimethoprim is among the five most used antibiotics worldwide and, especially in association with sulfonamides, is the fourth most consumed medicament in the world, after penicillins, macrolides, and fluoroquinolones [3, 25].

TMP and SMX are also administrated in combination and solely, for veterinary purposes, particularly to prevent and treat several animal bacterial diseases [26-29], for instance in the treatment of chicken diseases caused by pathogenic bacteria. Both have been frequently detected in various water domains [30], such as untreated municipal wastewaters [31, 32], hospital effluents [33], surface waters contaminated by pharmaceutical industries [34], in concentrations ranging from 10 to 2000 ng L⁻¹ [1-6]. Particularly, Verlicchi and coworkers reported in 2012 the highest concentration of TMP and SMX detected in secondary effluents, of 6.7 and 5 µg L⁻¹, respectively [7]. Since TMP and sulfonamides showed a high persistency, due to the recalcitrant nature for the first one and sufficient hydrophilicity of the second, both revealed considerable resistance to degradation.

It is accepted by the scientific community that these antibiotics' "pseudo-durability" in water environments for a long time may result in the development of antibiotic-resistant bacteria [35]. Bearing that in mind, in this chapter we describe two different strategies to degrade TMP: the first involves the antibiotic's oxidation using metalloporphyrin-based as catalysts, in presence of hydrogen peroxide as benign oxidant and the second uses porphyrin-based photocatalysts to promote antibiotic's degradation the presence of light and air as oxidant.

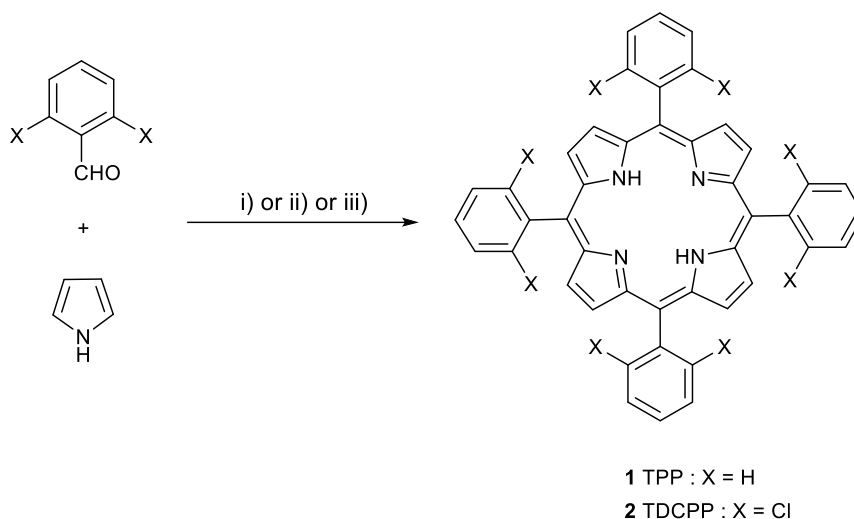
As mentioned in introduction, our first goal was to covalently immobilize a stable *meso*-aryl porphyrin onto suitably functionalized inorganic supports, such as silica gel and magnetic nanoparticles (MNPs), aiming to implement a heterogeneous reusable

system for the aqueous oxidative degradation of TMP, in presence of H₂O₂ as benign oxidant.

2.2 Synthesis of metalloporphyrins for homogeneous catalytic systems

One of the premises set in the design of this work was the knowledge that substitution in porphyrin's *meso* positions by electron-withdrawing groups, particularly chlorine at the *ortho*-positions of *meso*-phenyl groups, increases the porphyrin's stability against self-oxidation, providing both electronic and steric protection [36-40].

Regarding their synthesis, there are several methodologies providing symmetric *meso*-aryl porphyrins reported in literature [41-45]. In this work we followed the Nitrobenzene and NaY/Nitrobenzene [46, 47] approaches and the Water/MW (MW = microwave) [48] synthetic methods, as previously developed in Catalysis and Fine Chemistry group in Coimbra. These are one-step methodologies that allow a synthesis without using toxic quinones as oxidants [49]. The first two procedures just differ in the use of the NaY zeolite, as solid reusable Lewis acid catalyst that increases the activation of the aldehyde function towards nucleophilic attack. Furthermore, following the development of environmental sustainable processes, we extended the preparation of the tetrapyrrolic macrocycles to Water/MW synthetic method, where the polluting organic solvents are substituted by water, which is used as a pseudo-organic solvent at high temperatures and pressures [48]. Considering the nitrobenzene-based methods, in a typical experiment, pyrrole and the desired aldehyde, in equimolar amounts, were added in a mixture of glacial acetic acid/nitrobenzene (2:1) and, in absence (first method) or presence of NaY (second method), the reaction mixture was left under reflux, along 1 h or 2 h, respectively (Scheme 2.1 i and ii). Using the Water/MW method, in a typical experiment, equimolar amounts of aldehyde and pyrrole were put in a microwave vessel of 10 mL with distilled water. The reaction was left under microwave irradiation ($P_{\max} = 300$ W) at 200 °C for 10 minutes (Scheme 2.1 iii). It is worth mentioning that, in all cases, addition of methanol favored porphyrin's precipitation from reaction mixture.



Scheme 2.1 Synthesis of porphyrin **1** and **2** using i) Nitrobenzene method (mixture of CH₃COOH/Nitrobenzene, 140 °C and 1 h), ii) NaY/Nitrobenzene method (mixture of CH₃COOH/Nitrobenzene, NaY, 145 °C, 2 h) and iii) Water/MW method (300 W, 200 °C and 10 min).

The yields obtained on the synthesis of porphyrins **1** and **2**, using the three methods described above, are reported in Table 2.1.

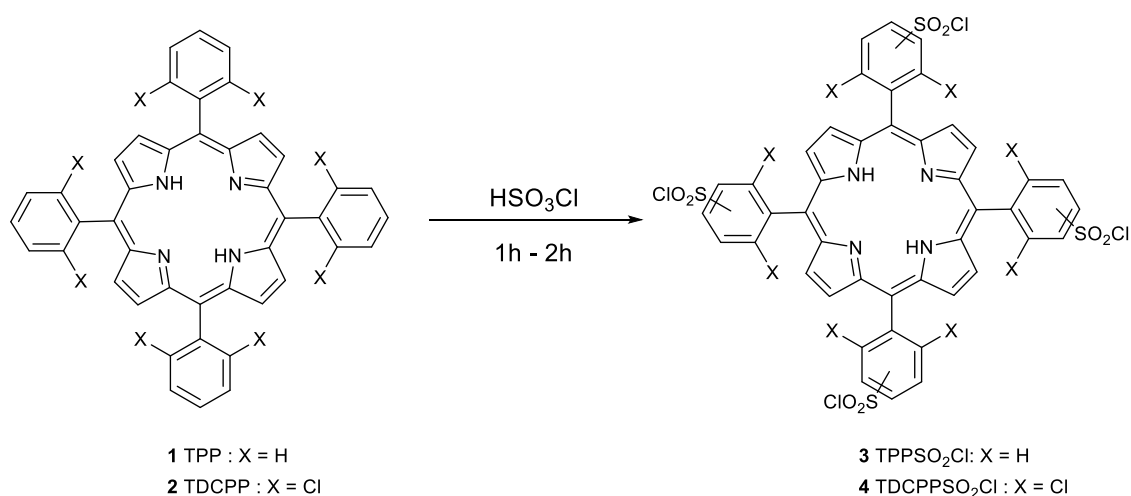
Table 2.1 Yields obtained for the two porphyrins using the three methods.

Entry	Porphyrin	Method	Yield (%)
1	1	Nitrobenzene	24
2		NaY/Nitrobenzene	35
3		Microwave/water	20
4	2	Nitrobenzene	3
5		NaY/Nitrobenzene	8
6		Microwave/water	5

The porphyrin **1** was synthesized using the three methods in yields of 24% (Table 2.1, entry 1), 35% (Table 2.1, entry 2) and 20% (Table 2.1, entry 3), while **2** was obtained in of 3%, 8% and 5% yields (Table 2.1, entries 4, 5 and 6) respectively. The NaY/Nitrobenzene offered the best porphyrin yields, however, the Water/MW method was preferred, due the more sustainable and green operational conditions, particularly

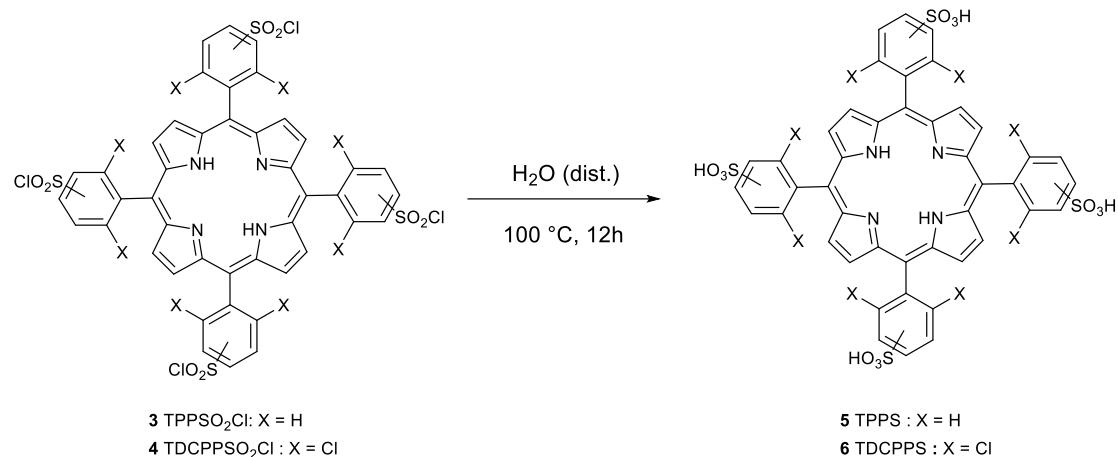
considering the use of toxic solvents and reaction times. These results are in agreement with previously described ones.

To study the porphyrin's structural influence in the homogenous degradation of the antibiotics, it was necessary to prepare water-soluble catalysts. To accomplish that, we envisaged the introduction of chlorosulfonyl group at the porphyrin's periphery, using the method reported by Gonsalves and Pereira [50]. In a typical experiment, porphyrins **1** and **2** were dissolved with 8 equivalents of chlorosulfonic acid at 25°C, for one hour (porphyrin **1**), or at 100 °C for two hours (porphyrin **2**), Scheme 2.2.



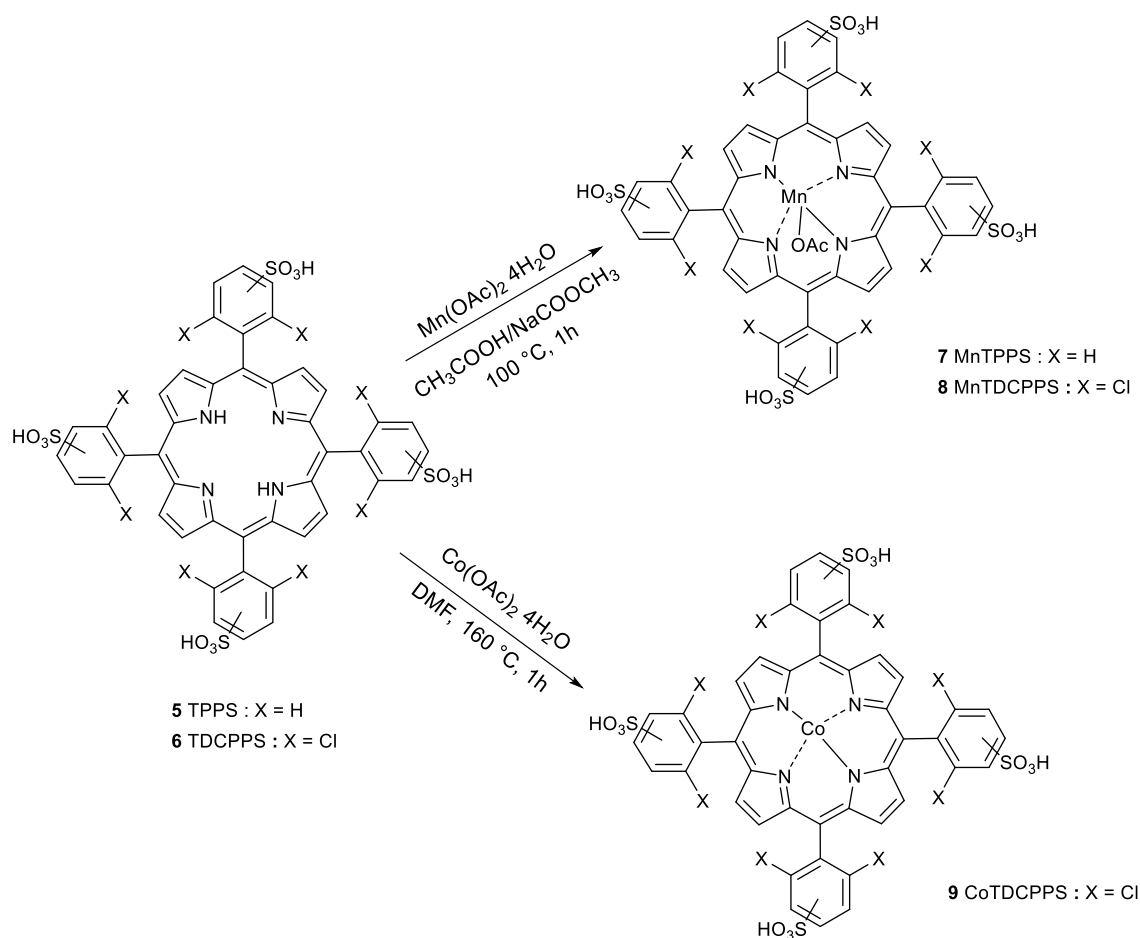
Scheme 2.2 Synthesis of chlorosulfonated porphyrin **3** and **4**.

The chlorosulfonated products, (**3** and **4**, Scheme 2.2), were isolated using a homemade continuous water extraction process, which removed the organic acids present. After standard work up, compounds **3** and **4** were either used directly in S_N reactions for immobilization in inorganic supports (section 2.4) or hydrolyzed to yield the water-soluble sulfonated porphyrins **5** and **6**, by refluxing **3** and **4** in water for 12 hours, respectively (Scheme 2.3). Compounds were isolated in 70% and 75% yield, respectively, in agreement with literature [51].



Scheme 2.3 Synthesis of hydrolyzed porphyrins **5** and **6**.

Finally, the last step to obtain the desired metal complex catalyst to perform the oxidative degradation of antibiotics, consisted in the porphyrin's metalation. The *meso*-tetraaryl porphyrins **5** and **6** were complexated with Mn(II) and Co(II) salts, using literature procedures, particularly the Wijesekera and Dolphin's method [52] to obtain **7** and **8**, in which a mixture of acetic acid and sodium acetate is used, and Adler's method [43] which used DMF as solvent, to obtain porphyrin **9**, Scheme 2.4.



Scheme 2.4 Synthesis of metalloporphyrins **7-9** using Mn(II) and Co(II) salts.

Thus, in a typical experiment, the sulfonated porphyrin and an excess of manganese(II) acetate tetrahydrate were dissolved in acetic acid and sodium acetate was added. The mixture was heated at $100\text{ }^\circ\text{C}$ for 1 hour, checked by TLC and UV-Vis. The desired compound was obtained by crystallization using ethyl acetate to precipitate both **6** and complexated porphyrins, **7** and **8**. Upon filtration, the solids were washed with isopropyl alcohol, to remove any residual impurities as well as the free-base sulfonated porphyrin, providing the desired complexated ones.

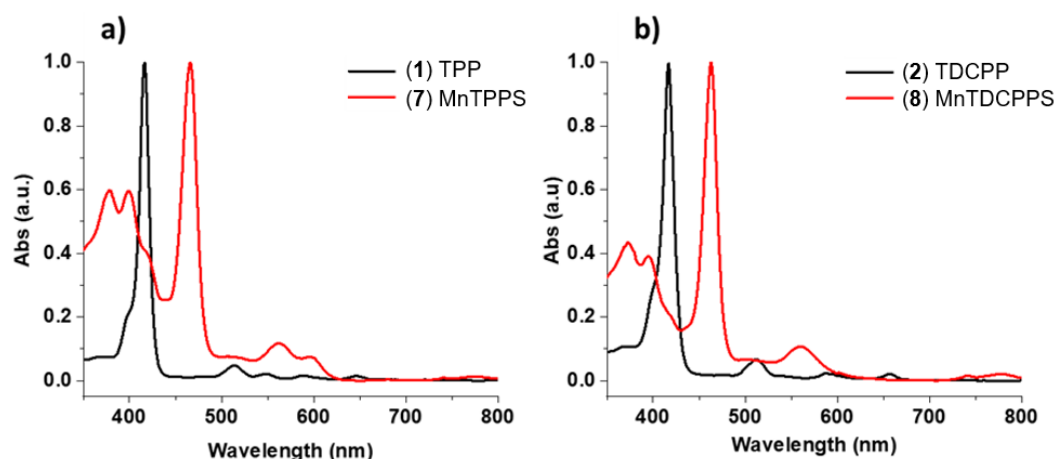


Figure 2.2 Normalized UV-Vis spectra of **a**) TPP (**1**, black line) and MnTPPS (**7**, red line) and **b**) TDCPP (**2**, black line) and MnTDCPPS (**8**, red line). The spectra were recorded in DMSO.

Figure 2.2 shows the differences between free base porphyrins **1** and **2**, and their manganese(III) complexes, **7** and **8**, respectively. Generally, the characteristic UV-Vis spectrum of the free base porphyrin shows its Soret band as the one with the highest absorptivity molar coefficient (ϵ), near 420 nm, whereas the other four bands, the Q bands, present a much lower intensity [53]. When the porphyrin forms a metallic complex, its UV-Vis spectrum changes and usually shows a bathochromically shifted Soret band, always characterized by a high ϵ and only two Q bands due to the change in the molecule's symmetry, from D_{2h} into D_{4h} [54]. In this case, the Soret band appeared at 416 nm for porphyrin **1**, (Q bands at 515, 547, 589 and 646 nm) and at 417 nm for porphyrin **2** (with Q bands at 515, 547, 583 and 652 nm). Upon metalation, porphyrins' Soret bands displayed a bathochromic shift, at 466 nm for **7** and 463 nm for **8**. The bathochromic shift deriving from the metalation with manganese has been already reported in literature [55].

In the case of Co(II) complexation reaction, the porphyrin **9** and the cobalt(II) acetate tetrahydrate were dissolved in the minimum amount of DMF, heated until reflux and left for 1 hour at that temperature. The metalation was also monitored by TLC and UV-Vis. After reaction completion, since the desired porphyrin was soluble in water, the complex **9** was simply obtained by precipitation, using diethyl ether. The UV-Vis spectral Soret band of cobalt porphyrin complex was coincident with the TDCPP's Soret band, at 416 nm, but the evidence of metalation could be corroborated by the transformation of the four Q bands into two Q bands (**Figure 2.3**).

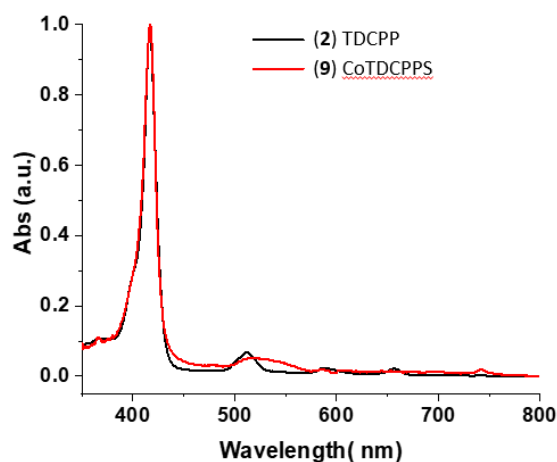


Figure 2.3 UV-Vis spectra of TDCPP (**2**, black line) and CoTDCPPS (**9**, red line). The spectra were recorded in DMSO.

The metalloporphyrins **7-9** were obtained in 89%, 88% and 80% isolated yields, respectively. Moreover, all synthesized porphyrins and metalloporphyrins were fully characterized by NMR and mass spectrometry, and the characterization data is in agreement with the literature (Chapter 4).

2.3 Homogeneous catalytic degradation of TMP

As mentioned in the introduction, the biomimetic metalloporphyrins have already been reported in literature to promote the oxidation of water pollutants [56-60]. However, since the use of metalloporphyrins was yet undisclosed in the degradation of antibiotics [61] at the beginning of this work, their evaluation as catalysts in the degradation of trimethoprim was devised and implemented.

The studies began by performing the degradation experiments under homogenous conditions, to obtain a structure-property relationship regarding the metalloporphyrin catalysts. In a typical experiment, the metalloporphyrins **7-9** and the TMP ($[\text{TMP}] = 0.23 \text{ mM}$) were dissolved in distilled water. A 900:1 ratio between the TMP and the catalyst was chosen, and the reaction was performed at room temperature ($25 \text{ }^\circ\text{C}$) under stirring and using H_2O_2 (30% w/v) as benign oxidant. The reaction started by slowly adding $30 \text{ }\mu\text{L}$ of H_2O_2 (30% w/v) and then additional H_2O_2 aliquots were added each 15 minutes, until reaching a total volume of $300 \text{ }\mu\text{L}$, corresponding to a 2.6 mmol totally

added, and proceeding for 150 minutes. In Table 2.2, the degradation results are reported for each catalyst tested.

Table 2.2 Homogeneous aqueous degradation of TMP, using metalloporphyrins **7-9** as catalysts and hydrogen peroxide.

Entry	Catalyst ^{a)}	Degradation ^{b)} (%)
1	(7) MnTPPS	7
2	(8) MnTDCPPS	95 ^{c)}
3	(9) CoTDCPPS	15

^{a)} number of moles of catalyst: 5.0×10^{-9} mol; ^{b)} TMP (1.3 mg, 4.5×10^{-6} mol); TMP:Cat ratio = 900:1; $V_{\text{H}_2\text{O}_2 (30\%)} = 30 \mu\text{L}$ added each 15 minutes; $V_{\text{total} [\text{H}_2\text{O}_2 (30\%)]} = 300 \mu\text{L}$; time = 150 min; ^{c)} after 90 min.

Each 15 minutes, before the addition of more 30 μL of H_2O_2 (30% w/v), an aliquot of reaction mixture was taken to be injected into the HPLC equipment to follow the degradation. In this case, it was intended to analyze the influence of porphyrin structure and the effect of the metal complexed inside the tetrapyrrolic macrocycle. Regarding the effect of the porphyrin structure, it was observed that the Mn(III) catalyst **7** led to a 7% oxidative degradation in 150 min (Table 2.2, entry 1), whereas Mn(III) catalyst **8** gave 95% TMP degradation in just 90 minutes (Table 2.2, entry 2). This difference may be attributed to the catalysts' stability, since porphyrin **7** has no substituents at the *meso*-phenyl rings, while **8** presents chlorine atoms at the *ortho*-positions of *meso*-phenyl groups. Literature reports many studies demonstrating that the presence of electron withdrawing atoms at the *ortho*-positions of *meso*-phenyl groups increase the porphyrin's stability against self-oxidation, providing both electronic and steric protection [36-39]. Nevertheless, each reaction was monitored by UV-Vis in order to corroborate these assumptions and the spectra are reported in **Figure 2.4**.

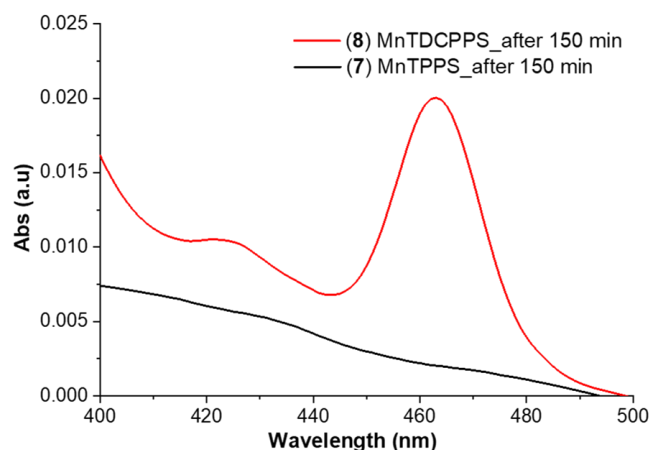


Figure 2.4 UV-Vis spectra recorded in distilled water at the end of the reaction by using catalyst **7**, reported with black line, and catalyst **8**, in red line.

The UV-Vis spectrum taken from an aliquot of the reaction mixture, after 150 min, clearly shows that the typical metalloporphyrin Soret band at 463 nm, was still present for catalyst **8** (red line), whereas it disappeared for catalyst **7** (black line). These results indicate that MnTDCPPS (**8**) is stable to this oxidation reaction conditions, while MnTPPS (**7**) suffers oxidative cleavage as previously described for other catalytic systems [37, 62].

The effect of the central metal used was also evaluated. As reported in Table 2.2, the catalyst **8** promoted 95% TMP degradation in just 90 minutes (Table 2.2, entry 2), while **9** only gave 15% of TMP degradation in 150 minutes (Table 2.2, entry 3).

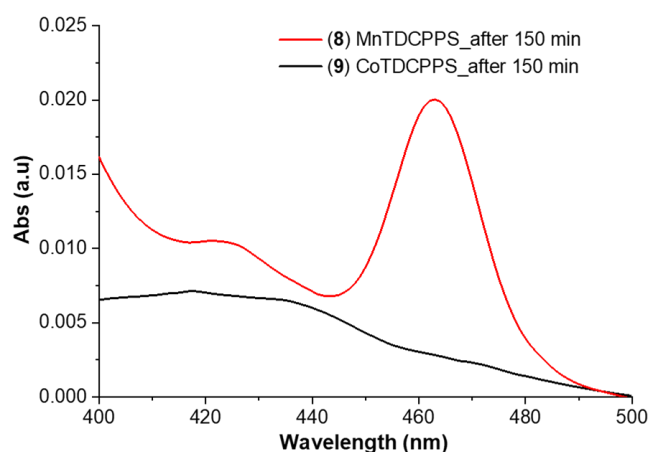
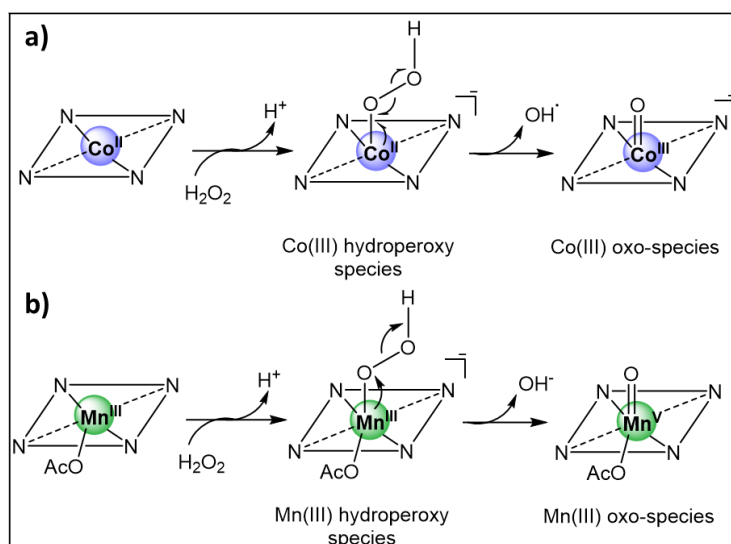


Figure 2.5 UV-Vis spectra recorded in distilled water at the end of the reaction when using **8**, red line, and **9**, black line.

Once again, we evaluated the catalyst stability by UV-Vis (**Figure 2.5**) and observed that catalyst **8** remained stable after the addition of the 300 μL of hydrogen peroxide, while the catalyst **9** was completely degraded, after the same 150 min reaction time (**Figure 2.5**). Despite the presence of chlorine atoms at the ortho positions of the phenyl rings in both catalysts, the metal ion influenced the catalyst stability due to the formation of different species (Scheme 2.5).



Scheme 2.5 General pathway for the formation of **a)** Co and **b)** Mn active species.

As depicted in the Scheme 2.5 a, for the Co(II) complexes, the Co(II) hydroperoxide species is transformed into the Co(III)=O oxo-species, liberating OH· radicals that can easily react with **9**, causing its degradation. Contrarily, in the Mn(III) complexes, the Mn(III) hydroperoxide species are transformed into Mn(V)=O *via* heterolytic cleavage, releasing the non-reactive OH⁻ (Scheme 2.5 b) [63].

In addition, UV-Vis spectroscopy was also used to check the antibiotic degradation, recorded before starting the experiment and after reaction (**Figure 2.6**).

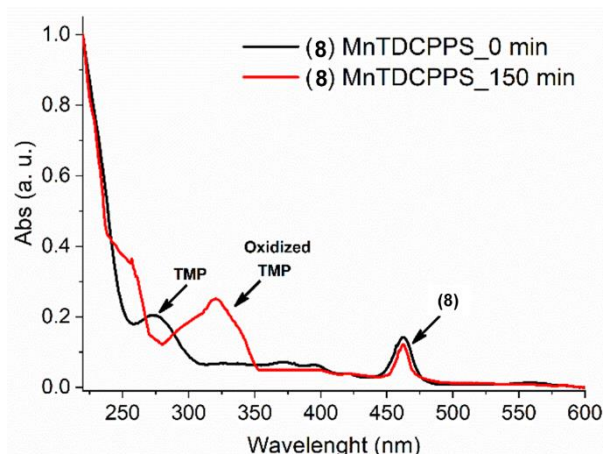


Figure 2.6 Normalized UV-Vis spectra recorded in distilled water using **8** at the beginning of reaction (black line) and at the end of the reaction (red line).

TMP is visible by UV-Vis and showed a peak at 273 nm, recorded at reaction time = zero, whereas a shift of this peak was observed around 321 nm, attributed to oxidized products, after degradation reaction (**Figure 2.6**).

In parallel, the degradation was also followed by HPLC, by taking aliquots of the reactions before each H_2O_2 addition (**Figure 2.7 a**).

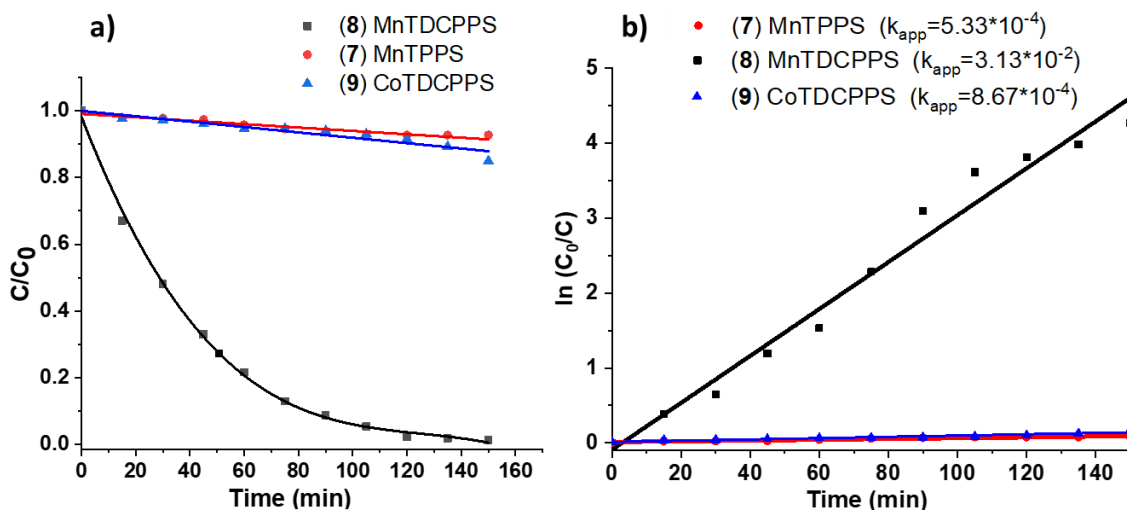


Figure 2.7 a) Homogeneous catalytic degradation TMP curves for each catalyst tested **7-9**; **b)** Kinetic curves of homogeneous TMP degradation.

The reaction profiles, when homogeneous catalysts **7** and **9** were used (**Figure 2.7 a**), showed linearity, exhibiting low activities which could be considered negligible along the time, 7% and 15% respectively. On the other hand, considering the experiment with

8 (Figure 2.7 a) black line), the reaction pathway showed an exponential behavior, and a 95% of degradation could be achieved after 150 minutes, as the asymptotic trend of the degradation curve suggests.

Considering the literature, the catalytic homogeneous oxidation of most organic pollutants follows the Langmuir-Hinshelwood (L-H) kinetic model. So, we calculated the kinetic constant for each of the three reactions making an approximation (Figure 2.7 b) [64, 65]. We were able to calculate the apparent first-order rate constant, k_{app} , considering that, at zero time, the chemical concentration is 1 millimolar solution. So, we considered this simplified equation (Eq. 2.1):

$$\ln\left(\frac{C_0}{C_t}\right) = kKt = k_{app}t \quad (2.1)$$

where C_t and C_0 are the TMP concentration at a designated time (t) and at zero time, respectively, k the reaction rate constant ($\text{mg L}^{-1} \text{min}^{-1}$), K the adsorption coefficient of the reactant (L mg^{-1}) and t is the time.

Table 2.3 k_{app} values calculated in the homogeneous aqueous degradation of TMP, using metalloporphyrins as catalysts **7-9** and hydrogen peroxide as green oxidant.

Entry	Catalyst ^{a)}	k_{app} ^{b)} (min^{-1})
1	(7) MnTPPS	5.33×10^{-4}
2	(8) MnTDCPPS	3.13×10^{-2}
3	(9) CoTDCPPS	8.67×10^{-4}

^{a)} number of moles of catalyst: 5.0×10^{-6} mol; ^{b)} apparent rate constant (k_{app}) calculated by the simplified equation $\ln\frac{[TMP]_0}{[TMP]_t} = k_{app}t$.

Plotting the values of $\ln C_0/C_t$ versus time, the slope of the linear regression was the value of k_{app} (Figure 2.7 b). It could be observed that, when catalyst **8** was used, the reaction proceeded with an apparent rate constant of 0.0313 min^{-1} , whereas in the presence of the others two porphyrins, **7** and **9**, the reaction was $62\times$ and $36\times$ slower, respectively. We can conclude that the porphyrin **8** was the best catalyst in the

homogeneous oxidation of TMP, due to its higher activity and stability against self-oxidation.

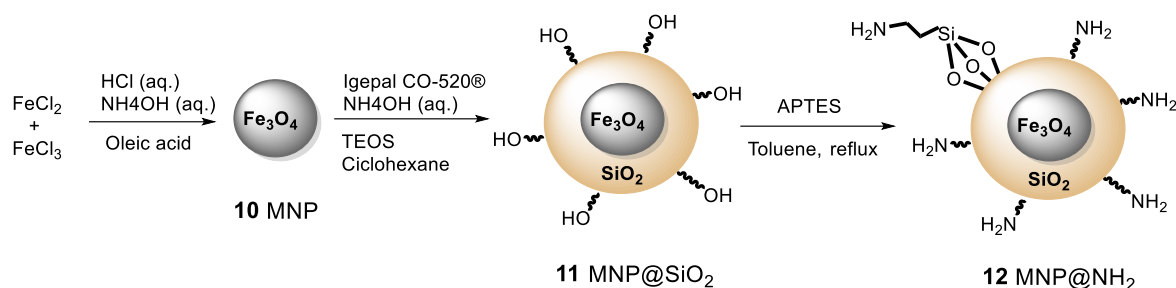
2.4 Synthesis and characterization of hybrid materials for heterogeneous catalysis

As mentioned before, the goal was to find the most stable metalloporphyrin to use in the heterogeneous degradation of the ABs. The immobilization of the metalloporphyrin in an inorganic support is a major driving force in our studies, since it enables the catalyst reutilization, simultaneously offering protection, to a certain extent, against its degradation. In literature, several immobilization methods, as well as various inorganic solid supports, have been already reported, allowing the development of new hybrid organic–inorganic materials based on tetrapyrrolic macrocycles, to conjugate the best performance of both fields [66].

In this chapter, suitably functionalized magnetic nanoparticles (**MNPs**) and silica gel (**SiO₂**) were chosen as inorganic platforms for the development of the heterogeneous catalysts, with particular focus on the immobilization *via* covalent bonding of the metalloporphyrin to the inorganic support. This type of immobilization guarantees the maintenance of the tetrapyrrolic macrocycle into/onto the inorganic support, avoiding leaching [61]. This choice was led by the attractive advantages in the use of **MNPs** and silica as supports. In fact, on the one hand, **MNPs** are widely recognized in literature for their low toxicity and superparamagnetic properties [67] and their easy recovery and reutilization by applying an external magnet [68-70]. On the other hand, silica is used as solid support in heterogeneous catalysis for its abundance, low cost, easy handling, non-corrosive nature, low toxicity and relatively simple separation after reaction [71-73].

2.4.1 Synthesis, functionalization, and characterization of MNPs

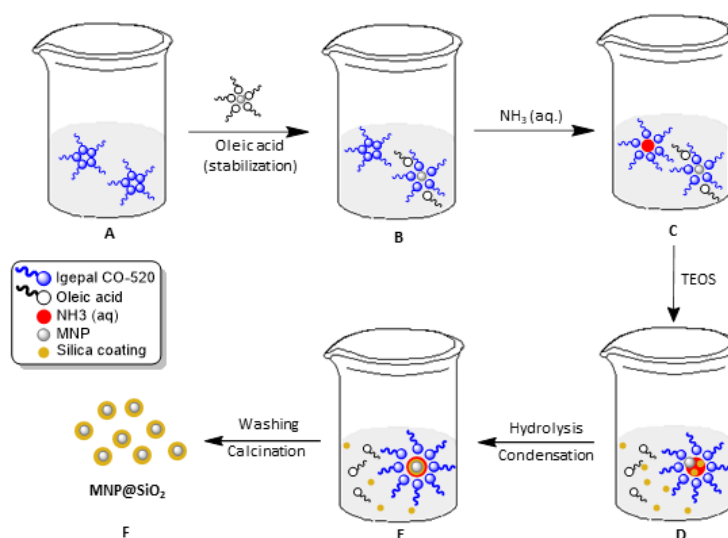
Following previous studies described in the literature on the synthesis of **MNPs**, the magnetic nanoparticles were obtained using the methodology depicted in Scheme 2.6, starting from the synthesis of magnetite, Fe₃O₄, followed by silica coating and finally amine functionalization [74, 75].



Scheme 2.6 Synthesis and functionalization of magnetic nanoparticles, **MNP@NH₂**, **12**.

Fe_3O_4 was obtained by co-precipitating Fe^{2+} and Fe^{3+} ions in basic conditions. A mixture of an aqueous solution of 1 M FeCl_3 and a 2 M HCl solution of FeCl_2 was added to a 1 M aqueous NH_3 and stirred for 30 min. The nanoparticles were washed with acetone and re-dissolved in distilled water. Then, **MNPs** were stabilized by adding oleic acid dropwise, previously dissolved in acetone, under vigorous mechanical stirring for 30 min. Finally, the stabilized MNPs were recovered by an external magnet, dispersed in cyclohexane and centrifugated to remove the non-stabilized nanoparticles. A stock solution of 72 mg of **MNPs** mL^{-1} in cyclohexane was obtained.

The coating with silica was carried out according to the microemulsion method (Scheme 2.7) [76].



Scheme 2.7 Reverse microemulsion methodology for **MNP@SiO₂**, **11**.

Firstly, the Igepal CO-520® was dispersed in cyclohexane to form micelles (A). Then, the MNPs, previously prepared, were added to promote ligand exchange between the oleic acid and the Igepal CO-520® (B). After that, an aqueous solution of ammonium hydroxide was added to this microemulsion, to fill the residual micelles of Igepal CO-520® interior (C). Subsequently, tetraethyl orthosilicate (TEOS), was added dropwise and the reaction was carried out for 16 h, under mechanical stirring (300 rpm). The TEOS hydrolysis occurs in the oil/water interface permitting the ligand exchange to the water (D). The condensation of hydrolyzed TEOS promotes the growth of silica coating around MNPs (E). The system was left for 16 h, under stirring (300 rpm) and at room temperature. After this period, the MNPs were precipitated with methanol and recovered by centrifugation (7000 rpm, 30 min) and washed several times with ethanol. Finally, silica coated nanoparticles (**11**) were dried at room temperature for 24 h and calcinated at 500 °C for other 2 h (F).

The nanoparticles (**11**) were characterized by transmission electron microscopy (TEM) to observe the nanoparticles morphology before and after the silica coating (**Figure 2.8 a** and **c**, respectively). TEM images of oleic acid stabilized MNP showed nanoparticles with a mean size of ~ 5.5 nm (**Figure 2.8 b**); whereas (**11**) MNP@SiO₂ presented a mean size of ~ 44.5 nm (**Figure 2.8 d**).

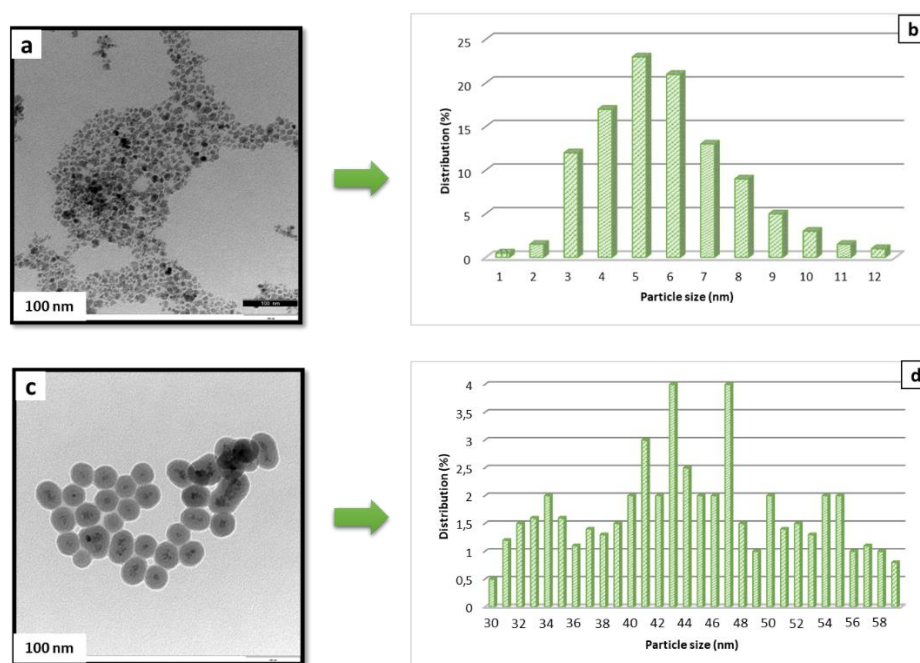


Figure 2.8 TEM images of: **a)** MNP stabilized in oleic acid; **b)** MNP size distribution histogram; **c)** MNP@SiO₂; **d)** corresponding size distribution histogram.

The functionalization of **11** was carried out using 3-aminopropyltriethoxysilane (APTES), in dry toluene for 2 h, following the Grobet's method [77]. Then, after washing procedures and centrifugation, the amino-functionalized MNP@NH_2 , **12**, were collected. The material was characterized by TG (Figure 2.9 a) and FTIR analysis (Figure 2.9 b).

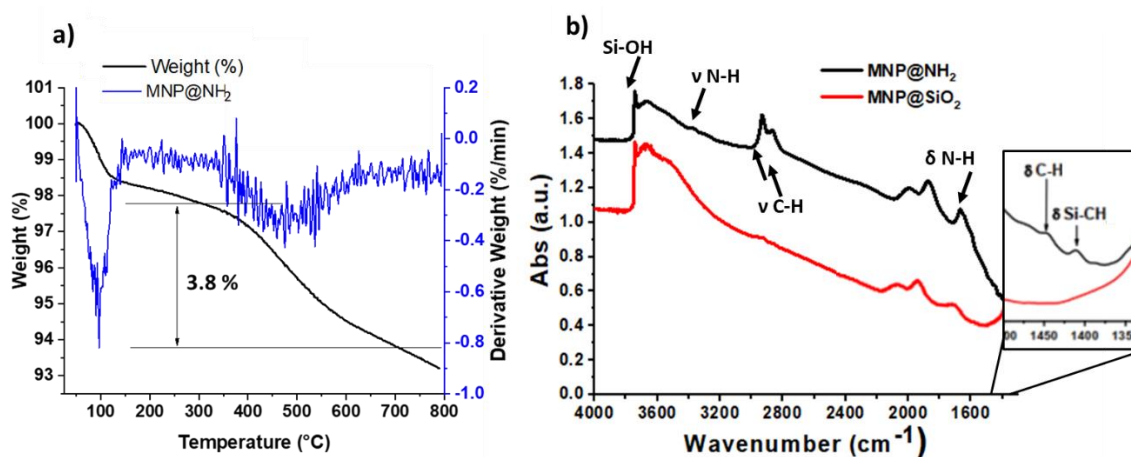


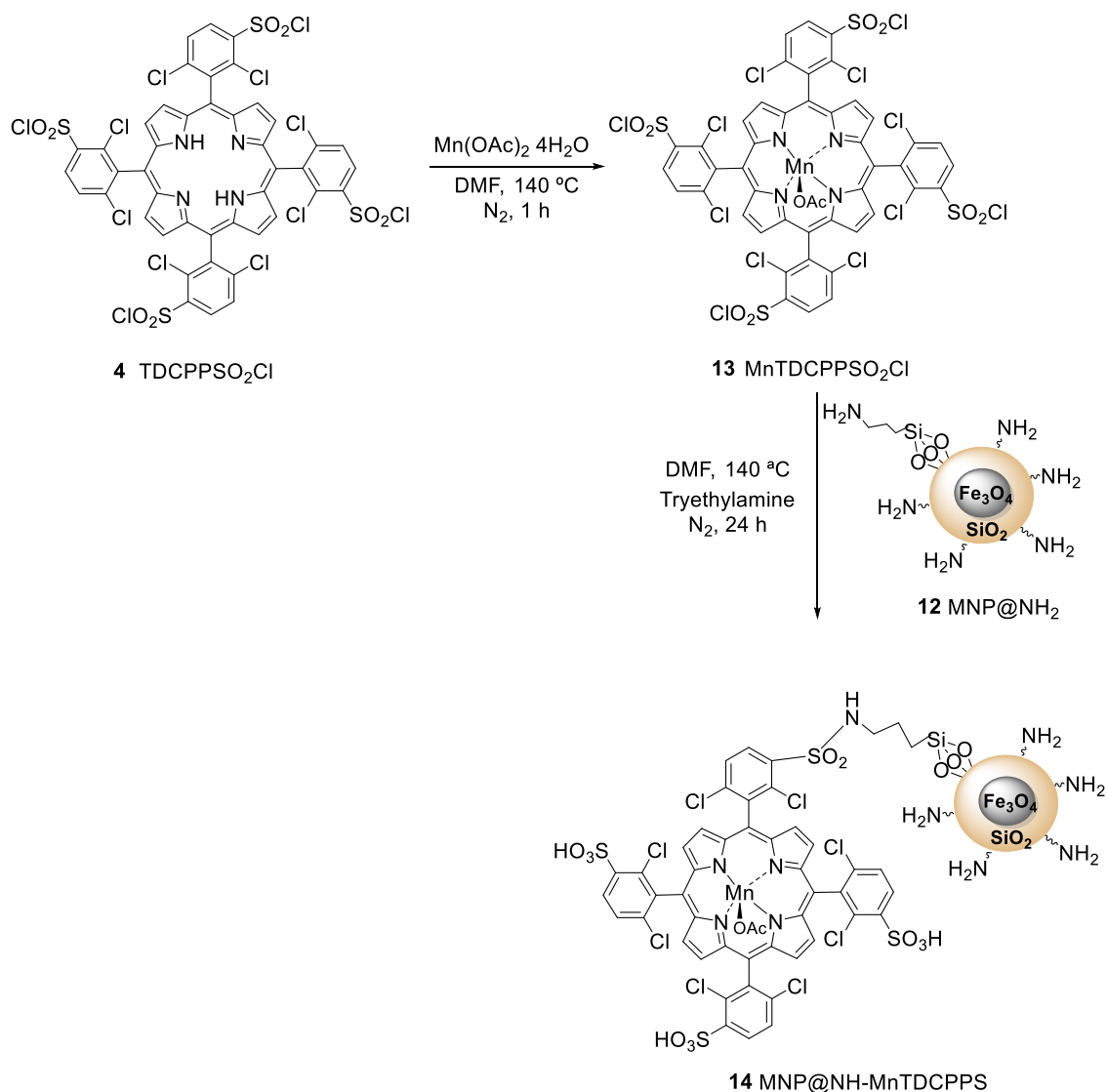
Figure 2.9. a) TG curve of MNP@NH_2 (weight loss- black line); b) FTIR spectra of MNP@SiO_2 (red line) and MNP@NH_2 (black line).

The thermogravimetry was recorded between 20 °C and 800 °C to quantify the organic counterparts on the **MNP**. The thermogram showed a peak between 20 °C and 100 °C, normally attributed to the adsorbed water. Then, another peak between 200 °C and 600 °C with a weight loss of 3.8%, ascribed to the decomposition of propylamine groups. This means that nanoparticles contain 0.65 mmol of propylamine groups *per gram* of **12**.

Furthermore, the FTIR characterization was crucial to detect the bands related to the functionalization of the material comparing **11** with **12**. The MNP@SiO_2 spectrum (red line) showed only a narrow band at 3740 cm^{-1} , normally ascribed to the silanol groups related to the silica coating. In turn, MNP@NH_2 spectrum (black line) displayed several characteristic peaks of functionalization beyond that of silanol groups, previously mentioned. Particularly, peaks at 3371 and 3309 cm^{-1} were attributed to the stretching of NH_2 groups and at 1597 cm^{-1} ascribed to NH_2 groups bending. A peak was detected at $2931\text{--}2865\text{ cm}^{-1}$, assigned to the stretching of CH_2 groups. Other peaks were detected and are showed in the small zoom: at 1450 cm^{-1} for the bending of CH_2 groups and at 1410 cm^{-1} attributed to the bending of Si-CH_2 bond which is another evidence of this functionalization [78, 79].

2.4.2 Synthesis of MNPs@NH-MnTDCPPS

The hybrid metalloporphyrin-based magnetic catalyst, **MNPs@NH-MnTDCPPS (14)**, was prepared using a two-step strategy: the first step involved the metalation of **TDCPPSO₂Cl (4)** with Mn(OAc)₂·4H₂O, followed by the covalently linkage of **MnTDCPPSO₂Cl (13)** to **MNP@NH₂ (12)**, as reported in the Scheme 2.8.



Scheme 2.8 Synthetic pathways for the MnTDCPPSO₂Cl (**13**) anchoring on **12**.

Compound **4** was complexated using manganese(II) acetate and DMF, to avoid potential hydrolysis of chlorosulfonic groups. The complexation occurred in 2 h, at 140 °C under nitrogen atmosphere. After observation that the UV-Vis spectrum is typical of Mn(III) porphyrin, material **12** was added to the reaction mixture, along with dry

triethylamine and the reaction pursued for further 24 h, under stirring. The desired MNPs@NH-MnTDCPPS, **14**, was washed several times with water and dichloromethane, to remove the DMF and left one night to permit the slow accumulation of nanoparticles. Then, an external magnet was applied to isolate **14**, which was fully characterized.

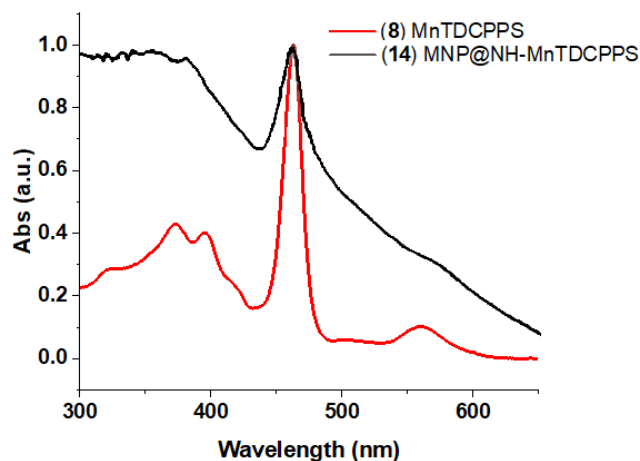


Figure 2.10 Normalized UV-Vis spectra overlap of **14**, in DMF (black line) and **8**, recorded in water (red line).

Figure 2.10 displays the UV-Vis spectrum of the hybrid material **14** (black line) and MnTDCPPS (**8**). The presence of porphyrin was confirmed in the hybrid material, by the observation of the typical broad Soret band at 465 nm, similar to that seen also in the spectrum of MnTDCPPS **8**. Moreover, the manganese content was determined by ICP, revealing a Mn amount of 0.095%, corresponding to a 2% of MnTDCPPS covalently linked to the support (0.018 mmol per gram of magnetic nanoparticles).

Additionally, TG-dTGA analysis was also used to quantify the porphyrin content anchored to magnetic nanoparticles (**Figure 2.11**).

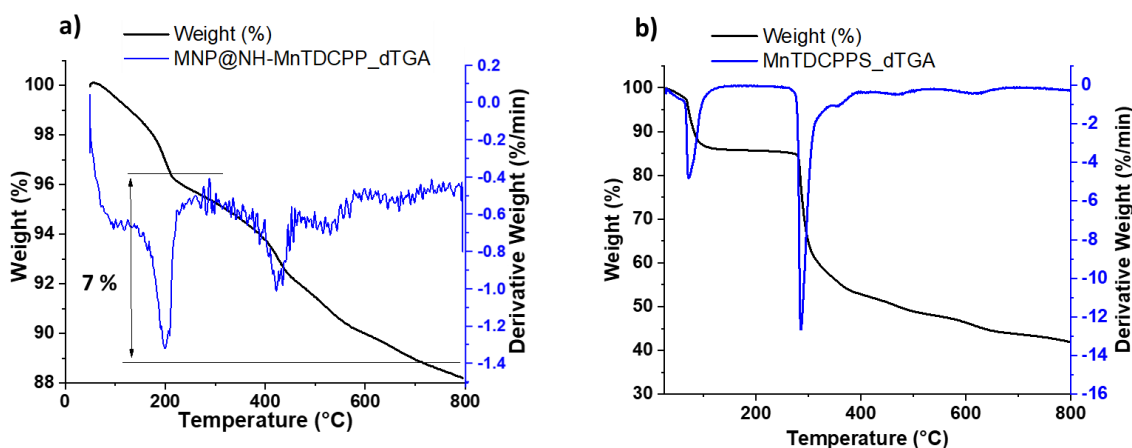
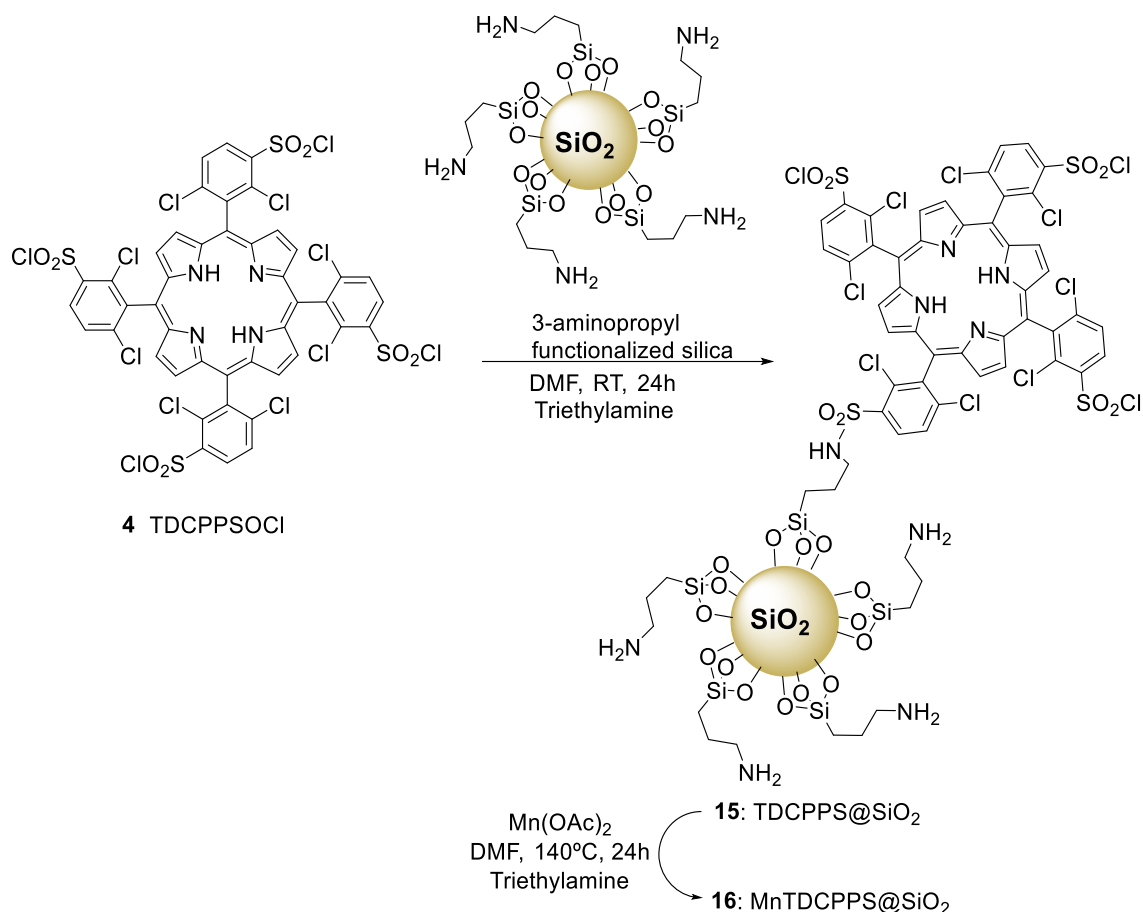


Figure 2.11 TG curves of: **a)** MNPs@NH-MnTDCPPS (**14**) (weight loss- black line; derivative weight- blue line); **b)** MnTDCPPS (**8**) (weight loss- black line; derivative weight- blue line).

The measurements were carried out in a range of temperature between 25 °C and 800 °C, using the Mn(II) porphyrin as the reference material (**Figure 2.12 b**). Comparing the thermogram of the desired compound (**14**) with the previous ones (**8**), a weight loss between 50 °C and 200 °C ascribed to the desorption of water and residual organic solvents, while other weight losses were displayed between 200 °C and 800 °C, due to the porphyrin organic decomposition. The Mn(III) porphyrin counterpart immobilized into magnetic nanoparticles was calculated based on the previous thermogram (**Figure 2.9 a**), used as blank, and a mass loss of ~3% was observed.

2.4.3 Synthesis of MnTDCPP-based 3-aminopropyl functionalized silica, MnTDCPPS@SiO₂

Aiming to establish a comparison of the effect of the support, the immobilization by covalent linkage of MnTDCPPS, **8** onto 3-aminopropyl functionalized SiO₂ was also promoted, Scheme 2.9.



Scheme 2.9 Synthetic pathways for the immobilization of chlorosulfonated porphyrin **4** onto 3-aminopropyl functionalized silica.

In a typical experiment, the 3-aminopropyl functionalized silica was dissolved in dry DMF and triethylamine was then added. The chlorosulfonated porphyrin **4**, previously dissolved in a minimal amount of dry DMF, was added dropwise to the flask. The reaction was stirred at room temperature for 24 hours, after which, without isolation, an excess of Mn(OAc)₂ was added to the reaction mixture and stirred under reflux (140 °C) for another 24 hours. After cooling, the solid material was isolated by centrifugation and washed several times with water, ethanol, and acetonitrile to remove the residue of metal salt and the non-linked porphyrin. At the end, the desired catalyst MnTDCPPS@SiO₂, **16**, was isolated and dried in an oven at 60 °C for 48 hours.

The hybrid material **16** was analyzed by scanning electron microscopy (SEM) to obtain information about its morphology and compared with the one of the 3-aminopropyl functionalized silica.

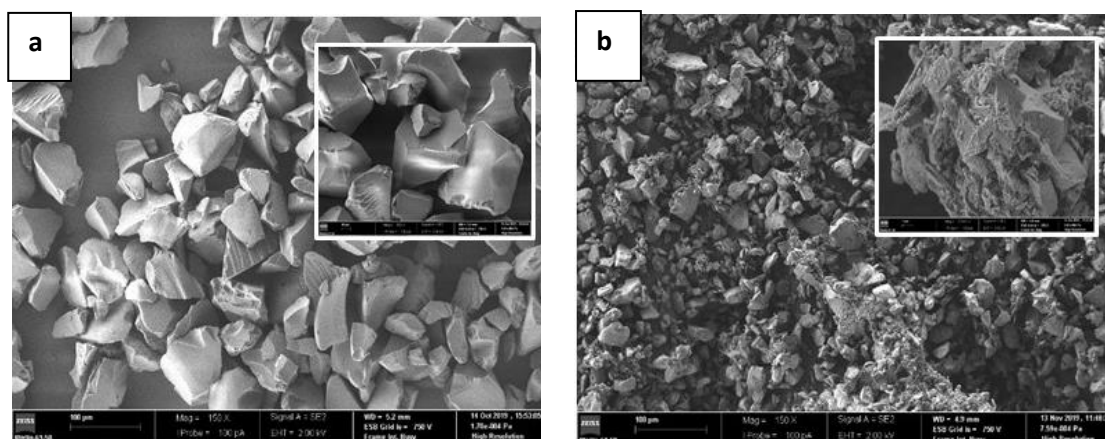


Figure 2.12 SEM images: **a**) of 3-aminopropyl functionalized silica (obtained with magnification = $\times 150$, zoom was obtained with a magnification of $\times 500$); **b**) of **MnTDCPPS@SiO₂** catalyst **16** (obtained with magnification = $\times 150$, zoom was obtained with a magnification of $\times 5000$).

SEM images of the 3-aminopropyl functionalized silica showed a granular nature with irregular particles, which is characteristic of silica gel. The particles size is variable, a range between 40 and 63 μm was observed, which is in agreement with the selling company data (Sigma Aldrich). In **Figure 2.12. a**, it is possible to observe a uniform distribution with smooth surface and using the zoom image, collected with a magnification of $500\times$, some roughs on the surface are visible. According to the **Figure 2.12 b**, the new catalyst **16** presented a size decrease, derived from the several processes of homogenizing and mixing. Particularly, the distribution remained uniform with sharp particles with various size, indeed the Feret diameter was in a range between 5 μm and 40 μm .

The solid-state UV-Vis spectrum of hybrid material **16** was also recorded to see if its characteristic bands were visible and to compare it with that of metalloporphyrin catalyst **8** (**Figure 2.13**).

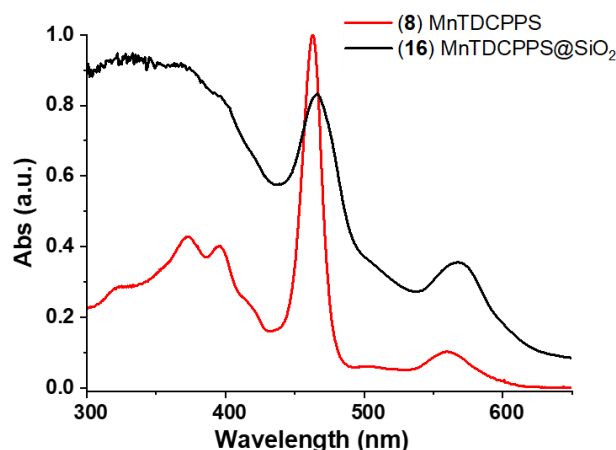


Figure 2.13 Normalized solid-state and solution UV-Vis spectra of **16** (black) and metalloporphyrin **8** (red). Spectrum of compound **8** was recorded in distilled water at 1×10^{-5} M.

As seen in **Figure 2.13**, the presence of porphyrin in the hybrid catalyst **16** was confirmed by the detection of Soret band at 466 nm and Q band at 568 nm, displaying a negligible bathochromic shift (~ 3 nm) when compared with the UV-Vis spectrum of **8**. Additionally, it is also possible to distinguish the Metal to Ligand charge transfer (MLCT) and Ligand to Metal charge transfer (LMCT) bands for **MnTDCPPS**.

Thermogravimetry was also used to quantify the organic part immobilized on the material **16** (**Figure 2.14**).

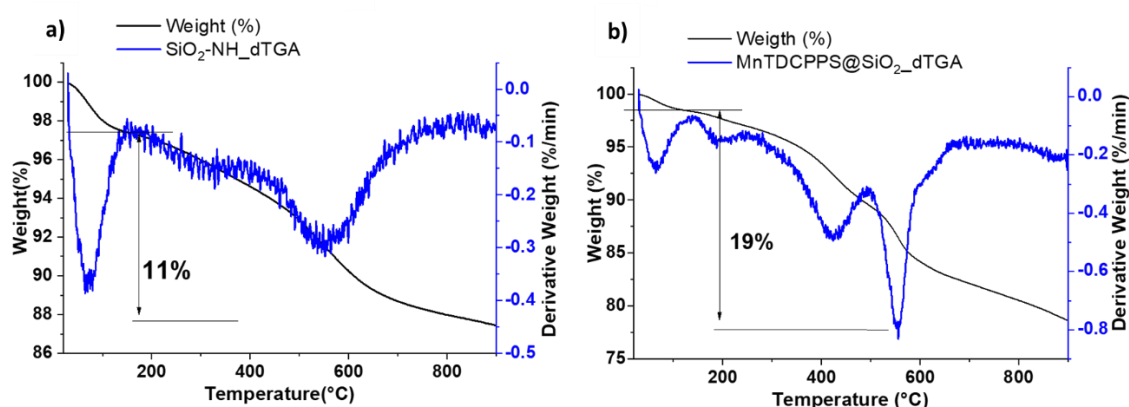


Figure 2.14 TG/DSC curves (derivate of weight – blue line, weight loss – black line): a) $\text{SiO}_2\text{-NH}_2$, b) **16**.

The thermogravimetric analysis was carried out in a range of temperatures between 25 °C and 900 °C, for both 3-aminopropyl functionalized silica and the new catalyst **16**. For the starting inorganic support, as **Figure 2.14 a** shows, a peak is observed between 25 °C and 100 °C relative to the adsorbed water. Another peak, corresponding to a weight loss of 11 %, is observed between 100 °C and 900 °C, with the most intense step between 500-900 °C, related to the decomposition of the aminopropylsilyl groups. The **Figure 2.14 b** is related to the hybrid **16**, and in this case a peak is recorded between 25 °C and 100 °C, always attributed to the weight loss of water molecules. Apparently the two thermograms showed a similar weight loss curve's profile, but the weight derivate curve presents two steps for the catalyst **16**. The first step appears between 200 °C and 450 °C and it was attributed to the loss of the organic porphyrin counterpart; whereas a second peak is observed in a range of 500 °C and 900 °C, related to the loss of aminopropylsilyl groups. Since the last weight loss mentioned was similar to that one recorded in the case of 3-aminopropyl functionalized silica, the metalloporphyrin content in the hybrid material **16** could be directly calculated through TG. In fact, comparing the two thermograms we could assume that the porphyrin mass loss was about 8 %.

Besides the TG analysis, the UV-Vis allowed to determine the amount of metalloporphyrin incorporated onto the silica-based support. To calculate the percentage of **16** linked to the 3-aminopropyl functionalized silica, an UV-Vis spectrum of the combination of all washing was recorded. This spectrum was compared with that one of the metalloporphyrin **8** using Beer's Law and it was observed that the immobilization yield was 37 % and the porphyrin loading is 3.7×10^{-4} mol of **MnTDCPPS** per gram of functionalized silica. Moreover, an additional experiment of inductively coupled plasma-optical emission spectrometry (ICP-OES) was carried out to quantify the metal content in the porphyrin involved in the covalently bond. In this case, the ICP-OES detected a Mn percentage of 3.6 % w/w.

Furthermore, to characterize the hybrid material **16**, infrared spectra were recorded for 3-aminopropyl functionalized silica, **8** and **16** and are presented in **Figure 2.15**.

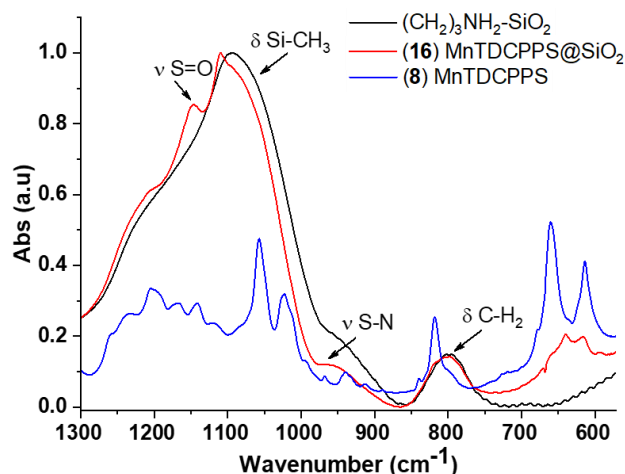


Figure 2.15 Infrared spectra of 3-aminopropyl functionalized silica (black line), MnTDCPPS@SiO₂, **16**, (red line) and MnTDCPPS, **8**, (blue line).

Comparing the IR-spectra, the peaks of 3-amino-propyl functionalized silica (black line) may be observed, particularly, a narrow band at 1090 cm⁻¹ ascribed to the bending of Si-CH₃ groups and a peak at 800 cm⁻¹ for the bending of CH₂ groups. Regarding, the MnTDCPPS@SiO₂, **16**, the bending of CH₂ groups, at 800 cm⁻¹, another peak was observed at 1146 cm⁻¹ ascribed to the stretching S=O. The proof of the covalent linkage between the nitrogen of the silica support and the sulfur of porphyrin was observed at 956 cm⁻¹ (stretching of S-N).

2.5 Heterogeneous catalytic oxidative degradation of TMP

These hybrid materials, **14** (MnTDCPPS@MNP) and **16** (MnTDCPPS@SiO₂), were then applied as heterogeneous catalysts in the antibiotic oxidative degradation using hydrogen peroxide as benign oxidant. So, in a typical experiment, the TMP (0.45 mM) and the heterogeneous catalyst, **14** or **16**, were placed in a round bottom flask and 100 mL of distilled water were added, in a ratio of 500:1 (TMP:Cat). The reaction mixture was stirred at room temperature (25 °C) for 15 min. After this time, similarly to the homogeneous catalytic system, the reaction started with the dropwise addition of 30 μL of H₂O₂ (30% w/v), and then subsequent aliquots of H₂O₂ were added each 15 minutes, to achieve a total volume of 300 μL. This total volume of oxidant corresponds to 2.6 mmol added, and the reaction proceeded for 150 minutes. The reaction was followed by HPLC

using the same chromatographic conditions reported for the homogeneous system (**Figure 2.16 a-c**).

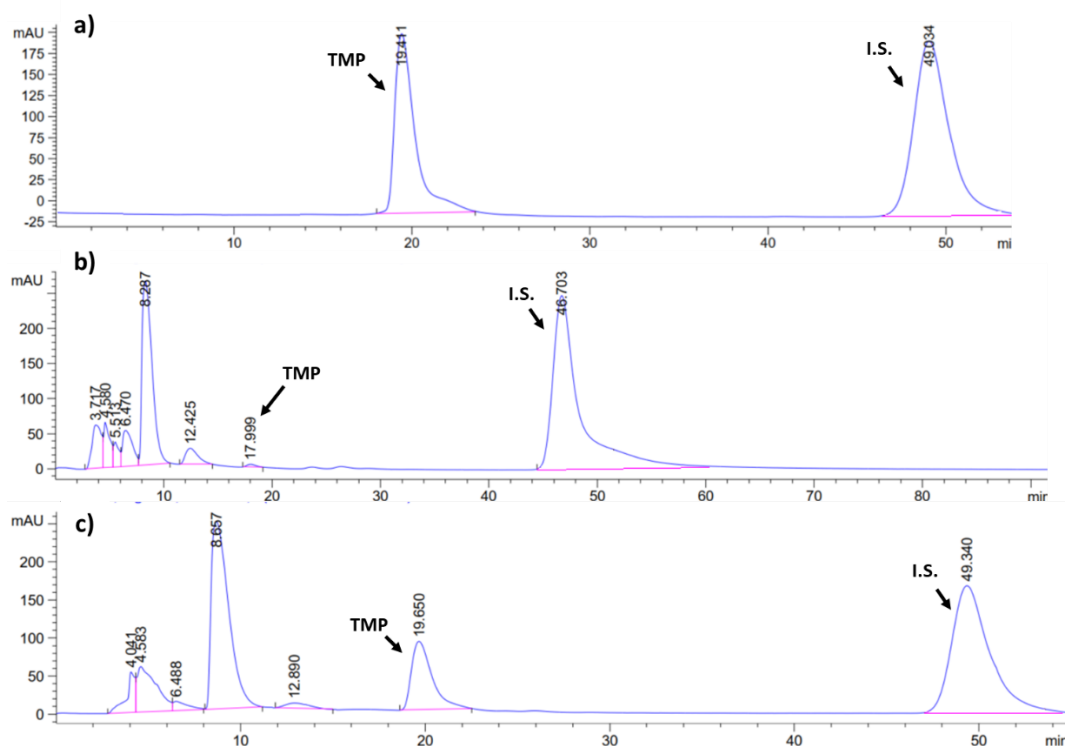


Figure 2.16 HPLC chromatograms recorded for TMP heterogeneous catalytic degradation: **a)** at time 0 h; **b)** after 150 min, adding 300 μL of H_2O_2 and using **16** as hybrid catalyst and **c)** after 150 min, adding 300 μL of H_2O_2 and using **14** as catalyst. The experimental elution conditions were: mobile phase of ACN:MeOH: NH_4OAc buffer (pH=9.0 adjusted with ammonium hydroxide) (15:15:70 v/v), flow rate of 0.400 mL min^{-1} , $T=25^\circ\text{C}$ and the I.S. was 3-methoxybenzaldehyde.

As shown in **Figure 2.16 a**, before starting the reaction, only the peaks of TMP and I.S. were detected by HPLC at 19.41 min and 49.03 min while, after adding 300 μL of H_2O_2 using **16** as catalyst, a negligible peak of TMP with a retention time of 17.99 min was registered, indicating a complete antibiotic degradation ($> 99\%$) (**Figure 2.16 b**). Furthermore, several new peaks have been detected, indicating the formation of degradation products (DPs) during the catalytic reaction. On the other hand, when using catalyst **14** and after 150 min of reaction time (**Figure 2.16 c**), the TMP peak at 19.65 min was still observed, besides the peaks of its DPs, showing only partial degradation of TMP ($\sim 40\%$). These findings demonstrate that, under the exact same

reaction conditions for the two catalytic systems, the reaction performed using **16** was faster in TMP oxidation.

Hence, the material **16** was chosen to pursue the studies and was evaluated under the catalytic conditions used for the homogeneous system. Thus, implementing a general experiment as previously described, the ratio between antibiotic and **16** was varied to establish the best operational ratio to achieve the full degradation of TMP. In Table 2.4, the results obtained by HPLC are reported.

Table 2.4 Heterogeneous reaction scheme and results obtained varying the TMP:Cat ratio in the oxidation of TMP using catalyst **16**.

Entry	TMP:Cat ^{a)}	Degradation ^{b)}	Required Time (min)
1	900	28	150
2	600	82	150
3	500	95	150
4	50	96	15 ^{c)}

^{a)} TMP:Cat = substrate to **16** molar ratio; ^{b)} reaction conditions: TMP (13 mg, 4.5×10^{-5} mol), $V_{\text{H}_2\text{O}_2(30\%)} = 30 \mu\text{L}$ for each 15 minutes until achieving a $V_{\text{H}_2\text{O}_2(30\%)} = 300 \mu\text{L}$; ^{c)} reaction was stopped after 15 min, because no more degradation was observed.

Similar to previous experiments, the reaction was followed by HPLC analysis. Every 15 minutes, before the addition of each 30 μL portions of H_2O_2 (30% w/v), an aliquot of reaction mixture was taken from the round bottom flask. It is worth mentioning that the sample was filtered using a 0.2 μm syringe filter before being injected into the HPLC equipment, to ensure that no catalyst particles could enter in the apparatus during the injection.

As mentioned in Table 2.4, the TMP:**16** ratios were calculated keeping the substrate's quantity constant, expressed in mol, and varying the quantity of catalyst used during each experiment, also expressed in mol. The first trial was conducted using the same TMP: **16** ratio tested for the homogeneous catalytic experiments. So, for the TMP: **16** ratio of 900:1 (Table 2.4, entry 1), after the same reaction time of 150 minutes,

the trimethoprim was degraded only in 28%. Hence, the TMP: **16** ratio was decreased, and we pursued the studies by using ratios of 600:1, 500:1, and 50:1, (Table 2.4, entries 2,3 and 4). When the 50:1 ratio was tested, the TMP degradation reached 96%, in only 15 minutes, at the cost of using a large amount of catalyst. Considering the other two ratios evaluated, the results indicate that the best performance was achieved when TMP:**16** ratio was 500:1, reaching a highly efficient degradation, in a reasonable reaction time.

All the data obtained from the HPLC analysis were plotted and used to study the reaction kinetics. (**Figure 2.17 a and b** and Table 2.5)

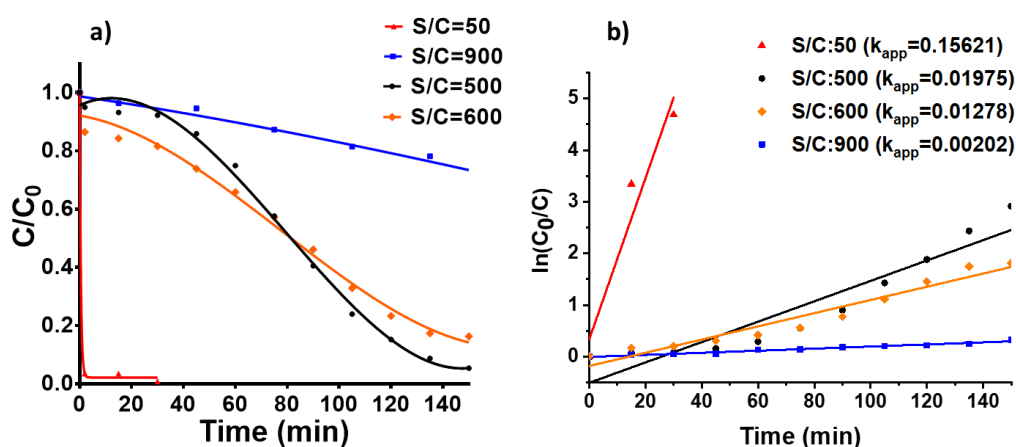


Figure 2.17 a) Heterogeneous catalytic degradation TMP curves using new catalyst **16**, under several TMP:Cat ratios; **b)** Kinetic curves of heterogeneous TMP degradation.

The k_{app} values were calculated, for each TMP:**16** ratio, considering HPLC chromatogram peak areas, and approximated to the L-H kinetic model [64, 65]. Plotting the data, straight lines were obtained for each ratio, where each k_{app} value is represented by the slope. Using catalyst **16**, k_{app} was dependent on the S/C ratio, as expected, showing a k_{app} of $1.6 \times 10^{-1} \text{ min}^{-1}$, $2.0 \times 10^{-3} \text{ min}^{-1}$, $1.28 \times 10^{-2} \text{ min}^{-1}$ and $2.0 \times 10^{-2} \text{ min}^{-1}$, respectively for S/C =50, 900, 600 and 500. From these results, it can be concluded that the ideal reaction conditions to perform the degradation of TMP, under heterogeneous conditions, were a TMP:**16** = 500:1 ratio, using $2.6 \times 10^{-3} \text{ mol}$ of H_2O_2 oxidant.

Table 2.5 k_{app} values calculated in the heterogeneous aqueous degradation of TMP, for each TMP:**16** ratio and using the hybrid material **16**.

Entry	TMP:Cat ^{a)}	k_{app} (min ⁻¹) ^{b)}
1	900	2.0×10^{-3}
2	600	1.3×10^{-2}
3	500	2.0×10^{-2}
4	50	1.6×10^{-1}

a) TMP:Cat = substrate to **16** molar ratio; b) apparent rate constant (k_{app}) calculated by the simplified equation $\ln \frac{[TMP]_0}{[TMP]_t} = k_{app} t$.

Furthermore, catalyst blank reaction was also carried out. An experiment was performed using the same reaction conditions, but in absence of catalyst. After the addition of 300 μ L of H₂O₂, a chromatogram of the final solution was registered and as depicted in **Figure 2.18**, the two chromatograms are very similar demonstrating no degradation ($\leq 1\%$ of TMP degraded after 150 min of reaction time), corroborating once again the importance of the catalyst for the substrate oxidation.

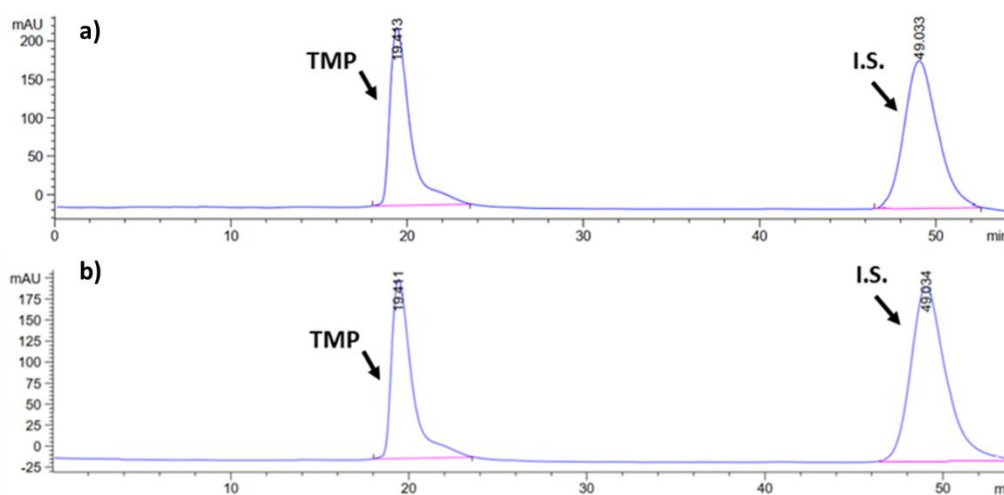


Figure 2.18 HPLC chromatograms recorded for TMP heterogeneous blank catalytic reaction, without catalyst **16**: **a)** at time 0 h; **b)** after adding 300 μ L of H₂O₂. The experimental elution conditions were: mobile phase of ACN:MeOH:NH₄OAc buffer

(pH=9.0 adjusted with ammonium hydroxide) (15:15:70 v/v), flow rate of $0.400 \text{ mL min}^{-1}$, $T=25 \text{ }^\circ\text{C}$ and the I.S. was 3-methoxybenzaldehyde.

Subsequently, upon optimization of the experimental heterogeneous conditions, the reutilization and recovery tests for the catalyst were performed. The catalyst was reused in 5 cycles and each catalytic cycle was set by preparing new fresh reaction mixture and using the recovered catalyst, under the same catalytic conditions (**Figure 2.19**). Recovery was fulfilled by separating the catalyst **16** from the medium by centrifugation and decantation, to isolate the material. Then, it was consecutively washed by centrifugation 2 times with distilled water, ethanol, and acetonitrile, respectively, for 40 minutes at 4000 rpm in each case. Finally, **16** was dried during 16 h in an oven at $60 \text{ }^\circ\text{C}$, before the next run.

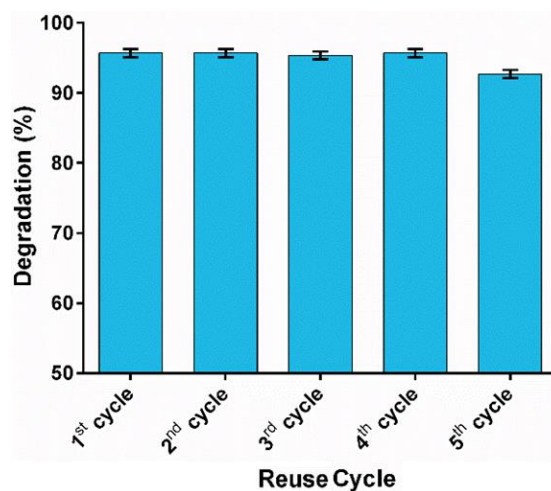


Figure 2.19 Heterogeneous degradation (%) of trimethoprim using catalyst **16**, after 5 cycles.

As **Figure 2.19** showed, the new material **16** was able to degrade the TMP for 5 catalytic cycles with negligible loss of activity. Moreover, after each run, the medium was checked by UV-Vis and ICP-OES ($< 2 \text{ ppb Mn}$) and no leached metalloporphyrin was found.

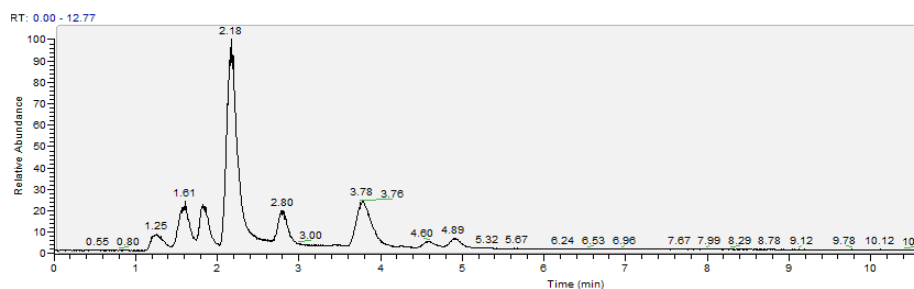
In addition, the amount of total TMP decomposition was also evaluated, by performing the Total Organic Carbon (TOC) analysis. Two experiments were simultaneously conducted where, at $t = 0 \text{ min}$, an average TOC of 334 mg C L^{-1} was observed, whereas, after 150 min, an average TOC of 253 mg C L^{-1} was measured for

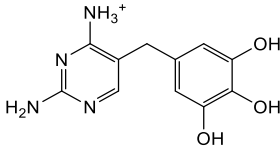
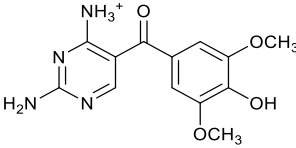
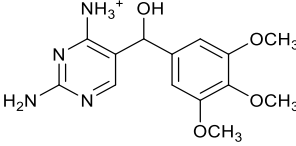
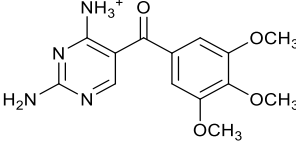
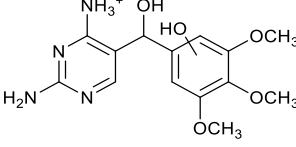
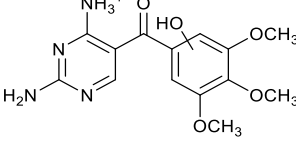
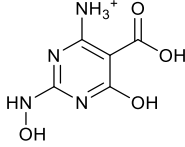
both experiments. This result demonstrated that a release of 81 mg C L^{-1} , which represents 24%, was obtained during this short reaction time.

2.6 Product analysis and possible degradation pathway

Besides the optimization studies on TMP degradation, another important part of this study was focused on the identification of degradation products, produced during the catalytic oxidation process. In literature, many articles reported the identification of TMP's degradation products deriving from various AOP catalytic processes [80-83].

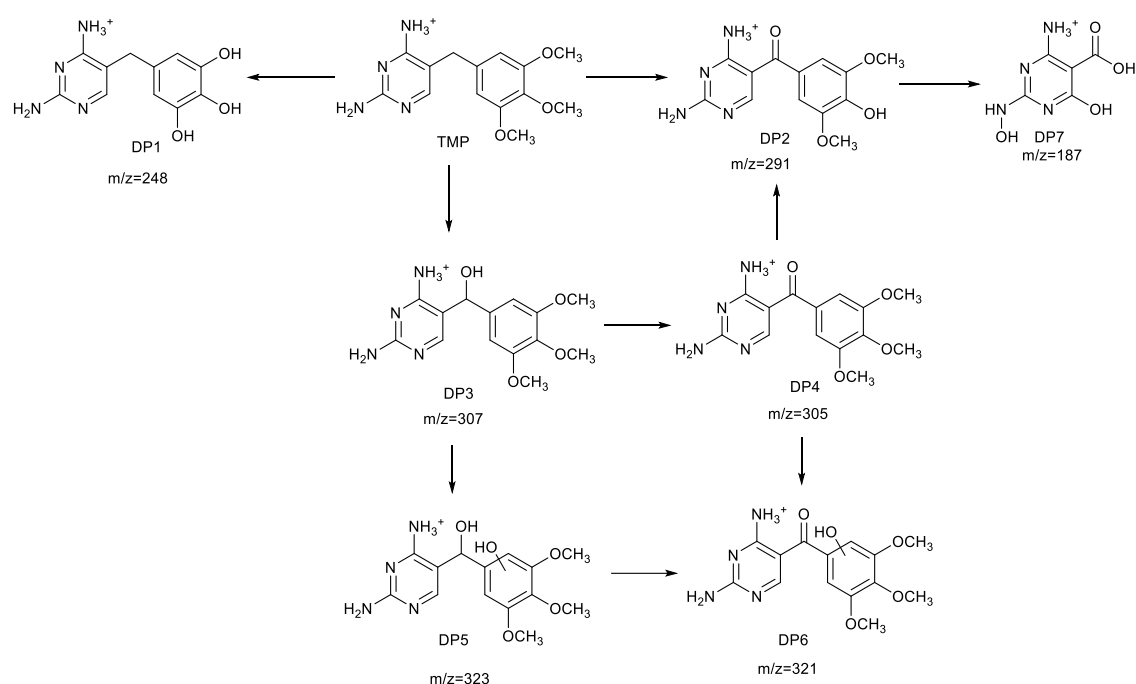
In our case, a Ultra Performance Liquid Chromatography – tandem Mass Spectrometer (UPLC-MS) technique was used to identify the degradation products. The mobile phase was composed by a mixture of acetonitrile, methanol, and a buffer solution of ammonium acetate, in a proportion of 15:15:70, adjusted to a pH of 9.5 using a solution of ammonium hydroxide, since basic pH is fundamental to avoid the protonation of amine groups in the TMP structure. In addition, the mobile phase mixture was degassed by ultrasounds for 30 minutes to avoid that the excess of air produced during the mixing could bubble out, in order to prevent the creation of dead volumes and spurious peaks on the chromatograms. For our study, the column used was a C18 reverse phase, since aqueous samples were used. Moreover, after the catalytic degradation, the reaction mixture was filtered through a $0.2 \mu\text{m}$ syringe filter, to ensure that no solid particles could be injected with the sample into the equipment. Upon filtration, a small volume of sample, $60 \mu\text{L}$, was placed into the HPLC flask to be automatically injected into the equipment with a flow rate of 0.15 mL/min . To determine the relative abundance of each degradation product, an internal standard, the 3-methoxybenzaldehyde, was introduced in each sample before the injection. At the end, we obtained a total ion chromatogram (TIC) in which for each peak there is a characteristic mass spectrum associated, which is fundamental to identify the degradation products (Table 2.6).

Table 2.6 Total ion current chromatogram (TIC) of TMP catalytic degradation and identified DPs.

Degradation Products	Identified DPs	m/z (Da)	t _r ^{a)} (min)	Relative %
DP1		249	1.25	17
DP2		291	3.78	3
DP3		307	2.18	47
DP4		305	4.60	< 1%
DP5		323	1.81	13
DP6		321	2.80	8
DP7		187	1.61	11

^{a)} t_r = retention time (min).

Particularly as showed in Table 2.6, a qualitative analysis was made, by calculating the relative abundance percentage of each single generated degradation product, using the area of each product related to the total area. Moreover, it was observed that, during the catalytic process, many degradation products were generated in negligible quantities, such as DP2 and DP4. Only DP3 was detected in a higher quantity, with respect to the others (relative abundance of 47%) and it was produced from the hydroxylation of TMP. Analyzing the mass fragments, reported in Table 2.6 above, we proposed a possible TMP degradation pathway, in order to explain the formation of these degradation products (Scheme 2.10).



Scheme 2.10 Possible TMP degradation pathways, using heterogeneous catalyst **16** and hydrogen peroxide as oxidant agent.

The analysis of the catalytic degradation products led us to propose the mechanism presented in Scheme 2.10. Along this process, hydroxylation, oxidation and demethylation occurred [83-85]. Particularly, DP1 derived from the full demethylation of TMP; whereas the DP2 was generated for its partial demethylation. Simultaneously, the process could undergo hydroxylation on the benzylic position of TMP, which produces the product DP3. When the alcoholic intermediate was formed, it could react in two different ways. Then, it could further undergo hydroxylation on one of two *ortho*-free positions of 3-methoxybenzyl ring giving the di-alcoholic specie DP2, and, in the other

hand, it could generate the ketonic species, DP4, by oxidation of the alcohols. At this point, the intermediate DP4 could produce different species for further hydroxylation or demethylation. The DP4 can be hydroxylated on the *ortho*-free positions of 3-methoxybenzyl ring, providing the DP6. Moreover, the DP5 could give the intermediate DP6 through the oxidation of the alcohol into a ketone (tertiary carbon/ secondary alcohol). Otherwise, it may suffer a demethylation on one of the three methoxy groups, generating the specie DP2. Finally, the DP2 could also suffer cleavage to yield the DP7.

2.7 Ecotoxicity studies

In literature, some articles described the ecotoxicity of TMP in different organisms [86, 87] but only a very few reported the ecotoxicity of its degradation products [84, 88, 89]. Taking this into account, ecotoxicity studies on the initial antibiotic and its degradation products were performed on three different organisms, attempting to study the potential environmental damage caused by the presence of TMP and its degradation products.

Specifically, the three selected species were the bacterium *Vibrio fischeri*, the microalgae *Raphidocelis subcapitata* and the rotifer *Brachionus calyciflorus*, and two toxicity tests were conducted for each one. Although some data about the intrinsic toxicity of TMP was already reported in literature [6, 90-93], this antibiotic was first tested to determine the toxicity of the solution before the degradation process and also to complement the database already existing about its toxicity for aquatic organisms. The second test was performed on the solution containing the oxidized products derived from the catalytic degradation process.

Firstly, a 494.4 mg L⁻¹ solution of TMP was prepared in a standard artificial moderately hard freshwater to perform the first tests, which presents a pH of 7.25 and a conductivity of 325 μS cm⁻¹ [94]. This was necessary because using distilled water would kill the organisms due to the osmotic stress. Furthermore, according to the previous literature reports [29, 91, 95, 96], the highest tested TMP concentrations were 225 mg L⁻¹ for the bacterium and the rotifer and 285 mg L⁻¹ for the microalgae. Then, starting from these concentrations, a serial dilution was performed for each test; six concentrations were prepared using the control medium with a dilution factor of 2 in case of the bacterium and of 1.75 for the microalga and rotifer. Concerning the assays

conducted using the degradation products solution, the highest used concentration was the 100% collected solution after the degradation and recovery of heterogeneous catalyst.

The first tested organism was *V. fischeri*, which is a marine Gram-negative bacterium, commonly used for the bioluminescence inhibition assay. Its solution was obtained by suspending the preserved lyophilized bacteria into a suspension, at known concentration, using a purchased reconstitution solution and the test protocol (Azur Environmental, Carlsbad, CA, USA). According to the Microtox 81.9 % basic test protocol for water samples (Azur Environmental, Carlsbad, CA, USA), the 5 min *V. fischeri* luminescence inhibition test was performed using the toxicity analyzer model 500 (Strategic Diagnosis, Newark, DE, USA), to measure the light emission of the bacteria suspension. Since the light production is directly proportional to the metabolic activity of bacteria, an inhibition of enzymatic activity corresponds to a decrease in bioluminescence. Since tests with TMP solution showed similar results after 5, 15 and 30 min of exposure, only a 5 min exposure test was selected.

The second test was performed with green freshwater microalga *R. subcapitata*, used as model aquatic organism. The microalga was conserved with a Woods Hole MBL growth medium in 100 mL of nonaxenic batch cultures, under cool-white fluorescent illumination ($100 \mu\text{E m}^{-2} \text{s}^{-1}$) with a controlled temperature (19-21 °C). The 72 h growth inhibition test was carried out following the OECD (2011) and EC (1992) guidelines [97, 98]. In this case, the algal growth was estimated in two ways: as total cell density, EbC (cells mL^{-1}) and as specific growth rate, ErC (1 d^{-1}) [99]. This choice was made because although the first measurement is 3 to 7 times more sensitive than the other, normally the second parameter is the most used in ecological risk assessment at regulatory level. The 900 μL replicate cultures were prepared and inoculated with 100 μL of algal inoculum. Moreover, the 285 mg L^{-1} TMP solution and degradation product one was supplemented with the same amounts of nutrients as the control to discriminate potential toxicity of the examined samples respect to that due to differences in nutrient levels. After 72 h of exposure, final cell densities were counted and mean specific growth rates per day calculated [99].

The third organism was *B. calyciflorus* a planktonic rotifer species arising in freshwater. The organisms were hatched from cysts, exposed to six 0.3 mL test solutions and incubated in darkness with a controlled temperature of 24-26 °C for 48 h. After this

time, the lethality was estimated counting which are alive or dead, due to the Rotoxkit F standard operational procedure [100].

The ecotoxicity results, representing the toxicity of TMP solution in a standard medium against the three organisms, expressed as EC₅₀ and EC₂₀ are reported in Table 2.7. The predicted percentage of toxicity caused by the 494.4 mg L⁻¹ TMP solution in distilled water was calculated by the software PriProbit 1.63 [101], using the regression model made between the probit transformation of the proportion of responses and the log transformation of the concentrations. The degradation products solution, after the addition of sodium bisulfite hydrogen peroxide quencher, was also checked.

Table 2.7 EC₅₀ and EC₂₀ values of TMP solution for the three tested organisms with corresponding 95% confidence limits, predicted percentages (%) of toxicity caused by the saturated TMP solution (494 mg L⁻¹) and the degradation products solution.

Toxicity test	EC₅₀ (mg L⁻¹)	EC₂₀ (mg L⁻¹)	TMP sol^a (% effect)	products sol^b (% effect)
<i>V. fischeri</i>	221.7 (185.7 – 293.3)	118.7 (102.2 – 136.4)	85.9	97.0
<i>R. subcapitata</i>	33.4 (25.3 – 41.4)	16.3 (9.5 – 23.1)	99.4	98.9
EbCx	81.9 (75.1 – 88.6)	49.7 (42.8 – 56.7)	99.3	99.9
ErCx				
<i>B. calyciflorus</i>	301.3 (184.9 – 850.2)	82.14 (54.9 – 121.4)	62.7	100.0

^{a)} predicted values for [TMP]= 494 mg L⁻¹; ^{b)} products solution concentration = 100%.

Concerning the toxicity of TMP solution in standard medium, the 5 min *V. fischeri* test showed a value of EC₅₀ and EC₂₀ of 221.7 mg L⁻¹ and 118.7 mg L⁻¹, respectively. The 72 h *R. subcapitata* growth tests revealed a specific growth rate of 81.9 mg L⁻¹ and 49.7 mg L⁻¹ for ErC₅₀ and ErC₂₀, respectively and, in terms of the increase in cell density values of 33.4 mg L⁻¹ and 16.3 mg L⁻¹ for the EbC₅₀ and EbC₂₀. Lastly, the *B. calyciflorus* showed a EC₅₀ of 301.3 mg L⁻¹ and an EC₂₀ of 82.1 mg L⁻¹. The obtained results showed that the microalga was the most sensitive species with ratios of EC₅₀ respect to the other two species close to one order of magnitude (6.6 and 9.9, to *V. fischeri* and *B. calyciflorus*) and ratios of EC₂₀ of 1.7 and 2.4, respectively without 95% CL overlapping. The other

two species revealed the same sensitivity to TMP since both EC₅₀ and EC₂₀ values did not differ more than 1.4 times.

Comparing with literature, these results are quite similar and are in agreement with the Category Acute 3 attributed to TMP [102], based on short-term data according to the Globally Harmonized System of the Classification and Labelling of Chemicals, where *V. fischeri* showed TMP values of EC₅₀ between 165 and 177 mg L⁻¹ [95]. Also, TMP EC₅₀ values reported for *R. subcapitata* are between 80 and 129 mg L⁻¹ [29, 36, 96, 103]. To the best of our knowledge, no data is yet reported in literature for the rotifer, but the sensitivity revealed in this study was similar to other invertebrates, such as the cladoceran *Daphnia magna* (from 100 to 167 mg L⁻¹ [95, 103, 104]). The extrapolated value of toxicity for the 494.4 mg L⁻¹ TMP solution was higher for the microalga (99%) and lower for the rotifer (62%). Comparing the degradation products solution with the initial TMP one, the ecotoxicity was similar for the microalga and increased for the bacterium (13%) and for the rotifer (37%).

Therefore, the obtained results revealed an intrinsic toxicity of the degradation products, but a toxic effect related to the degradation conditions used in the laboratory cannot be excluded, particularly the use of hydrogen peroxide and bisulfite as quencher. To try to discriminate between these toxicities, other tests were carried out on the *R. subcapitata*. Hence, four solutions were also tested: one containing the degradation products, H₂O₂ and equimolar quencher (0.265 M); a second solution containing degradation products and only H₂O₂ (0.265 M); the third solution, prepared in fresh water, containing only H₂O₂, at estimated concentration after degradation (0.132 M) and a fourth one, also prepared in fresh water, containing only bisulfite (0.265 M). The obtained EC₅₀ values and the measured physico-chemical parameters are reported in Table 2.8.

Table 2.8 Ecotoxicity results, in terms of percentage of growth inhibition relatively to the standard control (Er%) and physico-chemical results of measured parameters.

Solution	Er(%)*	pH	Conductivity (μS/cm)	Salinity
1	99.3%	1.51	31400	22.2
2	94.1%	6.40	39.9	0.0
3	86.5%	7.65	498	0.0
4	96.5%	4.30	24100	17.4

* Er for growth as specific growth rate

The presence of sodium bisulfite, normally used as a peroxide quencher in the laboratory, created high conductivity and salinity in the tested solutions, a decrease in the pH value and clearly inhibiting the microorganism growth. Furthermore, the solution containing only H₂O₂ showed a strong inhibition (86.5%) of the microalga growth in 72 h. This result is understandable considering that H₂O₂ has antimicrobial properties and is toxic to a wide range of microorganisms [105]. Taking these results into account, the observed toxicity of the DPs aqueous solution can be at least partly explained, considering the intrinsic toxicity of bisulfite and peroxide. Certainly, this does not exclude any possible toxicity associated with the DPs themselves.

2.8 Photocatalytic homogeneous degradation of TMP

To pursue our main goal to develop sustainable catalytic process for the degradation of antibiotics in water, in this section we describe the photodegradation of TMP and SMX. So, we selected a suitable porphyrin to be used as photosensitizer under homogeneous and heterogeneous conditions. Herein, we describe the immobilization, by encapsulation, into acetylated lignin nanoparticles, used as organic support of natural origin. All reactions were performed in a photoreactor, which is schematized in **Figure 2.20**.

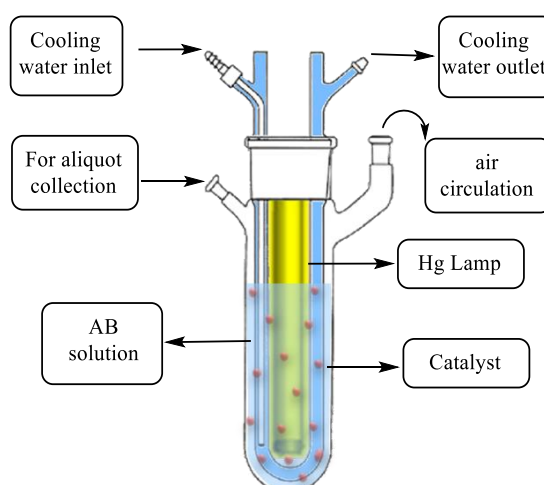


Figure 2.20 Schematic representation of the photoreactor vessel used in this work.

The reactor is constituted by two vessels and the Hg lamp is located in the double-walled immersion quartz vessel. This is formed by inlet and outlet tubes that provide

water cooling with a polytetrafluoroethylene tube, which allows the water to flow upwards from the bottom. The second 300 mL cylindrical flask, containing the quartz vessel, is made of borosilicate glass with a flattened bottom to insert a magnet stirrer bar and is constituted by two small sockets, one for the sampling and the other one for air circulation (**Figure 2.20**).

The device was equipped with a 400 W medium pressure Hg lamp with an irradiance spectrum covering the visible and ultraviolet region, predominantly producing 365-366 nm radiation and significant amount of radiation at 405-408, 436, 546 and 577-579 nm and 365-366 nm. Also, smaller amounts of irradiation were generated at 254, 265, 270, 289, 297, 302, 313 and 334 nm (**Figure 2.21**).

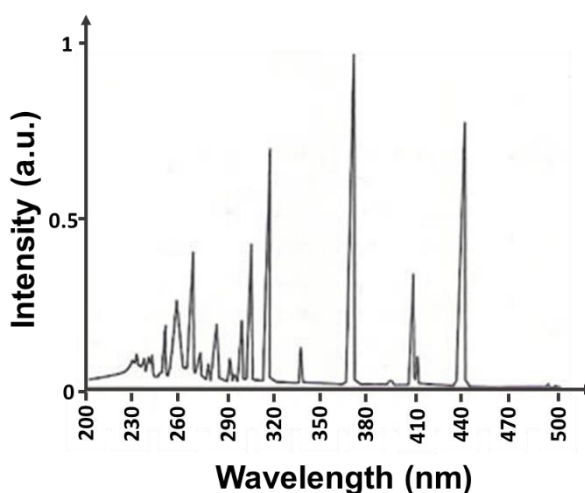
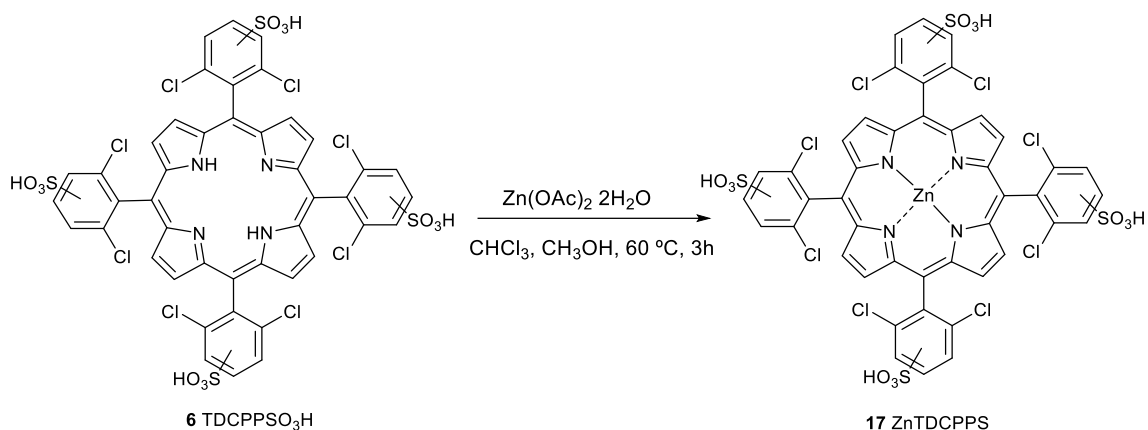


Figure 2.21 Emission spectrum of medium pressure Hg lamp (Adapted from [106]).

Aiming the development of an efficient and reusable heterogeneous photocatalyst system, the studies started with the evaluation of photocatalysts **TDCPPS, 6**, and **ZnTDCPPS, 17**, under homogeneous conditions.

So, the porphyrin **6** was complexated using zinc acetate salt (Scheme 2.11).



Scheme 2.11 Synthesis of Zn(II) metalloporphyrin **17**.

The sulfonated porphyrin **6** was dissolved in chloroform in a round bottom flask and an excess of zinc(II) acetate di-hydrate, dissolved in methanol, was added. The mixture was heated to 60 °C for 2 hours, monitoring by TLC and UV-Vis. The desired compound **17** was isolated after solvent evaporation and extraction with CHCl₃/H₂O to remove the salt excess. The metalation was checked by UV-Vis, where the typical disappearance of two Q bands was followed, since the Soret' shift was not significant (420 nm) (**Figure 2.22**).

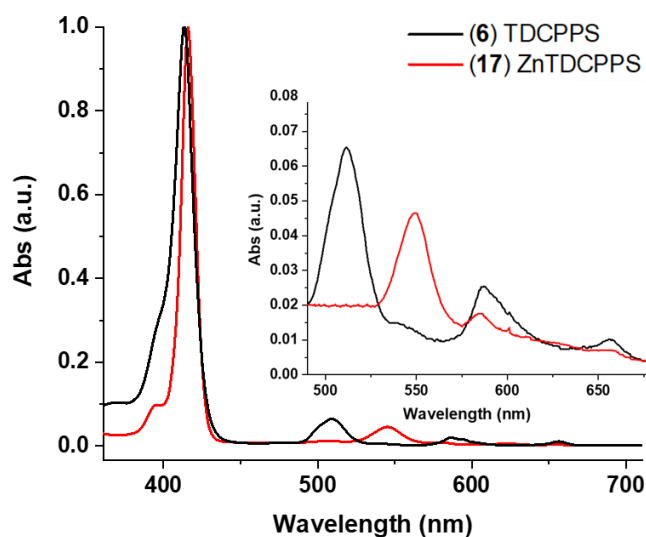


Figure 2.22 UV-Vis spectra of **6** (black line) and **17** (red line) recorded in water.

The photodegradation studies started by performing the homogenous photodegradation tests. So, in a typical photocatalytic experiment, the photocatalyst (**6** or **17**) and 0.1 mM TMP stock solutions (1.0×10^{-5} mol) were added into the

photoreactor vessel in a molar ratio of 500:1 (TMP:Cat). The solution was stirred for 30 min, in the dark and then irradiated for 24 h, under stirring. The reaction evolution was followed by HPLC using the same method mentioned before. The mobile phase was composed by a mixture of ammonium acetate (70% v/v), acetonitrile (15% v/v) and methanol (15% v/v) and adjusted to pH 9.2 with a stock solution of ammonium hydroxide. The elution was in isocratic mode, with a flow rate of 0.4 mL min^{-1} and the temperature of the oven was set at $30 \text{ }^\circ\text{C}$ to allow the reproducibility of retention times. The chromatograms of the two TMP photodegradation reactions, are reported in **Figure 2.23 b and c**.

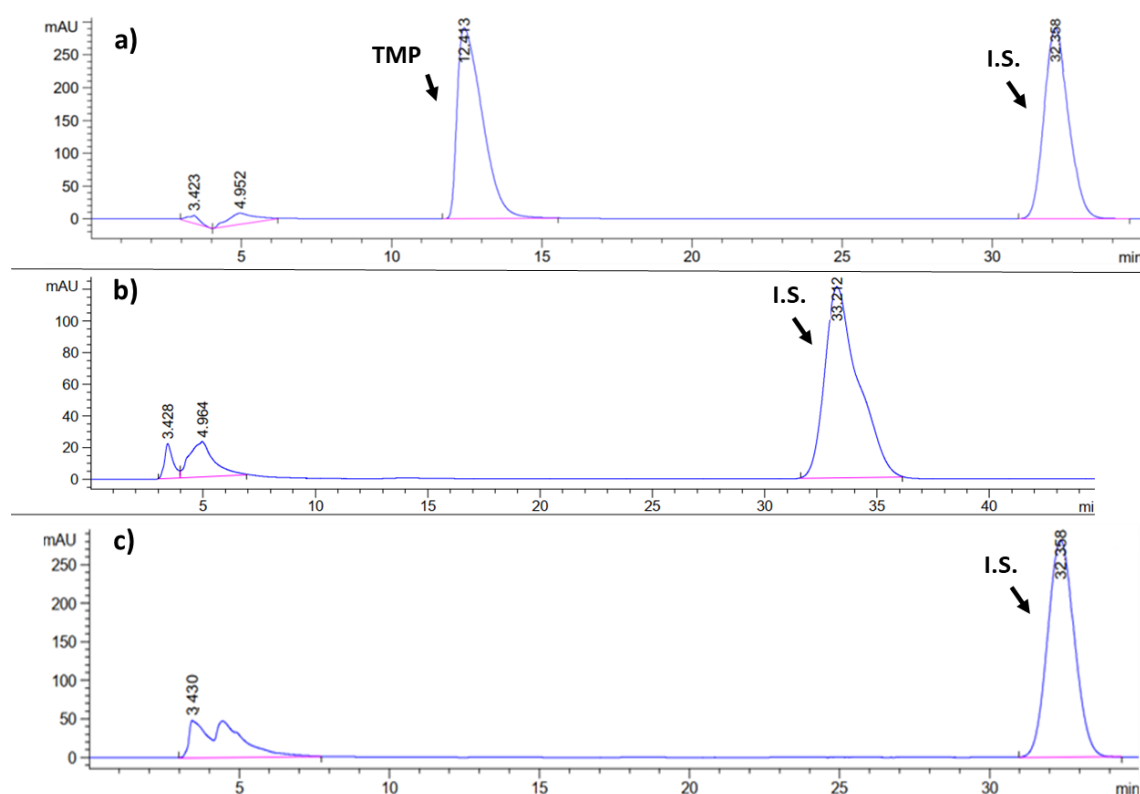


Figure 2.23 HPLC chromatogram of TMP photodegradation recorded: **a)** at time zero, **b)** after 24 h of irradiation, using **17** as catalyst and **c)** **6** as catalyst.

It can be seen that, in both cases, TMP was completely degraded after 24 h of irradiation. This would indicate that any of the photocatalysts could efficiently promote antibiotic degradation. Moreover, it should be mentioned that during the photoreaction a pH decrease was observed, and acidic pH is deleterious for the porphyrin Zn(II) complex, which is known for its lability inside porphyrin core under acidic pH. It is well reported that in acidic media, the nitrogen-core atoms may be protonated, producing a distortion

in the macrocycle planar geometry toward a saddled structure [107, 108]. For this reason, and also to avoid additional steps such as the metalation and its workup/purification, it was decided to proceed the studies using photocatalyst **TDCPPS, 6**, as photosensitizer.

The photocatalytic studies pursued with a new set of experiments where the ratio between the TMP and catalyst was varied, to determine the best catalyst to substrate proportion. So, two stock solutions were prepared: an aqueous 10^{-4} M TMP stock solution and an aqueous 1.6×10^{-5} M catalyst stock solution. In a typical experiment, porphyrin **6** and 0.1 mM TMP stock solutions (1.0×10^{-5} mol) were added into the photoreactor vessel, under the selected molar ratios and stirred in the dark, at room temperature, for 30 min. Then, the mixture was irradiated using the Hg lamp along 24 h, under stirring. The reaction was followed by HPLC, by taking aliquots each 30 min, maintaining the same operational conditions as before, and the results are reported in Table 2.9.

Table 2.9 TMP homogeneous aqueous photodegradation using **6** as photocatalyst.

Entry	TMP: 6	Photodegradation Time (h)	Photodegradation ^{a)} (%)	k_{app} (min^{-1})
1	50	2	>99.9	2.1×10^{-1}
2	500	4	>99.9	9.7×10^{-2}
3	1000	12	>99.9	4.3×10^{-2}

^{a)} reaction conditions: TMP (2.9 mg, 1.0×10^{-5} mol); **6** (0.024 mg, 2.0×10^{-8} mol); $V_{\text{total (mixture)}} = 100$ mL.

From HPLC analysis, we observed that, with ratios of 50:1 and 500:1, the full degradation of TMP was achieved in 2 h and 4 h, respectively, (**Table 2.9**, entries 1 and 2). Then, we evaluated the ratio of 1000:1 and the time required to complete the photodegradation was 12 h (**Table 2.9**, entry 3). Furthermore, reaction kinetics for homogeneous photocatalytic TMP degradation was also carried out, for the first 20 min, with the corresponding k_{app} calculated as previously reported for the oxidative catalysis with H_2O_2 (**Figure 2.24 a** and **b**, respectively).

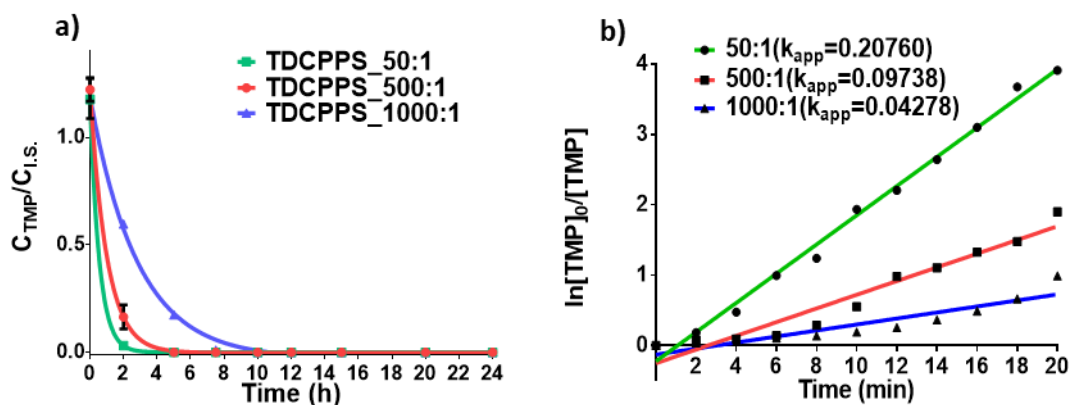


Figure 2.24 a) TMP photocatalytic oxidation curves in homogeneous conditions and with three TMP:6 ratios; b) TMP photodegradation kinetic curves, calculated for the first 20 min.

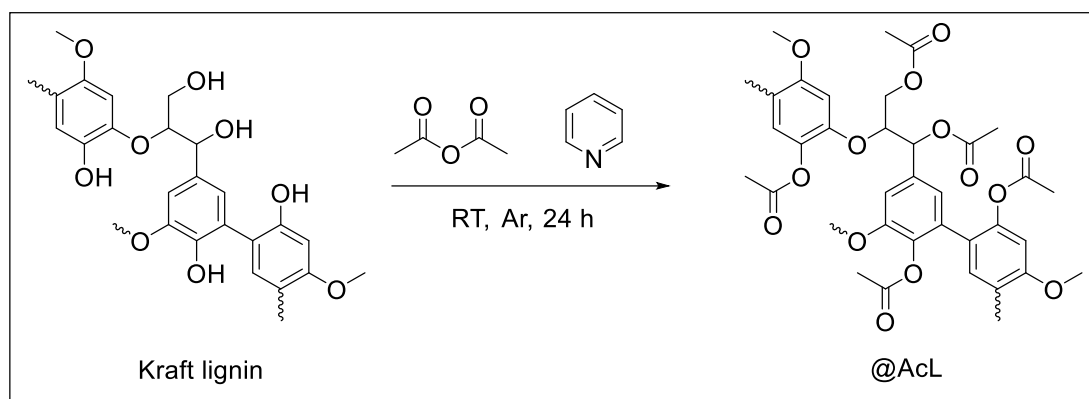
When the reaction was led with a molar ratio of 50:1 and 500:1 (**Figure 2.24 b** green and red line, respectively) the k_{app} values were $2.1 \times 10^{-1} \text{ min}^{-1}$ and $9.7 \times 10^{-2} \text{ min}^{-1}$ (Table 2.9, entries 1 and 2) respectively, confirming that in the second case the reaction was 2 times slower than the first one. On the other hand, the k_{app} was $4.3 \times 10^{-2} \text{ min}^{-1}$ (Table 2.9, entry 3) for the 1000:1 ratio (**Figure 2.24 b** blue line), which means that the reaction was 5 times slower than using the first ratio. According to these results, it is evident that the increase in the TMP:6 ratio leads to a slowdown in the reaction. Therefore, the 500:1 ratio was chosen as the most convenient to transpose into the heterogeneous photocatalytic degradation of TMP.

2.9 Development of porphyrin-based lignin heterogeneous photocatalyst

The goal was to develop a hybrid photocatalyst based on a natural compound used as biomaterial matrix to encapsulate the porphyrin photosensitizer. For this purpose, several natural polymers have been already reported in literature, such as cellulose and lignin [109-113]. Lignin is of great interest since it is a common by-product of paper and bioethanol industries and was recently applied in photocatalysis [114, 115]. Considering our collaboration with University of Limoges and their previous studies involving the use of lignin as an organic material to encapsulate photosensitizers for photodynamic therapy [116], we extended the scope of lignin's use and developed a new photocatalyst based on

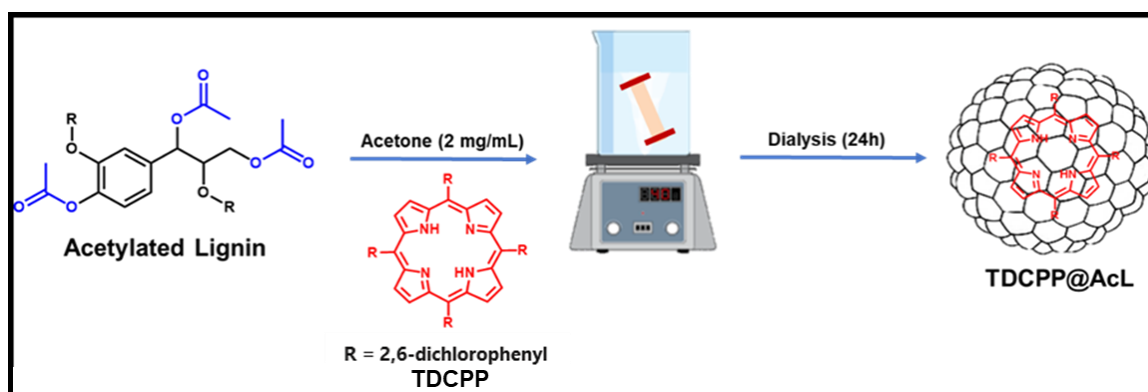
this renewable material aiming the development of a sustainable process to degrade antibiotics in aqueous matrices.

The studies started by appropriately modulating the lignin biomaterial. Hence, Kraft lignin was acetylated following Marchand method [117] using a mixture of acetic anhydride/ pyridine (1:1, v/v) for 24 h at room temperature (Scheme 2.12). Then, ethanol was added to the mixture and evaporated several times to steam distill the excess of acetic acid/anhydride present. Afterwards, chloroform and diethyl ether were added dropwise to this mixture, to induce the precipitation of the desired acetylated lignin, @AcL. This product was isolated by centrifugation, followed by several washings and drying in the oven.



Scheme 2.12 Synthesis of acetylated lignin (@AcL).

The porphyrins' encapsulation into the AcL nanoparticles was carried out following previous studies (Scheme 2.13) [109, 116, 118].



Scheme 2.13 Schematic representation of TDCPP@AcL nanoparticles formation.

Firstly, the **TDCPP (2)** was dissolved in acetone (a water-miscible solvent) and then the AcL, previously dissolved in the same solvent, was added (in a ratio of 1:10 w/w). After complete dissolution, the solution was introduced into a previously hydrated permeable cellulose membrane bag, to dialyze along 24 h, at room temperature and under slow stirring. The exchange of acetone and water through the membrane caused an increase in the medium's polarity, with consequent molecular reorganization and formation of spherical hydrophobic nanoparticles, around the porphyrins. Then, the desired nanoparticles **18** were collected after centrifugation ($10000 \times g$) and washing cycles and finally they were re-suspended in water and stored before catalytic evaluation. The dialysis process was easily followed by observing the decrease of dark purple **TDCPP** color inside the bag for the 24 h, as showed in **Figure 2.25**.

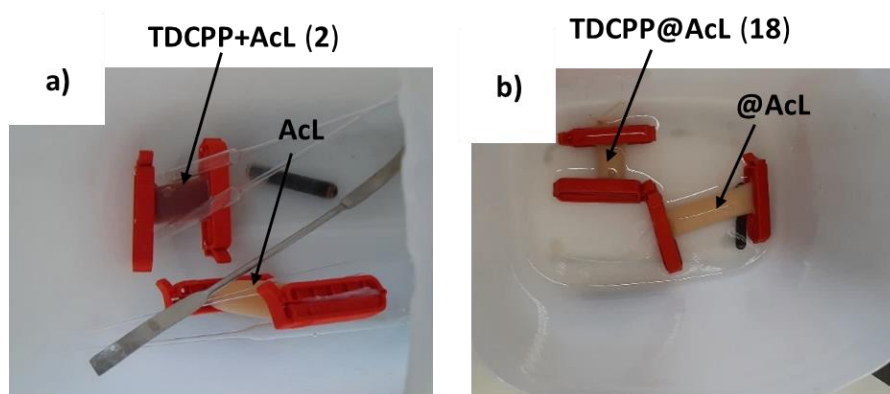


Figure 2.25 Dialysis process: **a)** before to start in which the purple solution was porphyrin **2** in acetone and the light brown solution was the **@AcL**; **b)** at the end in which the two solutions were light brown.

The observed color change occurs due to the porphyrin encapsulation inside the lignin nanoparticles. With the increase content of the water inside the membrane, the non-polar AcL forms spherical nanostructures in order to reduce the water accessible area [119]. This color changing may be explained by the medium polarity variation. The porphyrin has a non-polar nature, due to the presence of aromatic rings in its structure. Therefore, during the dialysis, as there is an exchange between organic solvent and water entering the bag, hydrophobic porphyrins form hydrophobic interactions with acetylated lignin, favoring the encapsulation. Simultaneously, the AcL is also non-polar: so, by increasing the amount of water, “crumpled globules” are formed, reducing the water

accessible surface areas, hence minimizing hydrophobic interactions, until the formation of nanometric size particles, when finally, the solvent inside the bag is mainly water.

The quantification of porphyrin inside the nanoparticles in **18** was performed by UV-Vis spectroscopy using acetone as solvent and using **2** as reference for the absorption coefficient (**Figure 2.26**).

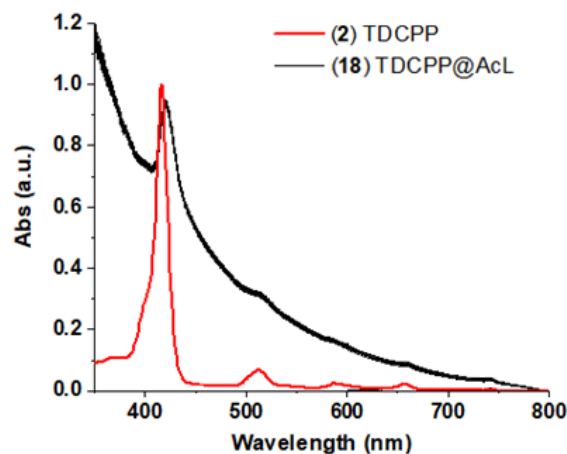


Figure 2.26 UV-Vis spectra of compound **2** (red line) and **18** (black line) in acetone.

As reported in **Figure 2.26**, the UV-vis spectrum of **TDCPP**, recorded in acetone (red line) shows the Soret band at 414 nm, whereas the **TDCPP@AcL** spectrum, recorded in acetone (black line) displayed a peak at 422 nm, which is ascribed to the porphyrin Soret band. This Soret band red-shift has been previously observed also in other porphyrins encapsulated into acetylated lignin nanoparticles, such as THPP and ZnTHPP [120, 121], resulting from the porphyrin load inside nanoparticles.

The porphyrin concentration into nanoparticles was calculated according to Eq. 2.2,

$$Concentration = \left(\frac{Abs_{Soret}}{\epsilon} \right) \times l \quad (2.2)$$

in which l , the optical path length, is 1 cm and the absorbance of each nanoparticle's solution is compared with the absorptivity coefficient (ϵ) of each porphyrins used, **2**. The absorptivity coefficients for **2** at the Soret band of 414 nm, was 366904 L mol⁻¹ cm⁻¹, in acetone. The calculated concentration of porphyrin in the suspension of nanoparticles corresponded to 504.5 μ M of **2**.

The morphology of **18** was also evaluated through TEM analysis (**Figure 2.27**).

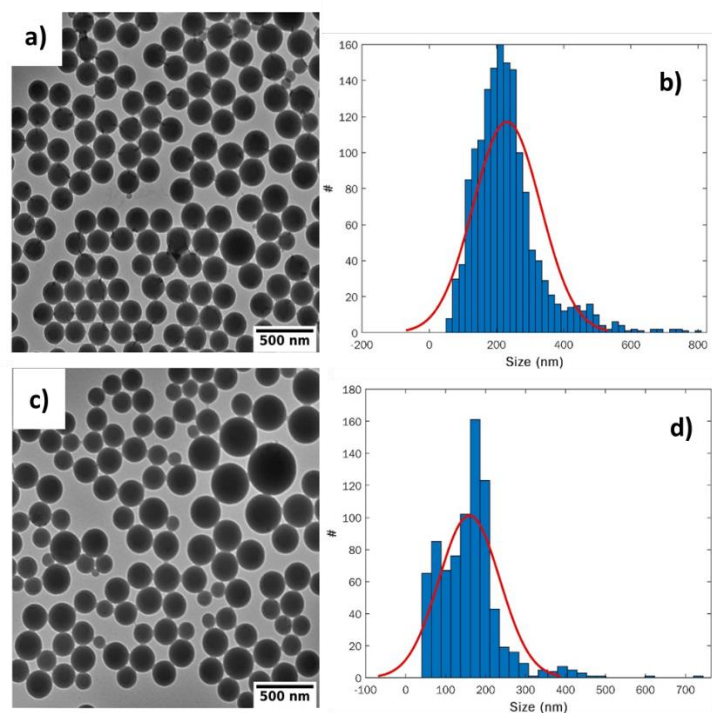


Figure 2.27 TEM images of **a)** **18** and **c)** **@AcL** nanoparticles and their size distribution **b)** and **d)**, respectively.

Particularly, the morphology of our photocatalyst (**Figure 2.27 a)** was compared to that one of the **@AcL** nanoparticles alone (**Figure 2.27 c)** and in both cases, nanoparticles showed homogeneous spherical shapes. Moreover, elaborating the experimental data *via* Gaussian fitting, they exhibited a wide size distribution, **@AcL** had a mean size of 156 nm (95% confidence bounds 154 to 165nm) (**Figure 2.27 d)** and **18** revealed a mean size of 231 nm (95% confidence bounds 226 to 236 nm) (**Figure 2.27 b)**.

2.10 Antibiotics photodegradation by Por@AcL photocatalyst

The work proceeded with the study on the photodegradation of antibiotics using the prepared Por@AcL photocatalyst, upon irradiation with a Hg medium pressure lamp, in aerobic conditions.

2.10.1 Photodegradation of trimethoprim

The studies started with TMP where, in a typical experiment, a 0.1 mM aqueous TMP solution was placed into the photoreactor vessel and 40 μL of a 504.5 μM of porphyrin in AcL (**18**) stock solution was also added. The antibiotic and the photocatalyst were added in a molar ratio of 500:1. The mixture was stirred in the dark, at room temperature, along 30 min, and then the Hg lamp was switched on and the mixture was irradiated for 24 h, under continuous stirring. Aliquots were taken periodically to analyze by HPLC.

The study was carried out to determine the best reaction conditions and the results obtained are reported in Table 2.10.

Table 2.10 Catalytically supported aqueous photodegradation of TMP, using **18** as catalyst and air as oxidant.

Entry	Catalyst (Cat)	Light	Oxidant	Degradation ^{a)} (%)	Required Time (h)
1	TDCPP@AcL	✓	O ₂	>99%	4
2	TDCPP@AcL	✗	O ₂	0	24
3	TDCPP@AcL	✓	- ^{b)}	4	24
4	AcL	✓	O ₂	21	24
5	AcL	✗	O ₂	0	24
6	No Cat	✓	O ₂	20	24

^{a)} reaction conditions: TMP (0.3 mg, 10 μmol); **TDCPP@AcL** (40 μL of 504.5 μM of catalyst stock solution, 20 nmol); V_{total} = 100 mL; ^{b)} Argon bubbling.

All reactions were performed in triplicate, using a TMP:**18** ratio of 500:1 and were performed for 24 hours. A complete disappearance of TMP peak was observed after 4 hours, in presence of light and under open vessel conditions (Table 2.10, entry 1). The reaction was continued for 24 h, in order to maximize mineralization of intermediate photoproducts. The chromatograms obtained before and after the photodegradation of TMP using compound catalyst **18**, were reported in **Figure 2.28 a-b**.

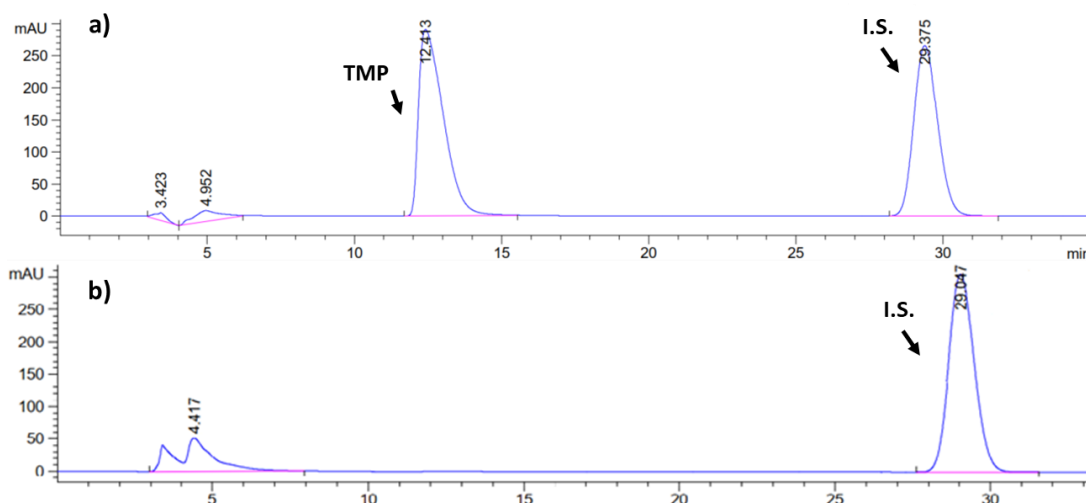


Figure 2.28 HPLC chromatograms for the TMP photodegradation recorded registered a) at time zero; b) after 24 hours of irradiation using **18** as catalyst (acetophenone as internal standard).

The first chromatogram (**Figure 2.28 a**) was recorded before starting the irradiation and two peaks were detected: one at 12.41 min, attributed to TMP and the second one at 29.37 min, ascribed to the I.S. (1-phenylethanone). After the irradiation, the chromatogram shown in **Figure 2.28 b** displayed the complete disappearance of TMP peak, which highlights the success of this degradation reaction. This promising result has led us to pursue further studies using compound **18** as photocatalyst.

To clarify the role of light irradiation, the same reaction was performed under the same conditions but in absence of light (Table 2.10, entry 2). In this situation, the degradation did not occur, confirming the importance of irradiation to produce the active oxidizing species. Additionally, the oxidant is one of the parameters that is crucial to optimize in the antibiotic oxidation. Therefore, the reaction was also performed with bubbling argon inside the reaction mixture to obtain a O₂-free reaction environment (Table 2.10, entry 3). Only 4% of degradation was achieved, probably due to vestigial O₂ present in water, indicating that the presence of oxygen has a key role in the reaction course. Moreover, the reaction was performed with bubbling O₂ from a bottle, but this did not improve the antibiotic oxidation, which corroborates the use of open vessel conditions, in terms of sustainability. Furthermore, the reaction was carried out using @AcL as catalyst, to check its contribution in the photooxidation, since its organic aromatic nature is sensitive to excitation, also triggering the production of ROS [117].

After 24 h of irradiation, only 21% of TMP degradation was observed, which corroborate the small contribution of @AcL support (Table 2.10, entry 4), since it is well known that AcL possesses low singlet oxygen quantum yields [116, 117]. Once again, the same reaction, using @AcL as catalyst, was checked in absence of light and, as expected, no degradation occurred (Table 2.10, entry 5). Finally, the last experiment conducted was leading the photoreaction without porphyrin or AcL to estimate the capability of the light alone to photooxidize the TMP. After 4 hours, just 20% of antibiotic was transformed (Table 2.10, entry 6). Furthermore, analysis of the chromatogram for this reaction indicated a complex mixture of several photoproducts (**Figure 2.29**).

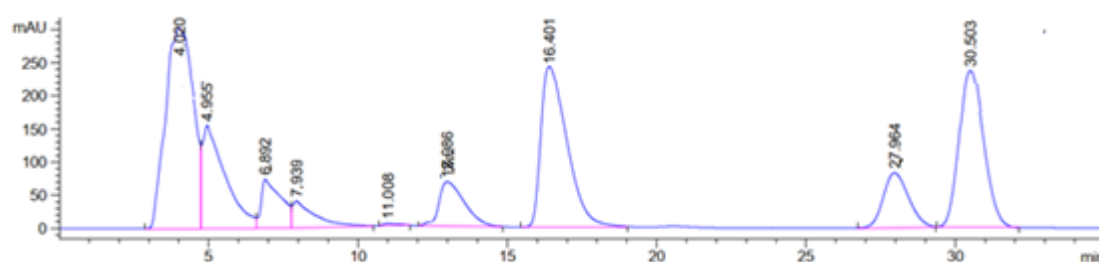


Figure 2.29 HPLC chromatogram of TMP photodegradation without photocatalyst after 24 h.

This result was in agreement with previous studies reported in literature about the direct photooxidation of TMP in which the main path of degradation was attributed to the antibiotic photolysis instead of singlet oxygen oxidation [122, 123].

All the results reported in Table 2.9 were also plotted in the graph below to show the reaction evolution along 24 hours (**Figure 2.30**).

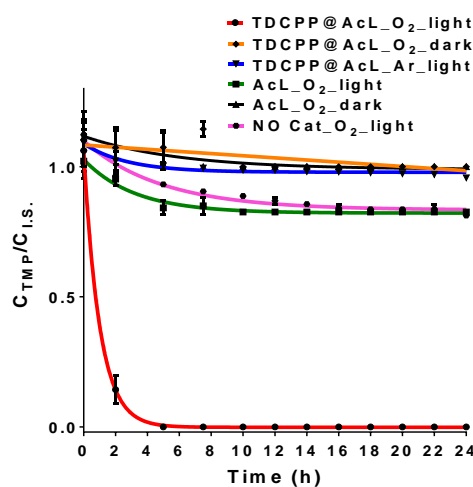


Figure 2.30 TMP photodegradation curves along 24 hours.

Additionally, the photodegradation kinetics and the oxidation mechanism were also studied (**Figure 2.31 a and b**).

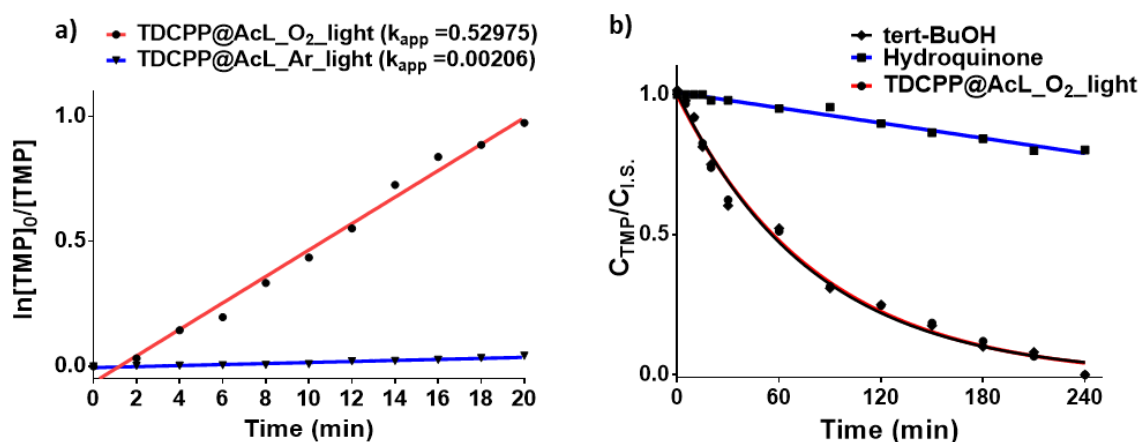


Figure. 2.31 a) Kinetic curves of TMP photodegradation using **18**, carried out for 20 min of irradiation; **b)** TMP photooxidation kinetic profile using **18** as catalyst (red line), *tert*-butyl alcohol (black line) and hydroquinone (black line) as scavengers, after 4 h of reaction.

The k_{app} values of $5.3 \times 10^{-1} \text{ min}^{-1}$ and $2.1 \times 10^{-3} \text{ min}^{-1}$ were obtained, calculated as mentioned before using the L-H kinetic model [64, 65], when photodegradation occurred using **18** in presence of oxygen and bubbling Ar, respectively (**Figure 2.31 a**). Comparing the value of k_{app} in presence of air with that one in argon, it was evident that the encapsulated photosensitizer and air are essentials on the mechanism of photodegradation. Moreover, these values showed that, using the same molar ratio of 500 to 1, the **18** photoactivity is five times higher when compared to the homogeneous photodegradation (for **6** the k_{app} was $9.7 \times 10^{-2} \text{ min}^{-1}$).

Furthermore, the oxidation mechanism of TMP's photodegradation was also analyzed carrying out two experiments, at the typical conditions previously mentioned and with **18** as photocatalyst, but in presence of hydroxyl radical (*tert*-butyl alcohol) or singlet oxygen (hydroquinone) scavengers (**Figure. 2.31 b**). The analysis of **Figure 2.31 b** clearly shows that, when the *tert*-butyl alcohol was present, the reaction occurred to its completion in *ca.* 4 hours, but the oxidation was considerably slowed down in the presence of hydroquinone. These results point out that the TMP preferential photooxidation mechanism is *via* singlet oxygen, rather than through the formation of the hydroxyl radical.

2.10.2 Photodegradation of sulfamethoxazole

Considering the results obtained in the TMP photodegradation, this catalytic system was extended to the photodegradation of another antibiotic, SMX. Thus, in a typical experiment, 0.1 mM of aqueous SMX stock solution was placed in the photoreactor vessel and 40 μ L of **18** solutions were also added. The mixture was stirred in the dark for 30 minutes and then irradiated along 24 hours. The study carried out for the SMX was similar to the one performed for TMP and the results are reported in Table 2.11.

Table 2.11 Heterogenous aqueous photodegradation of SMX, using **18** as catalyst (SMX:**18** ratio of 500:1) and air as oxidant.

Entry	Catalyst (Cat)	Light	Oxidant	Degradation ^{a)} (%)	Required Time (h)
1	TDCPP@AcL	✓	O ₂	>99	0.3
2	TDCPP@AcL	✗	O ₂	0	24
3	TDCPP@AcL	✓	- ^{b)}	7	24
4	AcL	✓	O ₂	23	24
5	AcL	✗	O ₂	0	24
6	No Cat	✓	O ₂	13	0.3

^{a)} reaction conditions: SMX (0.25 mg, 10 μ mol); **18** (40 μ L of 504.5 μ M of catalyst stock solution, 20 nmol); V_{total [TMP]} = 100 mL; ^{b)} Argon bubbling.

All reactions reported in Table 2.10 were performed in triplicate, maintaining a SMX:**18** ratio of 500:1. The complete SMX photodegradation, using **18** as catalyst and open vessel conditions, occurred in just 20 minutes (Table 2.11, entry 1) but was continued until 24 hours to maximize the mineralization of photoproducts. When the reaction was performed in absence of irradiation, no degradation occurred after 24 h (Table 2.11, entry 2), similarly to the result already obtained for TMP. Then, saturating the reaction solution with argon, negligible degradation was noticed, which corresponded to a 7% of TMP disappearance (Table 2.11, entry 3). According to this, both irradiation

and oxygen source were needed to promote the antibiotic photodegradation. Furthermore, comparing the reaction using **18** and that one using only @AcL as photocatalyst, a 23% of degradation was observed, after 24 h of irradiation, confirming the low capacity of @AcL to act as photosensitizer (Table 2.11, entry 4), and no degradation was achieved in absence of irradiation (Table 2.11, entry 5). Finally, when the experiment was performed under irradiation, but in absence of the photocatalyst, just 13% of SMX disappeared after 20 min, which was a negligible oxidation when compared to that one with **18** after the same time (Table 2.11, entry 6).

All the reactions reported in Table 2.11 were followed by HPLC, taking a sample each 30 minutes. For the SMX analysis, the HPLC method was adjusted to establish an acidic environment, so the mobile phase was formed by acetonitrile (25% v/v), water (65% v/v) and 25 mM of formic acid (10% v/v). The elution was carried out using a flow rate of 0.8 mL min⁻¹ and the oven was set at 25 °C. In **Figure 2.32**, we report the two HPLC chromatograms recorded before and after 24 hours of irradiation.

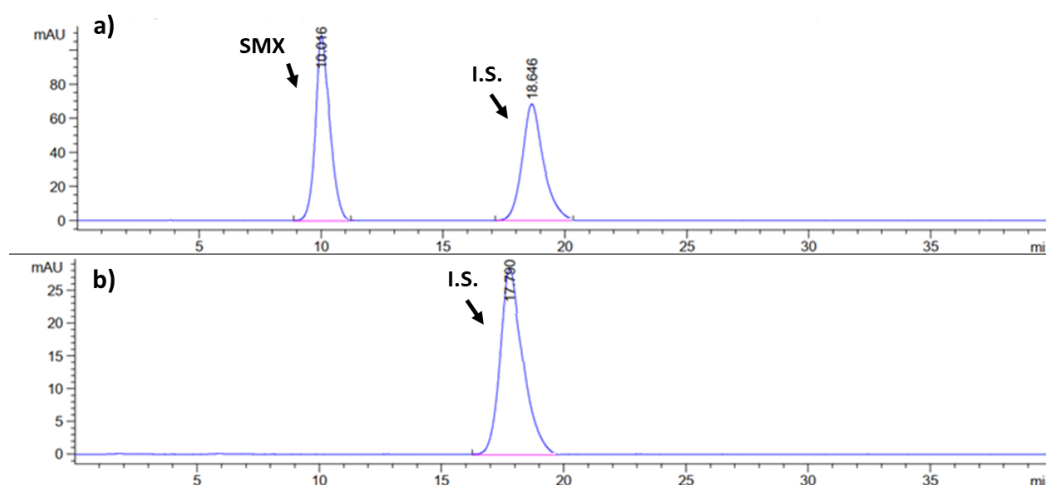


Figure 2.32 HPLC of SMX solution: **a)** before irradiation; **b)** after 24 hours of irradiation. (I.S. = 1-phenylethanone)

In the beginning of the reaction, the chromatogram exhibited 2 peaks, being the first one at retention time of 10.04 min attributed to SMX and the second one at 18.64 min ascribed to the I.S. (**Figure 2.32 a**). After 24 hours of irradiation, the chromatogram shows exclusively the I.S. peak (**Figure 2.32 b**).

The degradation yield was determined introducing in each sample a specific volume of a solution of 1-phenylethanone, used as internal standard, before the injections.

All the results are plotted in the graph below to show the reaction evolution for 24 h (**Figure 2.33 a**). Similarly, to the TMP study, apparent first-order rate constants (k_{app}) were also observed (**Figure 2.33 b**).

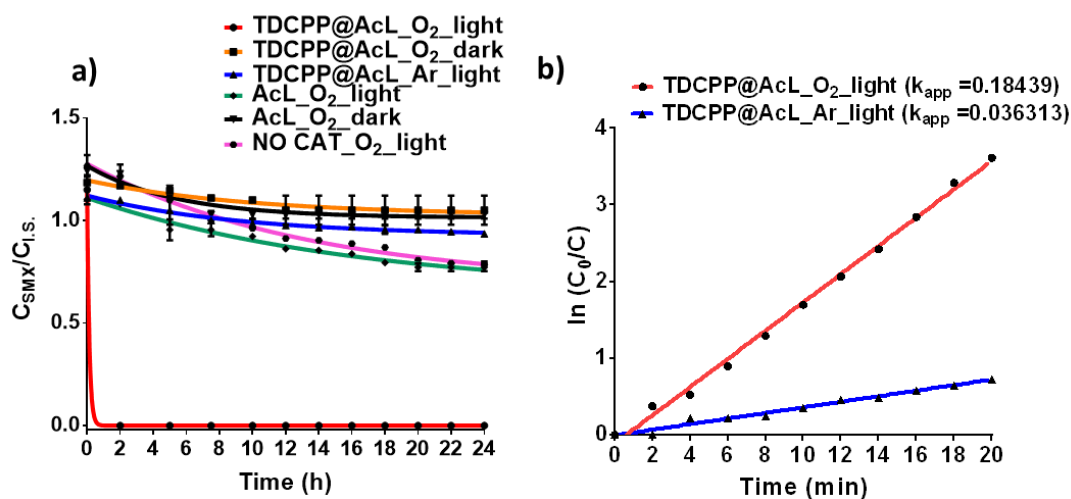


Figure 2.33 a) Photodegradation SMX curves along 24 hours; **b)** kinetic curves of SMX photooxidation obtained after 20 min of irradiation and using catalyst **18**.

Considering the reaction of SMX photodegradation using **18** as catalyst and air an oxidant, the (k_{app}) values were $1.8 \times 10^{-1} \text{ min}^{-1}$ and $3.6 \times 10^{-2} \text{ min}^{-1}$, in presence and absence of oxygen respectively (**Figure 2.33 b**). Once again, these values confirmed the relevance of the combination of both **18**, oxygen and as well as light to achieve high rates of SMX photodegradation, showing that the irradiation produced a degradation kinetics five times higher than that one in its absence.

2.11 Photocatalyst reutilization studies

The stability of the photocatalyst after several cycles was also evaluated under the optimized experimental conditions previously described. Reutilization studies of **18** were performed individually for TMP and SMX. It should be noted that attempts to collect the photocatalyst material after the first cycle were carried out, by centrifugation and/or filtration, but these procedures proved ineffective, due to the high dispersibility of the photocatalyst in aqueous media. However, since we observed the complete degradation of the substrate after each reaction, the reaction vessel was simply recharged with more antibiotic after each cycle, ensuring the same initial AB concentration and AB:Cat ratio.

Following this straightforward reutilization strategy, ten photocatalytic reutilization cycles were performed for TMP and SMX (**Figure 2.34 a and b**, respectively).

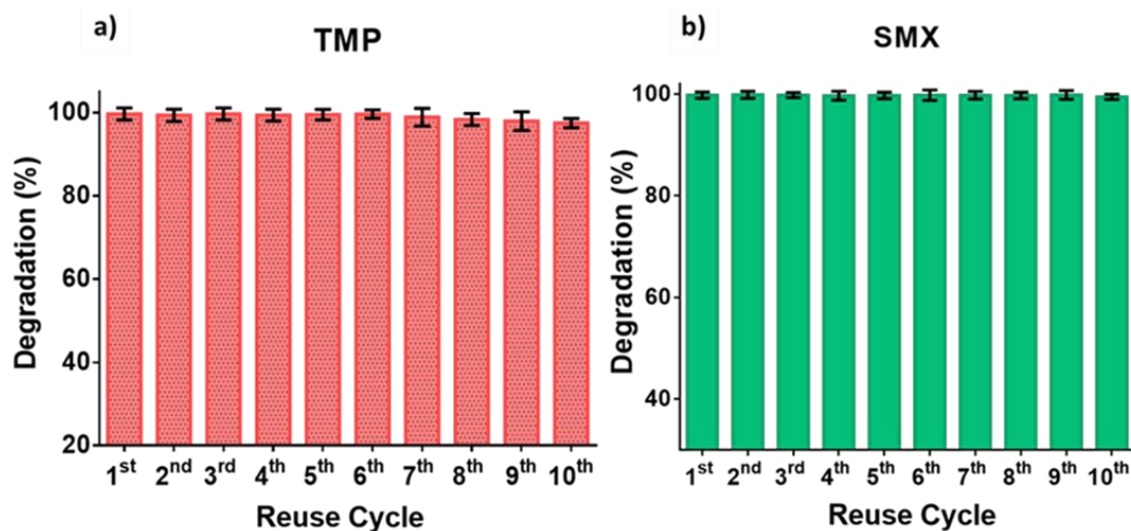


Figure 2.34 Photodegradation (%) of a) TMP and b) SMX after photocatalytic reutilization cycles of **18**.

We observed that the photocatalyst activity was not significantly changed, after ten reutilization cycles for TMP or SMX, confirming the relevant stability of the hybrid photocatalyst **18** under the reaction conditions, even upon consecutive additions of antibiotic substrates, before each run. Such accumulation of photoproducts could cause saturation due to concentration increase, which did not hamper catalyst activity. This may be attributed to the very high mineralization, which induced low accumulation of products in aqueous solution (see below, TOC analysis section 2.13). Furthermore, using this reutilization strategy, the catalyst's recovery process was avoided, contributing to a more sustainable overall process.

To corroborate the catalyst stability after the reutilization cycles, two complementary experiments for TMP and SMX were performed. Firstly, we analyzed the reaction mixtures before the first cycle and after the last cycle by UV-Vis and the spectra are reported in **Figure 2.35 a and b**.

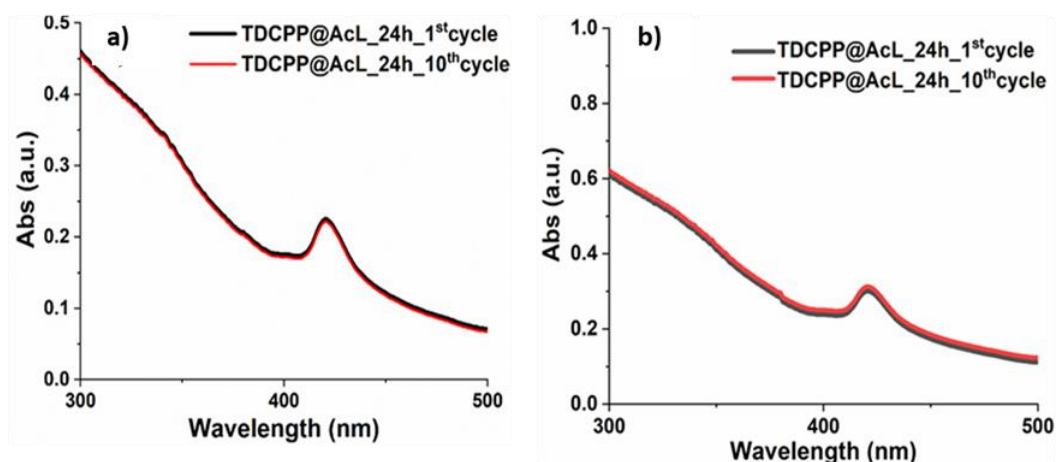


Figure 2.35. UV–vis spectra recorded before the first cycle (black line) and after the last reutilization one (red line), in distilled water, for the photodegradation of: **a)** TMP and **b)** SMX, using **18** as catalyst.

It should be mentioned that **18** exhibited a noticeable stability in both cases, showing negligible degradation after its reutilization. This high stability was also corroborated by analyzing the catalyst morphology by TEM, after the 10 reutilization cycles for TMP and SMX, respectively (**Figure 2.36**).

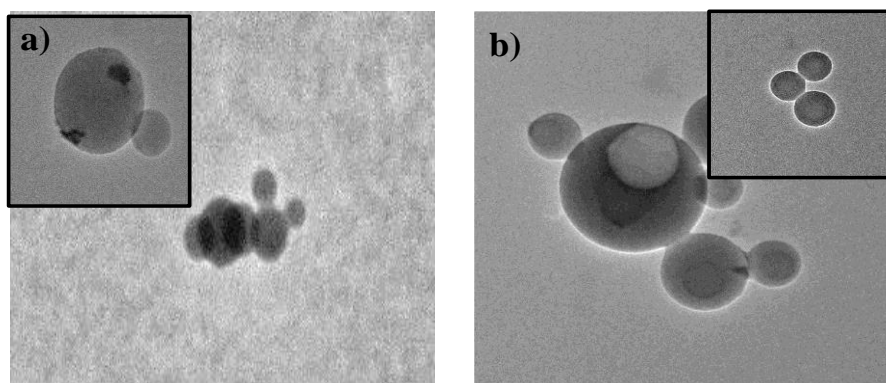


Fig. 2.36 TEM images of **18** photocatalyst: **a)** TMP degradation, before the first cycle (large image, magnification = 5000 \times) and after the tenth cycle (small image, magnification = 15000 \times); **b)** SMX degradation, before the first cycle (large image, magnification = 15000 \times) and after the tenth cycle (small image, magnification = 35000 \times).

The TEM images showed that the catalyst morphology remained unaltered in both cases, which accounts for their high stability. This may be explained by the encapsulation effect, which prevents, to a certain extent, photosensitizer degradation. To confirm this effect of acetylated lignin, reutilization studies have also been taken for homogenous photocatalyst **6**, as water soluble surrogate for hybrid catalyst **18**. After the first cycle, which led to a full degradation of TMP, a second reuse was performed. This revealed a

drastic decrease of the catalyst activity, showing only 36% of photooxidation after 24 h of irradiation. This result was confirmed by UV-Vis spectroscopy as reported in **Figure 2.37**.

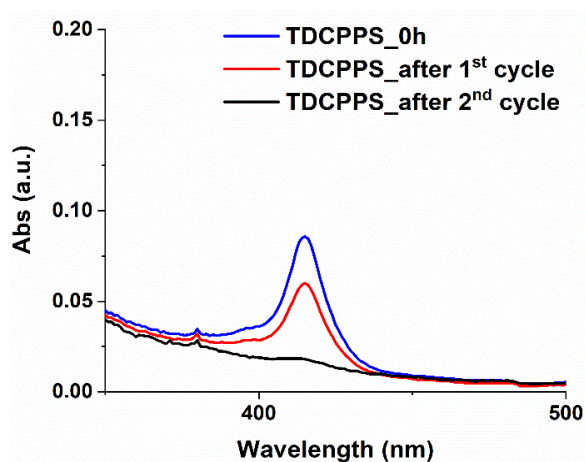


Figure 2.37 UV–vis spectra of the aqueous TMP solution using **6** as homogeneous catalyst, before the photodegradation (blue line), after the 1st reutilization cycle (red line) and after the 2nd cycle (black line).

After the first cycle, the UV-Vis of the TMP photodegradation products mixture showed a noticeable decrease in the **6** Soret' band absorbance, reflecting a catalyst degradation (red line), when compared with the spectra recorded before starting the reaction (blue line). After the second cycle, the catalyst's Soret band almost completely disappeared (black line) meaning that the porphyrin was no longer present in the reaction. This effect was corroborated by HPLC, as depicted in **Figure 2.38 a**, since the TMP was fully degraded after the 1st cycle of reutilization, while the TMP peak (eluted at ~15.6 min) was still present after the second cycle, displaying also other photodegradation products (PPs) (**Figure 2.38 b**).

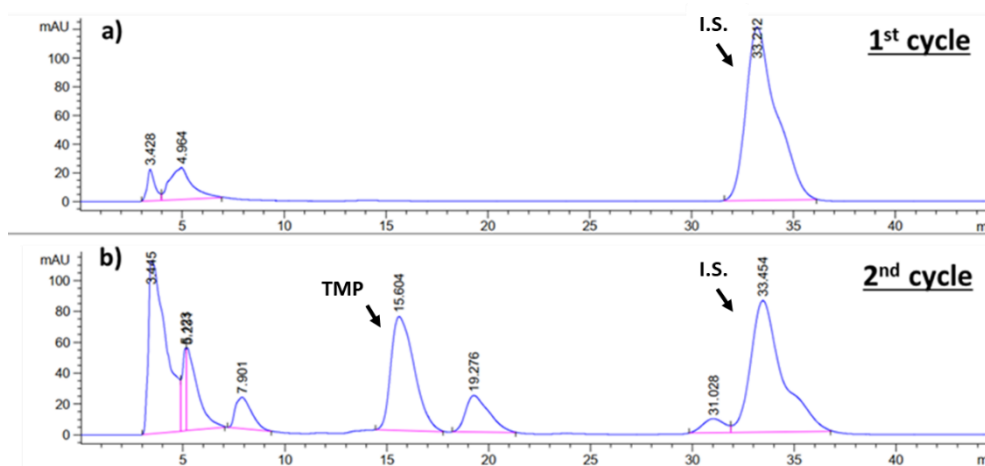


Figure 2.38 HPLC chromatograms recorded for reutilization of **6** (TDCPPS), under homogeneous photocatalytic conditions, after: **a**) first cycle, **b**) second cycle.

2.12 Photodegradation of cotrimoxazole

After evaluating the hybrid photocatalyst **18**'s performance in each antibiotic photodegradation studies, the same system was extended and applied to the study of the cotrimoxazole degradation behavior. Since these two antibiotics are mostly found as a mixture, particularly in a commercial dosage of TMP:SMX of 1:5 mass ratio, its photodegradation was evaluated under the same conditions reported above. Therefore, in a typical experiment, the aqueous antibiotics' mixture (AB_{mix}) was added into the photoreactor as well as **18**, in a ratio of AB_{mix} and catalyst of 500:1, and after 30 minutes of stirring in dark, was irradiated. The results obtained after 24 h of irradiation are reported in Table 2.12.

Table 2.12. Photocatalytic aqueous degradation of co-trimoxazole, using **18** as a catalyst ($AB_{\text{mix}}:\text{Cat} = 500:1$) and air as oxidant.

Entry	Catalyst (Cat)	Light	Oxidant	Degradation ^{a)} (%)	Required Time (h)
1	TDCPP@AcL	✓	O ₂	>99	2
2	AcL	✓	O ₂	30	24
3	No Cat	✓	O ₂	5	2

^{a)} reaction conditions: SMX (2.16 mg, 8.5 μmol) and TMP (0.45 mg, 1.5 μmol); **18** (40 μL of 504.5 μM of catalyst stock solution, 20 nmol), AB:Cat ratio = 500:1; $V_{\text{total}} = 100 \text{ mL}$.

Considering the absence of degradation when the reactions were performed in the dark and bubbling argon, this evaluation only considered the photodegradation of the $AB_{S_{mix}}$ using **18** and AcL as photocatalysts and in their absence. The complete photodegradation of the $AB_{S_{mix}}$ was achieved after 2 hours of irradiation (Table 2.12, entry 1). Additional experiments were carried out using only AcL as photocatalyst and, after 24 h of irradiation, only a 30% of degradation was achieved (Table 2.12, entry 2). When the photodegradation was carried out without catalyst, negligible oxidation was observed (< 5%), after 2 hours (Table 2.12, entry 3). Once again, these results confirmed the key role of the porphyrin photosensitizer in the degradation.

Additionally, the antibiotics' mixture photodegradation was sampled and followed by HPLC and the results are plotted in **Figure 2.39**.

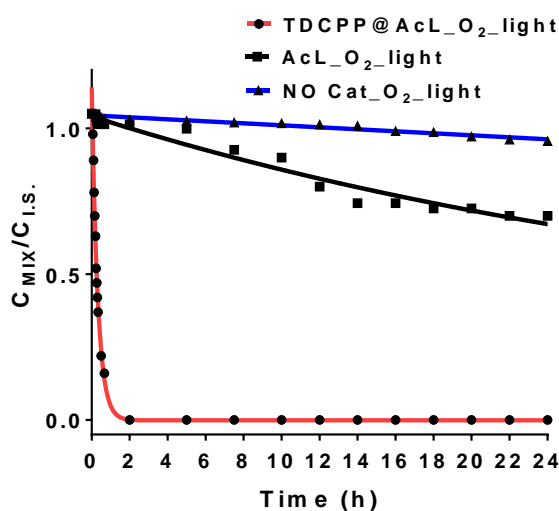


Figure 2.39 Photocatalytic degradation curves of $AB_{S_{mix}}$ using **18** (red line), @AcL (black line) and without photocatalyst (blue line), after 24 h of irradiation.

For the $AB_{S_{mix}}$ analysis, the mobile phase was changed into 0.1% of aqueous formic acid solution (v/v), water (v/v) and acetonitrile (v/v). The elution was carried out by a gradient and the parameters are reported in Table 2.13.

Table 2.13 HPLC gradient elution method for the AB_S_{mix} analysis.

Time (min)	Acetonitrile (%)	Water (%)	0.1% aq. formic acid (%)
0	0	85	15
3	0	85	15
4	10	80	10
14	10	80	10
15	35	55	10
22	35	55	10
25	0	85	15
36	0	85	15

The method started with water (85% v/v) and formic acid (15% v/v) in isocratic mode for the first 3 min, then the eluents were changed to acetonitrile (10% v/v), water (80% v/v) and formic acid (10% v/v) from the 4th min until the 14th one. Next, the organic phase was increased into acetonitrile (35% v/v), water (55% v/v) and formic acid (10% v/v) from the 15th min until the 22nd one. At the end, the mobile phase was brought back to the initial operational conditions for the last eleven minutes. The HPLC chromatograms of the time zero and after 24 hours of irradiation are reported bellow (**Figure 2.40 a** and **b**).

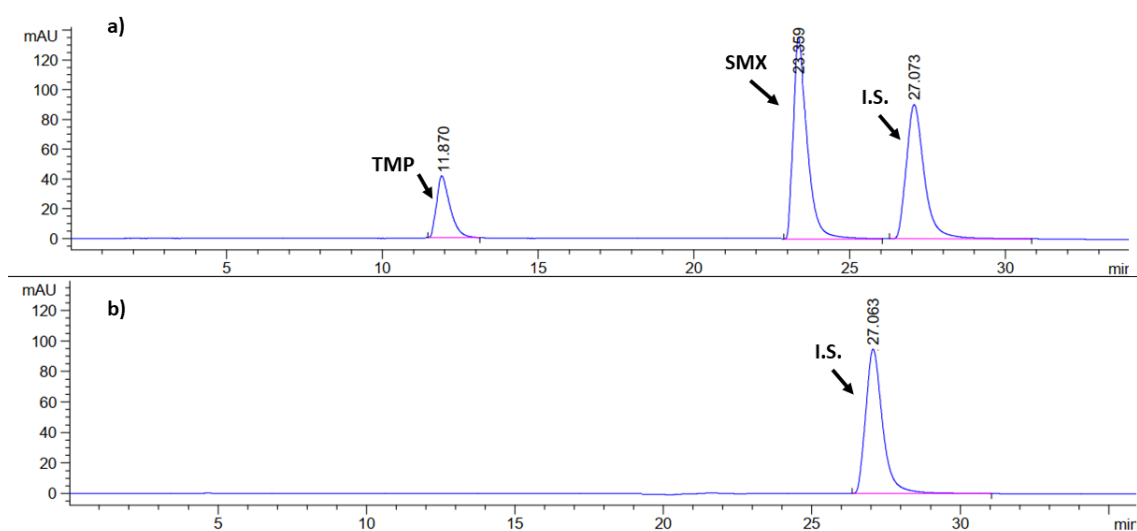


Figure 2.40 HPLC of the AB_S_{mix} solution using TDCPP@AcL, **18**: **a**) before the irradiation; **b**) after 24 hours of irradiation.

2.13 TOC analysis

As it is known, ideal oxidation processes promote the total mineralization of pollutant/pharmaceuticals into CO₂, H₂O and inorganic compounds. Usually, also other innocuous compounds are generated during the degradation. Considering this, we tried to determine the antibiotics mineralization degree using TOC removal analysis, by comparing the values before and after the photodegradation reaction and the results are in Table 2.14.

Table 2.14. TOC measurements (in triplicate) for TMP and SMX degradation using TDCPP@AcL, **18**.

Entry	Substrate	TOC (mg C L ⁻¹)		TOC removal (%)
		t = 0 h	t = 24 h	
1	TMP	37.6 ± 2.5	9.9 ± 2.5	75
2	SMX	109.0 ± 2.5	20.0 ± 2.5	83
3	TMP:SMX (1:5 w/w)	39.0 ± 2.5	8.2 ± 2.5	79

Considering the TMP photodegradation, an initial TOC of 37.6 ± 2.5 mg C L⁻¹ was detected, while, after 24 hours the value measured was 9.9 ± 2.5 mg C L⁻¹, representing a TOC removal of 27.7 ± 2.5 mg C L⁻¹, corresponding to 75% of TOC removal (Table 2.14, entry 1). In the case of SMX, a TOC removal value of 83.0 mg C L⁻¹ was determined, resulting from the difference between an initial average TOC of 109.0 ± 2.5 mg C L⁻¹ and a TOC = 20.0 ± 2.5 mg C L⁻¹, recorded after a 24 h degradation process, implying 83% of TOC removal (Table 2.14, entry 2). Moreover, the antibiotics' mixture was also analyzed, and an initial average value of 39.0 ± 2.5 mg C L⁻¹ was detected before prior to photodegradation, while a value of 8.2 ± 2.5 mg C L⁻¹ was recorded after 24 h of photooxidation, indicating a TOC removal of 79% (Table 2.14, entry 3).

The TOC analysis was performed also after the photolysis process of TMP, SMX and TMP:SMX (1:5 w/w). The values obtained were very low for each antibiotic solution, corroborating the low photodegradation values obtained experimentally through HPLC analysis.

Considering the few studies reported in literature, these TOC values confirm the high efficiency of the developed catalytic system, which promoted full antibiotic degradation in aqueous media and their high mineralization. For SMX, Gong *et al.* reported a TOC value of 50% after a complete degradation using a photocatalyst formed by CoFe_2O_4 and TiO_2 under UV irradiation [124], while Lima *et al.* described a 25% of TOC removal for a mixture of antibiotics including SMX and TMP, when it was treated in homogeneous photo-Fenton conditions and under simulated solar light [125, 126].

2.14 Degradation products analysis

To complete our study, the antibiotics' and photoproducts' solutions were analyzed by LC-MS, in collaboration with the *Instituto Superior Técnico* (IST) of the University of Lisbon, to determine the structure of the possible photoproducts arising from the catalyzed TMP, SMX and its mixture degradation processes. Hence, the LC-MS chromatogram before and after TMP degradation is presented in **Figure 2.41**, and the identified degradation products are reported in Table 2.15.

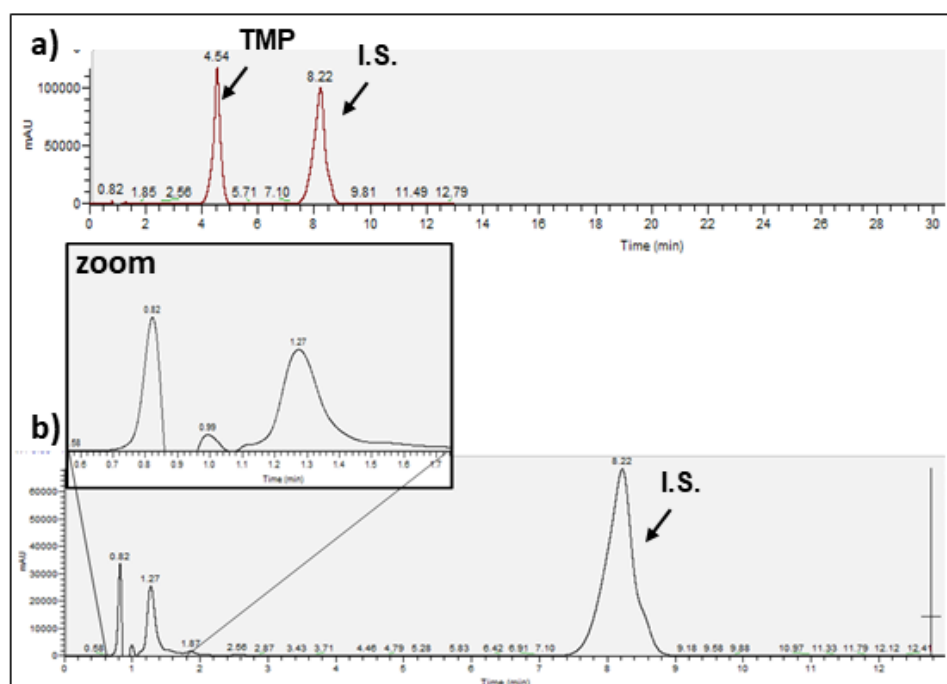
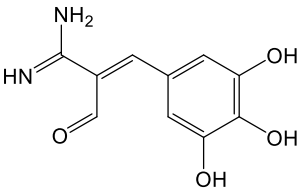
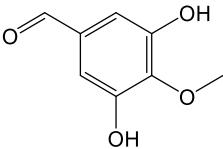
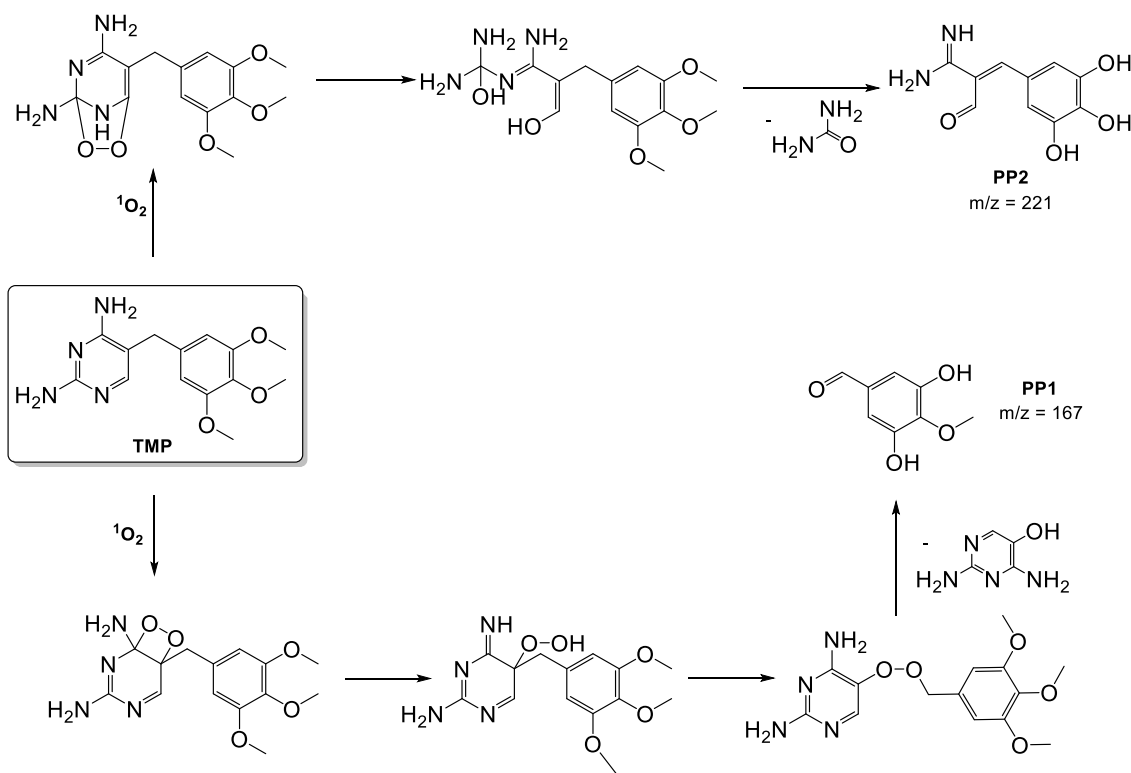


Figure 2.41 LC-MS analysis for the photocatalytic degradation of TMP using TDCPP@AcL, **18**, with acetophenone as internal standard; **a)** $t = 0$ h; **b)** after 24 h of irradiation (zoom: TMP degradation product detected by LC-MS).

Table 2.15 Identification of residual TMP photoproducts (PPs) by LC-MS.

PPs	t _r (min)	m/z	Relative %	Identified products
PP1	0.82	221	23	
PP2	1.27	167	67	

In this case, the elution was performed with a flow rate of 0.4 mL min⁻¹ and using a mixture acetonitrile (15% v/v), methanol (15% v/v) and a buffer solution of ammonium acetate (70% v/v) adjusted to pH 9.2. In **Figure 2.41 a**, the TMP chromatogram, recorded before the irradiation, displayed two peaks: the first one corresponding to TMP at 4.54 min and the second one is related to the internal standard at 8.22 min. In the TMP photodegradation chromatogram, two photoproducts, PP1 and PP2, were identified, when using **18** as catalyst and after 24 hours. Particularly, PP1 showed with a retention time (t_r) of 0.82 min and a m/z of 221 Da, while PP2 with a t_r of 1.27 min and a m/z of 167 Da, respectively (**Figure 2.41 b**). The identified PPs are in agreement with the literature and are supported by the reported mechanistic insights on photooxidations using singlet oxygen as the main effector [122, 123]. So, considering these previous studies, a possible pathway for TMP photodegradation is proposed, based on the reactivity of singlet oxygen towards aromatic heterocycles [33, 82, 88, 127-129] (Scheme 2.14).



Scheme 2.14 Possible TMP photodegradation pathways.

The same study was extended to SMX, so after 24 h of irradiation and using **18** as catalyst, LC-MS analysis was performed (**Figure 2.42 a and b**).

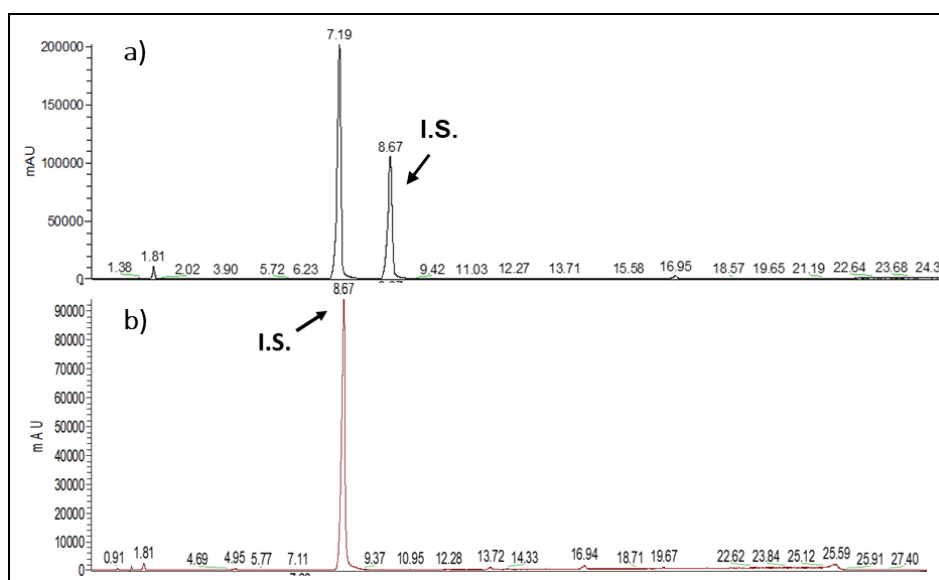


Figure 2.42 LC-MS analysis for the identification products in the photocatalytic degradation of SMX using TDCPP@AcL, **18**, with acetophenone as internal standard: **a)** t = 0 h, **b)** after 24 h.

In this case, the elution was performed with a flow rate of 0.4 mL min^{-1} , using a mobile phase formed by H_2O with 0.1% of formic acid (Eluent A) and acetonitrile with 0.1% of formic acid (Eluent B). Table 2.16 displays the elution gradient used.

Table 2.16 Mobile phase and elution gradient used for the LC-MS analysis of SMX.

Time (min)	Eluent A ^{a)}	Eluent B ^{b)}
0	90	10
20	0	100
23	0	100
25	90	10
35	90	10

^{a)} H_2O (0.1% Formic Acid); ^{b)} Acetonitrile (0.1% Formic Acid).

During the LC-MS run, a linear gradient starting with 90% A and 10% B was performed for the first 20 min until to achieve a 100% of B. Then, an isocratic gradient (100% B) was maintained along 3 min, and after this time another linear gradient was carried out to return to the initial eluents' percentages (90% A and 10% B) during 2 min. Thus, this mobile phase composition was maintained until the end of the run. The peak of SMX pre-irradiation was detected at 7.19 min and the internal standard corresponded to the peak at 8.67 min (**Figure 2.42 a**). After 24 h of irradiation, no degradation products were spotted, in fact only the peak of internal standard at 8.67 min was obtained (**Figure 2.42 b**). This result may be attributed to the high mineralization, corroborating the high TOC removal value (83%) and to the less recalcitrant nature of SMX. Moreover, it is necessary to mention that the mass interval used in this analysis was between $m/z = 50 \text{ Da}$ and 10000 Da , which points out that any remaining carbon-containing PPs possess very low molecular weights.

Next, we performed the LC-MS analysis for the photodegradation of the TMP:SMX 1:5 w/w mixture, carried out under the same reaction conditions as for the SMX individual experiments (**Figure 2.43**).

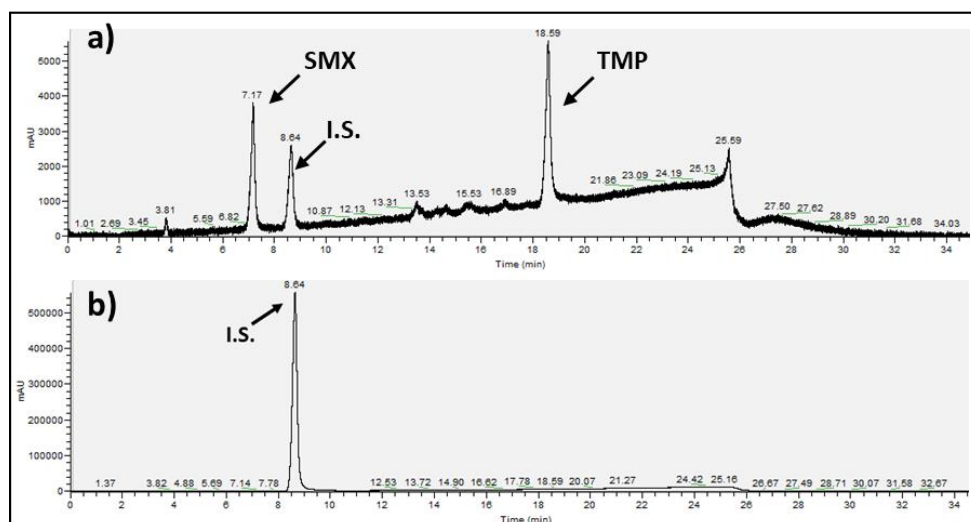


Figure 2.43 LC-MC analysis of: **a)** the sample before irradiation; **b)** the sample obtained after 24 h of irradiation to identify the products in the catalytic degradation of co-trimoxazole (TMP:SMX 1:5 w/w ratio), using acetophenone as internal standard.

Also in this case, the chromatogram of the solution in the beginning of the reaction showed the peaks corresponding to the two antibiotics involved, SMX and TMP, at 7.17 min and 18.59 min, respectively and the acetophenone one at 8.64 min (**Figure 2.43 a**). After 24 hours of irradiation, no degradation products with m/z above 100 Da were observed, as showed in **Figure 2.43 b**, in which the only peak detected corresponding to the acetophenone ($t_r = 8.64$ min), again corroborating the previous findings. As in previous experiments, this result may be explained due to the high value for TOC removal.

2.15 *E. coli* resistance assay

Considering that the primary goal of this thesis was the TMP degradation to avoid its accumulation in water, and thus prevent development of bacterial resistance, we evaluated if bacterial exposure to the main photodegradation products (PPs) obtained after the degradation process, along 10 days, could cause resistance to TMP. To achieve that, firstly we determined i) the minimum inhibitory concentration (MIC) value of TMP and ii) if solution of 1 mg of PPs *per* mL has any inhibitory activity on *E. coli* ATCC 8739 growth. Regarding the MIC of TMP, the value obtained ($0.4882 \mu\text{g mL}^{-1}$) is within the normal range expected for an *E. coli* strain susceptible to TMP. On the other hand, a

solution of 1 mg of PPs *per* mL did not have any appreciable inhibitory activity. This is a consequence of two key aspects. The first one is related to the almost full TMP degradation (> 99%) as previously demonstrated by HPLC. Given the antibiotic's low MIC value, even small quantities of TMP in the PPs solution would have caused bacterial growth inhibition. The second factor is that the PPs don't have a significant MIC, which was expectable due to the huge fragmentation observed after the TMP degradation (as previously reported in Table 2.15).

After determining the inhibitory activity of both TMP and the PPs solution, an *E. coli* resistance inducing assay was conducted, with a schematic representation presented in **Figure 2.44**.

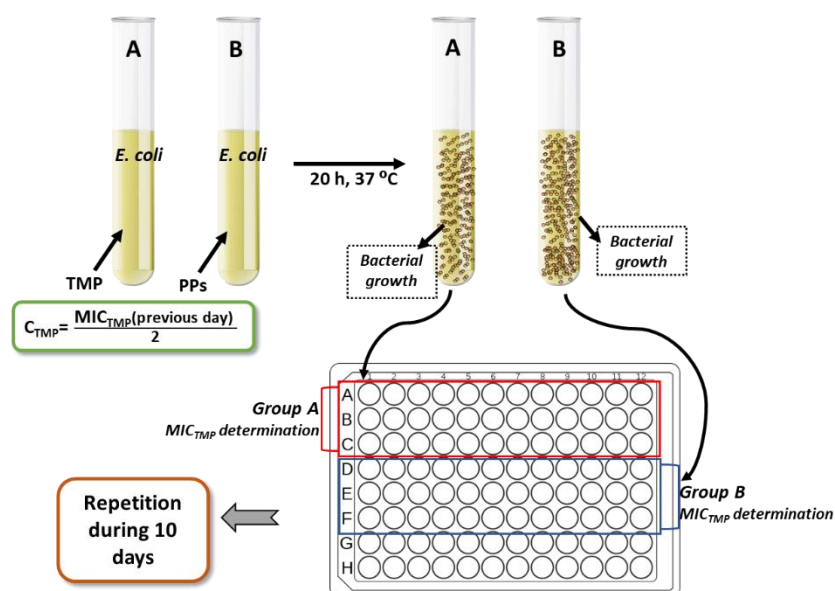


Figure 2.44 Schematic representation of *E. coli* resistance assay.

Considering that continuous bacterial exposure to subinhibitory antibiotic concentrations is of the main mechanisms of bacterial resistance, we developed a protocol to evaluate *E. coli*'s ability to generate resistance to TMP when exposed to a subinhibitory concentration of PPs, using an exposure to a subinhibitory concentration of TMP as a control experiment. On the 1st day, bacteria of group A were exposed to a concentration of TMP equal to its MIC/2 value ($\sim 0.2441 \mu\text{g mL}^{-1}$), and bacteria of group B were exposed to a solution of 1 mg of PPs *per* mL. Then, after incubation at 37 °C in MH medium during 20 h, bacterial growth is expectedly observed due to the presence of subinhibitory antibiotic concentrations. In the 2nd day, two standard inocula of approximately 5×10^5 CFU/mL were prepared using the bacteria that grew in each group (A and B) and

the TMP MIC was determined for each inoculum according to the experimental procedure described in Chapter 4, section 4.3.3. This cycle of tests was repeated along 10 days. It is necessary to highlight that, each day that the TMP MIC value increases, bacteria will be exposed to a newly prepared TMP concentration, which is always equal to the half MIC value. The results of the *E. coli* TMP resistance inducing assay, after continuous exposure to subinhibitory concentrations of TMP and PPs, is reported in **Figure 2.45**.

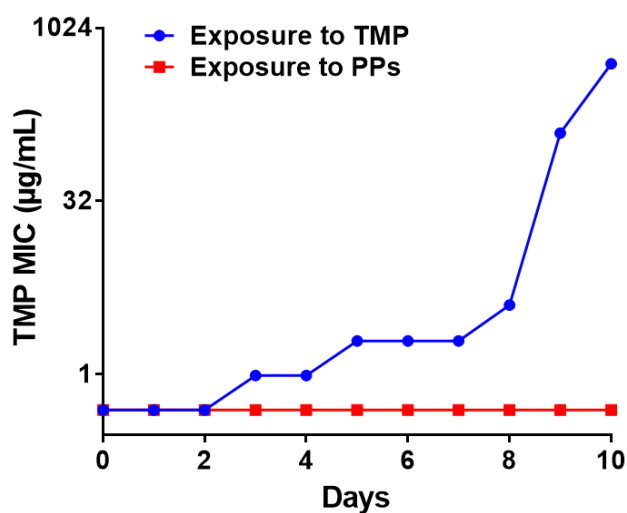


Figure 2.45 Resistance of *E. coli* to TMP after continuous exposure to subinhibitory concentrations of TMP and PPs. Results are presented as MIC of TMP in function of the number of days of *E. coli* exposure to TMP and PPs.

Regarding the bacteria exposed to TMP, we observed an increase in the TMP MIC values along the 10 days. For instance, the MIC value of $\sim 0.4882 \mu\text{g mL}^{-1}$, determined on the day zero, remains constant for the first two days. Then, an increase to $\sim 0.9765 \mu\text{g mL}^{-1}$ was registered until the 4th day with a consecutive enhancement until $\sim 1.953 \mu\text{g mL}^{-1}$ in the next day. Only in the 8th day we observed another MIC value change, $\sim 3.906 \mu\text{g mL}^{-1}$, reaching $\sim 500.0 \mu\text{g mL}^{-1}$ in the last day. This result is expectable as it has already been reported that exposure to sub-therapeutic TMP concentrations can cause resistance in bacteria, and several mechanisms have been identified [13]. Concerning the group of bacteria exposed to the PPs solution, no development of resistance was detected during the 10 days of this essay. Indeed, in the 10th day, the MIC of bacteria exposed to TMP (group A) was already ~ 1000 -fold higher than that of bacteria exposed to PPs (group B), which shows the efficiency of the photodegradation process developed in this thesis to promote the transformation of TMP

into low molecular weight products without any appreciable antimicrobial activity. In this way, the proposed goal of contributing for the decrease of bacterial resistance to the TMP was achieved.

2.16 Conclusion

In this chapter, two different approaches for the degradation of the TMP using porphyrin-based catalysts were described and discussed. The first method consisted in the development of a metalloporphyrin-based heterogeneous oxidative catalytic system, in which hydrogen peroxide was used as benign oxidant. To that end, the Mn(III) *meso*-tetrakis(2,6-dichloro-3-sulfonatophenyl)porphyrin acetate (**TDCPP**) was found to act as the best catalyst under homogeneous aqueous conditions (in terms of stability and activity), for which the best TMP:Cat ratio of 500:1 promoted AB's full degradation in 150 min, in the presence of H₂O₂ as oxidant. Then, this porphyrin was successfully immobilized through covalent linkage onto an inexpensive solid support such as the 3-aminopropyl functionalized silica gel. This new hybrid material was fully characterized by standard spectroscopic means and implemented in the heterogeneous approach. This system successfully achieved complete TMP degradation in 150 min, using a 500:1 TMP:Cat ratio and H₂O₂ as oxidant (2.6×10^{-3} mol). The notable **MnTDCPPS** stability was evidenced by five reutilization cycles without negligible loss of activity and no porphyrin leaching. The main degradation products were identified by UPLC-MS and a plausible degradation pathway was proposed. Moreover, ecotoxicity studies were carried out for a TMP solution, considering the worst-case scenario, in which the TMP was present at saturated concentrations, and for the degradation products solution towards the bacterium *V. fischeri*, the microalgae *R. subcapitata* and the invertebrate *B. calyciflorus* microorganisms. These results only allowed to conclude that the examined solutions did not cause an increase in toxicity, even considering the laboratorial conditions, which required the use of an excess of hydrogen peroxide as well as the sodium bisulfite as quencher.

In the search of even more sustainable catalytic processes, the second degradation method involved the action of light to catalytically promote the degradation of TMP in aerobic conditions. After implementing the best conditions for the homogeneous aqueous photocatalytic system, using the *meso*-tetra(2,6-dichloro-3-sulfonatophenyl)porphyrin

(TDCPP) as catalyst, a 400 W medium pressure mercury lamp as irradiation source and atmospheric oxygen as oxidant, a new photocatalyst was developed by encapsulating this free-base porphyrin into modified biopolymer nanoparticles of acetylated lignin, which was used as organic matrix. This novel hybrid catalyst **18** was applied in the photooxidation of TMP and extended to SMX, using a 500:1 AB:Cat ratio. This system showed successful performances, with complete degradation of the antibiotics in 4 h and 20 min, respectively. One of the highest TOC values removal reported in literature was achieved, with 75% and 85% for TMP and SMX, respectively. In addition, we checked the material's stability, where ten consecutive photocatalytic reutilization cycles were performed for TMP and SMX, without loss of catalytic activity or photosensitizer leaching. It should be emphasized that no photocatalyst recovery/reactivation was necessary in these experiments, as new antibiotic samples were added before each cycle. These results clearly demonstrate the activity, stability and reusability of the heterogeneous photocatalyst. In addition, this catalytic system was also applied to a mixture of TMP and SMX in a TMP:SMX 1:5 w/w ratio, using the commercial dosage of co-trimoxazole. Once again, 79% of TOC removal was obtained, showing a similar outcome to what was previously described for both antibiotics in separate. We analyzed the resulting reaction mixtures by LC-MS to identify possible degradation photoproducts and only the TMP revealed the formation of 2 photoproducts, while the other did not indicate the presence of products having m/z above 50 Da after 24 h of irradiation.

Considering the AOPs herein described, for instance regarding the AB:Cat ratios, both in oxidative catalysis and in photocatalysis, our systems use much higher ratios of antibiotic towards the catalyst amount, representing a breakthrough by the fact that very low amounts of catalysts are necessary to efficiently degrade the target antibiotics.

Nevertheless, in sum, we can undoubtedly conclude that the photocatalytic approach involving atmospheric O₂ is a more sustainable and straightforward system, since it does not require the addition of an oxidant agent such as H₂O₂. Another important factor is that the heterogeneous catalyst material used lignin as organic catalyst support, the second most abundant natural organic polymer and a renewable resource on earth. Moreover, this photocatalytic system provides higher values of TOC removal, allowing to conclude that a superior amount of antibiotics was converted into CO₂ and water, as also corroborated by LC-MS results. Unlike previous literature reports, no significant metal leaching and no appreciable decrease in photocatalytic activity were observed

which highlights the great stability and efficiency of this photocatalyst. Actually, we consider the developed reutilization method as very sustainable and convenient, since it only requires the introduction of portions of antibiotic before each cycle, avoiding consecutive separation, recovery and reactivation steps, which obviously involve the use of organic solvents.

Finally, the success of this photocatalytic process in preventing the development of *E. coli* resistance to TMP must be highlighted. Indeed, along a 10-day exposure to the PPs solution, no change in *E. coli* TMP MIC was observed. In contrast, exposure to sub-inhibitory TMP concentrations over the same period has resulted in a ~ 1000-fold increase in the TMP MIC. Bottom line, this means that the PPs produced by this heterogeneous photodegradation system could not promote the development of antimicrobial resistance. Overall, the work presented in this chapter successfully accomplished the initially described goals regarding the development of new systems that can potentially reduce antibiotic accumulation in the environment and bacterial resistance development, through a downstream approach (environmental remediation).

2.17 References

- [1] R. Hirsch, T. Ternes, K. Haberer, K.L. Kratz, Occurrence of antibiotics in the aquatic environment, *Science of the Total Environment*, 225 (1999) 109. [https://doi.org/10.1016/S0048-9697\(98\)00337-4](https://doi.org/10.1016/S0048-9697(98)00337-4)
- [2] K. Kummerer, Antibiotics in the aquatic environment - A review - Part I, *Chemosphere*, 75 (2009) 417. <https://doi.org/10.1016/j.chemosphere.2008.11.086>
- [3] T. Thiebault, Sulfamethoxazole/Trimethoprim ratio as a new marker in raw wastewaters: A critical review, *Science of the Total Environment*, 715 (2020) 136916. <https://doi.org/10.1016/j.scitotenv.2020.136916>
- [4] H. Gelband, M. Miller-Petrie, S. Pant, S. Gandra, J. Levinson, D. Barter, A. White, R. Laxminarayan, The state of the world's antibiotics, *Human use of antibiotics*, by Center for Disease Dynamics Economics and Policy, CDDEP, Washington, D.C., 2015.
- [5] Q.T. Dinh, E. Moreau-Guigon, P. Labadie, F. Alliot, M.J. Teil, M. Blanchard, M. Chevreuil, Occurrence of antibiotics in rural catchments, *Chemosphere*, 168 (2017) 483. <https://doi.org/10.1016/j.chemosphere.2016.10.106>
- [6] A.C. Johnson, V. Keller, E. Dumont, J.P. Sumpter, Assessing the concentrations and risks of toxicity from the antibiotics ciprofloxacin, sulfamethoxazole, trimethoprim and erythromycin in European rivers, *Science of the Total Environment*, 511 (2015) 747. <https://doi.org/10.1016/j.scitotenv.2014.12.055>
- [7] P. Verlicchi, M. Al Aukidy, E. Zambello, Occurrence of pharmaceutical compounds in urban wastewater: Removal, mass load and environmental risk after a secondary treatment—A review, *Science of the Total Environment*, 429 (2012) 123. <https://doi.org/10.1016/j.scitotenv.2012.04.028>
- [8] R.J. Hamilton, *Tarascon Pocket Pharmacopoeia 2015 Deluxe Lab-Coat Edition*, Jones & Bartlett Learning, LLC, 2015.
- [9] World Health Organization (WHO), Guidelines for registration of fixed-dose combination medicinal products. Technical Report Series, 2005. https://www.gmp-compliance.org/files/guidemgr/WHO_TRS_929_annex5.pdf (last accessed on 11/11/2022).
- [10] B. Bortone, C. Jackson, Y. Hsia, J. Bielicki, N. Magrini, M. Sharland, High global consumption of potentially inappropriate fixed dose combination antibiotics: Analysis of data from 75 countries, *PLOS ONE*, 16 (2021) e0241899. <https://doi.org/10.1371/journal.pone.0241899>

- [11] D. Bakdach, R. Elajej, Trimethoprim–Sulfamethoxazole: new lessons on an old antimicrobial; a retrospective analysis, *Journal of Pharmaceutical Health Services Research*, 11 (2020) 269. <https://doi.org/10.1111/jphs.12358>
- [12] WHO model list of essential medicines - 21st list, 2019. <https://www.who.int/publications/i/item/WHOMVPEMPIAU2019.06> (last accessed on 07/10/2022)
- [13] S.H. Zinner, K.H. Mayer, 33 - Sulfonamides and Trimethoprim, in: J.E. Bennett, R. Dolin, M.J. Blaser (Eds.) *Mandell, Douglas, and Bennett's Principles and Practice of Infectious Diseases (Eighth Edition)*, W.B. Saunders, Philadelphia, 2015, pp. 410.
- [14] S.R. Bushby, G.H. Hitchings, Trimethoprim, a sulphonamide potentiator, *British Journal of Pharmacology and Chemotherapy*, 33 (1968) 72. <https://doi.org/10.1111/j.1476-5381.1968.tb00475.x>
- [15] C.D. Wan, J.B. Zhou, Y.P. Song, X.J. Zou, Y.Q. Ma, Pathogens of prostatitis and their drug resistance: an epidemiological survey, *National Journal of Andrology*, 19 (2013) 912. (DOI not found)
- [16] K. Gupta, T.M. Hooton, K.G. Naber, B. Wullt, R. Colgan, L.G. Miller, G.J. Moran, L.E. Nicolle, R. Raz, A.J. Schaeffer, D.E. Soper, International Clinical Practice Guidelines for the treatment of acute uncomplicated cystitis and pyelonephritis in women: a 2010 update by the infectious diseases society of America and the European society for microbiology and infectious diseases, *Clinical Infectious Diseases*, 52 (2011) e103. <https://doi.org/10.1093/cid/ciq257>
- [17] M.E. Stryjewski, H.F. Chambers, Skin and soft-tissue infections caused by community-acquired methicillin-resistant *Staphylococcus aureus*, *Clinical Infectious Diseases*, 46 (2008) S368. <https://doi.org/10.1086/533593>
- [18] S.Y. Tong, R.M. Andrews, T. Kearns, R. Gundjirryirr, M.I. McDonald, B.J. Currie, J.R. Carapetis, Trimethopim-sulfamethoxazole compared with benzathine penicillin for treatment of impetigo in aboriginal children: a pilot randomised controlled trial, *Journal of Paediatrics and Child Health*, 46 (2010) 131. <https://doi.org/10.1111/j.1440-1754.2010.01697.x>
- [19] G.R. Schmitz, D. Bruner, R. Pitotti, C. Olderog, T. Livengood, J. Williams, K. Huebner, J. Lightfoot, B. Ritz, C. Bates, M. Schmitz, M. Mete, G. Deye, Randomized controlled trial of trimethoprim-sulfamethoxazole for uncomplicated skin abscesses in patients at risk for community-associated methicillin-resistant *Staphylococcus aureus*

- infection, *Annals of Emergency Medicine*, 56 (2010) 283. <https://doi.org/10.1016/j.annemergmed.2010.03.002>
- [20] T.R. Kemnic, M. Coleman, Trimethoprim Sulfamethoxazole, StatPearls, StatPearls Publishing Copyright © 2022, StatPearls Publishing LLC., Treasure Island (FL), 2022.
- [21] M. Falcon, C. Iberico, F. Guerra, I. Reyes, E. Felix, M. Flores, J. de Los Ríos, M.E. Diaz, A. Casas, S. Sanchez-Gambetta, R. Carrasco, A pilot study of safety of sulfamethoxazole, trimethoprim and guaifenesin in pediatric and adult patients with acute bronchitis, *BMC Research Notes*, 12 (2019) 119. <https://doi.org/10.1186/s13104-019-4150-2>
- [22] S. Nouira, S. Marghli, L. Besbes, R. Boukef, M. Daami, N. Nciri, S. Elatrous, F. Abroug, Standard versus newer antibacterial agents in the treatment of severe acute exacerbation of chronic obstructive pulmonary disease: a randomized trial of trimethoprim-sulfamethoxazole versus ciprofloxacin, *Clinical Infectious Diseases*, 51 (2010) 143. <https://doi.org/10.1086/653527>
- [23] R.B. Weyant, D. Kabbani, K. Doucette, C. Lau, C. Cervera, *Pneumocystis jirovecii*: a review with a focus on prevention and treatment, *Expert Opinion on Pharmacotherapy*, 22 (2021) 1579. <https://doi.org/10.1080/14656566.2021.1915989>
- [24] N. Kraupner, S. Ebmeyer, M. Hutinel, J. Fick, C.-F. Flach, D.G.J. Larsson, Selective concentrations for trimethoprim resistance in aquatic environments, *Environment International*, 144 (2020) 106083. <https://doi.org/10.1016/j.envint.2020.106083>
- [25] T.P. Van Boeckel, S. Gandra, A. Ashok, Q. Caudron, B.T. Grenfell, S.A. Levin, R. Laxminarayan, Global antibiotic consumption 2000 to 2010: an analysis of national pharmaceutical sales data, *The Lancet Infectious Diseases*, 14 (2014) 742. [https://doi.org/10.1016/s1473-3099\(14\)70780-7](https://doi.org/10.1016/s1473-3099(14)70780-7)
- [26] N.A. Haulisah, L. Hassan, S.K. Bejo, S.M. Jajere, N.I. Ahmad, High levels of antibiotic resistance in isolates from diseased livestock, *Frontiers in Veterinary Science*, 8 (2021) 1. <https://doi.org/10.3389/fvets.2021.652351>
- [27] S.A. Kools, A. Boxall, J.F. Moltmann, G. Bryning, J. Koschorreck, T. Knacker, A ranking of european veterinary medicines based on environmental risks, *Integrated Environmental Assessment and Management*, 4 (2008) 399. https://doi.org/10.1897/ieam_2008-002.1
- [28] R. Gothwal, T. Shashidhar, Antibiotic pollution in the environment: a review, *Clean-Soil Air Water*, 43 (2015) 479. <https://doi.org/10.1002/clen.201300989>

- [29] M.C. Danner, A. Robertson, V. Behrends, J. Reiss, Antibiotic pollution in surface fresh waters: occurrence and effects, *Science of the Total Environment*, 664 (2019) 793. <https://doi.org/10.1016/j.scitotenv.2019.01.406>
- [30] Q. Liu, M. Li, X. Liu, Q. Zhang, R. Liu, Z. Wang, X. Shi, J. Quan, X. Shen, F. Zhang, Removal of sulfamethoxazole and trimethoprim from reclaimed water and the biodegradation mechanism, *Frontiers of Environmental Science & Engineering*, 12 (2018) 6. <http://dx.doi.org/10.1007/s11783-018-1048-5>
- [31] A.C. Faleye, A.A. Adegoke, K. Ramluckan, J. Fick, F. Bux, T.A. Stenström, Concentration and reduction of antibiotic residues in selected wastewater treatment plants and receiving waterbodies in Durban, South Africa, *Science of the Total Environment*, 678 (2019) 10. <https://doi.org/10.1016/j.scitotenv.2019.04.410>
- [32] C.-F. Flach, M. Genheden, J. Fick, D.G. Joakim Larsson, A comprehensive screening of *Escherichia coli* isolates from Scandinavia's largest sewage treatment plant indicates no selection for antibiotic resistance, *Environmental Science & Technology*, 52 (2018) 11419. <https://doi.org/10.1021/acs.est.8b03354>
- [33] C.G.B. Brenner, C.A. Mallmann, D.R. Arsand, F.M. Mayer, A.F. Martins, Determination of sulfamethoxazole and trimethoprim and their metabolites in hospital effluent, *CLEAN – Soil, Air, Water*, 39 (2011) 28. <https://doi.org/10.1002/clen.201000162>
- [34] G.A. Khan, B. Berglund, K.M. Khan, P.-E. Lindgren, J. Fick, Occurrence and abundance of antibiotics and resistance genes in rivers, canal and near drug formulation facilities – A study in Pakistan, *PLOS ONE*, 8 (2013) e62712. <https://doi.org/10.1371/journal.pone.0062712>
- [35] B. Li, T. Zhang, Biodegradation and adsorption of antibiotics in the activated sludge process, *Environmental Science & Technology*, 44 (2010) 3468. <https://doi.org/10.1021/es903490h>
- [36] D. Dolphin, T.G. Traylor, L.Y. Xie, Polyhaloporphyrins: unusual ligands for metals and metal-catalyzed oxidations, *Accounts of Chemical Research*, 30 (1997) 251. <https://doi.org/10.1021/Ar960126u>
- [37] A.M.D.R. Gonsalves, M.M. Pereira, State of the art in the development of biomimetic oxidation catalysts, *Journal of Molecular Catalysis A-Chemical*, 113 (1996) 209. [https://doi.org/10.1016/S1381-1169\(96\)00050-7](https://doi.org/10.1016/S1381-1169(96)00050-7)
- [38] E.G. Azenha, A.C. Serra, M. Pineiro, M.M. Pereira, J.S. de Melo, L.G. Arnaut, S.J. Formosinho, A.M.D.R. Gonsalves, Heavy-atom effects on metalloporphyrins and

- polyhalogenated porphyrins, *Chemical Physics*, 280 (2002) 177. [https://doi.org/10.1016/S0301-0104\(02\)00485-8](https://doi.org/10.1016/S0301-0104(02)00485-8)
- [39] S.L.H. Rebelo, M.M. Pereira, M.M.Q. Simoes, M.G.P.M.S. Neves, J.A.S. Cavaleiro, Mechanistic studies on metalloporphyrin epoxidation reactions with hydrogen peroxide: evidence for two active oxidative species, *Journal of Catalysis*, 234 (2005) 76. <https://doi.org/10.1016/j.jcat.2005.05.026>
- [40] J. Haber, L. Matachowski, K. Pamin, J. Poltowicz, The effect of peripheral substituents in metalloporphyrins on their catalytic activity in Lyons system, *Journal of Molecular Catalysis A: Chemical*, 198 (2003) 215. [https://doi.org/10.1016/S1381-1169\(02\)00688-X](https://doi.org/10.1016/S1381-1169(02)00688-X)
- [41] S.M.A. Pinto, C.S. Vinagreiro, V.A. Tomé, G. Piccirillo, L. Damas, M.M. Pereira, Nitrobenzene method: A keystone in meso-substituted halogenated porphyrin synthesis and applications, 23 (2019) 329. <https://doi.org/10.1142/s1088424619300039>
- [42] P. Rothmund, Formation of porphyrins from pyrrole and aldehydes, *Journal of the American Chemical Society*, 57 (1935) 2010. <https://doi.org/10.1021/ja01313a510>
- [43] A.D. Adler, F.R. Longo, F. Kampas, J. Kim, On preparation of metalloporphyrins, *Journal of Inorganic & Nuclear Chemistry*, 32 (1970) 2443. [https://doi.org/10.1016/0022-1902\(70\)80535-8](https://doi.org/10.1016/0022-1902(70)80535-8)
- [44] J.S. Lindsey, H.C. Hsu, I.C. Schreiman, Synthesis of tetraphenylporphyrins under very mild conditions, *Tetrahedron Letters*, 27 (1986) 4969. [https://doi.org/10.1016/S0040-4039\(00\)85109-6](https://doi.org/10.1016/S0040-4039(00)85109-6)
- [45] J.S. Lindsey, I.C. Schreiman, H.C. Hsu, P.C. Kearney, A.M. Marguerettaz, Rothmund and Adler-Longo reactions revisited: synthesis of tetraphenylporphyrins under equilibrium conditions, *The Journal of Organic Chemistry*, 52 (1987) 827. <https://doi.org/10.1021/jo00381a022>
- [46] A.M.D.R. Gonsalves, J.M.T.B. Varejão, M.M. Pereira, Some new aspects related to the synthesis of meso-substituted porphyrins, *Journal of Heterocyclic Chemistry*, 28 (1991) 635. <https://doi.org/10.1002/jhet.5570280317>
- [47] M. Silva, A. Fernandes, S.S. Bebiano, M.J.F. Calvete, M.F. Ribeiro, H.D. Burrows, M.M. Pereira, Size and ability do matter! Influence of acidity and pore size on the synthesis of hindered halogenated meso-phenyl porphyrins catalysed by porous solid oxides, *Chemical Communications*, 50 (2014) 6571. <https://doi.org/10.1039/c4cc01100g>

- [48] C.A. Henriques, S.M.A. Pinto, G.L.B. Aquino, M. Pineiro, M.J.F. Calvete, M.M. Pereira, Ecofriendly porphyrin synthesis by using water under microwave irradiation, *ChemSusChem*, 7 (2014) 2821. <https://doi.org/10.1002/cssc.201402464>
- [49] J.L. Bolton, M.A. Trush, T.M. Penning, G. Dryhurst, T.J. Monks, Role of quinones in toxicology, *Chemical Research in Toxicology*, 13 (2000) 135. <https://doi.org/10.1021/tx9902082>
- [50] A.M.D.R. Gonsalves, R.A.W. Johnstone, M.M. Pereira, A.M.P. deSantAna, A.C. Serra, A.J.F.N. Sobral, P.A. Stocks, New procedures for the synthesis and analysis of 5,10,15,20-tetrakis(sulphophenyl)porphyrins and derivatives through chlorosulphonation, *Heterocycles*, 43 (1996) 829. <https://doi.org/10.3987/COM-95-7372>
- [51] C.J.P. Monteiro, M.M. Pereira, S.M.A. Pinto, A.V.C. Simoes, G.F.F. Sa, L.G. Arnaut, S.J. Formosinho, S. Simoes, M.F. Wyatt, Synthesis of amphiphilic sulfonamide halogenated porphyrins: MALDI-TOFMS characterization and evaluation of 1-octanol/water partition coefficients, *Tetrahedron*, 64 (2008) 5132. <https://doi.org/10.1016/j.tet.2008.03.055>
- [52] T.P. Wijesekera, D. Dolphin, Synthetic aspects of porphyrin and metalloporphyrin chemistry, in: R. Sheldon (Ed.) *Metalloporphyrins in Catalytic Oxidations*, Marcel Dekker, Inc., New York, 1994, pp. 193.
- [53] J.R. Platt, Molecular orbital predictions of organic spectra, 18 (1950) 1168. <https://di.org/10.1063/1.1747906>
- [54] A. Giraudeau, H.J. Callot, J. Jordan, I. Ezhar, M. Gross, Substituent effects in the electroreduction of porphyrins and metalloporphyrins, *Journal of the American Chemical Society*, 101 (1979) 3857. <https://doi.org/10.1021/ja00508a024>
- [55] L.J. Boucher, Manganese porphyrin complexes. III. Spectroscopy of chloroquo complexes of several porphyrins, *Journal of the American Chemical Society*, 92 (1970) 2725. <https://doi.org/10.1021/ja00712a024>
- [56] L. Fernandez, V.I. Esteves, A. Cunha, R.J. Schneider, J.P.C. Tome, Photodegradation of organic pollutants in water by immobilized porphyrins and phthalocyanines, *Journal of Porphyrins and Phthalocyanines*, 20 (2016) 150. <https://doi.org/10.1142/s108842461630007x>
- [57] M.L. Marin, L. Santos-Juanes, A. Arques, A.M. Amat, M.A. Miranda, Organic photocatalysts for the oxidation of pollutants and model compounds, *Chemical Reviews*, 112 (2012) 1710. <https://doi.org/10.1021/cr2000543>

- [58] G. Lofrano, R. Pedrazzani, G. Libralato, M. Carotenuto, Advanced oxidation processes for antibiotics removal: a review, *Current Organic Chemistry*, 21 (2017) 1054. <https://doi.org/10.2174/1385272821666170103162813>
- [59] M.J.F. Calvete, G. Piccirillo, C.S. Vinagreiro, M.M. Pereira, Hybrid materials for heterogeneous photocatalytic degradation of antibiotics, *Coordination Chemistry Reviews*, 395 (2019) 63. <https://doi.org/10.1016/j.ccr.2019.05.004>
- [60] A.R.L. Ribeiro, N.F.F. Moreira, G.L. Puma, A.M.T. Silva, Impact of water matrix on the removal of micropollutants by advanced oxidation technologies, *Chemical Engineering Journal*, 363 (2019) 155. <https://doi.org/10.1016/j.cej.2019.01.080>
- [61] M.J.F. Calvete, M. Silva, M.M. Pereira, H.D. Burrows, Inorganic helping organic: recent advances in catalytic heterogeneous oxidations by immobilised tetrapyrrolic macrocycles in micro and mesoporous supports, *RSC Advances*, 3 (2013) 22774. <https://doi.org/10.1039/C3RA44038A>
- [62] S.L.H. Rebelo, M.M. Pereira, M.M.Q. Simões, M.G.P.M.S. Neves, J.A.S. Cavaleiro, Mechanistic studies on metalloporphyrin epoxidation reactions with hydrogen peroxide: evidence for two active oxidative species, *Journal of Catalysis*, 234 (2005) 76. <https://doi.org/10.1016/j.jcat.2005.05.026>
- [63] A. Ali, W. Akram, H.-Y. Liu, Reactive cobalt–oxo complexes of tetrapyrrolic macrocycles and N-based ligand in oxidative transformation reactions, *Molecules*, 24 (2019) 78. <https://doi.org/10.3390/molecules24010078>
- [64] I.K. Konstantinou, T.A. Albanis, Photocatalytic transformation of pesticides in aqueous titanium dioxide suspensions using artificial and solar light: intermediates and degradation pathways, *Applied Catalysis B: Environmental*, 42 (2003) 319. [https://doi.org/10.1016/S0926-3373\(02\)00266-7](https://doi.org/10.1016/S0926-3373(02)00266-7)
- [65] X.-J. Wen, C.-G. Niu, L. Zhang, C. Liang, G.-M. Zeng, A novel Ag₂O/CeO₂ heterojunction photocatalysts for photocatalytic degradation of enrofloxacin: possible degradation pathways, mineralization activity and an in depth mechanism insight, *Applied Catalysis B: Environmental*, 221 (2018) 701. <https://doi.org/10.1016/j.apcatb.2017.09.060>
- [66] M.J.F. Calvete, M. Piñeiro, L.D. Dias, M.M. Pereira, Hydrogen peroxide and metalloporphyrins in oxidation catalysis: old dogs with some new tricks, *ChemCatChem*, 10 (2018) 3615. <https://doi.org/10.1002/cctc.201800587>
- [67] C.-H. Yan, Z.-G. Xu, T. Zhu, Z.-M. Wang, F.-X. Cheng, Y.-H. Huang, C.-S. Liao, A large low field colossal magnetoresistance in the La_{0.7}Sr_{0.3}MnO₃ and CoFe₂O₄

- combined system, *Journal of Applied Physics*, 87 (2000) 5588. <https://doi.org/10.1063/1.372459>
- [68] V. Polshettiwar, R. Luque, A. Fihri, H. Zhu, M. Bouhrara, J.-M. Basset, Magnetically recoverable nanocatalysts, *Chemical Reviews*, 111 (2011) 3036. <https://doi.org/10.1021/cr100230z>
- [69] M.B. Gawande, P.S. Branco, R.S. Varma, Nano-magnetite (Fe₃O₄) as a support for recyclable catalysts in the development of sustainable methodologies, *Chemical Society Reviews*, 42 (2013) 3371. <https://doi.org/10.1039/C3CS35480F>
- [70] J. Kudr, Y. Haddad, L. Richtera, Z. Heger, M. Cernak, V. Adam, O. Zitka, Magnetic nanoparticles: from design and synthesis to real world applications, *Nanomaterials*, 7 (2017) 243. <https://doi.org/10.3390/nano7090243>
- [71] K.L. Ameta, A. Penoni, Application of silica based heterogeneous catalyst for the synthesis of bioactive heterocycles, *Heterogeneous Catalysis 2014*, pp. 163.
- [72] A. Erigoni, U. Diaz, Porous silica-based organic-inorganic hybrid catalysts: a review, *Catalysts*, 11 (2021) 79. <https://doi.org/10.3390/catal11010079>
- [73] S. Nakagaki, G.K.B. Ferreira, A.L. Marcalb, K.J. Ciuffi, Metalloporphyrins immobilized on silica and modified silica as catalysts in heterogeneous processes, *Current Organic Synthesis*, 11 (2014) 67. <https://doi.org/10.2174/15701794113106660087>
- [74] M.J. Jacinto, P.K. Kiyohara, S.H. Masunaga, R.F. Jardim, L.M. Rossi, Recoverable rhodium nanoparticles: synthesis, characterization and catalytic performance in hydrogenation reactions, *Applied Catalysis A: General*, 338 (2008) 52. <https://doi.org/10.1016/j.apcata.2007.12.018>
- [75] L.M. Rossi, L.L.R. Vono, F.P. Silva, P.K. Kiyohara, E.L. Duarte, J.R. Matos, A magnetically recoverable scavenger for palladium based on thiol-modified magnetite nanoparticles, *Applied Catalysis A: General*, 330 (2007) 139. <https://doi.org/10.1016/j.apcata.2007.07.018>
- [76] D.K. Yi, S.S. Lee, G.C. Papaefthymiou, J.Y. Ying, Nanoparticle architectures templated by SiO₂/Fe₂O₃ nanocomposites, *Chemistry of Materials*, 18 (2006) 614. <https://doi.org/10.1021/cm0512979>
- [77] K.C. Vrancken, L. De Coster, P. Van Der Voort, P.J. Grobet, E.F. Vansant, The role of silanols in the modification of silica gel with aminosilanes, *Journal of Colloid and Interface Science*, 170 (1995) 71. <https://doi.org/10.1006/jcis.1995.1073>
- [78] L.D. Dias, R.M.B. Carrilho, C.A. Henriques, M.J.F. Calvete, A.M. Masdeu-Bultó, C. Claver, L.M. Rossi, M.M. Pereira, Hybrid metalloporphyrin magnetic nanoparticles as

- catalysts for sequential transformation of alkenes and CO₂ into cyclic carbonates, 10 (2018) 2792. <https://doi.org/10.1002/cctc.201800397>
- [79] H. Guenzler, H.U. Gremlich, IR spectroscopy an introduction, Wiley-VCH, Germany, 2002.
- [80] G.A.K. Anquandah, V.K. Sharma, D.A. Knight, S.R. Batchu, P.R. Gardinali, Oxidation of trimethoprim by ferrate(VI): kinetics, products, and antibacterial activity, *Environmental Science & Technology*, 45 (2011) 10575. <https://doi.org/10.1021/es202237g>
- [81] Y. Liu, H. Guo, Y. Zhang, X. Cheng, P. Zhou, J. Deng, J. Wang, W. Li, Highly efficient removal of trimethoprim based on peroxymonosulfate activation by carbonized resin with Co doping: Performance, mechanism and degradation pathway, *Chemical Engineering Journal*, 356 (2019) 717. <https://doi.org/10.1016/j.cej.2018.09.086>
- [82] X. Luo, Z. Zheng, J. Greaves, W.J. Cooper, W. Song, Trimethoprim: kinetic and mechanistic considerations in photochemical environmental fate and AOP treatment, *Water Research*, 46 (2012) 1327. <https://doi.org/10.1016/j.watres.2011.12.052>
- [83] K.S. Jewell, S. Castronovo, A. Wick, P. Falas, A. Joss, T.A. Ternes, New insights into the transformation of trimethoprim during biological wastewater treatment, *Water Research*, 88 (2016) 550. <https://doi.org/10.1016/j.watres.2015.10.026>
- [84] R.C. Zhang, Y.K. Yang, C.H. Huang, N. Li, H. Liu, L. Zhao, P.Z. Sun, UV/H₂O₂ and UV/PDS treatment of trimethoprim and sulfamethoxazole in synthetic human urine: transformation products and toxicity, *Environmental Science & Technology*, 50 (2016) 2573. <https://doi.org/10.1021/acs.est.5b05604>
- [85] S.W. Yan, W.H. Song, Photo-transformation of pharmaceutically active compounds in the aqueous environment: a review, *Environmental Science-Processes & Impacts*, 16 (2014) 697. <https://doi.org/10.1039/c3em00502j>
- [86] A. Abou-Eisha, A. Creus, R. Marcos, Genotoxic evaluation of the antimicrobial drug, trimethoprim, in cultured human lymphocytes, *Mutation Research-Genetic Toxicology and Environmental Mutagenesis*, 440 (1999) 157. [https://doi.org/10.1016/S1383-5718\(99\)00022-4](https://doi.org/10.1016/S1383-5718(99)00022-4)
- [87] A. Binelli, D. Cogni, M. Parolini, C. Riva, A. Provini, Cytotoxic and genotoxic effects of in vitro exposure to Triclosan and Trimethoprim on zebra mussel (*Dreissena polymorpha*) hemocytes, *Comparative Biochemistry and Physiology C-Toxicology & Pharmacology*, 150 (2009) 50. <https://doi.org/10.1016/j.cbpc.2009.02.005>

- [88] C. Sirtori, A. Agüera, W. Gernjak, S. Malato, Effect of water-matrix composition on Trimethoprim solar photodegradation kinetics and pathways, *Water Research*, 44 (2010) 2735. <https://doi.org/10.1016/j.watres.2010.02.006>
- [89] J. Kuang, J. Huang, B. Wang, Q. Cao, S. Deng, G. Yu, Ozonation of trimethoprim in aqueous solution: identification of reaction products and their toxicity, *Water Research*, 47 (2013) 2863. <https://doi.org/10.1016/j.watres.2013.02.048>
- [90] M. Borecka, A. Białk-Bielińska, P. Haliński Ł, K. Pazdro, P. Stepnowski, S. Stolte, The influence of salinity on the toxicity of selected sulfonamides and trimethoprim towards the green algae *Chlorella vulgaris*, *Journal of Hazardous Materials*, 308 (2016) 179. <https://doi.org/10.1016/j.jhazmat.2016.01.041>
- [91] B. Kolar, L. Arnuš, B. Jeretin, A. Gutmaher, D. Drobne, M.K. Durjava, The toxic effect of oxytetracycline and trimethoprim in the aquatic environment, *Chemosphere*, 115 (2014) 75. <https://doi.org/10.1016/j.chemosphere.2014.02.049>
- [92] M. Dalla Bona, R. Zounková, R. Merlanti, L. Blaha, M. De Liguoro, Effects of enrofloxacin, ciprofloxacin, and trimethoprim on two generations of *Daphnia magna*, *Ecotoxicology and Environmental Safety*, 113 (2015) 152. <https://doi.org/10.1016/j.ecoenv.2014.11.018>
- [93] E.C. de Vasconcelos, C.R. Dalke, C.M.R. de Oliveira, Influence of select antibiotics on *Vibrio fischeri* and *Desmodesmus subspicatus* at $\mu\text{g L}^{-1}$ concentrations, *Environmental Management*, 60 (2017) 157. <https://doi.org/10.1007/s00267-017-0841-4>
- [94] Standard test methods for determining sediment concentration in water samples, ASTM D3977-97, ASTM International, West Conshohocken, PA, 2002.
- [95] S. Park, K. Choi, Hazard assessment of commonly used agricultural antibiotics on aquatic ecosystems, *Ecotoxicology*, 17 (2008) 526. <https://doi.org/10.1007/s10646-008-0209-x>
- [96] L. Santos, A.N. Araújo, A. Fachini, A. Pena, C. Delerue-Matos, M. Montenegro, Ecotoxicological aspects related to the presence of pharmaceuticals in the aquatic environment, *Journal of Hazardous Materials*, 175 (2009) 45. <https://doi.org/10.1016/j.jhazmat.2009.10.100>
- [97] OECD, Test No. 201: freshwater alga and cyanobacteria, growth inhibition test, OECD guidelines for the testing of chemicals, Section 2, OECD Publishing, Paris, (2011) <https://doi.org/10.1787/9789264069923-en> (last accessed on 08/10/2022)
- [98] G.o. CANADA, Biological test method: growth inhibition test using a freshwater alga, 2nd edition, (2007) - March. <https://www.canada.ca/en/environment-climate->

- change/services/wildlife-research-landscape-science/biological-test-method-publications/growth-inhibition-test-freshwater-alga.html (last accessed on 08/10/2022)
- [99] R. Rosa, M. Moreira-Santos, I. Lopes, L. Silva, J. Rebola, E. Mendonca, A. Picado, R. Ribeiro, Comparison of a test battery for assessing the toxicity of a bleached-kraft pulp mill effluent before and after secondary treatment implementation, *Environmental Monitoring and Assessment*, 161 (2010) 439. <https://doi.org/10.1007/s10661-009-0759-2>
- [100] ROTOXKIT F - Rotifer toxicity screening test for freshwater_STANDARD OPERATING PROCEDURE. https://www.microbiotests.com/wp-content/uploads/2019/07/freshwater-rotifer-toxicity-test_rotokit-f_standard-operating-procedure.pdf (last accessed on 08/10/2022)
- [101] Software PriProbit 1.63_ <http://bru.gmprc.ksu.edu/proj/priprobit/download.asp> (last accessed on 08/11/2022)
- [102] H. Sanderson, M. Thomsen, Comparative analysis of pharmaceuticals versus industrial chemicals acute aquatic toxicity classification according to the United Nations classification system for chemicals. Assessment of the (Q)SAR predictability of pharmaceuticals acute aquatic toxicity and their predominant acute toxic mode-of-action, *Toxicology Letters*, 187 (2009) 84. <https://doi.org/10.1016/j.toxlet.2009.02.003>
- [103] B. Kolar, L. Arnuš, B. Jeretin, A. Gutmaher, D. Drobne, M. Kos Durjava, The toxic effect of oxytetracycline and trimethoprim in the aquatic environment, *Chemosphere*, 115 (2014) 75. <https://doi.org/10.1016/j.chemosphere.2014.02.049>
- [104] H. Sugimoto, H. Ohshima, S. Inoue, Alternating copolymerization of carbon dioxide and epoxide by manganese porphyrin: the first example of polycarbonate synthesis from 1-atm carbon dioxide, *Journal of Polymer Science Part a-Polymer Chemistry*, 41 (2003) 3549. <https://doi.org/10.1002/pola.10835>
- [105] E. Linley, S.P. Denyer, G. McDonnell, C. Simons, J.Y. Maillard, Use of hydrogen peroxide as a biocide: new consideration of its mechanisms of biocidal action, *Journal of Antimicrobial Chemotherapy*, 67 (2012) 1589. <https://doi.org/10.1093/jac/dks129>
- [106] Photochemical Reactors Ltd. <http://www.photochemicalreactors.co.uk/> (last accessed on 11/08/2022)
- [107] M. Gaeta, D. Raciti, R. Randazzo, C.M.A. Gangemi, A. Raudino, A. D'Urso, M.E. Fragalà, R. Purrello, Chirality enhancement of porphyrin supramolecular assembly driven

- by a template preorganization effect, *Angewandte Chemie*, 57 (2018) 10656. <https://doi.org/10.1002/anie.201806192>
- [108] G. Magna, D. Monti, C. Di Natale, R. Paolesse, M. Stefanelli, The assembly of porphyrin systems in well-defined nanostructures: an update, *Molecules*, 24 (2019) 4307. <https://doi.org/10.3390/molecules24234307>
- [109] N. Maldonado-Carmona, T.S. Ouk, M.J.F. Calvete, M.M. Pereira, N. Villandier, S. Leroy-Lhez, Conjugating biomaterials with photosensitizers: advances and perspectives for photodynamic antimicrobial chemotherapy, *Photochemical & Photobiological Sciences*, 19 (2020) 445. <https://doi.org/10.1039/c9pp00398c>
- [110] A. Naeimi, M. Honarmand, O. Jawhid, Iron porphyrin immobilized on cellulose extracted from *Sesbania Sesban* plant: a novel eco-friendly and cost-effective catalyst for green oxidation of organic compounds, *Cellulose Chemistry and Technology*, 52 (2018) 343. [https://www.cellulosechemtechnol.ro/pdf/CCT5-6\(2018\)/p.%20343-351.pdf](https://www.cellulosechemtechnol.ro/pdf/CCT5-6(2018)/p.%20343-351.pdf)
- [111] Y.Y. Chu, Z.X. Huang, K. Liang, J. Guo, C. Boyer, J.T. Xu, A photocatalyst immobilized on fibrous and porous monolithic cellulose for heterogeneous catalysis of controlled radical polymerization, *Polymer Chemistry*, 9 (2018) 1666. <https://doi.org/10.1039/c7py01690e>
- [112] G. Huang, C.C. Guo, S.S. Tang, Catalysis of cyclohexane oxidation with air using various chitosan-supported metallotetraphenylporphyrin complexes, *Journal of Molecular Catalysis A-Chemical*, 261 (2007) 125. <https://doi.org/10.1016/j.molcata.2006.08.014>
- [113] N.A. Aksenova, V.A. Timofeeva, S.Z. Rogovina, P.S. Timashev, N.N. Glagolev, A.B. Solov'eva, Photocatalytic properties and structure of chitosan-based porphyrin-containing systems, *Polymer Science Series B*, 52 (2010) 67. <https://doi.org/10.1134/s1560090410010100>
- [114] K. Venkatesan Savunthari, D. Arunagiri, S. Shanmugam, S. Ganesan, M.V. Arasu, N.A. Al-Dhabi, N.T.L. Chi, V.K. Ponnusamy, Green synthesis of lignin nanorods/g-C₃N₄ nanocomposite materials for efficient photocatalytic degradation of triclosan in environmental water, *Chemosphere*, 272 (2021) 129801. <https://doi.org/10.1016/j.chemosphere.2021.129801>
- [115] M. Penas-Garzon, A. Gomez-Aviles, C. Belver, J.J. Rodriguez, J. Bedia, Degradation pathways of emerging contaminants using TiO₂-activated carbon heterostructures in aqueous solution under simulated solar light, *Chemical Engineering Journal*, 392 (2020) 124867. <https://doi.org/10.1016/j.cej.2020.124867>

- [116] N. Maldonado-Carmona, G. Marchand, N. Villandier, T.S. Ouk, M.M. Pereira, M.J.F. Calvete, C.A. Calliste, A. Zak, M. Piksa, K.J. Pawlik, K. Matczyszyn, S. Leroy-Lhez, Porphyrin-loaded lignin nanoparticles against bacteria: a photodynamic antimicrobial chemotherapy application, *Frontiers in Microbiology*, 11 (2020) 606185. <https://doi.org/10.3389/fmicb.2020.606185>
- [117] G. Marchand, C.A. Calliste, R.M. Williams, C. McLure, S. Leroy-Lhez, N. Villandier, Acetylated lignins: a potential bio-sourced photosensitizer, *Chemistryselect*, 3 (2018) 5512. <https://doi.org/10.1002/slct.201801039>
- [118] N. Maldonado-Carmona, T.S. Ouk, N. Villandier, C.A. Calliste, M.J.F. Calvete, M.M. Pereira, S. Leroy-Lhez, Photophysical and antibacterial properties of porphyrins encapsulated inside acetylated lignin nanoparticles, *Antibiotics*, 10 (2021) 513. <https://doi.org/10.3390/antibiotics10050513>
- [119] G. Marchand, G. Fabre, N. Maldonado-Carmona, N. Villandier, S. Leroy-Lhez, Acetylated lignin nanoparticles as a possible vehicle for photosensitizing molecules, *Nanoscale Advances*, 2 (2020) 5648. <https://doi.org/10.1039/D0NA00615G>
- [120] S. Leroy-Lhez, O. Rezazgui, M. Issawi, M. Elhabiri, C.A. Calliste, C. Riou, Why are the anionic porphyrins so efficient to induce plant cell death? A structure-activity relationship study to solve the puzzle, *Journal of Photochemistry and Photobiology A: Chemistry*, 368 (2019) 276. <https://doi.org/10.1016/j.jphotochem.2018.09.050>
- [121] M. Zannotti, R. Giovannetti, B. Minofar, D. Řeha, L. Plačková, C.A. D'Amato, E. Rommozzi, H.V. Dudko, N. Kari, M. Minicucci, Aggregation and metal-complexation behaviour of THPP porphyrin in ethanol/water solutions as function of pH, *Spectrochimica Acta Part A: Molecular and Biomolecular Spectroscopy*, 193 (2018) 235. <https://doi.org/10.1016/j.saa.2017.12.021>
- [122] C.C. Ryan, D.T. Tan, W.A. Arnold, Direct and indirect photolysis of sulfamethoxazole and trimethoprim in wastewater treatment plant effluent, *Water Research*, 45 (2011) 1280. <https://doi.org/10.1016/j.watres.2010.10.005>
- [123] S.K. Alharbi, J.G. Kang, L.D. Nghiem, J.P. van de Merwe, F.D.L. Leusch, W.E. Price, Photolysis and UV/H₂O₂ of diclofenac, sulfamethoxazole, carbamazepine, and trimethoprim: Identification of their major degradation products by ESI-LC-MS and assessment of the toxicity of reaction mixtures, *Process Safety and Environmental Protection*, 112 (2017) 222. <https://doi.org/10.1016/j.psep.2017.07.015>

- [124] H. Gong, W. Chu, Photodegradation of sulfamethoxazole with a recyclable catalyst, *Industrial & Engineering Chemistry Research*, 54 (2015) 12763. <https://doi.org/10.1021/acs.iecr.5b03849>
- [125] M.J. Lima, A.M.T. Silva, C.G. Silva, J.L. Faria, J.C.B. Lopes, M.M. Dias, An innovative static mixer photoreactor: proof of concept, *Chemical Engineering Journal*, 287 (2016) 419. <https://doi.org/10.1016/j.cej.2015.09.092>
- [126] M.J. Lima, C.G. Silva, A.M.T. Silva, J.C.B. Lopes, M.M. Dias, J.L. Faria, Homogeneous and heterogeneous photo-Fenton degradation of antibiotics using an innovative static mixer photoreactor, *Chemical Engineering Journal*, 310 (2017) 342. <https://doi.org/10.1016/j.cej.2016.04.032>
- [127] A. Kutuzova, T. Dontsova, W. Kwapinski, Application of TiO₂-based photocatalysts to antibiotics degradation: cases of sulfamethoxazole, trimethoprim and ciprofloxacin, *Catalysts*, 11 (2021) 728. <https://doi.org/10.3390/catal11060728>
- [128] C. Eckers, J.J. Monaghan, J.-C. Wolff, Fragmentation of trimethoprim and other compounds containing alkoxy-phenyl groups in electrospray ionisation tandem mass spectrometry, *European Journal of Mass Spectrometry*, 11 (2005) 73. <https://doi.org/10.1255/ejms.719>
- [129] J. Yang, G. Lv, C. Zhang, Z. Wang, X. Sun, Indirect photodegradation of sulfamethoxazole and trimethoprim by hydroxyl radicals in aquatic environment: mechanisms, transformation products and eco-toxicity evaluation, *International Journal of Molecular Sciences*, 21 (2020) 6276. <https://doi.org/10.3390/ijms21176276>

Chapter 3

Development, characterization and evaluation of TMP-based multicomponent solid forms

3.1 Introduction

The process of pharmaceutical solid forms development involves several steps before the commercialization of the final product [1]. As we have already mentioned in the introductory Chapter 1, the selection of co-formers, when aiming at multicomponent forms, is the key step in the design process. After identification of possible co-formers, the multicomponent solid forms screening is the subsequent stage. Regarding this, several methods are available and may be divided into solvent-based and solvent-free techniques [2]. These last ones are emerging in both academia and industry due to their compliance with the 12 Green Chemistry Principles [3] and the 17 Sustainable Development Goals by United Nations [4]. These principles recommend the use of more sustainable technologies with less toxic by-products and avoiding large amounts of hazardous solvents. In that regard, mechanochemistry has emerged as an attractive alternative to solution based methods in crystal engineering and supramolecular chemistry [5, 6]: physical form transformations are achieved through mechanical forces, favouring fractures and increasing the surface area, without solvents or using them only in traces [7-9]. Mechanochemistry has been the golden method for co-crystal and salt screening, and also for eutectic mixtures preparation [2, 10-12]. Taking this into account, we used a grinding method to develop new TMP solid-state forms, more precisely liquid assisted grinding (LAG) [13-15]. LAG and neat grinding (NG) are very similar techniques and consist in mixing stoichiometric amounts of solid-state individual components, particularly TMP and the co-former and grinding them manually or mechanically [2, 16, 17]. Evidently, the use of pestle and mortar does not guarantee reproducibility of the process. To overcome this issue, solid components are normally loaded into a mill, quite often a ball mill one, as used in our work. The main difference between LAG and NG is the complete absence of solvent in NG, whereas it is used in traces in LAG. Nevertheless, this residual amount of solvent is enough to improve the kinetics, as in fact it acts as a

catalyst increasing the conformational, vibrational and rotational degrees of freedom and increasing molecular collisions [18]. The grinding outcome of LAG has often a higher degree of crystallinity when compared to that of NG processes which, quite often, give rise to amorphous phases.

The principal goal of the work presented in this chapter was the development of new multicomponent solid-state forms of TMP, a BCS Class II drug [19] (solubility of 0.4 mg mL^{-1} in water [20]), using mechanochemistry and several co-formers. The TMP tablets oral dosage is 100 mg every 12 h or 200 mg every 24 h, for 10 days. After oral administration, 10 to 20% is firstly metabolized in the liver and the residual portion is excreted unchanged [21]. This means that this remainder part, consisting of 80-90 %, will be released into the environment. Therefore, among the samples developed in this work, selected new solid forms are evaluated for their impact in TMP dissolution rate and/or antibacterial activity, in the pursuit of new candidate solid forms that can allow lowering TMP loads in solid drug products. Although the TMP-SMX combination is largely used, due to its low cost and its good action against common bacterial diseases, one of our intents is to enhance the TMP activity by using other cofomers as an alternative to SMX, to achieve the same therapeutic effect.

In literature, several research studies about the development of new multicomponent solids involving TMP as API have been reported. As an example, a series of salts have been developed such as TMP-nitrate [22], TMP-formate [23], TMP-maleate [24]. Egert and co-workers studied two co-crystals solvates, TMP+glutarimide and TMP+3,3-dimethylglutarimide by cocrystallization from DMSO and CH_3OH solutions, respectively [25]. They discovered that the structures involved three adjacent hydrogen bonds (one $\text{N-H}\cdots\text{N}$ and two $\text{N-H}\cdots\text{O}$) between the pyrimidine ring of TMP and the glutarimide imide group.

TMP salt hydrates or solvates [26-28] have also been reported as well as multidrug TMP-based co-crystals [29, 30], stability tests have also been carried out and the real efficacy of the new combinations in relation to the API evaluated. Concerning this, Bhattacharya *et al.* prepared, by LAG, three TMP based salts with mefenamic (TMP-MFA- H_2O), tolfenamic (TMP-TFA- H_2O) and flufenamic acids (TMP-FFA- H_2O), which are non-steroidal anti-inflammatory drugs [31]. After kinetic solubility tests, two of the three salt hydrates, TMP-MFA- H_2O and TMP-TFA- H_2O , showed an increase in solubility at pH 7.4, which consequently resulted in bioavailability enhancement when

compared to the reference APIs. Concerning multidrug co-crystals, in 2000 Bettinetti's group discovered two co-crystal structures between TMP and sulfamethoxypyridazine (SMPD): an anhydrous form (TMP-SMPD) and an hydrate one (TMP-SMPD-H₂O) [32]. After exposing the two crystals to humidity, authors concluded that the two forms were interconvertible.

Furthermore, several studies showed that new solid forms TMP-based led to an improvement in the antibacterial activity compared to the API [1, 32]. For instance, ElShaer *et al* developed salts with a 1:1 molar ratio between TMP and anionic amino acids, aspartic and glutamic, by lyophilization [33]. These salts showed a 280-fold improvement in solubility at acidic pH (~ 5). Additionally, authors compared the antibacterial activity of the two salts and TMP alone against *E. coli* and *Pseudomonas aeruginosa*. The salts revealed higher inhibition zone for *E. coli* but no activity against *P. aeruginosa*, probably due to its complex membrane structure.

As we mentioned before, the selection of the co-formers is crucial in the screening of API new solid-state forms. In this work, the co-formers were chosen in order to be able, *a priori*, to form reliable supramolecular heterosynthons with TMP, therefore having functional groups that are complementary to those of the API [34]. This is the most relevant starting point for co-crystal screening. Of course, acidic co-formers are important for TMP new salts screening. Even if supramolecular association will not be successful, eutectic mixtures are also of interest, in the context of our work. Therefore, we tried compounds belonging to the GRAS list and, besides the FDA approval, we also considered their great aqueous solubility, for instance for leucine (LEU), mannitol (MAN) and riboflavin (RIB). In addition, some of the chosen GRAS compounds were also selected due to their reported effects as antibacterial agents: uracil (URA) [35, 36], curcumin (CURC) [37], nicotinic acid (NIC) [38] and picolinic acid (PIC) [39]. Some APIs were also chosen as co-formers, in a potential dual-drug therapy perspective [40]. We tested acetaminophen (PARA), ibuprofen (IBU) mainly due to their massive use in the human daily life as analgesic, antipyretic and anti-inflammatory agents [41] as well as salicylic acid (SAL) and ciprofloxacin (CIP) (**Figure 3.1**). Paracetamol and ibuprofen have been pointed as bacterial growth inhibitor [42] and ciprofloxacin is a known antibiotic [43].

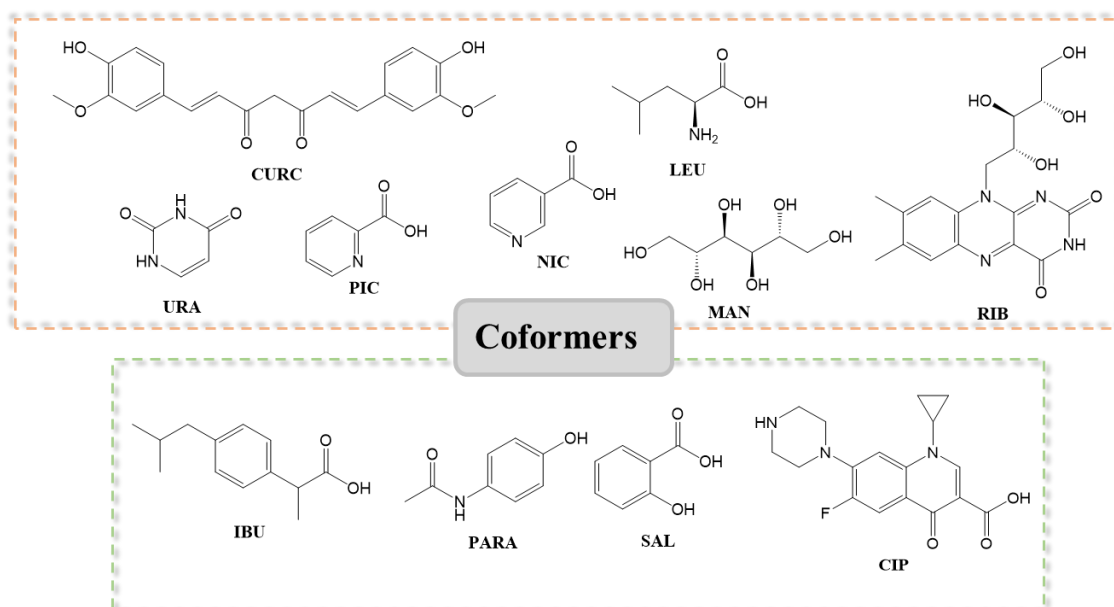


Figure 3.1 Structures of co-formers tested in TPM-based solid-state forms.

As already mentioned in Chapter 1, *in silico* approaches have been developed to try to predict the propensity of two compounds to associate in supramolecular crystalline forms, particularly in what concerns co-crystals. Up to now, none of the tools could give correct predictions in all investigated cases. Nevertheless, promising results have been reported using the COSMO-Quick software [44, 45]. This thermodynamic approach considers the intermolecular interaction between the target API and the potential co-former, in a specific stoichiometry, as the excess enthalpy, ΔH^{ex} , of an undercooled melt made up of the components. The molecular flexibility is also considered in the f_{fit} parameter that conjugates both ΔH^{ex} and the number of rotatable bonds in the compounds. A higher propensity for supramolecular association is expected if negative ΔH^{ex} and low f_{fit} values are obtained, although thresholds could not be established so far. The ΔH^{ex} and f_{fit} values obtained using COSMO-Quick, for TMP and the selected co-formers, in an equimolar ratio, are shown in Table 3.1. Negative ΔH^{ex} are observed, except for LEU, and the highest f_{fit} parameter is obtained for the combination of TMP with CURC, RIB, MAN and LEU, as expected.

Table 3.1. ΔH^{ex} and f_{fit} values obtained using COSMO-Quick, for TMP and the selected co-formers, in an equimolar ratio.

Cofomer	ΔH^{ex} (kcal mol⁻¹)	f_{fit}
SAL	-3.04623	2.05577
IBU	-1.87031	4.25209
NIC	-1.18164	3.41015
PARA	-1.10386	3.99814
CURC	-1.01694	7.65645
RIB	-0.78577	7.37743
MAN	-0.77937	8.40423
CIP	-0.26305	5.34915
PIC	-0.22054	4.37126
URA	-0.08226	3.99934
LEU	0.0691	6.1915

3.2 Screening, preparation and characterization of TMP-based multicomponent solid forms

In this work, we used a TMP commercial sample, purchased from Sigma-Aldrich, with a purity greater than 98%. A preliminary study of pure commercial TMP was carried out by DSC, FTIR and X-ray powder diffraction in the same experimental conditions used for the solid forms screening (**Figure 3.2 a-c**). Thus, in a typical experiment, ~ 70-80 mg of a total amount of individual compounds was placed into a 10 mL stainless-steel jar with two 7 mm balls. Then, 10 μL of dry ethanol were added to assist the grinding process accomplished at 30 Hz for 60 min.

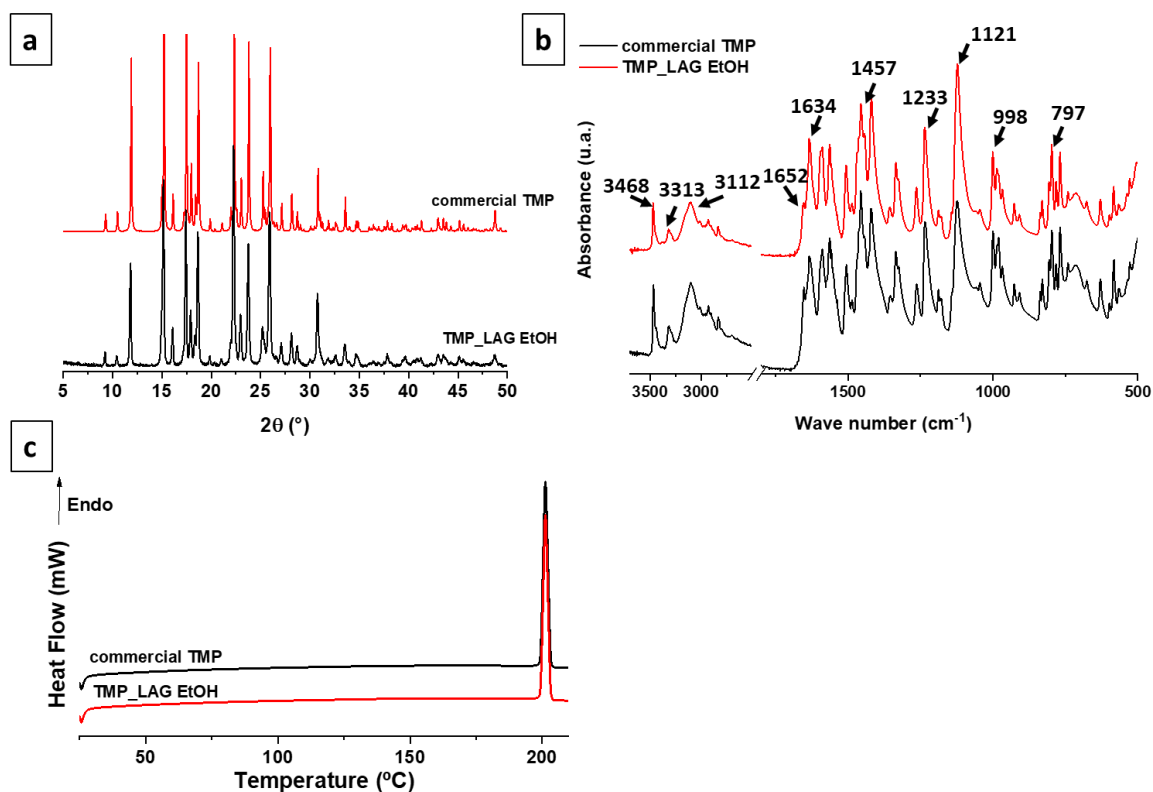


Figure 3.2 a) X-ray powder diffractograms of commercial TMP (red line) and after grinding, LAG EtOH (black line); b) FTIR spectra of commercial TMP (black line) and TMP after LAG EtOH (red line), registered between 3600 and 500 cm^{-1} ; c) Heating DSC curves of commercial TMP (black line) and TMP after LAG ethanol-assisted (red line), registered between 25 °C and 210 °C ($\beta = 10$ °C min^{-1}).

Diffractograms of commercial TMP and TMP after LAG experiments (**Figure 3.2 a**) agreed with literature [30, 46] corroborating the evidence that after grinding the API maintained the same polymorphic form, Form I, reported by Koetzle and co-workers [47] and deposited on the Cambridge Crystallographic Data Centre (CCDC, online database) with the reference nr 1102864.

This non-alteration of the crystalline form was also confirmed by IR spectroscopy (**Figure 3.2 b**). Indeed, the experimental FTIR spectra of the two samples recorded between 3600 and 500 cm^{-1} , are in agreement with the experimental results obtained by Ungurean *et al* [48]. Especially, the two characteristic bands at 3468 and 3313 cm^{-1} ascribed to stretching of amino group are visible. Then, the band between 3112 and 2600 cm^{-1} are related to the C-H stretching vibrations of methylene and methyl groups. In the other part of the spectra, we have the first two bands at 1652 and

1634 cm^{-1} attributed to the bending deformation of amino groups, whereas bands at 1457 and 1233 cm^{-1} are mainly ascribed to the bending vibrations of the amino groups and benzene ring, respectively. Additionally, an intense band is reported at 1121 cm^{-1} for the C-O stretching as well as that one registered at 998 cm^{-1} . Finally, the last TMP characteristic band is at 797 cm^{-1} and corresponds to the bending deformations of the pyrimidine ring. As expected, both TMP samples show the same thermal behaviour (**Figure 3.2 c**). A single event is observed in the heating DSC curve, corresponding to the fusion at $T_{\text{fus}} = (199.45 \pm 0.2) \text{ }^\circ\text{C}$, $\Delta_{\text{fus}}H = (48.8 \pm 0.6) \text{ kJ mol}^{-1}$.

3.2.1 Development of TMP-based multicomponent forms using GRAS compounds

The results of TMP multicomponent solid-form screening and development with GRAS substances are presented in this section.

- Trimethoprim-curcumin system

Our preliminary study started with the combination of TMP with CURC, one of the curcuminoids most abundant in nature and with promising features such as antioxidant, antibacterial, antiviral, anti-inflammatory [37]. CURC has two tautomeric forms, ketone and enol one and is structurally formed by two phenols connected by two α,β -unsaturated carbonyl groups. Despite its poor solubility in water ($\sim 0.8 \text{ } \mu\text{g mL}^{-1}$), Nangia and co-workers have already studied several co-crystal systems between CURC and other APIs demonstrating that an enhancement of solubility of the new association may occur comparing with pure CURC and/or API [49]. Its association with TMP is also of interest, due to the potential additive antibacterial effect.

TMP and CURC mixtures of different TMP molar fraction, x_{TMP} , 0.2, 0.41, 0.43, 0.45, 0.5, 0.59 and 0.8, were prepared by LAG, ethanol assisted. Their XRPD and FTIR spectra confirmed that no association in a co-crystal took place, as displayed in **Figure 3.3 a and b** for $x_{\text{TMP}} = 0.43$ mixture.

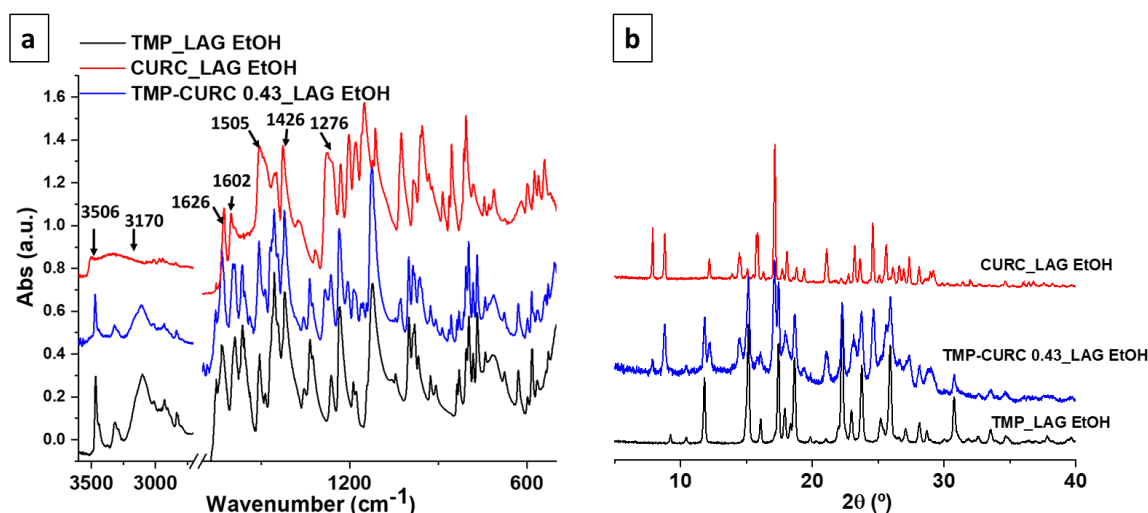


Figure 3.3 a) FTIR spectra registered between 3600 and 500 cm^{-1} of: TMP (black line), CURC (red line) and eutectic mixture of TMP-CURC mixture $x_{\text{TMP}} = 0.43$ (blue line); **b)** X-ray powder diffractograms of: TMP (black line), CURC (red line) and TMP-CURC mixture $x_{\text{TMP}} = 0.43$ (blue line). All the spectra were recorded after LAG with EtOH.

The mixture diffractogram (blue line, **Figure 3.3 b**), as well as the FTIR spectrum (blue line, **Figure 3.3 a**) are just the sum of the pure components' contributions. Particularly, among the TMP FTIR bands previously mentioned, the pure curcumin bands were detected. Indeed, considering this one (**Figure 3.3 a**, red line) a peculiar broad weak band between 3506 and 3170 cm^{-1} was attributed to the stretching of O-H groups. Then, at 1626 and 1602 cm^{-1} the C=C stretching of alkene groups and C=O of carbonyl were detected, as well as a broad band at 1505 cm^{-1} corresponding to C=O stretching and C-C-C and C-C=O bending. The aromatic carbon stretching at 1426 cm^{-1} and the C-O bending at 1276 cm^{-1} were also visible. All the obtained experimental data agreed with literature [50].

The DSC heating curves of the mixtures are depicted in **Figure 3.4 a** and the relevant thermodynamic parameters in Table 3.2.

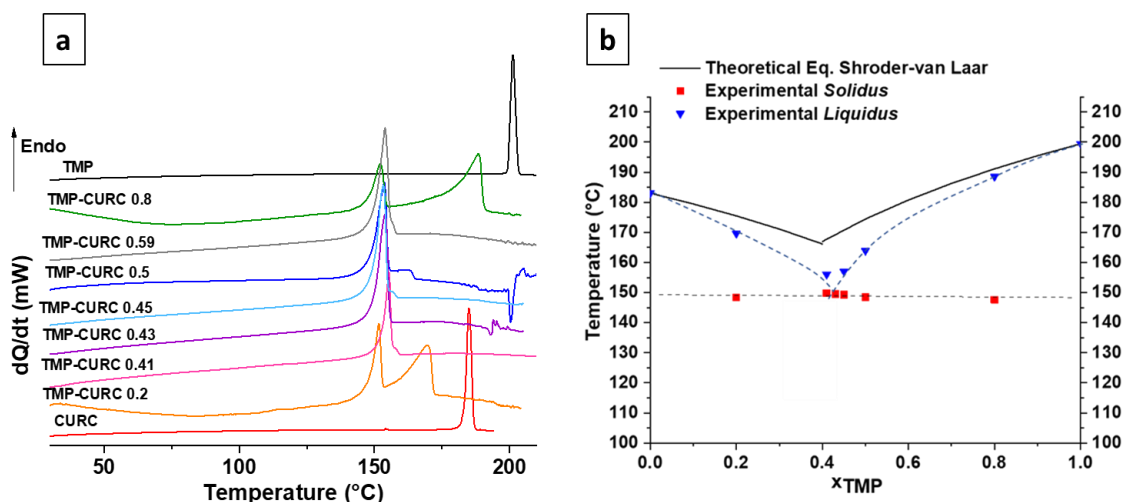


Figure 3.4 a) DSC heating curves registered in a range of 30 °C and 210 °C: TMP (black line), CURC (red line), TMP-CURC 0.20 (orange line), TMP-CURC 0.41 (pink line), TMP-CURC 0.43 (purple line), TMP-CURC 0.45 (light blue line), TMP-CURC 0.50 (grey line), TMP-CURC 0.80 (green line) and TMP-CURC 1:1 (blue line). All the thermograms were collected after LAG EtOH, ($\beta = 10 \text{ }^\circ\text{C min}^{-1}$). **b)** Binary solid-liquid phase diagram of TMP-CURC system at atmospheric pressure (dashed lines are guides for the eye).

Table 3.2 Thermodynamic parameters experimentally obtained from DSC thermograms of TMP, CURC and their mixtures.

Entry	Compound	$T_{\text{fus}} \text{ (}^\circ\text{C)}$	$T_{\text{fus}} \text{ (}^\circ\text{C)}_{\text{exc}}$
1	CURC	183.2 ± 0.2	-
2	TMP-CURC 0.80	147.6	188.5
3	TMP-CURC 0.50	148.5	163.9
4	TMP-CURC 0.45	149.3	157.0
5	TMP-CURC 0.43	149.5 ± 0.3	-
6	TMP-CURC 0.41	149.8	158.0
7	TMP-CURC 0.20	148.4	169.6

From the DSC heating curve of pure CURC after LAG EtOH (**Figure 3.4 a**, red line) the melting temperature $T_{\text{fus}} = (183.2 \pm 0.2) \text{ }^\circ\text{C}$ with a $\Delta_{\text{fus}}H = (50.5 \pm 0.5) \text{ kJ mol}^{-1}$ (Table 3.2, entry 1) is obtained in agreement with the work reported by Lee and co-workers [51]. The thermograms of mixtures are characteristic of a eutectic forming

system, showing an invariant melting peak, at $T_{\text{fus}} = 149$ °C, followed by melting of the excess component. The binary solid-liquid phase diagram (**Figure 3.4 b**), was built using the experimental thermodynamic data reported in Table 3.2, facilitated the determination of the eutectic composition, which corresponds to $x_{\text{TMP}} = 0.43$. In this graphic, the theoretical *liquidus* values obtained from the Equation of Schöder-Van Laar (solid line) are depicted as well as the experimental data for *liquidus* (blue triangles) and *solidus* (red squares) attained from each TMP-CURC mixture. Assuming ideal mixture between the API and the co-former in the liquid phase and its total no miscibility in the solid phase, the *liquidus* curve may be estimated using the melting temperature and the enthalpy of fusion of each pure compound by the Equation of Schöder-Van Laar (Eq. 3.1):

$$\frac{1}{T_{\text{fus}}} = \frac{1}{T_{\text{fus}}^*} - \frac{R \ln x_N}{\Delta_{\text{fus}} H^*} \quad (3.1)$$

in which, T_{fus} is the melting temperature, T_{fus}^* is the experimental melting temperature of pure compound, R is the ideal gas constant, x_N is the molar fraction of compound and $\Delta_{\text{fus}} H^*$ is the experimental enthalpy of fusion of the pure compound. For this system, negative deviation from the ideal liquid mixture is observed.

- **Trimethoprim - nicotinic acid and trimethoprim – picolinic acid system**

Nicotinic acid, NIC, is well known as vitamin B3 and was one of the first sell market efficient lipid modifying drugs, reducing the amount of cholesterol from blood [52]. During decades, its administration and use has been limited by side effects, such as skin flushing, nevertheless the NIC interest was renewed due to its features in combination with other drugs. At this regard, Caires and coworkers [38] reported the formation by mechanochemistry of a new (1:1) co-crystal of norfloxacin, NOR, and NIC, due to the multiple interaction between the amine group of NOR and the aromatic nitrogen as well as the carboxyl group of NIC. In their work, they emphasize the solubility enhancement reached with this association as well as that one already reported with CIP [53] and hydrochlorothiazide [54].

In our work, an equimolar mixture of TMP and NIC was submitted to LAG, ethanol assisted, and the XRPD analysis was carried out to attest the formation of a new solid form, TMP-NIC 1:1 LAG EtOH, **Figure 3.5 a** (blue line). The XRPD diffractograms

of NIC before and after grinding (**Figure 3.5 a** pink and red lines) were identical and in agreement with the X-ray pattern deposited with a CCDC 1219539 [55].

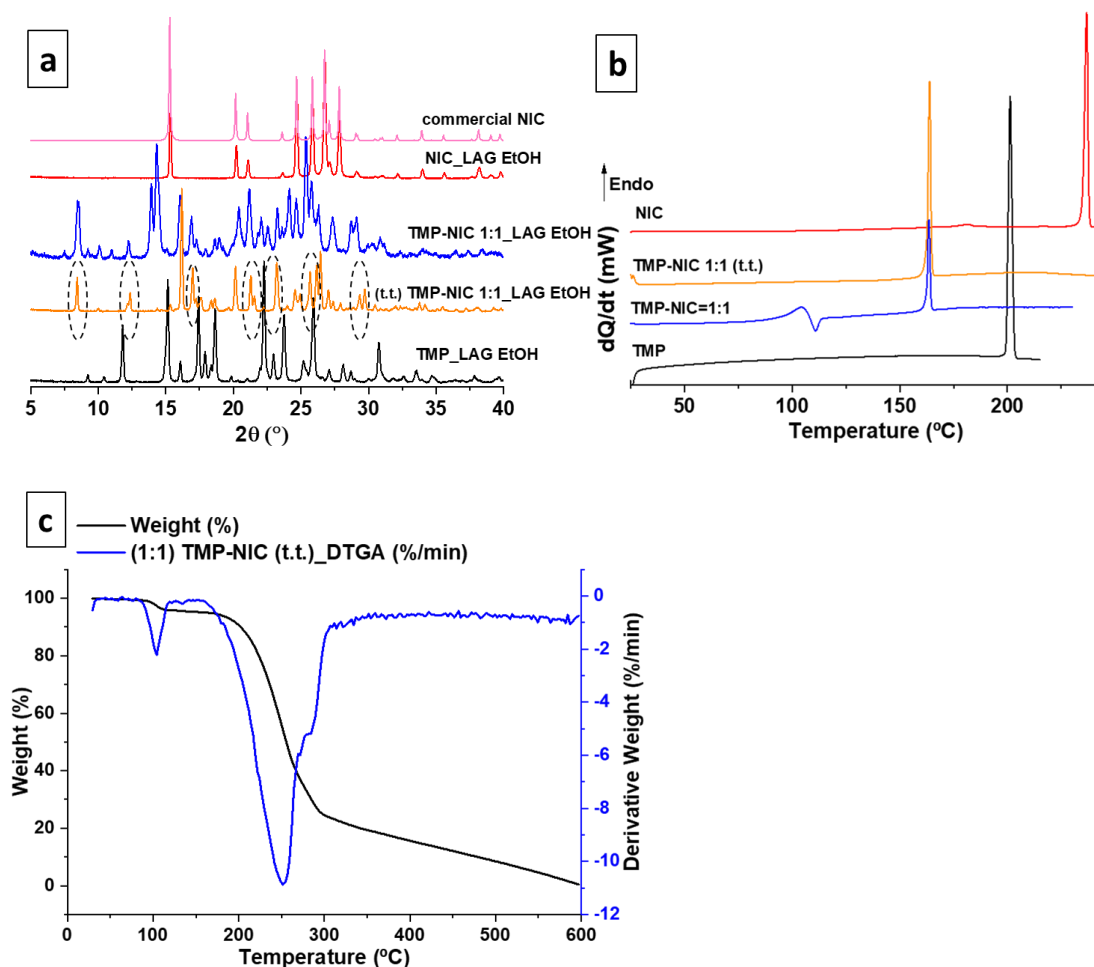


Figure 3.5 a) X-ray powder diffractograms of: commercial NIC (pink line), TMP (black line), NIC, LAG EtOH (red line), TMP-NIC 1:1 LAG EtOH (blue line) and TMP-NIC 1:1, thermal treatment, (orange line). The last four spectra were recorded after grinding with EtOH. **b)** DSC heating curves of: TMP (black line), NIC (red line), TMP-NIC 1:1, LAG EtOH (blue line) and TMP-NIC 1:1, after thermal treatment (orange line), collected in a range of 30-210 °C ($\beta = 10$ °C min^{-1}). **c)** TG and DTG curves for the TMP-NIC 1:1 EtOH, collected in a range of 30-600 °C ($\beta = 10$ °C min^{-1}).

The DSC heating curve of the TMP-NIC 1:1 LAG EtOH mixture and pure compounds are depicted in **Figure 3.5 b**. The melting temperatures of both pure compounds were at higher fusion temperatures than that one of the new solid form. The pure NIC heating profile (**Figure 3.5 b**, red line) showed $T_{\text{fus}} = (234.8 \pm 0.2)$ °C and $\Delta_{\text{fus}}H = (30.9 \pm 0.5)$ kJ mol^{-1} , in agreement to Caires report [38]. Regarding the (1:1)

TMP-NIC LAG, EtOH thermogram (blue line) it exhibits a complex profile with a low temperature endothermic event, $T \sim 101$ °C, immediately followed by an exothermic one and then a narrow peak of fusion at $T_{\text{fus}} = (162.0 \pm 0.2)$ °C. The thermogravimetric curve, shown in **Figure 3.5 c**, confirms the first event as corresponding to the melting of a solvate which must be followed by crystallization of a new solid form. Thus, a sample of (1:1) TMP-NIC LAG EtOH mixture was placed in an oven at 100 °C under vacuum and for 12 h (t.t. TMP-NIC). The DSC thermogram of TMP-NIC, after this thermal treatment (orange line), presented a single endothermic event associated with fusion at $T_{\text{fus}} = (162.0 \pm 0.2)$ °C and $\Delta_{\text{fus}}H = (50.3 \pm 0.5)$ kJ mol⁻¹.

The X-ray powder diffractogram pattern of the (t.t.) TMP-NIC (**Figure 3.5 a**, orange line), has new unique Bragg reflections observed at 8.4°, 12°, 17°, 21.2°, 23.2°, 26.4°, 29.3° and 29.7° (highlighted by dashed ovals), as well as the absence of reflexions of the starting compounds, confirming the formation of a new solid form. Comparing this XRPD with the one of TMP-NIC, LAG (blue line), this last sample is identified as a mixture of TMP-NIC obtained after the thermal treatment (t.t.) with some other multicomponent form (a solvate).

The FTIR spectra of pure compounds and of the mixtures are reported in **Figure 3.6**.

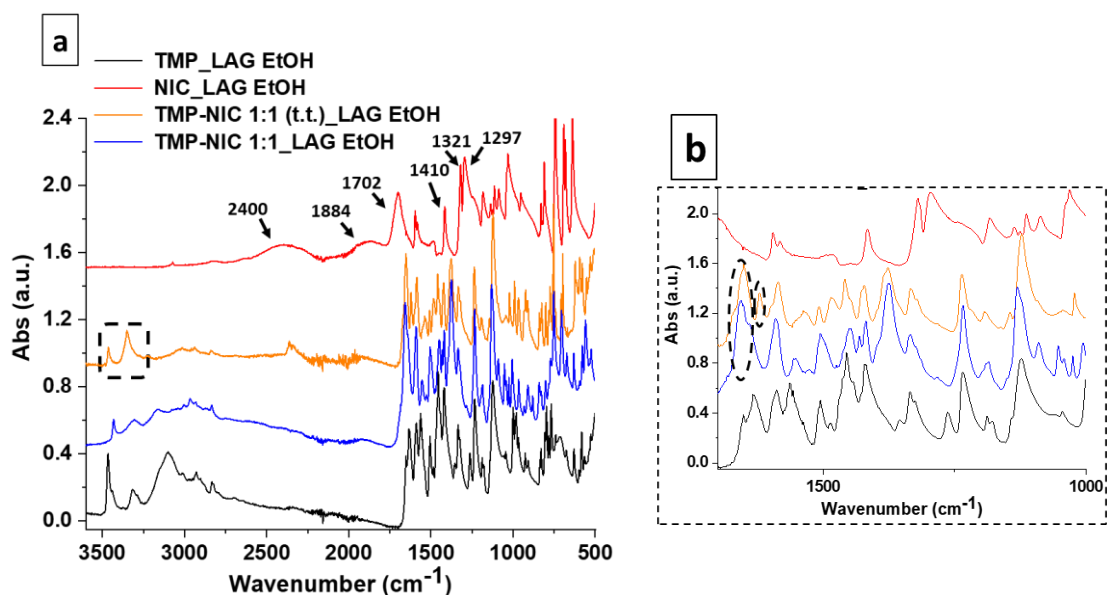


Figure 3.6 a) FTIR spectra registered between 3600 and 500 cm⁻¹ of: TMP (black line), NIC (red line), TMP-NIC 1:1 (blue line) and TMP-NIC 1:1, after thermal treatment,

(orange line) after LAG with ethanol; **b**) zoom of overlapped FTIR spectra showing bands at 1656 and 1618 cm^{-1} .

The FTIR spectrum of pure NIC (**Figure 3.6 a**, red line) showed characteristic bands agreeing with literature [53, 56], for instance two broad bands at 2400 and 1884 cm^{-1} resulting from intermolecular hydrogen bond between the aromatic nitrogen and carboxyl group and another one at 1702 cm^{-1} referred to the stretching of C=O carboxyl acid group. In the new solid form, this band is not observed and a new band around 1600 cm^{-1} appears ascribable to carboxylate anion C=O asymmetric stretching vibration. Attending to the pKa difference between trimethoprim (pKa=7.4) and nicotinic acid (pKa=4.4), the formation of a salt is expectable. The FTIR spectrum of TMP-NIC 1:1, after thermal treatment in the oven (**Figure 3.6 a**, orange line) is additionally characterized by clear peaks shifts particularly at 3349 and 3428 cm^{-1} (indicated by the dashed rectangle) and the band shift at 1656 cm^{-1} (**Figure 3.6 b**, highlighted by first dashed oval).

After the investigation on TMP-NIC performed in our work was completed, similar results were obtained by Hutchins and co-workers [57]. As we will perform further investigation concerning biopharmaceutical properties of this (1:1) TMP-NIC salt, we decided to keep the report of our results in this dissertation.

The result achieved with this system led us to test one of the nicotinic acid isomers, the picolinic acid. PIC was identified in several biological medium, including human milk and pancreatic juice [58] and is reported as antimicrobial agent [59]. Caires and his research group [60] studied the formation of a new (1:1) co-crystal between CIP and PIC by mechanochemistry highlighting the solubility increment of cocrystals compared to the pure CIP. Thus, we ground TMP and PIC in a (1:1) stoichiometric ratio and the thermal as well as the X-ray analysis are exhibited below (**Figure 3.7 a and b**, respectively).

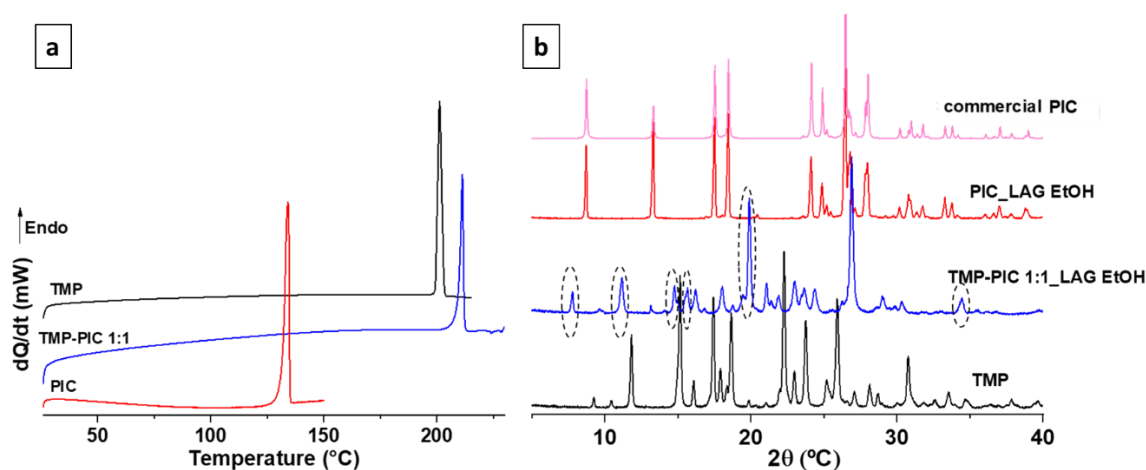


Figure 3.7 a) DSC heating curves of: TMP (black line), PIC (red line), TMP-PIC 1:1 (blue line) in a range of 25-250 °C ($\beta = 10 \text{ }^\circ\text{C min}^{-1}$); **b)** X-ray powder diffractogram of: commercial PIC (pink line), TMP (black line), PIC (red line) and TMP-PIC 1:1 (blue line). These last three diffractograms were recorded after LAG, EtOH assisted.

The pure PIC (**Figure 3.7 a**, red line) presented an endothermic peak with a $T_{\text{fus}} = (136.1 \pm 0.2) \text{ }^\circ\text{C}$ with $\Delta_{\text{fus}}H = 29.2 \pm 0.5 \text{ kJ mol}^{-1}$ which are similar to those reported by Nascimento and co-workers [61]. The thermogram of the 1:1 TMP-PIC sample showed a single event with a $T_{\text{fus}} = (209.6 \pm 0.3) \text{ }^\circ\text{C}$ and a $\Delta_{\text{fus}}H = (70.1 \pm 0.5) \text{ kJ mol}^{-1}$, higher than those of the pure components, which is the decisive evidence of the formation of a new supramolecular solid form. Regarding the X-ray analysis, the PIC did not modify its crystalline form after the grinding process as showed **Figure 3.7 b** (pink and red line) and the diffractogram was the same reported by Hamazaki *et al* (CCDC n° 130513) [62]. As expected, the diffraction pattern of the (1:1) TMP-PIC sample showed new 2θ reflexions confirming the formation of a new supramolecular solid form, namely at 7.7° , 11.1° , 14.7° , 15.7° , 19.8° , 34.4° . Then, the infrared study was also carried out for all the individual compounds and the new form (**Figure 3.8**).

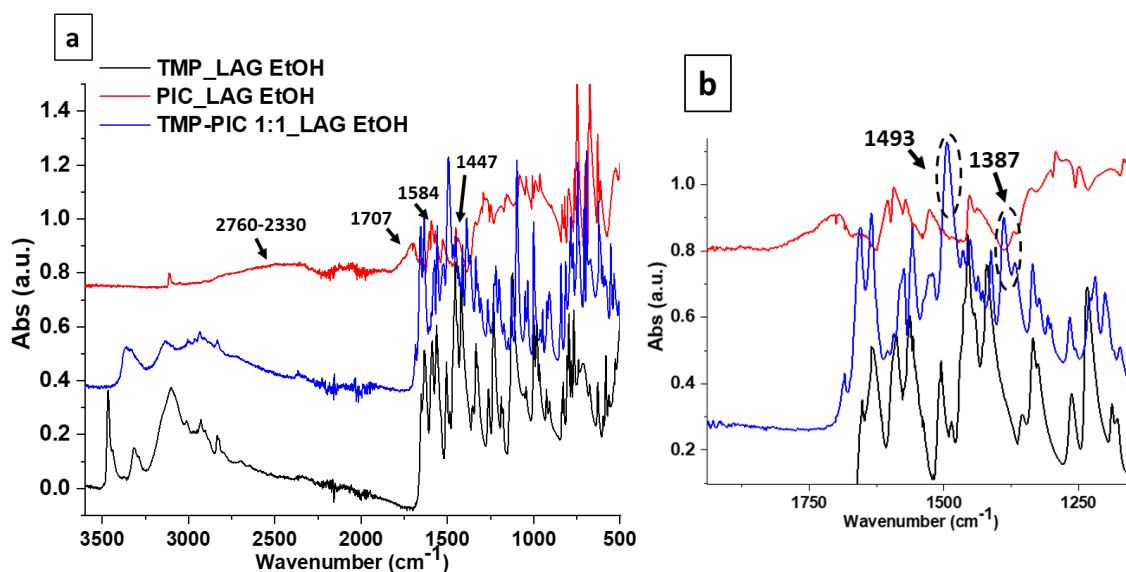


Figure 3.8 a) FTIR spectra registered between 3600 and 500 cm^{-1} of: TMP (black line), PIC (red line) and (1:1) TMP-PIC (blue line); **b)** zoom of overlapped FTIR spectra showing the formation of new bands.

IR spectrum of PIC (**Figure 3.8**, red line) exhibited two broad bands between 2770 and 2330 cm^{-1} resulting from the intermolecular hydrogen bonds existing between the carboxyl acid group and the nitrogen of the aromatic ring. These bands are not presented in the mixture, confirming a new association involving picolinic acid molecules. Then, in the fingerprint region we could distinguished other three bands at 1707, 1584 and 1447 cm^{-1} which may be assigned to the C=O of carboxylic group, C=C and C=N in the aromatic ring respectively. All these bands are typically ascribed to the PIC as Koczoń and co-workers have already reported [56]. As for the TMP-NIC association, the carboxylic acid stretching of PIC is absent in the new system spectrum and two new bands at 1493 and 1387 cm^{-1} appear, which are attributable to the asymmetric and symmetric C=O stretching vibration of the carboxylate anion, respectively. Additionally, the $\Delta\text{pK}_a = \text{pK}_{a_{\text{base}}} - \text{pK}_{a_{\text{acid}}} = 2$ points out to a salt formation.

- Trimethoprim – other GRAS compounds' systems

Mannitol, leucine, riboflavin and uracil were GRAS compounds also investigated as co-formers in the screening of TMP multicomponent solid forms. Their choice results from their structural features, high aqueous solubility and from their biological effects.

MAN is a natural polyol (1,2,3,4,5,6-hexanehexol) commonly found in nature, such as in mushrooms and marine algae, widely used in food, particularly for diabetics, [63]. It is a common excipient in the pharmaceutical industry and, additionally, activity as an antianginal drug used as cardiovascular agent has been reported [64]. Leucine, LEU, is an essential amino acid with amino and carboxylic groups which may interact with API functional groups as donors and acceptors of hydrogen bonds. Indeed, this class of compounds was considered the main co-former to developed ionic co-crystals due to their suitability [65]. In addition, they are extremely soluble in water: for instance, the solubility of LEU in water is 69.8 g L^{-1} at $25 \text{ }^\circ\text{C}$, so in association with API it has potential to increase the solubility/dissolution rate [66]. Regarding riboflavin, RIB, it is normally known as water-soluble vitamin B2 and essentially found in food. Several research studies have demonstrated its nature as antioxidant agent as well as its correlation with neurological disorders and some cancers [67]. As we mentioned in the beginning of this paragraph, since our co-formers choice was led on both the possibility of formation of reliable heterosynthons with TMP and on the relevance of their use, it is easy to realize why the URA was chosen. It is one of the four nitrogenous bases constituting the RNA and one of the most relevant pharmacophores being a scaffold for a huge variety of commercial drug. Furthermore, URA and its derivatives are normally associated to several cancer treatments [68].

The results obtained in the screening of TMP solid forms using LEU, RIB and URA as co-formers, confirmed that neither co-crystals nor salts could be obtained with neither of them. This confirms the predictions made using the COSMO-Quick software: the ΔH^{ex} values obtained, Table 3.1, are positive for the association of TMP with LEU and close to zero for URA as co-former. The f_{fit} values are quite high for LEU, RIB and also for MAN (of the order of 6 -8), as was observed for TMP-CURC.

For these three systems, the X-ray powder diffraction analysis, **Figure 3.9**, showed that all the co-formers after grinding, EtOH assisted, exhibited reflections at the same 2θ values. Furthermore, the diffractograms unequivocally demonstrate the formation of physical mixtures.

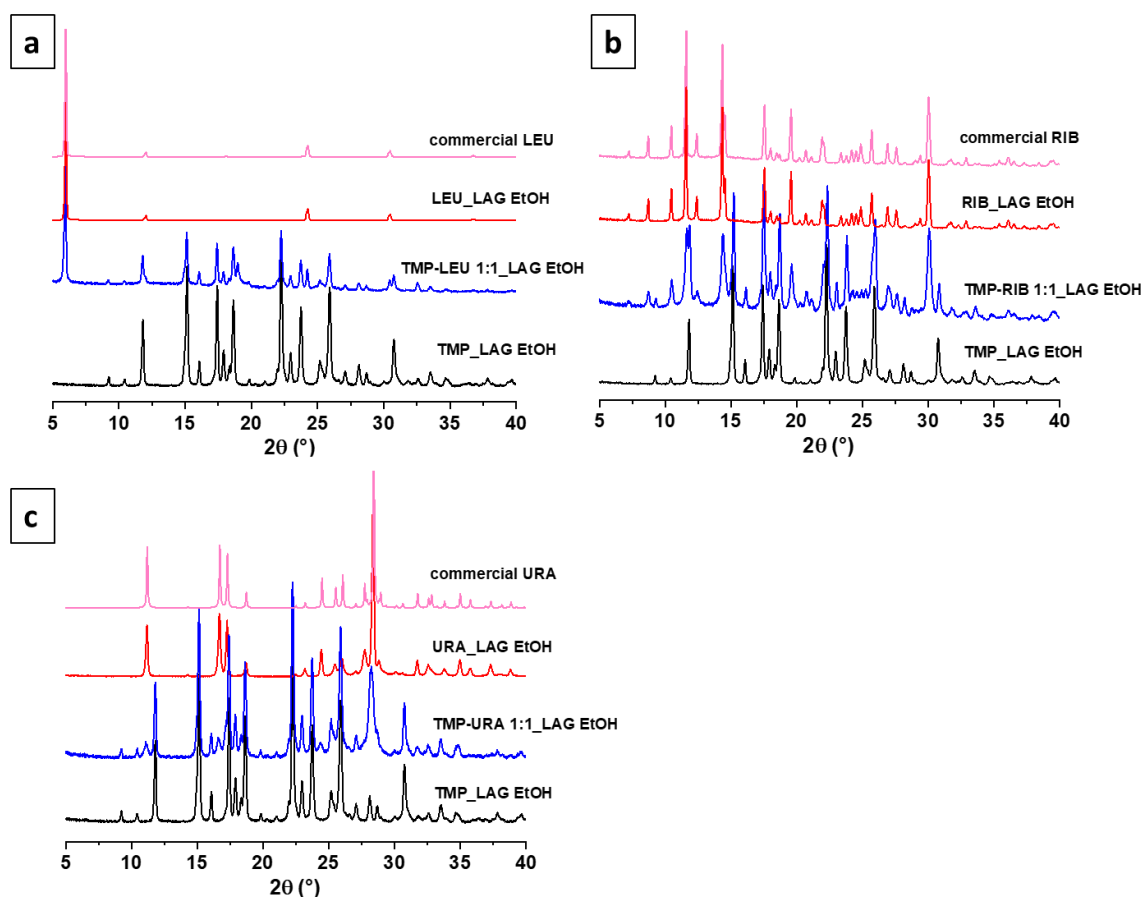


Figure 3.9 X-Ray powder diffractograms for: **a)** TMP-LEU system: commercial LEU (pink line), LEU (red line), TMP (black line) and TMP-LEU 1:1 (blue line) all after LAG with EtOH; **b)** TMP-RIB system: commercial RIB (pink line), RIB (red line), TMP (black line) and TMP-RIB 1:1 (blue line) all after LAG with EtOH; **c)** TMP-URA system: commercial URA (pink line), URA (red line), TMP (black line) and TMP-LEU 1:1 (blue line) all after LAG with EtOH.

The FTIR spectra reported in **Figure 3.10** for each system are, as expected, the sum of those of the pure solid compounds. Regarding pure LEU (**Figure 3.10 a**, red line), all the experimental bands agreed with literature [69]. A broad band was detected in the region of 2955 cm^{-1} ascribed to the stretching of CH_2 group. In the other region of the spectrum, bands at 1600 and 1571 cm^{-1} may be attributed to the carboxylate group stretch, then at 1401 cm^{-1} was identified the bending of CH_3 group and in the region between 1360 and 1315 cm^{-1} a series of bands are attributed to the C-C stretching. Furthermore, a broad peak at 1001 cm^{-1} corresponds to the stretching of CN group. The same evaluation was performed for the RIB (**Figure 3.10 b**, red line), displaying typical bands already

described in literature [70]. Especially, in the first section of the spectrum, a broad band between 3492 and 3110 cm^{-1} was attributed to the stretching of NH and OH. Then, we observed at 1730 cm^{-1} the C=O stretching and the C=C (of the rings) stretching between 1641 and 1498 cm^{-1} , at 1241 cm^{-1} the OH bending and the C-O stretching between 1069 and 987 cm^{-1} . In pure URA (**Figure 3.10 c**, red line) infrared spectra, a broad band between 3084 and 2925 cm^{-1} corresponding to the N-H and C-H (ring) stretching were distinguished, as well as two bands at 1712 and 1637 cm^{-1} for the C=O and C=C stretching. Then, the NH bending, and the stretching of C-N were displayed at 1414 and 1388 cm^{-1} , respectively.

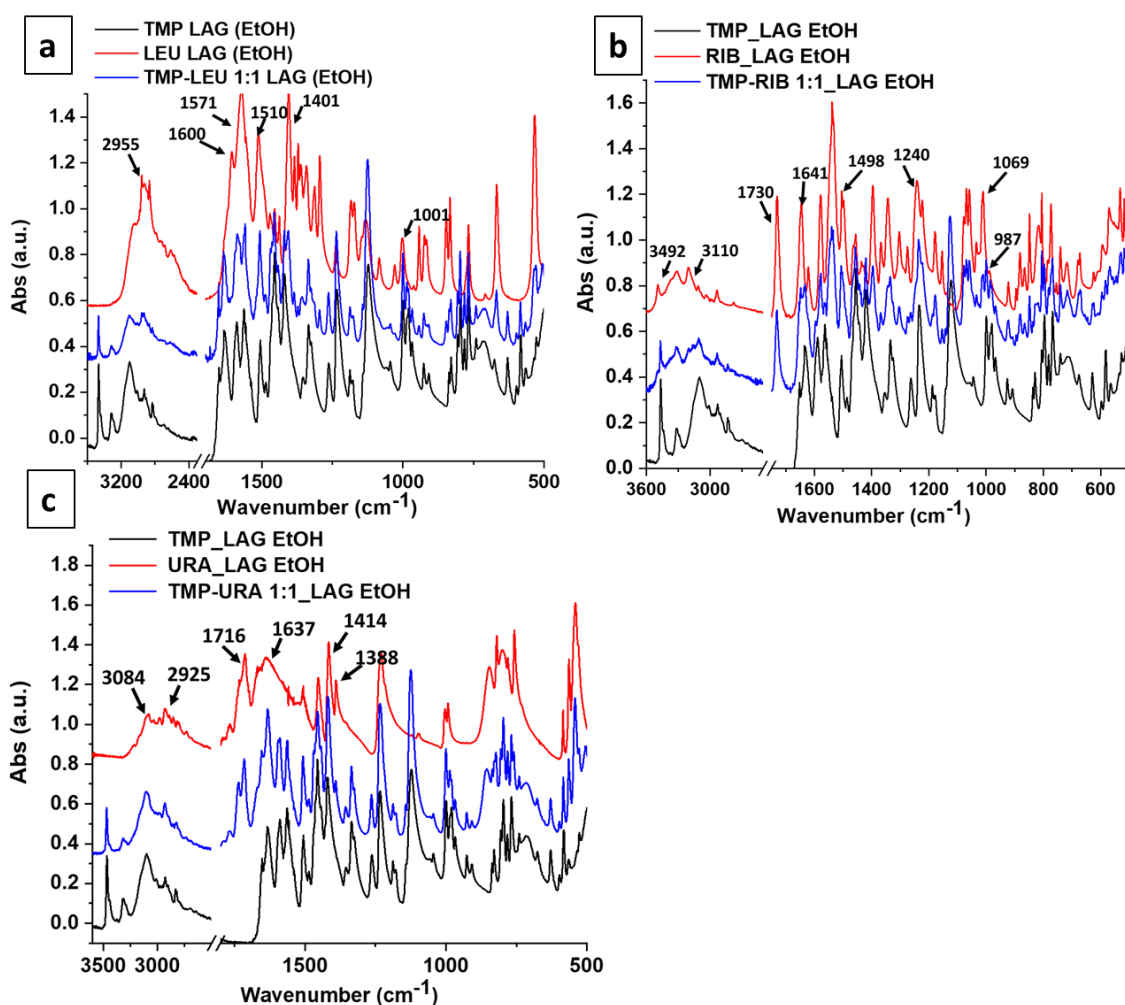


Figure 3.10 FTIR spectra registered between 3600 and 500 cm^{-1} of: **a)** TMP (black line), LEU (red line) and TMP-LEU 1:1 (blue line) after LAG with EtOH; **b)** TMP (black line), RIB (red line) and TMP-RIB 1:1 (blue line) after LAG with EtOH; **c)** TMP (black line), URA (red line) and TMP-URA 1:1 (blue line) after LAG with EtOH.

The thermal behaviour of the equimolar binary mixtures of trimethoprim with these co-formers is shown in **Figure 3.11**, all presenting melting temperatures below that of pure TMP, as expected, TMP-LEU $T_{\text{fus}} = (196.7 \pm 0.3) ^\circ\text{C}$; TMP-RIB $T_{\text{fus}} = (192.8 \pm 0.2) ^\circ\text{C}$; TMP-URA $T_{\text{fus}} = (188.4 \pm 0.3) ^\circ\text{C}$.

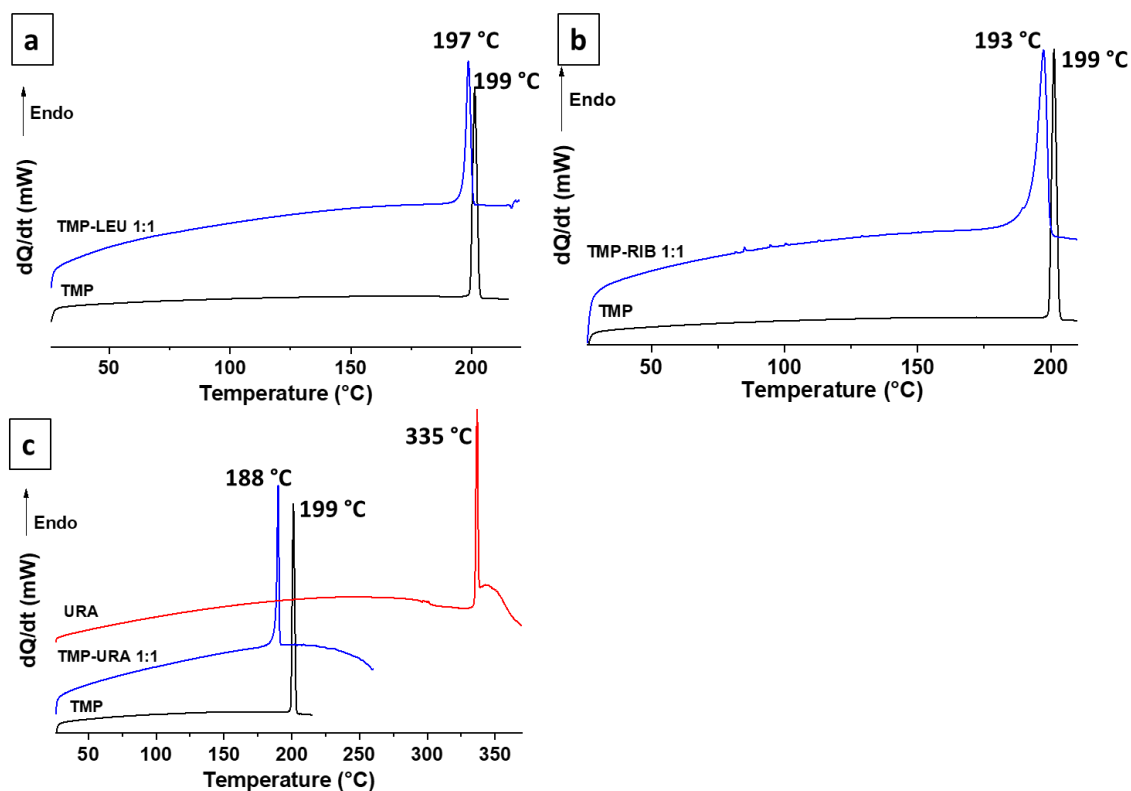


Figure 3.11 DSC heating curves registered between 25 °C and 220 °C ($\beta = 10 ^\circ\text{C min}^{-1}$) of: **a**) TMP (black line), TMP-LEU 1:1 (blue line) after grinding with EtOH; **b**) TMP (black line), TMP-RIB 1:1 (blue line) after grinding with EtOH; **c**) TMP (black line), TMP-URA 1:1 (blue line), URA (red line) after grinding with EtOH.

All these three co-formers have high melting/decomposition temperatures. In the case of LEU and RIB, we were not able to collect the DSC thermograms due to their high melting temperature. This value has been reported in literature at a temperature $> 300 ^\circ\text{C}$ for LEU [71] and above $298 ^\circ\text{C}$ for RIB [72] followed by a decomposition. This fact precludes further thermal behaviour investigation for these systems.

Concerning TMP-MAN mixtures, no association in a supramolecular form was also observed as confirmed by the FTIR spectrum, depicted in **Figure 3.12** for a (1:1) TMP-MAN, LAG EtOH, mixture and from the DSC curves obtained for several mixtures with different composition (**Figure 3.13 a**).

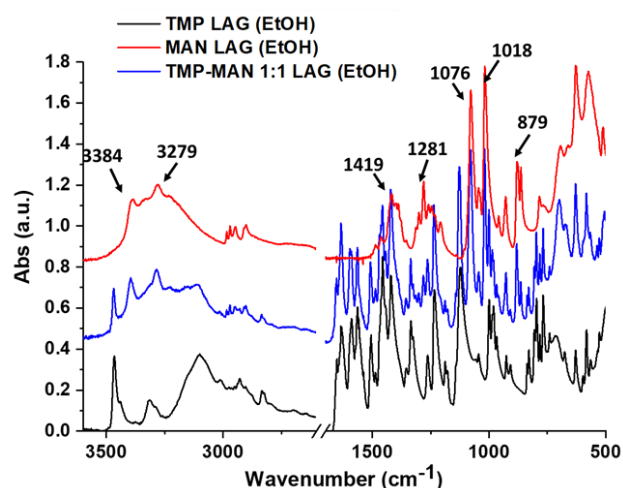


Figure 3.12 FTIR spectra registered between 3600 and 500 cm^{-1} of TMP (black line), MAN (red line) and mixture of TMP and MAN (blue line) in a proportion of 1:1 after LAG.

The FTIR spectrum of pure MAN (**Figure 3.12**, red line) shows sharp peaks at 3384 and 3279 cm^{-1} ascribed to stretching vibrations of O-H, and other feature peaks detectable in the "fingerprint" region: at 1419 and 1281 cm^{-1} the H-C-O bending, at 1076 and 1018 cm^{-1} the stretching of C-O and at 879 cm^{-1} the C-C stretching, agreeing with what is found in literature [73]. Comparing the pure compounds FTIR spectra with that of the 0.5 mixture (**Figure 3.12**, blue line), it is evident that the TMP-MAN spectrum is the sum of each pure component FTIR bands. The thermograms showed in **Figure 3.13 a** are typical of an eutectic forming system. The thermogram of MAN before and after the LAG with EtOH (**Figure 3.13**, dashed dark red and red line) showed the same melting temperature at $T_{\text{fus}} = (165.7 \pm 0.2) \text{ } ^\circ\text{C}$, $\Delta_{\text{fus}}H = (52.1 \pm 0.5) \text{ kJ mol}^{-1}$ (Table 3.3, entry 1), agreeing with Gombás *et al* [74]. The binary solid liquid phase diagram for TMP-MAN system was also simulated using Eq. 3.1 and is presented in **Figure 3.13 b**, together with the experimental *liquidus* and *solidus* points.

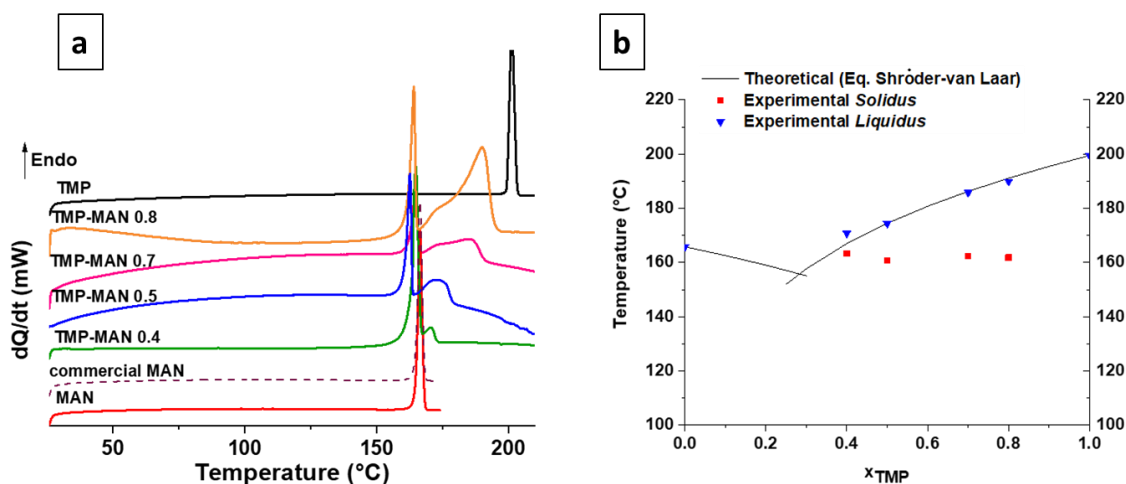


Figure 3.13 a) DSC heating curves registered between 25 °C and 350 °C of: commercial MAN (dashed red line), TMP (black line), MAN (red line), TMP-MAN 0.80 (orange line), TMP-MAN 0.70 (pink line), TMP-MAN 0.50 (blue line) and TMP-MAN 0.40 (green line) after LAG EtOH; b) Binary solid-liquid phase diagram of TMP-MAN system at atmospheric pressure.

Table 3.3 Thermodynamic parameters obtained for TMP, MAN and their mixtures from their DSC thermograms.

Entry	Compound	T_{fus} (°C)	T_{fus} (°C) _{exc}
1	MAN	165.7 ± 0.2	-
2	TMP-MAN 0.40	163.3	170.8
3	TMP-MAN 0.50	160.7	174.4
4	TMP-MAN 0.70	162.3	185.8
5	TMP-MAN 0.80	161.8	189.9

The eutectic mixture is expected to be mainly composed of MAN, which would not be useful and, therefore, no further investigation on this system was carried out.

3.2.2 Development of TMP-based multicomponent solid forms using co-API molecules

During our investigation, in addition to GRAS compounds, other API molecules were also tested in combination with TMP to screen the formation of multi-API co-crystals/multicomponent solid forms. Although these forms have great potential for

drug development with combined action as reported in the introduction, this type of co-crystal/multicomponent solid form has not yet been extensively investigated [75].

- Trimethoprim-paracetamol system

Paracetamol was chosen as it is one of the most worldwide used drugs for pain and fever, due to its antipyretic, non-opioid analgesic, and non-steroidal anti-inflammatory effect [76]. It is classified as class III compound in the BCS, meaning an high solubility and low permeability API [77]. This compound has already been quite explored in co-crystallization experiments, for instance with oxalic acid [78] and trimethylglycine [79]. In both cases, co-crystals enhanced its stability and tableability, since PARA alone collapses after tablet formation. It has also been investigated as an antibacterial agent for Gram positive bacteria [42].

We tried several TMP-PARA mixtures and the corresponding DSC curves are exhibited in **Figure 3.14 a**, and selected X-ray powder diffractograms and FTIR spectra in **Figures 3.14 b** and **c**, respectively.

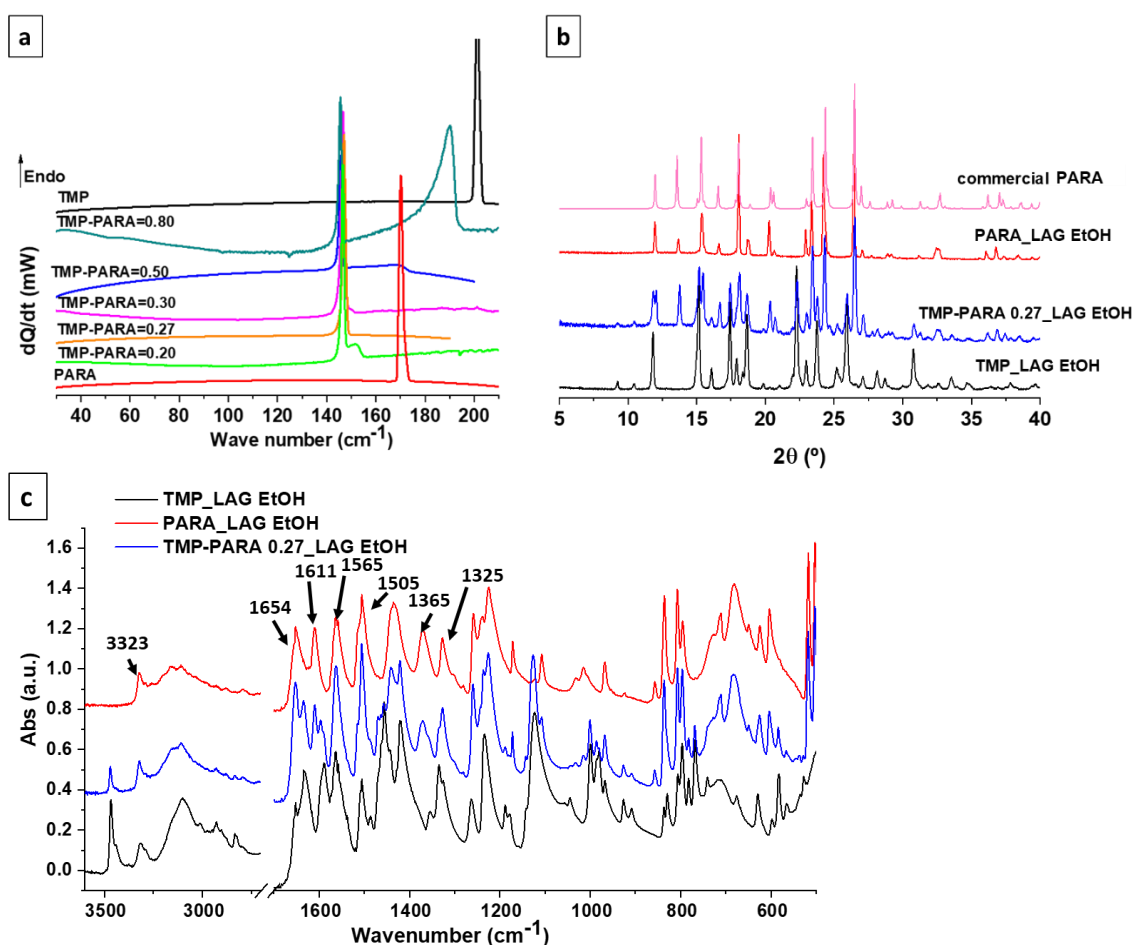


Figure 3.14 a) DSC curves registered in a range from 30 °C to 210 °C of: TMP (black line), PARA (red line), TMP-PARA 0.20 (green line), TMP-PARA 0.27 (orange line), TMP-PARA 0.30 (pink line), TMP-PARA 0.50 (blue line), TMP-PARA 0.80 (dark green line) (β of 10 °C min⁻¹); **b)** X-ray powder diffractograms of commercial PARA (pink line), TMP (black line), PARA (red line) and TMP-PARA 0.27 (blue line); **c)** FTIR spectra registered between 3600 and 500 cm⁻¹ of TMP (black line), PARA (red line) and TMP-PARA 0.27 (blue line), LAG EtOH.

Thermodynamic relevant parameters obtained from DSC curves, are presented in Table 3.4.

Table 3.4 Thermodynamic parameters experimentally obtained for TMP, PARA and their mixtures, from DSC thermograms.

Entry	Compound	T_{fus} (°C)	T_{fus} (°C) _{exc}
1	PARA	168.6 ± 0.2	-
2	TMP-PARA 0.80	144.1	190.2
3	TMP-PARA 0.50	144.5	169.4
4	TMP-PARA 0.30	145.1	151.3
5	TMP-PARA 0.27	145.6 ± 0.3	-
6	TMP-PARA 0.20	145.4	152.4

PARA melting temperature is equal to that reported by Zeitler and co-workers [80], $T_{\text{fus}} = (168.6 \pm 0.2)$ °C with a corresponding enthalpy of fusion of $\Delta_{\text{fus}}H = (28.0 \pm 0.5)$ kJ mol⁻¹ (Table 3.4, entry 1). The diffractograms of PARA before and after LAG experiments confirms that no changes occur and that we are working with its stable form reported by Howard and co-workers (CCDC nr 129925) [81]. The experimental results concerning the mixtures, confirm a eutectic forming system behaviour, with a sum of the pure compounds contribution registered both in the XRP diffractograms and FTIR spectra. Analysing the FTIR spectrum of TMP-PARA 0.27 mixture (**Figure 3.14 c**, blue line), among the TMP characteristic peaks, those of pure PARA (**Figure 3.14 c**, red line) are in accordance with other research studies [82]: bands

at 3323 cm^{-1} ascribed to O-H, C=O and C=C stretching appeared at 1654 and 1611 cm^{-1} , respectively. Furthermore, the bending of N-H amide and asymmetrical C-H were assigned at 1565 and 1505 cm^{-1} and symmetrical bending in C-H and C-N of aryl group stretching were identified at 1365 - 1325 cm^{-1} .

The eutectic composition $x_{\text{TMP}} = 0.27$, was obtained from the binary solid-liquid phase diagram (**Figure 3.15**), built using the experimental data reported in Table 3.4. the experimental eutectic composition is not much different from the value estimated using Eq. 3.1 (**Figure 3.15**).

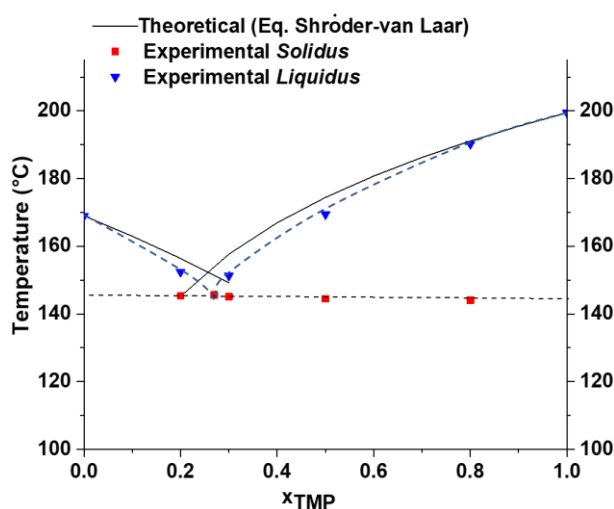


Figure 3.15 Binary solid-liquid phase diagram of TMP-PARA system at atmospheric pressure.

- Trimethoprim – salicylic acid and trimethoprim - ibuprofen systems

Considering the results obtained when acid co-formers were associated with TMP, namely NIC and PIC reported above, investigation was also carried out with salicylic acid and ibuprofen.

SAL is a natural compound, typically known as an active metabolite of aspirin. It is a mono-hydroxyl benzoic acid widely used as anti-inflammatory, bacteriostatic and fungicidal agent to treat skin diseases such as dermatitis, psoriasis and acne [83]. Hence, an equimolar mixture of this co-former with TMP was submitted to LAG EtOH, and DSC heating curves registered, **Figure 3.16 a**.

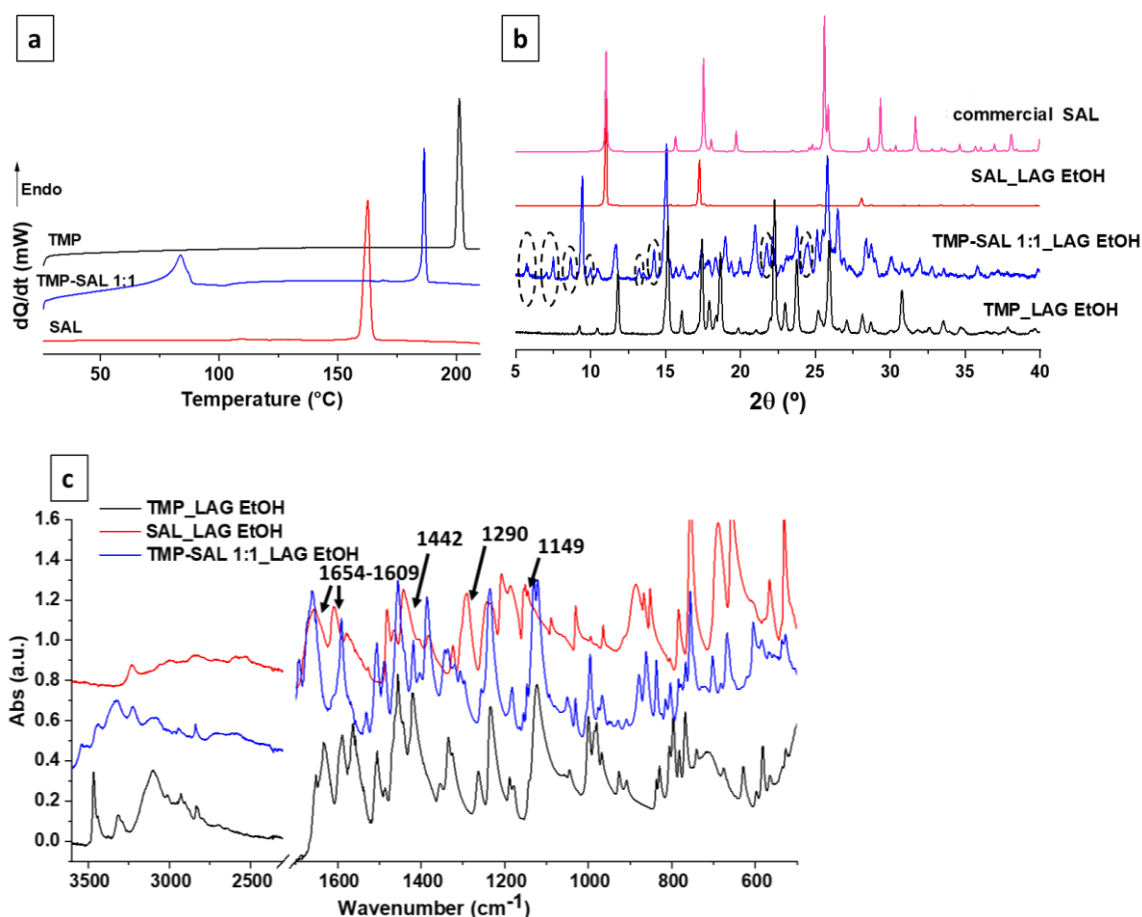


Figure 3.16 **a)** DSC heating curves registered between 30 °C and 210 °C ($\beta= 10$ °C min^{-1}) of: TMP (black line), SAL (red line), TMP-SAL 1:1 (blue line) after LAG experiments; **b)** X-ray powder diffractograms of: SAL commercial (pink line), TMP (black line), SAL (red line) and TMP-SAL 1:1 (blue line). These last three were recorded after grinding with EtOH; **c)** FTIR spectra registered between 3600 and 500 cm^{-1} of: TMP (black line), SAL (red line) and TMP-SAL 1:1 (blue line) after grinding with ethanol.

The thermogram of pure SAL (**Figure 3.16 a**, red line) showed a melting peak at $T_{\text{fus}} = (154.4 \pm 0.2)$ °C as that documented in literature [84], with fusion enthalpy of $\Delta_{\text{fus}}H = (22.3 \pm 0.5)$ kJ mol^{-1} . The DSC curve of 1:1 TMP-SAL combination (**Figure 3.16 a**, blue line) revealed a sharp endothermic peak at $T_{\text{fus}} = (185.3 \pm 0.2)$ °C, $\Delta_{\text{fus}}H = (49.0 \pm 0.5)$ kJ mol^{-1} . The presence of this narrow peak with a fusion temperature between those of the individual pure compounds is conclusive evidence of the formation of a new solid form composed of both components. Furthermore, this thermogram also showed another broad peak with an onset temperature < 100 °C, which is compatible with desolvation of a solvate during the heating run, giving rise to the solid form that melts at

$T_{\text{fus}} = 185.3$ °C. This result is not unexpected as salt-solvate/hydrate formation between TMP and acid co-formers has been quite documented [27, 31] and was also identified in our work for the TMP-NIC system. Considering the TMP and SAL pKa values of 7.4 [85] and 3 [84], respectively, the ΔpKa value is 4.4, which points to salt formation, as predicted by the salt proton-transfer rule [86].

The SAL diffractogram registered after the EtOH-assisted grinding process is different from that of the commercialized sample. This means that a rearrangement in the SAL crystalline form occurs during the milling process. This diffractogram was not found in the CCDC database, which contains all the crystalline forms resolved worldwide, therefore, at this regard, future studies will have to be performed. In **Figure 3.16 b** we obtained clear evidence that TMP-SAL mixed in a stoichiometric ratio, LAG EtOH (blue line) produced a new X-ray diffraction pattern, with reflexions at 2θ values different from those of the starting materials: new Bragg reflections were detected at 5.7° , 7.5° , 8.6° , 13.2° , 14.2° , 21.7° , 24.5° .

The FTIR spectrum of pure SAL (**Figure 3.16 c**, red line) showed at 3230 cm^{-1} and between 2993 and 2840 cm^{-1} , O-H and C-H stretching bands, respectively. Then, the stretching band of C=O was identified at 1654 cm^{-1} , while at 1609 and 1442 cm^{-1} C=C and C-C stretching bands are visible. The phenolic stretching vibrations (C-OH) were assigned to 1290 and 1149 cm^{-1} and of the phenolic O-H bending at 1323 cm^{-1} . The detected wavenumbers are coherent with those described by Jana and co-workers [83]. As expected, the infrared spectrum of 1:1 TMP-SAL solid form obtained by LAG EtOH, **Figure 3.16 c**, shows remarkable differences when compared with the pure components.

The association between TMP and IBU (as racemate) was also investigated during this thesis. IBU a non-steroidal anti-inflammatory drug, is one of the most worldwide prescribed APIs. Despite being classified as BSC class II [87], its association with TMP may be of interest in a dual-drug therapy perspective. [88, 89]. DSC heating curves and X-ray powder diffractograms of the starting compounds and of a (1:1) TMP-IBU mixture prepared by grinding, ethanol assisted, are presented in **Figures 3.17 a** and **b**.

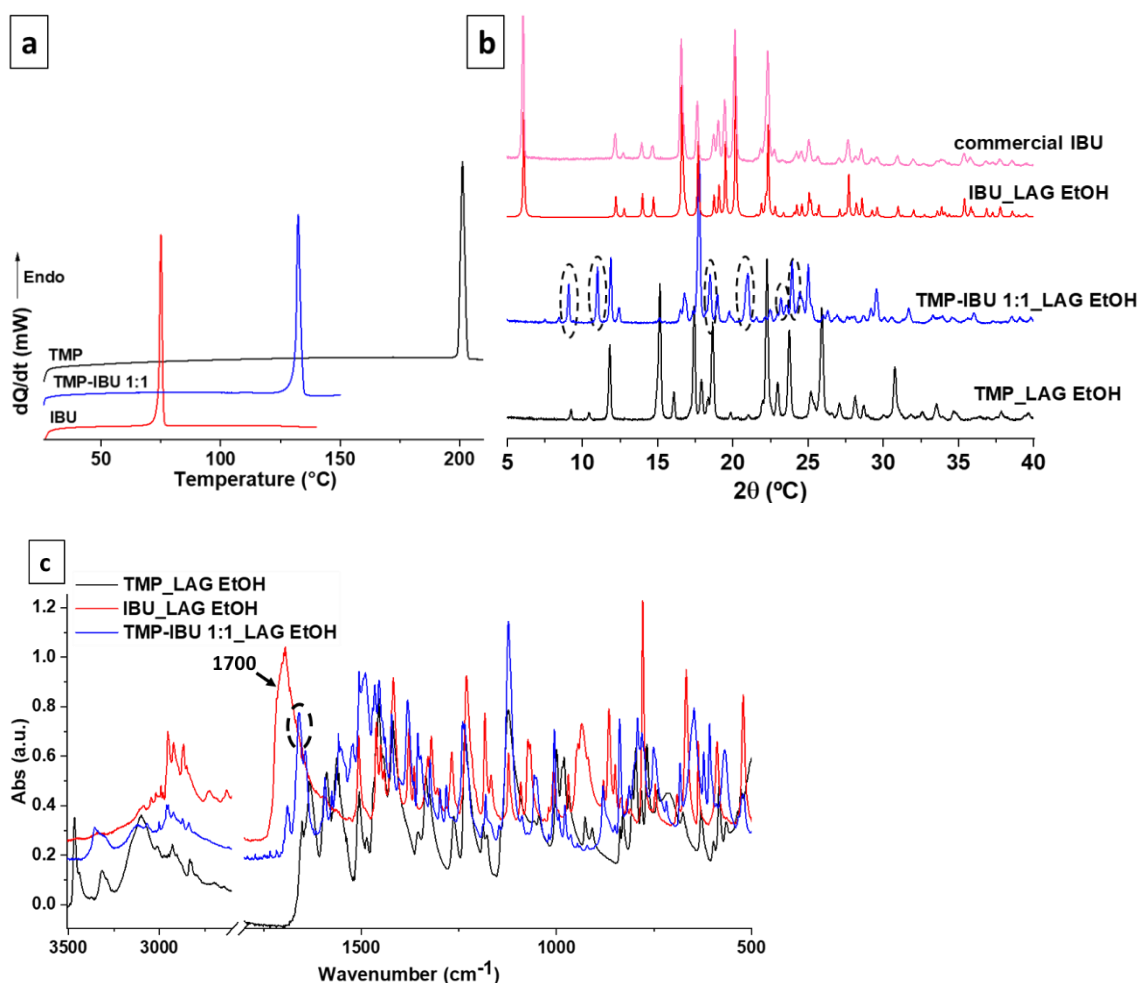


Figure 3.17 **a)** DSC curves of: TMP (black line), IBU (red line), TMP-IBU 1:1 (blue line), after EtOH-assisted grinding and collected in a range of 25-210 °C ($\beta = 10 \text{ °C min}^{-1}$); **b)** X-ray powder diffractogram of: commercial IBU (pink line), TMP (black line), IBU (red line) and TMP-IBU 1:1 before the oven (blue line). These last three spectra were recorded after grinding with EtOH; **c)** FTIR spectra registered between 3600 and 500 cm^{-1} of: TMP (black line), IBU (red line) and TMP-IBU 1:1 (blue line).

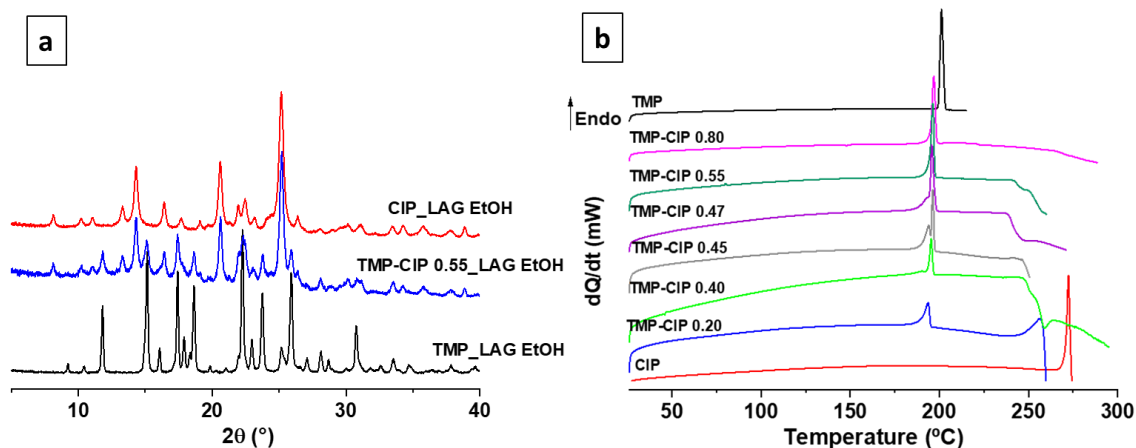
The results clearly show the association of these two APIs in a new supramolecular solid form. The DSC curves (**Figure 3.17 a**) of the (1:1) TMP-IBU (LAG) displayed a single, sharp melting peak at $T_{\text{fus}} = (131.2 \pm 0.2) \text{ °C}$ and $\Delta_{\text{fus}}H = (76.9 \pm 0.5) \text{ kJ mol}^{-1}$, well above the melting temperature of pure IBU ($T_{\text{fus}} = (75.7 \pm 0.2) \text{ °C}$, in agreement to the literature [87], $\Delta_{\text{fus}}H = (24.8 \pm 0.6) \text{ kJ mol}^{-1}$). In the X-ray powder diffractogram of the mixture (**Figure 3.17 b**, blue line), a new set of reflections is observed, for instance at 2θ values of 9.0°, 11.0°, 18.4°, 20.9°, 23.1°, 23.9°, corroborating the formation of a new supramolecular

solid form, with no evidence of excess of starting materials. In this case, considering the TMP pKa and that one of the IBU [90], the $\Delta pK_a = pK_{a_{base}} - pK_{a_{acid}} = 3$, meaning that both cocrystal or salt formation are expectable [86]. FTIR spectra of IBU, TMP and the new solid form were recorded between 3600 and 500 cm^{-1} and are reported below (**Figure 3.17, c**). IBU after grinding preserved its initial crystalline form, that one reported by McConnell in 1974 [91] and deposited with a CCDC nr 1179382, and its FTIR spectrum (**Figure 3.17 a**, red line) showed bands with the same maxima values reported by Ramachandran and co-workers [92]. In IBU spectrum, the band at 1700 cm^{-1} corresponds to the C=O stretching and, regarding the (1:1) TMP-IBU FTIR spectrum (**Figure 3.17 c** blue line), evidence exists that carboxylate anion is formed, and therefore that a salt was obtained. This is corroborated by the high shift of the NH stretching vibration of TMP.

Despite a considerable number of attempts to obtain single crystal suitable to X-ray diffraction resolution of the crystalline structure of these new supramolecular TMP-based solid forms, until now, as it is not uncommon, we were not successful.

- Trimethoprim – ciprofloxacin system

The last compound combined with TMP was CIP due to its broad spectrum of activity and many therapeutic options. Indeed, it is sold worldwide with ~ 300 different names showing huge antibacterial activity and so it is used also for urinary infections [93]. Several research works have already been reported in literature about combination of CIP with other co-formers particularly to enhance the antibacterial activity against *E. coli* [94]. The investigation of binary TMP-CIP mixtures obtained by LAG, EtOH, allows concluding that physical mixtures are obtained, **Figure 3.18 a, b, c** and **d**.



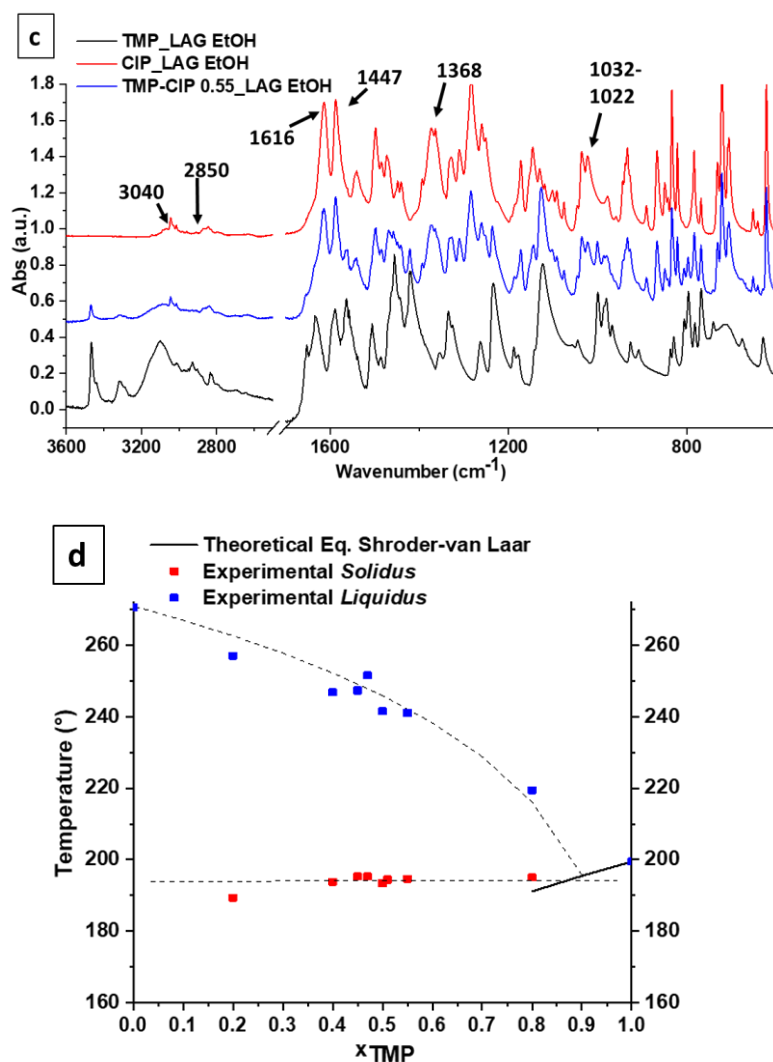


Figure 3.18 a) X-ray powder diffractograms of: TMP (black line), CIP (red line) and TMP-CIP 0.55 (blue line) after grinding with EtOH; **b)** DSC curves registered with $\beta = 10 \text{ }^\circ\text{C min}^{-1}$ of: TMP (black line), CIP (red line), TMP-CIP 0.20 (blue line), TMP-CIP 0.40 (light green line), TMP-CIP 0.45 (grey line), TMP-CIP 0.47 (purple line), TMP-CIP 0.55 (dark green line), TMP-CIP 0.80 (pink line); **c)** FTIR spectra registered between 3600 and 500 cm^{-1} of: TMP (black line), CIP (red line) and TMP-CIP 0.51 (blue line); **d)** Representation of *solidus* temperature and final melting/decomposition temperature as a function of composition for TMP-CIP mixtures; simulated *liquidus* line for TMP (dashed lines are guides for the eye).

Pure CIP X-ray powder diffractogram shows that we are working with polymorph B described in the patent WO 2019/067851 A1 [95]. The mixtures diffractogram, exemplified in **Figure 3.18 a)** for a $x_{\text{TMP}} = 0.55$ mixture, blue line, are the overlap of pure

TMP and CIP XPRD ones. The FTIR spectrum of the mixture is also, as expected, the sum of those of the pure components. Relevant bands of CIP are marked in **Figure 3.18 c**, in accordance to the literature reports [53], showing a low intense band between 3040-2850 cm^{-1} , representing the C-H stretching, and the two stretching bands of the carboxyl group at 1584 and 1368 cm^{-1} confirming the zwitterionic form of this API. Additionally, a strong band at 1616 cm^{-1} was observed and assigned to the ketone group stretching while the C-F group was exhibited bands at 1032 and 1022 cm^{-1} .

Pure CIP was analysed by DSC (**Figure 3.18 b**, red line) showing melting point at $T_{\text{fus}} = (270.6 \pm 0.2) \text{ }^\circ\text{C}$ (Table 3.5, entry 1), in agreeing with literature [53], followed by decomposition. The *solidus* and final melting/decomposition temperature values obtained from DSC curves for TMP-CIP mixtures are presented in Table 3.5. Although decomposition precludes the drawing of a reliable solid-liquid binary phase diagram, the representation shown in **Figure 3.18 d**, points to a minimum value of melting temperature for a $x_{\text{TMP}} = 0.85$ mole fraction. Mixtures of this composition, as well as an equimolar one, were chosen to be the object of further investigation concerning their antibacterial activity.

Table 3.5 Thermodynamic parameters experimentally obtained from TMP, CIP and their mixture thermograms.

Entry	Compound	$T_{\text{fus}} \text{ (}^\circ\text{C)}$	$T_{\text{fus}} \text{ (}^\circ\text{C)}_{\text{exc}}$
1	CIP	270.6 ± 0.2	-
2	TMP- CIP 0.80	195.0	215.4
3	TMP- CIP 0.55	194.5	241.8
4	TMP- CIP 0.47	192.0	240.6
5	TMP- CIP 0.45	195.3	245.8
6	TMP- CIP 0.40	193.8	247.2
7	TMP- CIP 0.20	189.3	257.0

3.3 Dissolution rate tests

The next step of our research involved the selection among all multicomponent solid-forms described above, of those which will undergo intrinsic dissolution rate tests.

So, TMP-NIC, TMP-PARA and TMP-IBU were the three-systems selected to continue this study.

These systems were selected according to the TMP potentiality when associated to these co-formers. In the case of PARA and IBU, these APIs are typically administrated to reduce pain due to their analgesic and anti-inflammatory properties and in addition to TMP may facilitate the patients' treatments. Additionally, rare side effects are documented for PARA and in fact it may be taken by pregnant women which often suffer of urinary infection problems [96]. Also, it is well reported that these two drugs as well as other analgesics represent a huge production percentage in the pharmaceutical industry and evaluations show that their demand will grow exponentially in next years [97]. Whereas it is well described that using NIC in combination with other APIs of BCS Class II may produce an enhancement in the API solubility/dissolution rate [98].

The dissolution rate testes were carried out with SOTAX dissolution rate tester (USP 2 model) with 6 glass vessels (1 L) (**Figure 3.19**) according to the United States Pharmacopeia (USP) [99].



Figure 3.19 SOTAX dissolution rate tester, USP 2 model. Zoom image shows tablet assembled with the shaft and immersed into the 0.01 M HCl solution at time zero.

In a typical experiment, we firstly prepared a solution of HCl 0.01 M, 900 mL were added into each glass vessel and then heated for 2 h until reaching a temperature of 37 °C. After that, tablets with 8 mm of diameter were prepared for TMP, each cofomer and for the 3 multicomponent solid-forms, using ~ 50 mg of each powder by compression

with a hydraulic press and applying 1 ton for 30 s. After the tablet preparation, each die containing the tablet was assembled with a shaft in the equipment to expose the tablet surface horizontally (zoom **Figure 3.19**). The experiment was led for 45 min at 37 °C and with a rotating stirrer speed of 50 rpm. During this time, 5 mL of sample was collected from each vessel after 5, 15, 25, 35 and 45 min and then injected in the HPLC. After the test, the samples were recovered and dried to be analysed by XRPD.

The HPLC analysis was led to detect the amount of TMP dissolved from the tablets in the medium along the run time. A TMP calibration curve (**Figure 3.20**) was carried out before the analysis to obtain the value of TMP concentration and consequently its mass values in each collected sample.

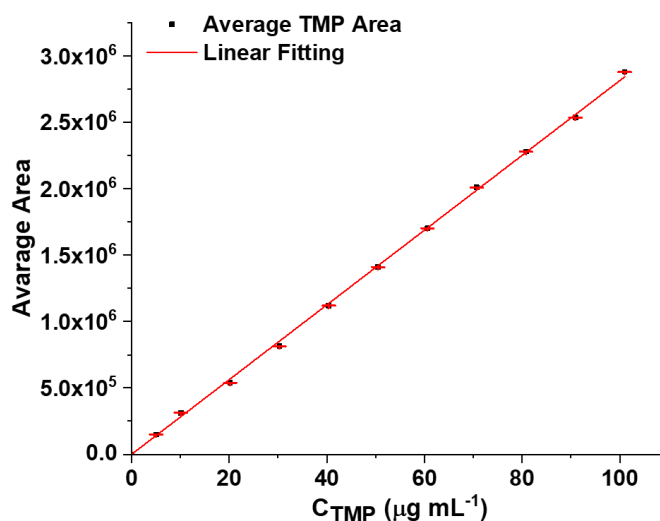


Figure 3.20 TMP calibration curve obtained with a mobile phase of formic acid: acetonitrile (85:15 w/w) in isocratic mode. $\text{Area}_{(\text{TMP})} = (28.29 \times 10^3 \pm 0.21 \times 10^3) [\text{TMP}] + (-0.8 \times 10^4 \pm 1.2 \times 10^4)$, $r = 0.99972$.

The HPLC analysis of TMP was performed using a mixture of formic acid and acetonitrile 85:15 (w/w) as mobile phase, with a flow rate of 1.5 mL min⁻¹. A RP column was used, the oven temperature was set at 30 °C and the TMP concentration was analysed in a range of 0.5 and 50 µg mL⁻¹. The concentration of dissolved TMP, retention time of 2.936 min, was detected at $\lambda = 270$ nm. In this case, we obtained a calibration curve with the equation of $\text{Area}_{(\text{TMP})} = (28.29 \times 10^3 \pm 0.21 \times 10^3) [\text{TMP}] + (-0.8 \times 10^4 \pm 1.2 \times 10^4)$, which will be used in the calculation of the concentration of TMP dissolved during the dissolution rate tests. The results for each system are reported in **Figure 3.21**.

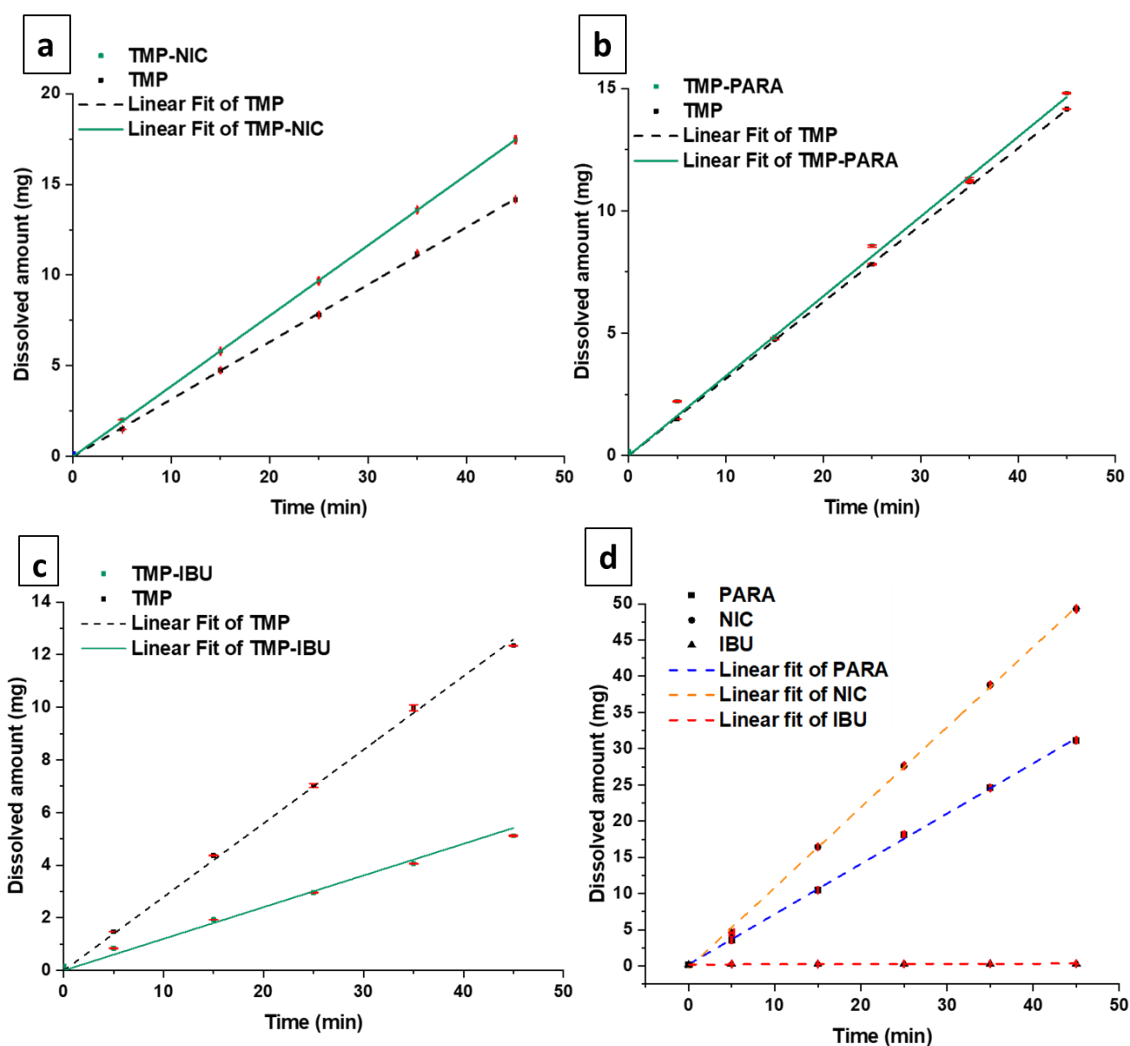


Figure 3.21 TMP amount (a-c) or co-former (d) dissolved as a function of time: **a)** from pure TMP (dashed black line), and from TMP-NIC salt (green line); **b)** from pure TMP (dashed black line), and from TMP-PARA eutectic mixture (green line); **c)** from pure TMP (dashed black line), and from TMP-IBU salt (green line). **d)** amount of co-formers dissolved from pure solids, as a function of time. All values were obtained by HPLC using a mobile phase of formic acid and acetonitrile (85:15 w/w) in isocratic mode.

Table 3.6 TMP dissolution rate values experimentally obtained after HPLC analysis.

Entry	Compound	TMP Dissolution rate ($\mu\text{g min}^{-1}$)
1	TMP ^{a)}	315 ± 3
2	TMP – NIC	388 ± 1
3	TMP ^{b)}	314 ± 2
4	TMP – PARA	327 ± 5
5	TMP ^{c)}	312 ± 3
6	TMP – IBU	120 ± 5

^{a)} TMP dissolution rate calculated during the TMP-NIC experiment; ^{b)} TMP dissolution rate calculated during the TMP-PARA experiment; ^{c)} TMP dissolution rate calculated during the TMP-IBU experiment.

As showed in Table 3.6 and **Figure 3.21 a**, the TMP dissolution rate from the TMP-NIC salt (green line) is 25% higher than the pure TMP dissolution rate (dashed black line) obtained in the same experiment (Table 3.6, entry 1 and 2). This may be caused by the high NIC (**Figure 3.21 d**, dashed orange line) showing a better dissolution rate in the same experimental conditions. In the case of TMP-PARA system, the TMP dissolution rate from the eutectic mixture (**Figure 3.21 b**, green line) showed only a slight increment of 5% compared to that of pure API (dashed black line) (Table 3.6, entry 3 and 4). In this case, we observed a visible enhancement in the tabletability when compared to the PARA alone as previously mentioned in literature by Fukami and co-workers in the pharmaceutical cocrystal between PARA and trimethylglycine [79]. Regarding the combination with IBU (Table 3.6, entry 5 and 6), the TMP dissolution rate in the salt-cocrystal (**Figure 3.21 c**, green line) was lower than the value of pure TMP dissolution rate (dashed black line).

Then, powders of mixtures were collected after each test and their X-ray diffractograms were registered (**Figure 3.22**).

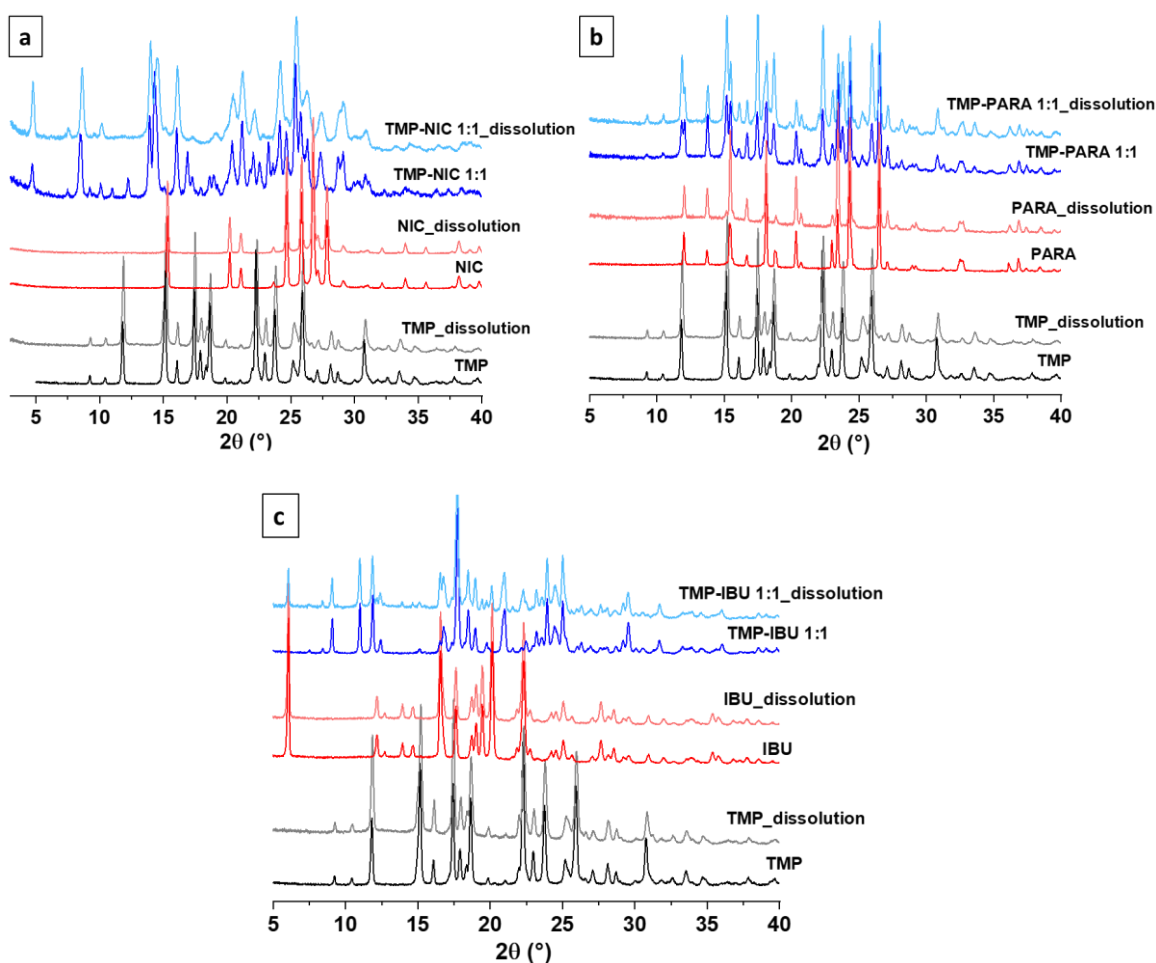


Figure 3.22 X-ray powder diffractograms of: **a)** TMP-NIC system; **b)** TMP-PARA system; **c)** TMP-IBU system. All spectra were acquired before and after the dissolution tests.

X-ray diffractograms prove that no changes of the initial solid forms were observed in any of the investigated systems.

3.4 Antibacterial activity

During our study another aspect that we need to considerate is the ability of the TMP contained in these mixtures to inhibit bacterial growth when compared with the activity of the pure API. While TMP shows antimicrobial activity against Gram-negative and some Gram-positive bacteria [100], it is mainly used in clinic to treat several *E. coli* infections [101]. On the other hand, some of the studied co-formers have already been tested against *S. aureus*, namely IBU and PARA, showing similar antimicrobial activities

among them [42] as well as CURC has also well-recognized antibacterial properties [102]. Thus, our intent was to evaluate if TMP in association with these co-formers shows improved antibacterial activity against both Gram-negative and Gram-positive bacteria. Several examples have been reported about how the development of drug-co-former and drug-drug co-crystals can increase either potentiate or decrease antibiotics' antibacterial activity [103-105]. For instance, Braga and co-workers developed CIP-based co-crystals with thymol and carvacrol with enhanced activity against *E. coli* [94]. Taking this in account, these new multicomponent solid-forms were evaluated against representative Gram-negative (*E. coli* ATCC 8739) and Gram-positive (*S. aureus* ATCC 29213) bacteria, using both agar dilution and broth microdilution assays.

In a typical agar dilution test, a bacterial suspension with a turbidity of 0.5 in the MacFarland scale was prepared in distilled water, which corresponds to $1-2 \times 10^8$ CFU mL⁻¹. Then, the Petri dishes containing Mueller-Hinton (MH) agar were inoculated using a swab soaked with the bacterial suspension. After this, sterile paper discs were applied onto the inoculated MH agar dish, as well as the TMP control disc of 1.25 μ L. Solutions containing the same mass concentration of co-formers and the new multicomponent solid-form were pipetted onto the sterile discs. The Petri dishes were placed in an incubator at 37 °C for 24 h and, after this time, the inhibition zone diameter around each disc was measured. This zone represents the area in which bacterial growth was inhibited by each compound (**Figure 3.23**).

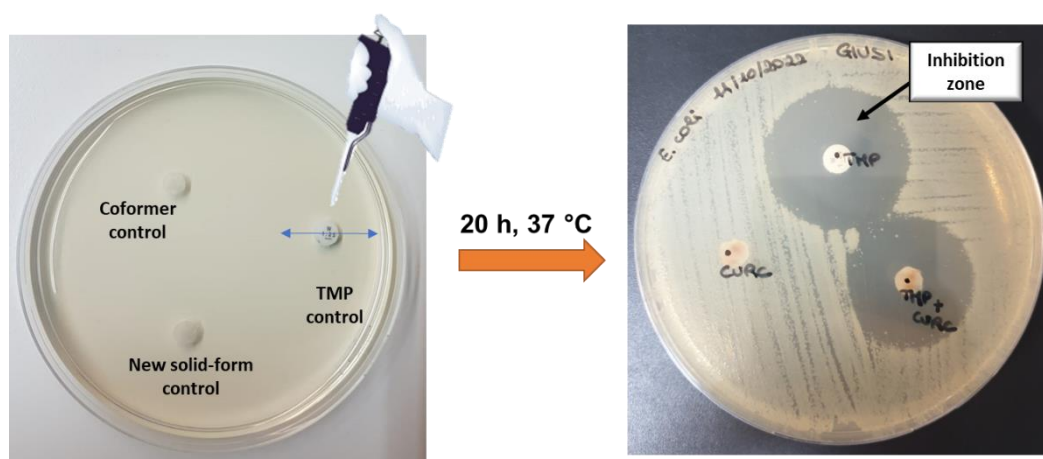


Figure 3.23 Representation of inhibition zone diameter in an agar dilution assay.

The evaluation of inhibition zone diameter was carried out in triplicate for each compound and all the results were presented in **Figure 3.24 a** and **b** for the two species *E. coli* and *S. aureus*, respectively.

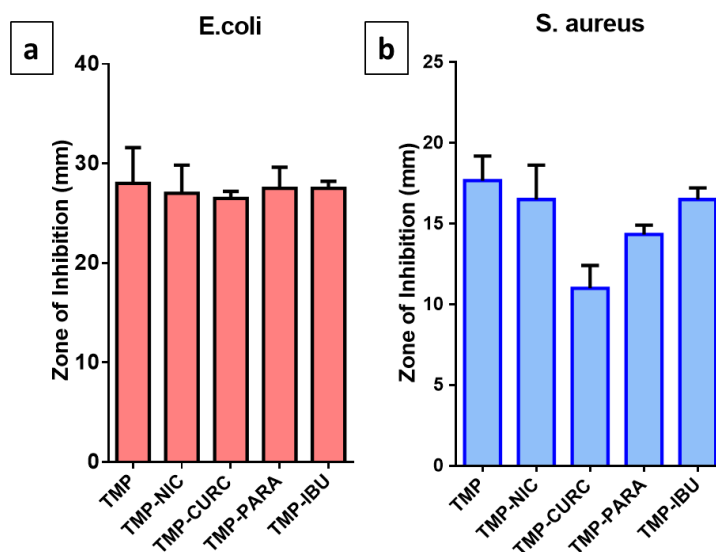


Figure 3.24 Bacterial inhibition studies (disc diffusion assay) using 1.25 μg of TMP (control), TMP-NIC, TMP-CURC, TMP-PARA and TMP-IBU, in: **a)** *E. coli* and **b)** *S. aureus*.

Regarding the **Figure 3.24 a**, TMP showed an average value of 28 mm as diameter of inhibition for *E. coli* which is in accordance with the range of values reported by the EUCAST [94]. In the cases concerning the new multicomponent systems, considering that the coformer did not exhibit antibacterial activity (mm zone of inhibition), the diameters of inhibition were similar to those of the pure API, although the amount of TMP used in the new formulations was less, namely 70 %, 41.5 %, 37 % and 58 % (w/w) for TMP-NIC, TMP-PARA, TMP-CURC and TMP-IBU, respectively. For the *S. aureus*, the TMP of the control disc displayed a value of ~ 18 mm (**Figure 3.24 b**). Additionally, the co-formers did not exhibit antibacterial activity also against this species and TMP in combination with NIC and IBU, showed the same activity as the control. Again, we need to highlight that, although the inhibition diameter was similar to the pure TMP, the amount of TMP used in both of these multicomponent forms was less than the pure TMP. On the other hand, when TMP-PARA was tested a slightly decrease in the diameter of inhibition value (~ 14 mm) was observed as well as for the TMP-CURC (~ 12 mm).

To complement the results obtained through this agar dilution methodology we decided to conduct a more quantitative experiment (broth microdilution), to determine the exact TMP concentration required to inhibit bacterial growth when pure TMP (control) or its multicomponent systems are used. Again, *E. coli* and *S. aureus* were selected as representative bacteria for evaluating the minimum inhibitory concentration (MIC) of TMP while contained in these formulations.

In a typical assay conducted using ISO-2076-1 guidelines [104], MH broth was added to 96 round-bottomed wells microplates. After this, 100 μL of the test ($62.5 \mu\text{g} \mu\text{L}^{-1}$ of pure TMP or TMP multicomponent systems) was added to the first microplate wells and then serially diluted 2-fold across a full line (12 wells total). Next, 5 μL of a $5 \times 10^5 \text{ CFU mL}^{-1}$ inoculum solution were added to each well. Finally, the plate was placed in an incubator at 37 °C along 20 h. After this incubation period, the minimum TMP concentration or which there is no appreciable bacterial growth is considered the MIC. The experimental MIC values for *E. coli* and *S. aureus* are reported in **Figure 3.25**.

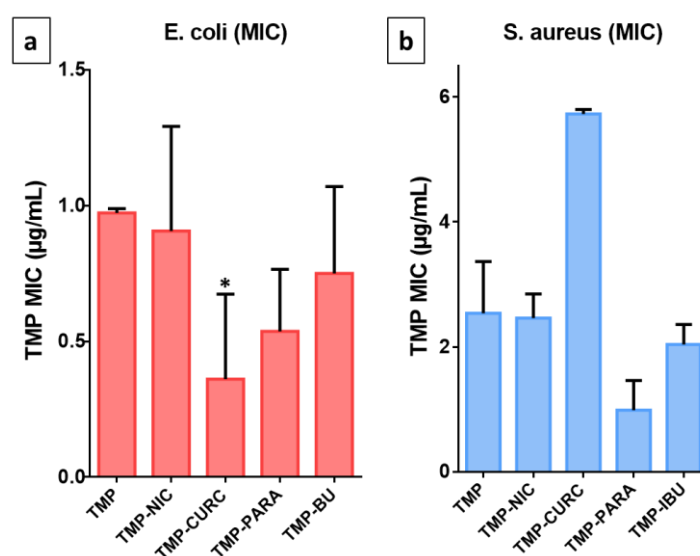


Figure 3.25 Bacterial inhibition studies (MIC assay) of TMP (control), TMP-NIC, TMP-CURC, TMP-PARA and TMP-IBU, in: **a)** *E. coli* and **b)** *S. aureus*. MIC results were normalized for the TMP mass contained in each formulation. The labels * ($p < 0.05$), ** ($p < 0.01$) and *** ($p < 0.001$) represent statistical difference.

The **Figure 3.25 a** showed a MIC value of $\sim 0.98 \mu\text{g mL}^{-1}$ for TMP which was similar to the range reported in the EUCAST [106]. The mean MIC values of TMP in each multicomponent system experimentally determined were ~ 0.91 , ~ 0.54 ,

$\sim 0.75 \mu\text{g mL}^{-1}$ for TMP-NIC, TMP-PARA and TMP-IBU, respectively. As **Figure 3.25 a** shows, the results obtained for these three systems did not exhibit huge differences when compared to the pure TMP MIC, and only the value for the association with PARA showed a higher difference. On the other side, a statistically significant decrease in the TMP MIC value ($\sim 0.36 \mu\text{g mL}^{-1}$), when in a mixture with CURC at the eutectic composition, was experimentally determined. For *S. aureus* (**Figure 3.25 b**), the MIC value of TMP was $\sim 2.54 \mu\text{g mL}^{-1}$, which is also in agreement with the EUCAT list [103]. The average MIC values of TMP in association with NIC was $\sim 2.46 \mu\text{g mL}^{-1}$, whereas when in combination with IBU was $\sim 2.04 \mu\text{g mL}^{-1}$. The system TMP-PARA showed the most relevant difference when compared to the MIC of pure TMP, with $\sim 0.98 \mu\text{g mL}^{-1}$. In the case of TMP-CURC, we observed an inverse effect with an increase in the TMP MIC value ($\sim 5.73 \mu\text{g mL}^{-1}$) meaning a decrease in the TMP antibacterial activity.

Furthermore, we evaluated the *E. coli* susceptibility for TMP and CIP individually and when combined in the estimated eutectic composition, TMP-CIP; $x_{\text{TMP}} = 0.85$, as well as in an equimolar ratio, due the potentiality of this combination, since CIP may be also administered to treat urinary *E. coli* infections (**Figure 3.26 a-d**) [107].

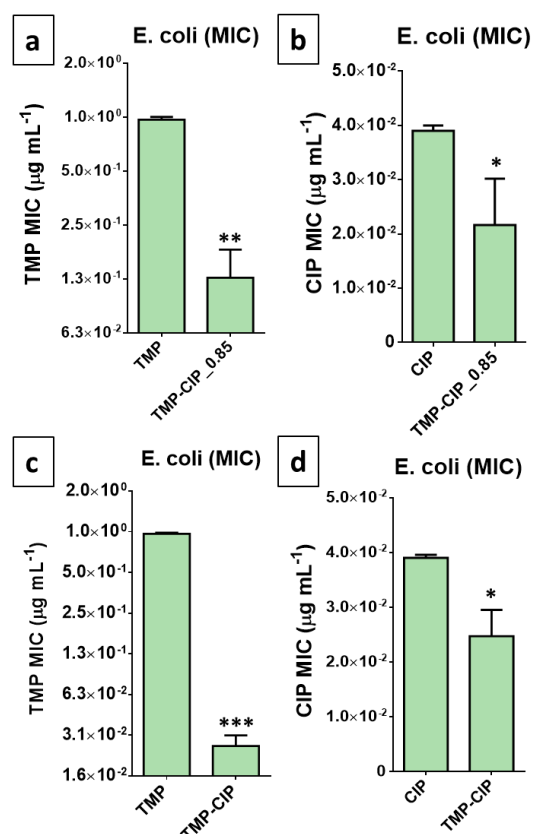


Figure 3.26 Bacterial inhibition studies (MIC assay) in *E. coli* of: **a**) MIC of TMP, while in pure form (TMP) and in an eutectic composition with CIP (TMP-CIP; $x_{\text{TMP}} = 0.85$); **b**) MIC of CIP, while in pure form (CIP) and in eutectic composition with TMP (TMP-CIP; $x_{\text{TMP}} = 0.85$); **c**) MIC of TMP, while in pure form (TMP) and in an equimolar ratio with CIP (TMP-CIP; $x_{\text{TMP}} = 0.50$); **d**) MIC of CIP, while in pure form (CIP) and in equimolar ratio with TMP (TMP-CIP; $x_{\text{TMP}} = 0.50$). The labels * ($p < 0.05$), ** ($p < 0.01$) and *** ($p < 0.001$) represent statistical difference.

In this case, we firstly evaluated the TMP-CIP system with the estimated eutectic composition ($x_{\text{TMP}} = 0.85$) (**Figure 3.26 a and b**). Regarding *E. coli*, the MIC of TMP decreased from $\sim 0.98 \mu\text{g mL}^{-1}$ (pure TMP) to $\sim 0.13 \mu\text{g mL}^{-1}$. At the same time, also the MIC of CIP was experimentally determined showing a MIC value of $\sim 0.039 \mu\text{g mL}^{-1}$ when in the pure form, while in association with TMP ($x_{\text{TMP}} = 0.85$) was $\sim 0.021 \mu\text{g mL}^{-1}$.

Considering the decrease in MIC values experimentally obtained for both antibiotics, when in a eutectic composition, as well as the potentiality of this association, we also tested another ratio increasing the amount of CIP (TMP-CIP, $x_{\text{TMP}} = 0.50$) against

E. coli. Regarding this composition, the MIC of TMP decreased from $\sim 0.98 \mu\text{g mL}^{-1}$ (pure TMP) to $\sim 0.026 \mu\text{g mL}^{-1}$. This result represents a statistically significant 37-fold enhancement of the TMP antibacterial activity [108]. Concerning the CIP antibacterial activity, we obtained experimentally a MIC value of $\sim 0.039 \mu\text{g mL}^{-1}$ while the average MIC for this API in association with TMP was $\sim 0.024 \mu\text{g mL}^{-1}$. Overall, the observed decrease in MIC for both antibiotics, clearly highlights the benefits of combining two antibiotics with different, but complementary, mechanisms of action. In the case of our study this combination had at least an additive effect. The concomitant use of antibiotics which target different enzymes, directly or indirectly involved in DNA synthesis/replication, can potentially lower the probability of resistance development, since it is highly unlikely that bacteria can simultaneously develop mutations that hinder the activity of both molecules. This type of strategy is already employed in clinic as a way to broaden the antibacterial activity spectrum of anti-infectious therapies, improving their chances of success against infections by MDR bacteria [109-111].

3.5 Conclusions

In this chapter, the strategy to prevent the TMP accumulation in environment is described, consisting of the development of TMP-based multicomponent solid forms, with potential to enhance TMP aqueous solubility/dissolution rate and/or its antibacterial activity. Several co-formers were chosen from the GRAS list due to their properties (aqueous solubility, antibacterial activity) and considering the possibility to form reliable heterosynthons with the API, therefore with potential, *a priori*, to give rise to co-crystals. For these reasons, CURC, NIC, PIC, URA, LEU, MAN and RIB were tested in combination with TMP by LAG, EtOH assisted, at 30 Hz along 60 min. Among all, two compounds, equimolarly mixed with TMP, formed two salts, (1:1) TMP-NIC and (1:1) TMP-PIC, that were characterized by XRPD, FTIR and DSC. Concerning the mixtures of TMP with the other GRAS compounds, all of them having highly flexible molecules, and without any free acidic groups, no heteromolecular association was observed, namely for TMP-URA, TMP-LEU, TMP-MAN, TMP-RIB and TMP-CURC, as confirmed by XRPD, FTIR and DSC. For the TMP-CURC eutectic forming system, the eutectic composition was experimentally determined, $x_{\text{TMP}} = 0.43$, due to the potential interest of TMP and CURC association and the pharmaceutical relevance of eutectic mixtures.

The co-former screening was also extended to a group of API compounds, to try to obtain multi-APIs solid forms, which may be of interest due the possibility to combine each API action. So, four APIs were tested namely PARA, IBU, SAL and CIP using the same mechanochemistry conditions. The combination of TMP with SAL and IBU resulted in the formation of two new equimolar supramolecular forms, two salts: TMP-SAL and TMP-IBU, characterized by XRPD, FTIR and DSC. Eutectic forming systems were identified for TMP-PARA and TMP-CIP, with a eutectic composition $x_{\text{TMP}} = 0.27$ and estimated eutectic composition $x_{\text{TMP}} = 0.85$, respectively.

The successful heteromolecular association, in most cases, was well in accordance with the COSMO-Quick software predictions.

Among all these new TMP-based multicomponent solid forms TMP-NIC, TMP-PARA and TMP-IBU were selected to led intrinsic dissolution rate tests, due to the cofomers' potentiality to enhance the TMP solubility/dissolution rate as well as to their importance in the pharmaceutical industry and in patients' daily life. After performing the dissolution rate tests, according to the USP protocol, TMP dissolution rate was 25% and 5% higher than the pure TMP dissolution rate when in combination with NIC and PARA, respectively. No changes in the solid forms took place during the experiments.

The last aspect evaluated was the ability of the TMP contained in selected binary systems to inhibit the *E. coli* (ATCC 8739) and *S. aureus* (ATCC 29213) growth when compared with the activity of the pure API. Systems were selected with co-formers for which there are reported references of some antibacterial effect. TMP-NIC and TMP-IBU salts were chosen, as well as TMP-PARA, TMP-CURC and TMP-CIP eutectic forming systems at the eutectic composition and also at an equimolar proportion for TMP-CIP. TMP diameters of inhibition, when in binary systems, were similar to those of the pure API in both Gram-positive and Gram-negative bacteria, although the amount of TMP used was less, namely 70 %, 41.5 %, 38% and 58 % (w/w) for TMP-NIC, TMP-PARA, TMP-CURC and TMP-IBU, respectively. Additionally, MIC of TMP while contained in these systems was also determined. In *E. coli*, the MIC value of pure TMP was $\sim 0.98 \mu\text{g mL}^{-1}$ and only when in a mixture with CURC, a statistically significant decrease was observed (TMP MIC $\sim 0.36 \mu\text{g mL}^{-1}$). For *S. aureus*, the MIC value of TMP was $\sim 2.54 \mu\text{g mL}^{-1}$ and the system TMP-PARA showed the most relevant difference with $\sim 0.98 \mu\text{g mL}^{-1}$. Since CIP is also clinically administered to treat urinary *E. coli* infections, we evaluated the *E. coli* susceptibility for both APIs individually and when in eutectic

and equimolar compositions. For the equimolar system, a statistically significant 37-fold and 2-fold enhancement of the TMP and CIP antibacterial activity respectively were observed, confirming an additive effect. Activity enhancement was also observed, when using the estimated eutectic composition. These results undoubtedly emphasise the clinical advantages of combining two antibiotics with different, but complementary, mechanisms of action.

3.6 References

- [1] G.R. Desiraju, Supramolecular synthons in crystal engineering—A new organic synthesis, *Angewandte Chemie*, 34 (1995) 2311. <https://doi.org/10.1002/anie.199523111>
- [2] M. Rodrigues, B. Baptista, J.A. Lopes, M.C. Sarraguça, Pharmaceutical cocrystallization techniques. Advances and challenges, *International Journal of Pharmaceutics*, 547 (2018) 404. <https://doi.org/10.1016/j.ijpharm.2018.06.024>
- [3] P.T. Anastas, J.C. Warner, *Green chemistry: theory and practice*, Oxford University Press 1998.
- [4] United Nations. 17 Sustainable Development Goals (2015). Available online: <https://sdgs.un.org/goals> (last accessed on 23/08/2022)
- [5] L. Takacs, The historical development of mechanochemistry, *Chemical Society Reviews*, 42 (2013) 7649. <https://doi.org/10.1039/C2CS35442J>
- [6] M. Solares-Briones, G. Coyote-Dotor, J.C. Páez-Franco, M.R. Zermeño-Ortega, O. de La, C.C. M., D. Canseco-González, A. Avila-Sorrosa, D. Morales-Morales, J.M. Germán-Acacio, Mechanochemistry: a green approach in the preparation of pharmaceutical cocrystals, *Pharmaceutics*, 13 (2021) 790. <https://doi.org/10.3390/pharmaceutics13060790>
- [7] D. Hasa, W. Jones, Screening for new pharmaceutical solid forms using mechanochemistry: a practical guide, *Advanced Drug Delivery Reviews*, 117 (2017) 147. <https://doi.org/10.1016/j.addr.2017.05.001>
- [8] B. Saikia, A. Seidel-Morgenstern, H. Lorenz, Role of mechanochemistry in solid form selection and identification of the drug praziquantel, *Crystal Growth & Design*, 21 (2021) 5854. <https://doi.org/10.1021/acs.cgd.1c00736>
- [9] D. Hasa, G. Schneider Rauber, D. Voinovich, W. Jones, Cocrystal formation through mechanochemistry: from neat and liquid-assisted grinding to polymer-assisted grinding, *Angewandte Chemie International Edition*, 54 (2015) 7371. <https://doi.org/10.1002/anie.201501638>
- [10] M. Karimi-Jafari, L. Padrela, G.M. Walker, D.M. Croker, Creating cocrystals: a review of pharmaceutical cocrystal preparation routes and applications, *Crystal Growth & Design*, 18 (2018) 6370. <https://doi.org/10.1021/acs.cgd.8b00933>
- [11] A. Delori, T. Friščić, W. Jones, The role of mechanochemistry and supramolecular design in the development of pharmaceutical materials, *Crystal Engineering Communications*, 14 (2012) 2350. <https://doi.org/10.1039/C2CE06582G>

- [12] S.M.T. Machado, R.A.E. Castro, T.M.R. Maria, J. Canotilho, M.E.S. Eusébio, Levetiracetam+nonsteroidal anti-inflammatory drug binary systems: a contribution to the development of new solid dosage forms, *International Journal of Pharmaceutics*, 533 (2017) 1. <http://doi.org/10.1016/j.ijpharm.2017.09.012>
- [13] G.A. Bowmaker, Solvent-assisted mechanochemistry, *Chemical Communications*, 49 (2013) 334. <https://doi.org/10.1039/C2CC35694E>
- [14] D. Braga, L. Maini, F. Grepioni, Mechanochemical preparation of co-crystals, *Chemical Society Reviews*, 42 (2013) 7638. <https://doi.org/10.1039/C3CS60014A>
- [15] S.L. James, C.J. Adams, C. Bolm, D. Braga, P. Collier, T. Friščić, F. Grepioni, K.D.M. Harris, G. Hyett, W. Jones, A. Krebs, J. Mack, L. Maini, A.G. Orpen, I.P. Parkin, W.C. Shearouse, J.W. Steed, D.C. Waddell, Mechanochemistry: opportunities for new and cleaner synthesis, *Chemical Society Reviews*, 41 (2012) 413. <https://doi.org/10.1039/C1CS15171A>
- [16] V. André, M.T. Duarte, C.S.B. Gomes, M.C. Sarraguça, Mechanochemistry in Portugal - a step towards sustainable chemical synthesis, *Molecules*, 27 (2022) 241. <https://doi.org/10.3390/molecules27010241>
- [17] X. Liu, Y. Li, L. Zeng, X. Li, N. Chen, S. Bai, H. He, Q. Wang, C. Zhang, A review on mechanochemistry: approaching, advanced energy materials with greener force, *Advanced Materials*, 34 (2022) 2108327. <https://doi.org/10.1002/adma.202108327>
- [18] V. André, A. Fernandes, P.P. Santos, M.T. Duarte, On the track of new multicomponent gabapentin crystal forms: synthon competition and pH stability, *Crystal Growth & Design*, 11 (2011) 2325. <https://doi.org/10.1021/cg200008z>
- [19] M. Lindenberg, S. Kopp, J.B. Dressman, Classification of orally administered drugs on the World Health Organization model list of essential medicines according to the biopharmaceutics classification system, *European Journal of Pharmaceutics and Biopharmaceutics*, 58 (2004) 265. <https://doi.org/10.1016/j.ejpb.2004.03.001>
- [20] S. Budavari, M. O'Neil, A. Smith, P. Heckelman, J. Obenchain, *The Merck Index*, 12th ed., Entry 9840, 1996.
- [21] Trimethoprim monograph. Trimethoprim tablets USP 100 mg and 200 mg. https://pdf.hres.ca/dpd_pm/00025165.PDF (last accessed 20/09/2022)
- [22] S. Murugesan, P.T. Muthiah, Hydrogen-bonding patterns in trimethoprim nitrate, an antifolate drug, *Acta Crystallographica. Section C. Structural Chemistry*, C53 (1997) 763. <https://doi.org/10.1107/S0108270196015636>

- [23] B. Umadevi, P. Prabakaran, P.T. Muthiah, A pseudo-quadruple hydrogen-bonding motif consisting of six N-H...O hydrogen bonds in trimethoprim formate, *Acta Crystallographica. Section C. Structural Chemistry*, C58 (2002) o510. <https://doi.org/10.1107/S0108270102011150>
- [24] P. Prabakaran, J.J. Robert, P.T. Muthiah, G. Bocelli, L. Righi, Amino-pyrimidine-carboxyl-(ate) interactions in trimethoprim maleate, an antifolate drug, *Acta Crystallographica. Section C. Structural Chemistry*, C57 (2001) 459. <https://doi.org/10.1107/S0108270101000269>
- [25] Q.C. Ton, E. Egert, Cocrystals of the antibiotic trimethoprim with glutarimide and 3,3-dimethylglutarimide held together by three hydrogen bonds, *Acta Crystallographica. Section C. Structural Chemistry*, 71 (2015) 75. <https://doi.org/10.1107/s2053229614027193>
- [26] S. Baskar Raj, P.T. Muthiah, U. Rychlewska, B. Warzajtis, Pseudo-polymorphism and crystal engineering: hydrogen-bonded supramolecular networks in trimethoprim m-chlorobenzoate and trimethoprim m-chlorobenzoate dihydrate, *Crystal Engineering Communications*, 5 (2003) 48. <https://doi.org/10.1039/B211312K>
- [27] P.T. Muthiah, B. Umadevi, N. Stanley, X. Shui, D.S. Eggleston, Hydrogen bonding patterns in trimethoprim sulfate trihydrate [trimethoprim = 2,4-di-amino-5-(3,4,5-methoxy-benzyl)-pyrimidine], *Acta Crystallographica. Section E. Crystallographic Communications*, E57 (2001) o1179. <https://doi.org/10.1107/S1600536801018657>
- [28] P. Panneerselvam, N. Stanley, P.T. Muthiah, N-H...N hydrogen bonds in trimethoprim salicylate methanol solvate [trimethoprim is 2,4-di-amino-5-(3,4,5-tri-methoxy-benzyl)-pyrimidine], *Acta Crystallographica. Section E. Crystallographic Communications*, E58 (2002) o180. <https://doi.org/10.1107/S1600536802000909>
- [29] S. Umar, R. Farnandi, H. Salsabila, E. Zaini, Multicomponent crystal of trimethoprim and citric acid: solid state characterization and dissolution rate studies, *Open Access Macedonian Journal of Medical Sciences*, 10 (2022) 141. <https://doi.org/10.3889/oamjms.2022.7920>
- [30] Y. Yuliandra, L.J. Hutabarat, R. Ardila, M.D. Octavia, E. Zaini, Enhancing solubility and antibacterial activity using multi-component crystals of trimethoprim and malic acid, *Pharmacy Education*, 21 (2021) 296. <https://doi.org/10.46542/pe.2021.212.296304>
- [31] B. Bhattacharya, S. Das, G. Lal, S.R. Soni, A. Ghosh, C.M. Reddy, S. Ghosh, Screening, crystal structures and solubility studies of a series of multidrug salt hydrates and cocrystals of fenamic acids with trimethoprim and sulfamethazine, *Journal of*

- Molecular Structure, 1199 (2020) 127028.
<https://doi.org/10.1016/j.molstruc.2019.127028>
- [32] G. Bettinetti, M.R. Caira, A. Callegari, M. Merli, M. Sorrenti, C. Tadini, Structure and solid-state chemistry of anhydrous and hydrated crystal forms of the trimethoprim-sulfamethoxypyridazine 1:1 molecular complex, *Journal of Pharmaceutical Sciences*, 89 (2000) 478. [https://doi.org/10.1002/\(sici\)1520-6017\(200004\)89](https://doi.org/10.1002/(sici)1520-6017(200004)89)
- [33] A. ElShaer, P. Hanson, T. Worthington, P. Lambert, A.R. Mohammed, Preparation and characterization of amino acids-based trimethoprim salts, *Pharmaceutics*, 4 (2012) 179. <https://doi.org/10.3390/pharmaceutics4010179>
- [34] FDA-Generally Recognized as Safe (GRAS). <https://www.fda.gov/food/food-ingredients-packaging/generally-recognized-safe-gras> (last accessed 01/09/2022)
- [35] P. Cui, X. Li, M. Zhu, B. Wang, J. Liu, H. Chen, Design, synthesis and antimicrobial activities of thiouracil derivatives containing triazolo-thiadiazole as SecA inhibitors, *European Journal of Medicinal Chemistry*, 127 (2017) 159. <https://doi.org/10.1016/j.ejmech.2016.12.053>
- [36] M. Sanduja, J. Gupta, H. Singh, P.P. Pagare, A. Rana, Uracil-coumarin based hybrid molecules as potent anti-cancer and anti-bacterial agents, *Journal of Saudi Chemical Society*, 24 (2020) 251. <https://doi.org/10.1016/j.jscs.2019.12.001>
- [37] K. Suresh, A. Nangia, Curcumin: pharmaceutical solids as a platform to improve solubility and bioavailability, *Crystal Engineering Communications*, 20 (2018) 3277. <https://doi.org/10.1039/C8CE00469B>
- [38] P.O. Ferreira, A.C. de Almeida, É.C. dos Santos, R. Droppa, F.F. Ferreira, A.C. Kogawa, F.J. Caires, A norfloxacin-nicotinic acid cocrystal: mechanochemical synthesis, thermal and structural characterization and solubility assays, *Thermochimica Acta*, 694 (2020) 178782. <https://doi.org/10.1016/j.tca.2020.178782>
- [39] S. Cai, K. Sato, T. Shimizu, S. Yamabe, M. Hiraki, C. Sano, H. Tomioka, Antimicrobial activity of picolinic acid against extracellular and intracellular *Mycobacterium avium* complex and its combined activity with clarithromycin, rifampicin and fluoroquinolones, *Journal of Antimicrobial Chemotherapy*, 57 (2005) 85. <https://doi.org/10.1093/jac/dki418>
- [40] R. Thipparaboina, D. Kumar, R.B. Chavan, N.R. Shastri, Multidrug co-crystals: towards the development of effective therapeutic hybrids, *Drug Discov Today*, 21 (2016) 481. <https://doi.org/10.1016/j.drudis.2016.02.001>

- [41] T. Santarupa, Revisiting aspirin, paracetamol and ibuprofen: discovery of synthetic procedures and mode of actions, *Trends in Technical & Scientific Research*, 4 (2020) 555636. <https://doi.org/10.19080/TTSR.2020.04.555636>
- [42] A.A. Al-Janabi, In vitro antibacterial activity of ibuprofen and acetaminophen, *Journal of Global Infectious Diseases*, 2 (2010) 105. <https://doi.org/10.4103/0974-777x.62880>
- [43] D. Sharma, R.P. Patel, S.T.R. Zaidi, M.M.R. Sarker, Q.Y. Lean, L.C. Ming, Interplay of the quality of ciprofloxacin and antibiotic resistance in developing countries, *Frontiers in Pharmacology*, 8 (2017). <https://doi.org/10.3389/fphar.2017.00546>
- [44] R. Nunes Costa, D. Choquesillo-Lazarte, S.L. Cuffini, E. Pidcock, L. Infantes, Optimization and comparison of statistical tools for the prediction of multicomponent forms of a molecule: the antiretroviral nevirapine as a case study, *Crystal Engineering Communications*, 22 (2020) 7460. <https://doi.org/10.1039/D0CE00948B>
- [45] J.A. Baptista, M.T.S. Rosado, R.A.E. Castro, A.O.L. Évora, T.M.R. Maria, M. Ramos Silva, J. Canotilho, M.E.S. Eusébio, Dihydrofolate reductase inhibitors: the pharmacophore as a guide for co-crystal screening, *Molecules*, 26 (2021) 6721. <https://doi.org/10.3390/molecules26216721>
- [46] J. Hong, J.T. Golab, J.A. Kaduk, A.M. Gindhart, T.N. Blanton, Powder X-ray diffraction of trimethoprim Form I, C₁₄H₁₈N₄O₃, *Powder Diffraction*, 35 (2020) 69. <https://doi.org/10.1017/S0885715619000927>
- [47] T.F. Koetzle, G.J.B. Williams, The crystal and molecular structure of the antifolate drug trimethoprim (2,4-diamino-5-(3,4,5-trimethoxybenzyl)pyrimidine). A neutron diffraction study, *Journal of the American Chemical Society*, 98 (1976) 2074. <https://doi.org/10.1021/ja00424a009>
- [48] A. Ungurean, N. Leopold, L. David, V. Chiş, Vibrational spectroscopic and DFT study of trimethoprim, *Spectrochimica Acta Part A: Molecular and Biomolecular Spectroscopy*, 102 (2013) 52. <https://doi.org/10.1016/j.saa.2012.10.026>
- [49] P. Sanphui, N.R. Goud, U.B.R. Khandavilli, A. Nangia, Fast dissolving curcumin cocrystals, *crystal growth & design*, 11 (2011) 4135. <https://doi.org/10.1021/cg200704s>
- [50] E.H. Ismail, D.Y. Sabry, H. Mahdy, M.M.H. Khalil, Synthesis and characterization of some ternary metal complexes of curcumin with 1,10-phenanthroline and their anticancer applications, *Journal of Scientific Research*, 6 (2014) 509. <https://doi.org/10.3329/jsr.v6i3.18750>

- [51] W.H. Lee, C.Y. Loo, M. Bebawy, F. Luk, R.S. Mason, R. Rohanizadeh, Curcumin and its derivatives: their application in neuropharmacology and neuroscience in the 21st century, *Current Neuropharmacology*, 11 (2013) 338. <https://doi.org/10.2174/1570159x11311040002>
- [52] L.A. Carlson, Nicotinic acid: the broad-spectrum lipid drug. A 50th anniversary review, 258 (2005) 94. <https://doi.org/10.1111/j.1365-2796.2005.01528.x>
- [53] A.C. de Almeida, C. Torquetti, P.O. Ferreira, R.P. Fernandes, E.C. dos Santos, A.C. Kogawa, F.J. Caires, Cocrystals of ciprofloxacin with nicotinic and isonicotinic acids: mechanochemical synthesis, characterization, thermal and solubility study, *Thermochimica Acta*, 685 (2020) 178346. <https://doi.org/10.1016/j.tca.2019.178346>
- [54] P. Sanphui, L. Rajput, Tuning solubility and stability of hydrochlorothiazide co-crystals, *Acta crystallographica. Section B. Structural science, crystal engineering and materials*, 70 (2014) 81. <https://doi.org/10.1107/s2052520613026917>
- [55] W.B. Wright, G.S.D. King, The crystal structure of nicotinic acid, *Acta Crystallographica*, 6 (1953) 305. <https://doi.org/10.1107/S0365110X53000867>
- [56] P. Koczoń, J.C. Dobrowolski, W. Lewandowski, A.P. Mazurek, Experimental and theoretical IR and Raman spectra of picolinic, nicotinic and isonicotinic acids, *Journal of Molecular Structure*, 655 (2003) 89. [https://doi.org/10.1016/S0022-2860\(03\)00247-3](https://doi.org/10.1016/S0022-2860(03)00247-3)
- [57] Q. Zheng, D.K. Unruh, K.M. Hutchins, Cocrystallization of trimethoprim and solubility enhancement via salt formation, *Crystal Growth & Design*, 21 (2021) 1507. <https://doi.org/10.1021/acs.cgd.0c01197>
- [58] R.S. Grant, S.E. Coggan, G.A. Smythe, The physiological action of picolinic acid in the human brain, *International Journal of Tryptophan Research*, 2 (2009) 71. <https://doi.org/10.4137/ijtr.S2469>
- [59] M.H. Borawska, S.K. Czechowska, R. Markiewicz, J. Palka, R. Swislocka, W. Lewandowski, Antimicrobial activity and cytotoxicity of picolinic acid and selected picolinates as new potential food preservatives, *Polish Journal of Food and Nutrition Sciences*, 58 (2008) 415. <https://agro.icm.edu.pl/agro/element/bwmeta1.element.agro-64f57306-bf24-43b2-9e53-57321b4fa325>
- [60] C. Torquetti, P.O. Ferreira, A.C. de Almeida, R.P. Fernandes, F.J. Caires, Thermal study and characterization of new cocrystals of ciprofloxacin with picolinic acid, *Journal of Thermal Analysis and Calorimetry*, 147 (2022) 1299. <https://doi.org/10.1007/s10973-020-10479-3>

- [61] A.L.C.S. do Nascimento, J.A. Teixeira, W.D.G. Nunes, F.X. Campos, O. Treu-Filho, F.J. Caires, M. Ionashiro, Thermal behavior, spectroscopic study and evolved gas analysis (EGA) during pyrolysis of picolinic acid, sodium picolinate and its light trivalent lanthanide complexes in solid state, *Journal of Analytical and Applied Pyrolysis*, 119 (2016) 242. <https://doi.org/10.1016/j.jaap.2016.01.010>
- [62] H. Hamazaki, H. Hosomi, S. Takeda, H. Kataoka, S. Ohba, 2-pyridinecarboxylic acid, *Acta Crystallographica, Section C: Crystal Structure Communications*, 54 (1998) 9800049. <https://doi.org/10.1107/S0108270198099314>
- [63] S.M. Ghoreishi, R.G. Shahrestani, Innovative strategies for engineering mannitol production, *Trends in Food Science & Technology*, 20 (2009) 263. <https://doi.org/10.1016/j.tifs.2009.03.006>
- [64] H. Shawkat, M.M. Westwood, A. Mortimer, Mannitol: a review of its clinical uses, *Continuing Education in Anaesthesia Critical Care & Pain*, 12 (2012) 82. <https://doi.org/10.1093/bjaceaccp/mkr063>
- [65] I. Nugrahani, M.A. Jessica, Amino acids as the potential co-former for co-crystal development: a review, *Molecules*, 26 (2021) 3279. <https://doi.org/10.3390/molecules26113279>
- [66] K.D. Shah, S. Borhade, V.Y. Londhe, Utilization of co-crystallization for solubility enhancement of a poorly soluble antiretroviral drug-ritonavir, *International Journal of Pharmacy and Pharmaceutical Sciences*, 6 (2014) 556. <https://innovareacademics.in/journal/ijpps/Vol6Issue2/8819.pdf>
- [67] A. Saedisomeolia, M. Ashoori, Chapter two - Riboflavin in human health: a review of current evidences, *Advances in Food and Nutrition Research*, Academic Press 2018, pp. 57.
- [68] D. Ramesh, B.G. Vijayakumar, T. Kannan, Therapeutic potential of uracil and its derivatives in countering pathogenic and physiological disorders, *European Journal of Medicinal Chemistry*, 207 (2020) 112801. <https://doi.org/10.1016/j.ejmech.2020.112801>
- [69] S. Kumar, Spectroscopic studies of valine and leucine molecules a comparative study, *Elixir Vibrational Spectroscopy*, 39 (2011) 4996. [https://www.elixirpublishers.com/articles/1350637958_39%20\(2011\)%204996-4999.pdf](https://www.elixirpublishers.com/articles/1350637958_39%20(2011)%204996-4999.pdf)
- [70] M.-J. Yun, B.-S. Cheong, H.-G. Cho, Surface-enhanced Raman spectroscopy and density functional theory studies of riboflavin, lumiflavin, and lumichrome adsorbed on

silver colloids, *Bulletin of the Korean Chemical Society*, 40 (2019) 1183.
<https://doi.org/10.1002/bkcs.11898>

[71] Chemical Book-CAS DataBase List_ L-Leucine.
[https://www.chemicalbook.com/ChemicalProductProperty_EN_CB8742186.htm#:~:tex](https://www.chemicalbook.com/ChemicalProductProperty_EN_CB8742186.htm#:~:text=Chemical%20Properties,-)
[t=Chemical%20Properties,-](https://www.chemicalbook.com/ChemicalProductProperty_EN_CB8742186.htm#:~:text=Chemical%20Properties,-)

White%20shiny%20hexahedral&text=Sublimation%20at%20145~148%20%E2%84%83,~295%20%E2%84%83%20(decomposition) (last accessed on 14/09/2022)

[72] A.V. Knyazev, I.A. Letyanina, A.S. Plesovskikh, N.N. Smirnova, S.S. Knyazeva, Thermodynamic properties of vitamin B2, *Thermochimica Acta*, 575 (2014) 12.
<https://doi.org/10.1016/j.tca.2013.09.032>

[73] P.P. Moorthi, S. Gunasekaran, S. Swaminathan, G.R. Ramkumaar, Quantum chemical density functional theory studies on the molecular structure and vibrational spectra of mannitol, *Spectrochimica Acta Part A: Molecular and Biomolecular Spectroscopy*, 137 (2015) 412. <https://doi.org/10.1016/j.saa.2014.08.066>

[74] Á. Gombás, P. Szabó-Révész, G. Regdon, I. Erős, Study of thermal behaviour of sugar alcohols, *Journal of Thermal Analysis and Calorimetry*, 73 (2003) 615.
<https://doi.org/10.1023/A:1025490432142>

[75] B.S. Sekhon, Drug-drug co-crystals, *DARU Journal of Pharmaceutical Sciences*, 20 (2012) 45. <https://doi.org/10.1186/2008-2231-20-45>

[76] A. Bertolini, A. Ferrari, A. Ottani, S. Guerzoni, R. Tacchi, S. Leone, Paracetamol: new vistas of an old drug, *CNS Drug Reviews*, 12 (2006) 250.
<https://doi.org/10.1111/j.1527-3458.2006.00250.x>

[77] L. Kalantzi, C. Reppas, J.B. Dressman, G.L. Amidon, H.E. Junginger, K.K. Midha, V.P. Shah, S.A. Stavchansky, D.M. Barends, Biowaiver monographs for immediate release solid oral dosage forms: acetaminophen (paracetamol), *Journal of Pharmaceutical Sciences*, 95 (2006) 4. <https://doi.org/10.1002/jps.20477>

[78] S. Karki, T. Frišćić, L. Fábíán, P.R. Laity, G.M. Day, W. Jones, Improving mechanical properties of crystalline solids by cocrystal formation: new compressible forms of paracetamol, *Advanced Materials*, 21 (2009) 3905.
<https://doi.org/10.1002/adma.200900533>

[79] Y. Maeno, T. Fukami, M. Kawahata, K. Yamaguchi, T. Tagami, T. Ozeki, T. Suzuki, K. Tomono, Novel pharmaceutical cocrystal consisting of paracetamol and trimethylglycine, a new promising cocrystal former, *International Journal of Pharmaceutics*, 473 (2014) 179. <https://doi.org/10.1016/j.ijpharm.2014.07.008>

- [80] J. Sibik, M.J. Sargent, M. Franklin, J.A. Zeitler, Crystallization and phase changes in paracetamol from the amorphous solid to the liquid phase, *Molecular Pharmaceutics*, 11 (2014) 1326. <https://doi.org/10.1021/mp400768m>
- [81] D.Y. Naumov, M.A. Vasilchenko, J.A.K. Howard, The monoclinic form of acetaminophen at 150 K, *Acta Crystallographica, Section C: Crystal Structure Communications*, 54 (1998) 653. <https://doi.org/10.1107/S0108270197018386>
- [82] M.K. Trivedi, S. Patil, H. Shettigar, K. Bairwa, S. Jana, Effect of biofield treatment on spectral properties of paracetamol and piroxicam, *Chemical Sciences Journal*, 6 (2015) 1. <https://doi.org/10.4172/2150-3494.100098>
- [83] M.K. Trivedi, A. Branton, D. Trivedi, H. Shettigar, K. Bairwa, S. Patil, Fourier transform infrared and ultraviolet-visible spectroscopic characterization of biofield treated salicylic acid and sparfloxacin, *Natural Products Chemistry & Research*, 3 (2015) 1. <https://doi.org/10.4172/2329-6836.1000186>
- [84] Chemical Book-CAS DataBase List_ Salicylic acid. https://www.chemicalbook.com/ChemicalProductProperty_EN_CB1680010.htm. (last accessed on 15/09/2022)
- [85] H. AlRabiah, J.W. Allwood, E. Correa, Y. Xu, R. Goodacre, pH plays a role in the mode of action of trimethoprim on *Escherichia coli*, *PLOS ONE*, 13 (2018) e0200272. <https://doi.org/10.1371/journal.pone.0200272>
- [86] S.L. Childs, G.P. Stahly, A. Park, The salt–aocrystal aontinuum: the influence of crystal structure on ionization state, *Molecular Pharmaceutics*, 4 (2007) 323. <https://doi.org/10.1021/mp0601345>
- [87] Y. Yuliandra, E. Zaini, S. Syofyan, W. Pratiwi, L.N. Putri, Y.S. Pratiwi, H. Arifin, Cocrystal of ibuprofen-nicotinamide: solid-state characterization and in vivo analgesic activity evaluation, *Scientia Pharmaceutica*, 86 (2018) 1. <https://doi.org/10.3390/scipharm86020023>
- [88] F.L.F. Soares, R.L. Carneiro, Green synthesis of ibuprofen–nicotinamide cocrystals and in-line evaluation by Raman spectroscopy, *Crystal Growth & Design*, 13 (2013) 1510. <https://doi.org/10.1021/cg3017112>
- [89] M.F. Othman, N. Anuar, S. Ad Rahman, N.A. Ahmad Taifuddin, Cocrystal screening of ibuprofen with oxalic acid and citric acid via grinding method, *IOP Conference Series: Materials Science and Engineering*, 358 (2018) 012065. <https://doi.org/10.1088/1757-899x/358/1/012065>

- [90] U.S. Food & Drug Administration. https://www.accessdata.fda.gov/drugsatfda_docs/label/2007/019842s020lbl.pdf (last accessed on 17/09/2022)
- [91] J.F. McConnell, *Crystal Structure Communications*, 3 (1974) 73. (DOI not found)
- [92] S. Ramukutty, E. Ramachandran, Growth, spectral and thermal studies of ibuprofen crystals, *Crystal Research and Technology*, 47 (2012) 31. <https://doi.org/10.1002/crat.201100394>
- [93] P.C. Sharma, A. Jain, S. Jain, R. Pahwa, M.S. Yar, Ciprofloxacin: review on developments in synthetic, analytical, and medicinal aspects, *Journal of Enzyme Inhibition and Medicinal Chemistry*, 25 (2010) 577. <https://doi.org/10.3109/14756360903373350>
- [94] O. Shemchuk, S. d'Agostino, C. Fiore, V. Sambri, S. Zannoli, F. Grepioni, D. Braga, Natural antimicrobials meet a synthetic antibiotic: carvacrol/thymol and ciprofloxacin cocrystals as a promising solid-state route to activity enhancement, *Crystal Growth & Design*, 20 (2020) 6796. <https://doi.org/10.1021/acs.cgd.0c00900>
- [95] M. Williams, J. Sittenauer, S. Clark, J. Farthing, M. Baltezor, M. McClorey, Ciprofloxacin polymorph and its use, 2019.
- [96] U. Freo, C. Ruocco, A. Valerio, I. Scagnol, E. Nisoli, Paracetamol: a review of guideline recommendations, *Journal of Clinical Medicine*, 10 (2021) 3420. <https://doi.org/10.3390/jcm10153420>
- [97] Over the Counter (OTC) Analgesics Market. <https://www.factmr.com/report/75/otc-analgesics-market> (last accessed on 25/09/2022)
- [98] T. Ghosh, T. Juturu, S.N. Nagar, S. Kamath, Cocrystals of modafinil-nicotinic acid: a novel cocrystal for enhanced bioavailability, *Proceedings of the National Academy of Sciences*, 62 (2020) 12. <https://doi.org/10.3390/proceedings2020062012>
- [99] U.S. Pharmacopeia - USP Trimethoprim tablets. http://www.pharmacopeia.cn/v29240/usp29nf24s0_m85955.html (last accessed on 25/09/2022)
- [100] R. Gleckman, N. Blagg, D.W. Joubert, Trimethoprim: mechanisms of action, antimicrobial activity, bacterial resistance, pharmacokinetics, adverse reactions, and therapeutic indications, *Pharmacotherapy*, 1 (1981) 14. <https://doi.org/10.1002/j.1875-9114.1981.tb03548.x>
- [101] M.S. Manna, Y.T. Tamer, I. Gaszek, N. Poulides, A. Ahmed, X. Wang, F.C.R. Toprak, D.R. Woodard, A.Y. Koh, N.S. Williams, D. Borek, A.R. Atilgan, J.D.

- Hulleman, C. Atilgan, U. Tambar, E. Toprak, A trimethoprim derivative impedes antibiotic resistance evolution, *Nature Communications*, 12 (2021) 2949. <https://doi.org/10.1038/s41467-021-23191-z>
- [102] H. Gunes, D. Gulen, R. Mutlu, A. Gumus, T. Tas, A.E. Topkaya, Antibacterial effects of curcumin: an in vitro minimum inhibitory concentration study, *Toxicology and Industrial Health*, 32 (2016) 246. <https://doi.org/10.1177/0748233713498>
- [103] N. Ul Islam, E. Khan, M. Naveed Umar, A. Shah, M. Zahoor, R. Ullah, A. Bari, Enhancing dissolution rate and antibacterial efficiency of azithromycin through drug-drug cocrystals with paracetamol, *Antibiotics*, 10 (2021) 939. <https://doi.org/10.3390/antibiotics10080939>
- [104] C. Fiore, A. Baraghini, O. Shemchuk, V. Sambri, M. Morotti, F. Grepioni, D. Braga, Inhibition of the antibiotic activity of cephalosporines by co-crystallization with thymol, *Crystal Growth & Design*, 22 (2022) 1467. <https://doi.org/10.1021/acs.cgd.1c01435>
- [105] V.N. Lima, C.D.M. Oliveira-Tintino, E.S. Santos, L.P. Morais, S.R. Tintino, T.S. Freitas, Y.S. Geraldo, R.L.S. Pereira, R.P. Cruz, I.R.A. Menezes, H.D.M. Coutinho, Antimicrobial and enhancement of the antibiotic activity by phenolic compounds: gallic acid, caffeic acid and pyrogallol, *Microbial Pathogenesis*, 99 (2016) 56. <https://doi.org/10.1016/j.micpath.2016.08.004>
- [106] EUCAST_Antimicrobial wild type distributions of microorganisms. https://mic.eucast.org/search/?search%5Bmethod%5D=mic&search%5Bantibiotic%5D=-1&search%5Bspecies%5D=261&search%5Bdisk_content%5D=-1&search%5Blimit%5D=50&page=2 (last accessed on 28/09/2022)
- [107] L. Jakobsen, C.V. Lundberg, N. Frimodt-Møller, Ciprofloxacin pharmacokinetics/pharmacodynamics against susceptible and low-level resistant *Escherichia coli* isolates in an experimental ascending urinary tract infection model in mice, *Antimicrobial Agents and Chemotherapy*, 65 (2020) e01804. <https://doi.org/10.1128/AAC.01804-20>
- [108] E.I.G. Azenha, A.C. Serra, M. Pineiro, M.M. Pereira, J. Seixas de Melo, L.G. Arnaut, S.J. Formosinho, A.M.d.A. Rocha Gonsalves, Heavy-atom effects on metalloporphyrins and polyhalogenated porphyrins, *Chemical Physics*, 280 (2002) 177. [https://doi.org/10.1016/S0301-0104\(02\)00485-8](https://doi.org/10.1016/S0301-0104(02)00485-8)
- [109] D.C. Angst, B. Tepekule, L. Sun, B. Bogos, S. Bonhoeffer, Comparing treatment strategies to reduce antibiotic resistance in an in vitro epidemiological setting,

Proceedings of the National Academy of Sciences, 118 (2021) e2023467118.

<https://doi.org/10.1073/pnas.2023467118>

[110] M. Bassetti, E. Righi, New antibiotics and antimicrobial combination therapy for the treatment of gram-negative bacterial infections, *Current Opinion in Critical Care*, 21

(2015) 402. <https://doi.org/10.1097/mcc.0000000000000235>

[111] N. Wang, J. Luo, F. Deng, Y. Huang, H. Zhou, Antibiotic combination therapy: a strategy to overcome bacterial resistance to aminoglycoside antibiotics, *Frontiers in*

Pharmacology, 13 (2022) 839808. <https://doi.org/10.3389/fphar.2022.839808>

Chapter 4

Experimental Section

This chapter is divided in several sections, regarding the experimental work discussed in previous chapters and divided as follows: 4.1 – General Information; 4.2 - Experimental of Chapter 2; 4.3 – Experimental of Chapter 3.

The identification number used for the compounds in the present chapter is the same used for the discussion.

4.1 General information

4.1.1 Chemicals and solvents

All chemical materials were purchased from Sigma-Aldrich, Merck or FluoroChem. Air and moisture sensitive reagents were handled under nitrogen atmosphere, in a vacuum system, using Schlenk techniques. The solvents were purified or dried by distillation, when necessary, using the procedures reported by literature [1, 2]. Kraft lignin was kindly donated by the Université du Québec à Trois-Rivières, Canada.

4.1.2 Instrumentation and methodology

Thin Layer Chromatography (TLC)

The reaction controls were performed by thin layer chromatography (TLC) using silica plates coated with silica 60 (Fluka), with fluorescence indicator UV₂₅₄. The eluent was chosen depending on the reaction.

Column Adsorption Chromatography

When necessary, reaction products were purified by column chromatography, using silica gel 60 (Merck) as stationary phase and the eluent was chosen dependently by the reaction.

Ultrasound

To facilitate the dissolution of some synthesized compounds and reagents, Bandelin Sonorex TK52 was used as ultrasound device.

Microwave Assisted Reactions

The reactions assisted by microwave were performed into the CEM Discover[®] SP equipment with a gas addition kit (Discover[®] Gas Addition), connected to a gas line of the Chemistry Department in the University of Coimbra. Microwave glass tubes of 10 mL were used.

Nuclear Magnetic Resonance (NMR)

Proton (¹H) and carbon (¹³C) NMR spectra were recorded on a Bruker Avance 400 spectrometer (400, 101 MHz, respectively) in the Chemistry Department of the University of Coimbra, using CDCl₃ ($\delta = 7.26$ ppm) as deuterated solvent (unless otherwise stated). Both the signal of the residual deuterated solvent and the tetramethylsilane (TMS, $\delta = 0.00$ ppm) were used as internal standard to express the chemical shifts. The data obtained are indicated in the following order: Nucleus (apparatus, solvent): chemical shift (δ , ppm) [signal multiplicity (s - singlet, d - doublet, dd – doublet of doublets, t – triplet, m - multiplet), coupling constant (*J*, Hertz), relative intensity (nH, number of protons), assignment in the structure].

Mass spectrometry (MS)

High-resolution mass spectrometry was carried out on a Bruker Microtof apparatus, equipped with selective ESI detector (Unidade de Masas e Proteómica, University of Santiago de Compostela, Spain).

UV-Visible Absorption Spectroscopy (UV-Vis)

UV-visible absorption spectra were obtained on a Hitachi U-2010 and Shimadzu UV-1700 spectrophotometers using 1 cm double-stranded quartz cells with 1 cm optical path and using the corresponding solvent as reference. For magnetic nanocomposite spectra, material (1 mg) was placed in a solvent DMF, CH₃CN/H₂O or CHCl₃ (5 mL) and submitted to ultrasounds for 1 min.

Solid state UV–Visible absorption Spectroscopy

Solid-state UV–Vis absorption spectra were performed using a Cary 5000 UV-Vis-NIR spectrometer. The spectra were registered by reading diffuse reflectance by the Cary 5000 DRA. Background correction was made by using PTFE as

reference and the blocked beam to read the baseline with 100% and 0%, respectively. To obtain the absorption spectra for the samples, the Kubelkan-Munk function was used.

Transmission Electron Microscopy (TEM)

TEM analyses were carried out by slow evaporation of samples solutions deposited on square copper grids covered with carbon film from agar scientific. The analyses were performed on a Tecnai G2 20 S-TWIN from FEI company (Engineer Department, University of Coimbra, Portugal), with a LaB₆ emitter as electron source and operating at an acceleration voltage of 200 kV. The determination of size distributions was performed by analysing the images with Fiji [3] and the Gaussian fit was done with MatLab software.

Scanning electron microscope (SEM)

SEM analyses were carried out on FESEM Zeiss – GEMINI II operating at an accelerating voltage of 2 kV, using secondary electrons as detector. The SEM samples were covered with a monometric layer of gold by physical vapor deposition.

Infrared Spectroscopy (IR)

The infrared spectra were obtained using a ThermoNicolet IR380 (Thermo Scientific TM) Fourier transform infrared spectrometer, with a Smart Orbit Diamond Attenuated Total Reflection (ATR) system, Ge/KBr beam splitter and deuterated triglycine sulfate (DTGS) detector, 32 or 64 scans and a 2 cm⁻¹ spectral resolution.

Spectra of solids were also acquired at room temperature, using the same spectrometer, 64 scans with a resolution of 2 cm⁻¹, using the KBr pellet technique with a concentration of 1% (w/w) for each sample.

Inductively coupled plasma optical emission spectrometry (ICP-OES)

The amount of metals in complexes were determined using an ICP-OES iCAP™ 7000 Series spectrometer (Department of Chemistry, University of Aveiro).

Thermogravimetry (TG)

Thermogravimetric analyses were made using a TG-DSC Perkin-Elmer STA6000 with a heating rate of 10 °C min⁻¹ to a maximum temperature of 900 °C, in a

nitrogen atmosphere (20 mL min^{-1}), with alumina pans (Department of Physics, University of Coimbra).

Differential Scanning Calorimetry (DSC)

Thermograms were obtained using a Perkin Elmer DSC7 power compensation calorimeter, with an intracooler at $-10 \text{ }^\circ\text{C}$ (cooling mixture of ethylene glycol-water 1:1 V/V) and a 20 mL min^{-1} nitrogen purge. Aluminium pans suitable for volatile substances (Perkin Elmer, 30 or $15 \text{ }\mu\text{L}$) were used and an empty pan as reference. Certified reference materials were employed for temperature and enthalpy calibrations, following the procedure described elsewhere [4]. Thermograms were recorded with the heating rate $\beta = 10 \text{ }^\circ\text{C min}^{-1}$. The DSC curves were analysed with Perkin Elmer Pyris software, version 3.5.

High-performance liquid chromatography (HPLC)

The oxidative reactions were checked and analyzed by HPLC, with a Diode Array detector (model G1315D from Agilent), by using a C18 reversed-phase packing column (Luna® $5 \text{ }\mu\text{m}$ C18(2) 100 \AA , $150 \times 4.6 \text{ mm}$, RP) for the separation. The DAD acquisition wavelengths were set at 220.8 nm , 230.6 nm , 254.6 nm , 255.6 nm , 270.8 nm and 310.6 nm . The equipment has an automatic injector module (model G1329A, 1200 Infinity Series Agilent) and the injected volume was $50.0 \text{ }\mu\text{L}$. Suitable mobile phases were prepared according to the individual needs (see discussion in each chapter, for details).

The calibration curves and the samples analysis for the intrinsic dissolution rate tests were carried out by the Shimadzu HPLC, with a Photodiode Array detector (model SPD-M20A from Shimadzu), by using a C18 reversed-phase packing column (Ascentis® $5 \text{ }\mu\text{m}$ C18(2) 100 \AA , $150 \times 4.6 \text{ mm}$, RP) for the separation. The autosampler was an automatic injector (model SIL-20A HT, Shimadzu) and the injected volume was $50 \text{ }\mu\text{L}$. A flow rate of $1.500 \text{ mL min}^{-1}$ and the column oven was set at $30 \text{ }^\circ\text{C}$ were used.

Liquid chromatography–mass spectrometry (LC-MS)

The identification of degradation products discussed in Chapter 2 was performed by using an Ultimate 3000 RSLC UHPLC and LTQ XL Linear Ion Trap 2D Mass Spectrometer, with an orthogonal electrospray ion source (ESI) (Department of Chemistry, University of Aveiro, Portugal).

Photodegradation products discussed in Chapter 2 were detected by using HPLC Dionex Ultimate 3000 composed by a binary pump HPG3200, an autosampler WPS300 and a column oven TCC3000 coupled in-line to a LCQ Fleet ion trap mass spectrometer equipped with an ESI ion source (Thermo Scientific™) operating in positive and negative mode, with the following optimized parameters: ion spray voltage, ± 4.5 kV; capillary voltage, 16/-18 V; tube lens offset, -70/58 V; sheath gas (N₂), 40 arbitrary units; auxiliary gas (N₂), 20 arbitrary units; capillary temperature, 300 °C. Spectra typically correspond to the average of 20–35 scans and were recorded in the range between 50-1000 Da (Department of Chemistry, *Instituto Superior Técnico*, University of Lisbon, Portugal).

Total organic carbon (TOC) analysis

The total organic carbon (TOC) laboratorial analyses were conducted at Itecons - Instituto de Investigação e Desenvolvimento Tecnológico para a Construção, Energia, Ambiente e Sustentabilidade. The analysis was performed by ANALYTIK-JENA equipment, MULTI N/C 3100 model. TOC, as the sum of organically bound carbon present in the sample, was determined following the EN 1484 (1997) [5], based on the oxidation of organic carbon into carbon dioxide through thermocatalytic oxidation at high temperatures (800 °C), which permits the quantitative digestion of compounds with complex and stable carbon structures.

Ecotoxicity assay

All organisms were obtained from dormant stages (*Vibrio fischeri* and *Brachionus calyciflorus*) and standard laboratory cultures (*Raphidocelis subcapitata*) and all tests were conducted at Centro de Ecologia Funcional (CFE/FCT/UC) (University of Coimbra).

V. fischeri were prepared from the preserved lyophilized bacteria into a suspension of organisms, at known concentration, using a purchased reconstitution solution and following the protocol Microtox 81.9% basic test protocol for water samples (Azur Environmental, Carlsbad, 18 CA, USA). The toxicity tests on *V. fischeri* were performed by Microtox toxicity analyzer model 500 (Strategic Diagnosis, Newark, DE, USA).

The green freshwater microalga *R. subcapitata* (strain Nr. WW 15-2521, obtained from the Carolina Biological Supply Company, Burlington, NC,

USA) was obtained from cultures maintained in cotton-stoppered 250 mL sterile glass Erlenmeyer flasks filled with 100 mL Woods Hole (MBL) growth medium [6], enhanced with vitamins (0.1 mg L⁻¹ B1, 0.5 µg L⁻¹ B12 and 0.5 µg L⁻¹ biotin). These cultures were left at 19-21 °C under continuous cool-white, fluorescent illumination (8000 lx). Every 4-7 days, during the exponential phase of growth, the cultures were renewed. The 72-h growth inhibition test (with the 6 dilutions) was implemented following the OECD (2011) and EC (1992) guidelines [7, 8], to estimate algal growth as total cell density (cells mL⁻¹) or specific growth rate (1/day).

The rotifer *B. calyciflorus* was obtained incubating cysts in reconstituted moderately hard water [9] at 24-26 °C with continuous top illumination (3000-4000 lx) for 18 h. After the hatching, organisms were nutrified with artificial food for 2 hours. The lethality test (with the 6 dilutions) was performed according to the Rotoxkit F standard operational procedure (https://www.microbiotests.com/wp-content/uploads/2019/07/freshwater-rotifer-toxicity-test_rotokit-f-standardoperatingprocedure.pdf; conformed to the ISO standard 19827).

For the data analysis, the effective concentrations inducing 20% (EC₂₀) and 50% (EC₅₀) of responses (luminescence inhibition of bacterium or mortality of rotifer) and respective 95% confidence limits (CL) were computed using the software PriProbit 1.63 (<http://bru.gmpcr.ksu.edu/proj/priprobit/download.asp>), with the probit transformation of the proportion of responses and the log transformation of the concentrations. Regarding the effective concentrations inducing 20% and 50% inhibition in algal growth (EbC₂₀ and EbC₅₀ as cell density and ErC₂₀ and ErC₅₀ as specific growth rate) and respective 95% CL, organism responses were fitted to a logistic model using the least squares method [10].

Water Purification (Milli-Q grade)

The deionized water, used for all HPLC analysis, was obtained using a Water Purification Apparatus Milli-Q (Department of Chemistry, University of Coimbra).

Photochemical reactor

The photoreactor was acquired from Photochemical Reactors, equipped with a 400 W medium pressure lamp contained in a double-walled immersion quartz vessel. According to the Photochemical Reactors Ltd, the features of Hg lamp are reported below:

- Nominal Wattage = 400 W
- Overall Length = 380 mm
- Discharge Length = 110 mm
- Diameter = 18 mm

One vessel is formed by inlet and outlet tubes which provide water cooling, and a polytetrafluoroethylene tube extends to the bottom of the well to allow the cooling to flow upwards from the bottom. Medium pressure lamp produces significant amounts of radiation in the visible region at 405-408, 436, 546 and 577-579 nm and 365-366 nm radiation with smaller amounts also in the ultraviolet region at 254, 265, 270, 289, 297, 302, 313 and 334 nm.

Centrifuge

Centrifugations were performed using a Centromix-BLT centrifuge (Department of Chemistry, University of Coimbra).

Powder X-ray Diffraction (XRPD)

X-ray powder diffractograms were recorded with a Rigaku MiniFlex 600 diffractometer, Cu K α radiation ($\lambda = 1.540598 \text{ \AA}$), with a D/teX-Ultra high-speed detector. Calibration was performed using silicon as an external calibrant. A scan range from 3° to 40° 2 θ was used.

Mechanochemistry

Multicomponent solid-forms screening was performed by mechanochemistry, using a MM4100 Retsch ball mill, with 10 mL stainless steel jars and two 7 mm diameter stainless balls per jar, with a total sample mass of about 70 mg. Liquid-assisted grinding (LAG) was performed using 10 μ L dry ethanol, at 30 Hz for 60 min.

Dissolution rate tester apparatus

The dissolution rate tests were performed in the SOTAX dissolution rate tester (USP 2 model) with 6 glass vessels (1 L). Each vessel was equipped with a probe and a die. The die has a cavity into which the amount of sample was placed and after the insertion of a punch, the material is compressed with 1 ton of press. The die was attached to a steel shaft and then is immersed into 900 mL of a HCl 0.01 M, in a horizontal position. A rotating disk speed of 50 rpm was applied and the measurements run at 37 °C.

***In vitro* biological assays**

The assays were carried out using bacteria strains from the American Type Culture Collection (ATCC) normally used as a control in antibiotic susceptibility tests (antibiograms) [11]. Two bacterial species were selected: *Escherichia coli* ATCC 8739 and *Staphylococcus aureus* ATCC 29213. The Minimal Inhibitory Concentration (MIC) was determined by broth microdilution and agar dilution tests using Mueller-Hinton (MH) broth for overnight incubation and MH agar, respectively. The results were compared to the breakpoints of the European Committee on Antimicrobial Susceptibility Testing guidelines (EUCAST) [12]. All tests were carried out at the UCQFarma, Faculty of Pharmacy, University of Coimbra.

4.1.3 Solvent drying

***N,N*-Dimethylformamide:** DMF and calcium hydride was placed in a round-bottom flask equipped with a reflux condenser. The mixture was kept at 80 °C, for 6 hours. Then, the solvent was distilled under reduced pressure and after that was stored in a vessel with activated molecular sieves (3 Å).

Triethylamine: Triethylamine, sodium flakes and benzophenone were put in a round-bottom flask. The mixture was kept under reflux until the strong blue colour was observed. After distillation, the solvent was stored, under nitrogen atmosphere, in a vessel with activated molecular sieves (3 Å).

Toluene: Toluene was added into a round-bottom flask with sodium slivers and benzophenone. The mixture was left under reflux until the colour turned blue. After the distillation, the solvent was collected and stored in a vessel with activated molecular sieves (3 Å) and under nitrogen atmosphere.

4.2 Experimental of Chapter 2

4.2.1 Synthesis of porphyrins

Experimental procedures used for the synthesis of porphyrins, and their full characterization are described below. The 5,10,15,20-tetraphenylporphyrin (**1**) and

5,10,15,20-tetra(2,6-dichlorophenyl)porphyrin (**2**) were synthesized using three different methodologies, described below:

i) General Procedure for Nitrobenzene Method [13]: a mixture of glacial acetic acid (210 mL) and nitrobenzene (105 mL) was inserted in a 500 mL round bottom glass flask and the desired aldehyde (60 mmol) was added. The mixture was warmed under stirring to a gentle reflux. When the reflux started, pyrrole (60 mmol; 4.2 mL) was added dropwise and the reaction proceeded for 1 hour under stirring, at 140 °C. After cooling, the glacial acetic acid and the nitrobenzene were evaporated under reduced pressure. Then, methanol (200 mL) was added and the crude was left in cold, at 5 °C overnight, to facilitate the precipitation, after which the solid was filtered;

ii) General Procedure for NaY/Nitrobenzene Method [6]. A mixture of glacial acetic acid (575 mL) and nitrobenzene (325 mL) was inserted in a 1 L round bottom glass flask and the desired aldehyde (60 mmol) was added, along with NaY (3 g). The mixture was warmed under stirring to gentle reflux. When the reflux started, pyrrole (60 mmol; 4.2 mL) was added dropwise and then the reaction proceeded for 2 hours under stirring, at 145 °C. After this period, NaY was filtered while hot and washed with 50 mL THF. Then MeOH (400 mL) was added, and the mixture was left in the fridge at 5 °C overnight, to facilitate the precipitation. Finally, the precipitated solid was isolated by filtration and dried. The NaY catalyst was collected by filtration and washed with chloroform and tetrahydrofuran, followed by drying of the solid overnight, at 150 °C, for future reutilization;

iii) General Procedure for Microwave Method [7]: Pyrrole (9.8 mmol; 0.68 mL), aldehyde (9.8 mmol) and water (0.2 mL) were placed inside a 15 mL microwave vessel. For solid aldehydes, the mixture was previously subjected to ultrasounds for 10-15 min. Subsequently, the reaction mixture was heated under microwave irradiation at 200 °C for 10 min with an initial power of 300 W. In the end, the desired porphyrin was poured into ethanol (15 mL) to induce porphyrin precipitation. The solid was then filtered, washed with ethanol and dried under vacuum.

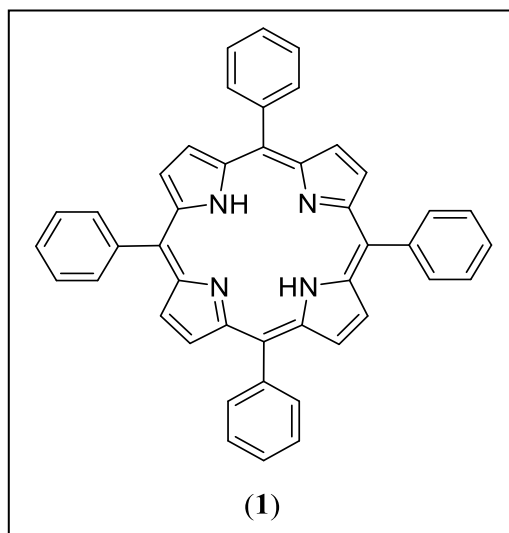
5,10,15,20-tetraphenylporphyrin (1)

Benzaldehyde (6.37 g, 60 mmol), (1.04 g, 9.8 mmol) was used as aldehyde in NaY/nitrobenzene and microwave methods, respectively. The synthetic procedures used were the ones mentioned above.

Yields (%):

- Nitrobenzene method: 24% (2.22 g);
- NaY/Nitrobenzene method: 35% (3.22 g);
- Microwave method: 20% (300 mg).

¹H-NMR (400 MHz, CDCl₃, TMS): δ , ppm = 8.81 (s, 8H, β -H), 8.22-8.12 (m, 8H, Ar-H), 7.78-7.66 (m, 12H, Ar-H), -2.82 (s, 2H, NH) (data is in good agreement with literature) [14].

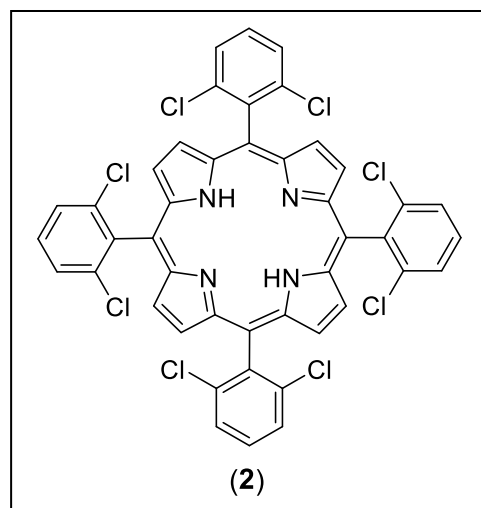
**5,10,15,20-tetrakis(2,6-dichlorophenyl)porphyrin (2)**

2,6-Dichlorobenzaldehyde (10.5 g; 60 mmol), (1.72 g, 9.8 mmol) was used as aldehyde and **2** was synthesized following the above mentioned NaY/nitrobenzene and microwave methods.

Yields (%):

- Nitrobenzene method: 3% (401 mg);
- NaY/Nitrobenzene method: 8% (1.07 g);
- Microwave method: 5% (109 mg);

¹H-NMR (400 MHz, CDCl₃, TMS): δ , ppm = 8.69 (s, 8H, β -H), 7.85-7.65 (m, 12H, Ar-H), -2.57 (s, 2H, NH) (data is in good agreement with literature) [15].



4.2.2 Chlorosulfonation of porphyrins

General Procedure [16]: The *meso*-aryl substituted porphyrin and an excess of chlorosulfonic acid were mixed in a round bottom flask and stirred for the appropriate time and temperature. Then, after cooling at room temperature, chloroform (400 mL) was added and the reaction mixture was poured into a 2 L washing beaker. Water was added slowly for the first 30 min without stirring and after this time, water flow was increased with stirring, to remove the excess of acid by continuous extraction. Afterwards, a saturated solution of sodium bicarbonate was added with stirring, to obtain a biphasic system. When the system changed the colour from green to red, the water phase was removed and the organic phase was dried by anhydrous sodium sulphate. Then, the solid was filtered and the solvent was evaporated.

5,10,15,20-*tetrakis*(4-chlorosulfonylphenyl)porphyrin (3)

Following the general procedure mentioned above, 5,10,15,20-tetraphenylporphyrin (200 mg; 0.32 mmol), chlorosulfonic acid (12 mL, 59 mmol) were used, with stirring and heating at 50 °C for 1 h.

Yield (%): 74% (239 mg).

¹H-NMR (400 MHz, CDCl₃):

δ, ppm = 8.90 (s, 8H, β-H),

8.20 (d, *J*=7.5 Hz, 4H, Ar-H),

7.50 (d, *J*=7.5 Hz, 4H, Ar-H), -

2.57 (s, 2H, NH);

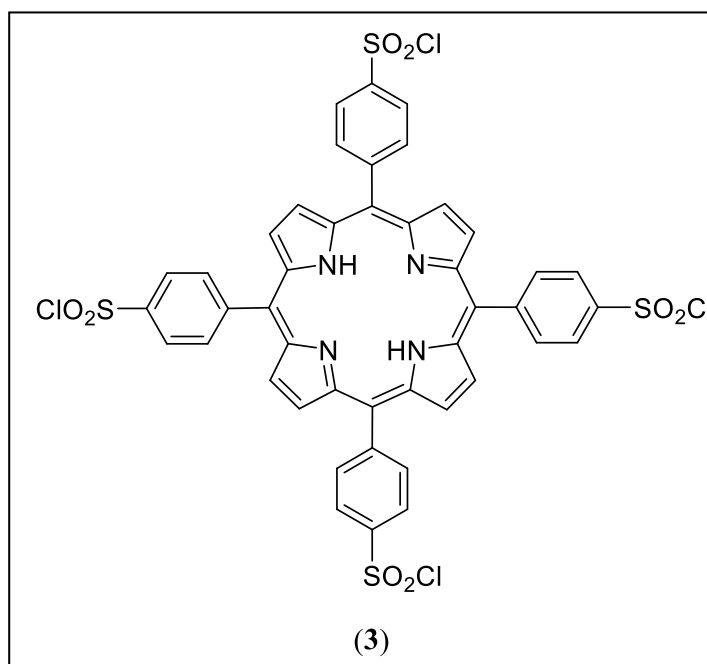
UV-Vis (toluene), λ_{max}/nm (ε

/M⁻¹ cm⁻¹): 417 (3.8×10⁵), 512

(1.9×10⁴), 546 (3.6×10³), 588

(6.5×10³), 644 (4.4×10³) (data

is in good agreement with literature) [17].



5,10,15,20-tetrakis(2,6-dichloro-3-chlorosulfonylphenyl)porphyrin (4)

5,10,15,20-tetrakis(2,6-dichlorophenyl)porphyrin (200 mg, 0.20 mmol) and chlorosulfonic acid (12 mL, 59 mmol) were used, with stirring and heating at 100 °C for 1 h.

Yield (%): 75% (212 mg);

MS (ESI-TOF), m/z: 1278.6353

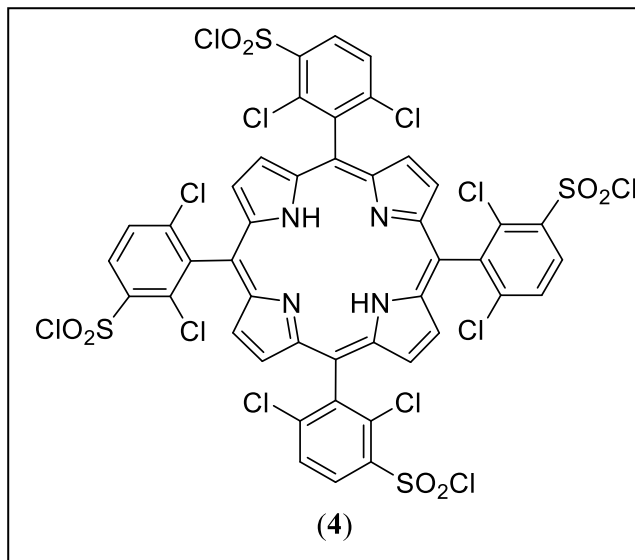
[M+H]⁺; calculated for

[C₄₄H₁₉Cl₁₂N₄O₈S₄] 1278.6348;

¹H NMR (400 MHz, CDCl₃): δ, ppm = 8.67–8.63 (m, 12H, β-H, Ar-H), 8.11–8.06 (m, 4H, Ar-H), -2.51 (s, 2H, NH);

UV-Vis (toluene), λ_{max}/nm (ε /M⁻¹

cm⁻¹): 421 (3.2×10⁵), 514 (2.1×10⁴), 544 (2.6×10³), 590 (6.7×10³), 650 (8.2×10²) (data is in good agreement with literature) [16].

**4.2.3 Hydrolysis of porphyrins**

General Procedure: The *meso*-aryl substituted porphyrin was suspended in distilled water (100 mL) in a round bottom flask and refluxed for the appropriate time. The resulting solution was then concentrated by rotary evaporation and acetone was added to precipitate the desired sulfonated porphyrin. The solid was finally dried in the oven at 100 °C.

5,10,15,20-tetrakis(4-sulfonatophenyl)porphyrin (5)

5,10,15,20-tetrakis(4-chlorosulfonylphenyl)porphyrin (100 mg, 0.1 mmol) was used and reaction time was 12 hours.

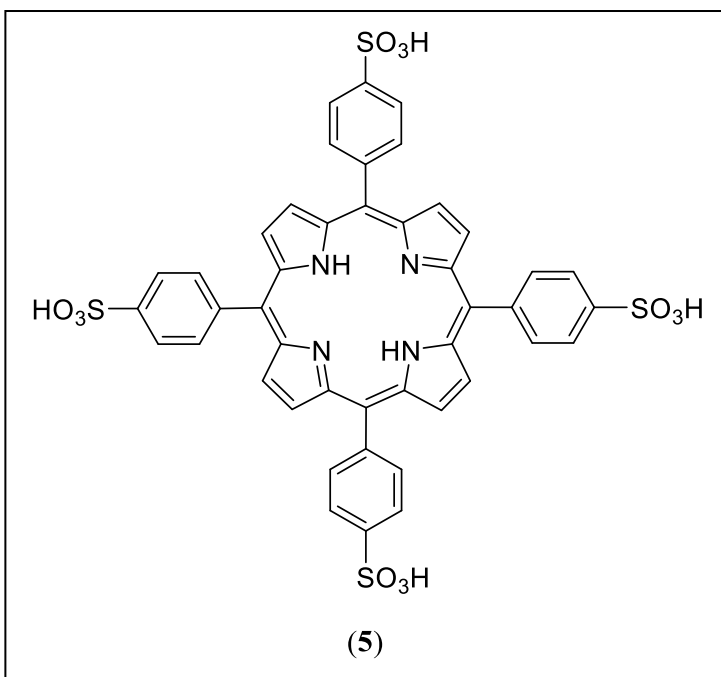
Yield (%): 70% (65 mg).

MS (ESI) m/z: 933 [M-H]⁻; calculated for [C₄₄H₂₉N₄O₁₂S₄] 933;

¹H NMR (400 MHz, D₂O), δ, ppm = 8.75 (s, 8H, β-H), 8.50-8.30 (m, 8H, Ar-H), 7.32-7.20 (m, 8H, Ar-H), -2.70 (s, 2H, NH);

UV-Vis (H₂O/PBS),

λ_{max}/nm (ε /M⁻¹ cm⁻¹): 413 (2.0×10⁵), 518 (5.8×10³), 554 (3.1×10³), 578 (2.4×10³), 634 (1.1×10³) (data is in good agreement with literature) [17, 18].

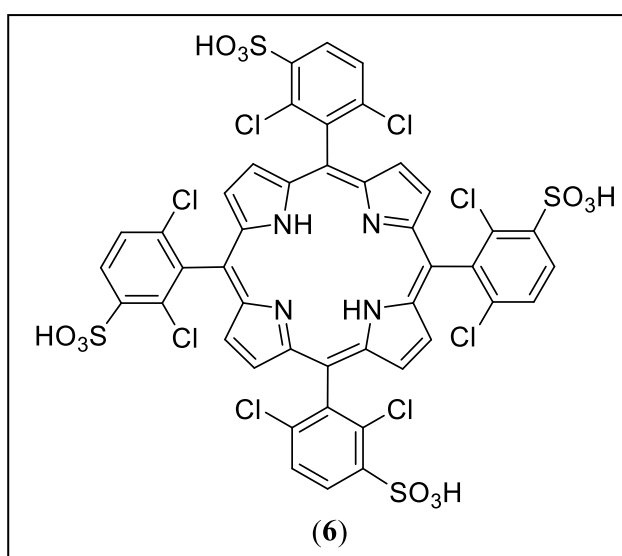
**5,10,15,20-tetrakis(2,6-dichloro-3-sulfophenyl)porphyrin (6)**

5,10,15,20-tetrakis(2,6-dichloro-3-chlorosulfonylphenyl)porphyrin (100 mg, 0.074 mmol) was used and reaction time was 24 hours.

Yield (%): 75% (67 mg).

MS (MALDI) m/z: 1206.76 [M+H]⁺; calculated for [C₄₄H₂₃Cl₈N₄O₁₂S₄] 1206.77;

¹H NMR (400 MHz, CD₃OD), δ, ppm = 9.00-8.60 (m, 8H, β-H), 8.50-8.21 (m, 4H, Ar-H), 8.02-7.85 (m, 4H, Ar-H), -2.32 (s, 2H, NH).



UV-Vis (H₂O/PBS), $\lambda_{\text{max}}/\text{nm}$ ($\epsilon / \text{M}^{-1} \text{cm}^{-1}$): 416 (1.0×10^5), 517 (4.5×10^3), 554 (8.6×10^2), 584 (1.8×10^3), 640 (3.8×10^2) (data is in good agreement with literature) [19].

4.2.4 Synthesis of metalloporphyrins

General Procedure for manganese (III) porphyrins: The sulfonated porphyrin (0.12 mmol), 5 equivalents of manganese (II) acetate tetrahydrate (150 mg, 0.60 mmol) and sodium acetate (49 mg, 0.60 mmol) were dissolved in glacial acetic acid and heated at 100 °C. The reaction was left under a vigorous stirring until full complexation (checked by UV-Vis, 1 h). Then, ethyl acetate was added to the reaction mixture in order to precipitate the metallic porphyrin. The compound was filtered and the solid obtained was washed with isopropyl alcohol to remove the free base porphyrin and the desired solid was then dried in the oven at 80 °C.

Manganese (III) 5,10,15,20-tetrakis(4-sulfonatophenyl)porphyrin acetate (7)

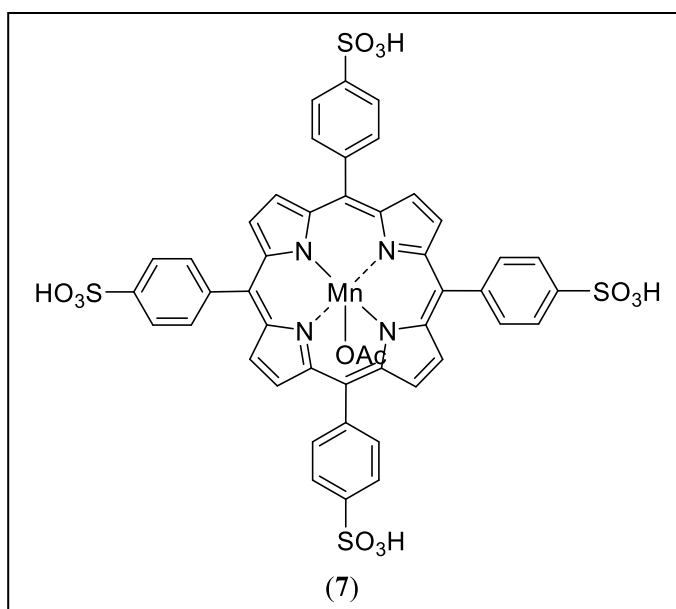
Following the above-described acetic acid /acetate salt method, 5,10,15,20-tetrakis(4-

sulfonatophenyl)porphyrin (112 mg, 0.12 mmol) was used.

Yield (%): 89% (130 mg).

MS (ESI-TOF) m/z: 1047.0201 [M+H]⁺; calculated for [C₄₆H₃₂MnN₄O₁₄S₄] 1047.0178;

UV-Vis (H₂O), $\lambda_{\text{max}}/\text{nm}$ ($\epsilon / \text{M}^{-1} \text{cm}^{-1}$): 466 (8.3×10^4), 564 (7.2×10^3), 596 (3.5×10^3) (data is in good agreement with literature) [18].



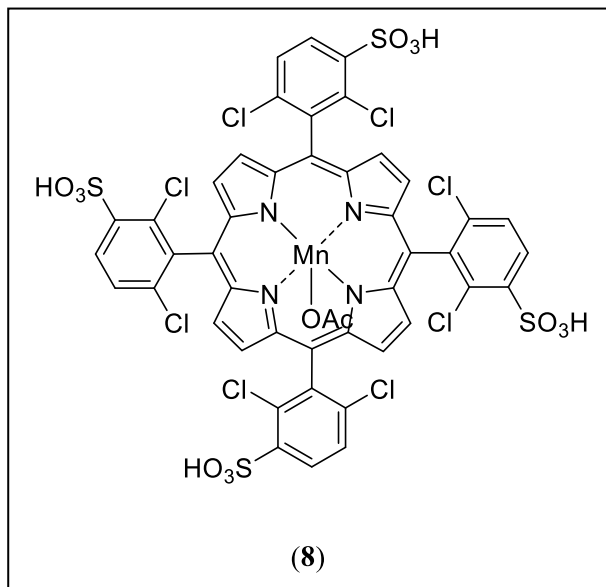
Manganese (III) 5,10,15,20-tetrakis(2,6-dichloro-3-sulfonatophenyl)porphyrin acetate (8)

Following the manganese metalation procedure mentioned above, 5,10,15,20-tetrakis(2,6-dichloro-3-sulfonatophenyl)porphyrin (145 mg, 0.12 mmol) was used.

Yield (%): 88% (140 mg).

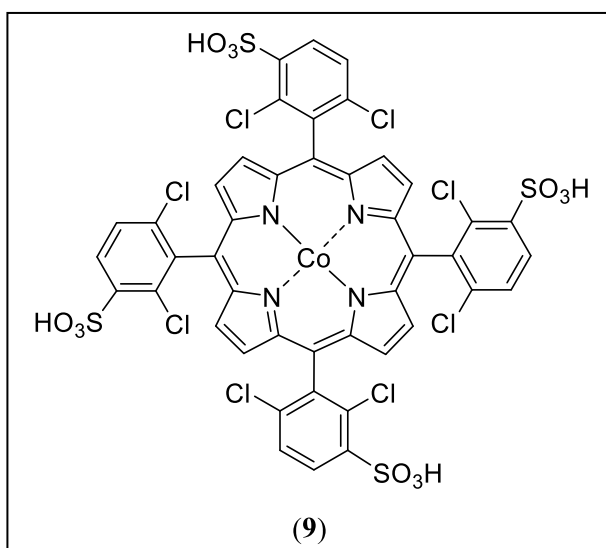
MS (ESI-TOF) m/z: 1258.6836 [M-OAc]⁺; calculated for [C₄₄H₂₀Cl₈MnN₄O₁₂S₄] 1258.6849;

UV-Vis (H₂O), λ_{max}/nm (ε /M⁻¹ cm⁻¹): 463 (6.7×10⁴), 516 (6.2×10³), 562 (1.6×10³) (data is in good agreement with literature) [18].



Cobalt (III) 5,10,15,20-tetrakis(2,6-dichloro-3-sulfonatophenyl)porphyrin acetate (9)

The DMF/ metallic salts method was followed and 5,10,15,20-tetrakis(2,6-dichloro-3-sulfonatophenyl)porphyrin (150 mg, 0.12 mmol) and 6 equivalents of cobalt(II) acetate tetrahydrate (180 mg; 0.7 mmol) were mixed in DMF (10 mL) and the reaction was left for 1 h, at 160 °C with stirring. The amount of DMF was reduced by rotary evaporation and the compound was precipitated by adding diethyl ether and leaving the crude on the fridge overnight. Isopropyl alcohol was added to wash the precipitate and remove the metal-free porphyrin, so the desired porphyrin was obtained.



Yield (%): 80% (127 mg).

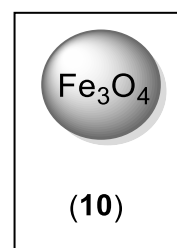
MS (ESI-TOF) m/z: 1262.6812 [M-OAc]⁺; calculated for [C₄₄H₂₀Cl₈CoN₄O₁₂S₄] 1262.6801;

UV-Vis (H₂O), λ_{max}/nm (ε /M⁻¹ cm⁻¹): 419 (5.3×10⁴), 535 (3.4×10³), 560 (6.4×10²) (data is in good agreement with literature) [20].

4.2.5 Synthesis, coating and functionalization of magnetic nanoparticles

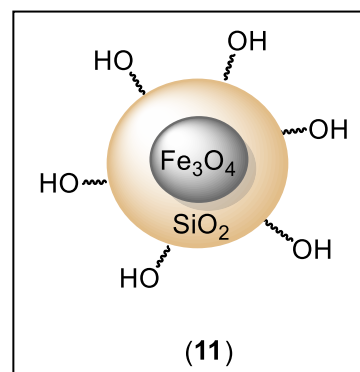
(MNPs)

The preparation of MNPs (**10**) was performed according with Rossi's co-precipitation method [21]. A 1 M aqueous solution of iron chloride (III) (10 mL) and 2 M hydrochloric acid of iron chloride (II) (2.5 mL) mixture was added to a 1 M aqueous solution of NH₄OH (250 mL), under mechanical stirring (10000 rpm). After 30 minutes, the material was magnetically separated and washed 3 times with 250 mL of distilled water. The MNPs were dispersed into 250 mL of distilled water and, under mechanical stirring. A solution of oleic acid (2 mL, 7×10⁻³ mol) diluted in 5 mL of acetone was added dropwise. After more 30 minutes, the precipitate was magnetically separated and dispersed in cyclohexane (15 mL) and centrifugated for 30 min (2000 rpm). After solvent evaporation, the stock solution contained 72 mg of MNPs/mL of cyclohexane. The characterization was performed by TEM (using ImageToll software version 3.0):



-TEM: ~ 5.5 nm

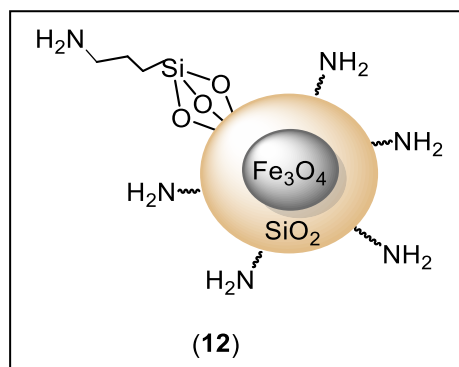
The silica coating was obtained by reverse microemulsion [22]. In a 5 L round bottom flask was consecutively added cyclohexane (2.8 L) and Igepal CO-520 ® (178.4 g), MNPs (800 mg, 11.11 mL of stock solution in cyclohexane) and NH₄OH 29 % (38 mL). Then, tetraethyl orthosilicate (TEOS) (30.8 mL) was added dropwise and the mixture was left under slow stirring (300 rpm) for 16 h. The magnetic material was extracted by methanol (250 mL), centrifugated (7000 rpm, 30 min) and washed three times with ethanol. Subsequently, the solid compound was dried at room temperature for 24 h



and calcinated in the oven at 500 °C for 2 h. An amount of 5.41 g of silica coated magnetic nanoparticles **11** were obtained. The characterization of MNPs@SiO₂ was performed by TEM images and IR spectroscopy:

- **TEM**: ~ 44.5 nm
- **FT-IR**: 3740 cm⁻¹ (stretching Si-OH)

After the coating, **11** (1 g) and (3-aminopropyl) triethoxysilane (APTES, 0.5 mL, 2.1 mmol) were added in 50 mL dry toluene and left stirring under reflux for 2 h. Then, the amine-functionalized material **12**, MNP@SiO₂-NH₂ was washed three times with toluene, separated by centrifugation and dried in the oven (100 °C) for 20 h. The characterization was performed by FT-IR and TG-DSC:



- **FT-IR**: 3371-3309 cm⁻¹ (stretching of N-H), 1597 cm⁻¹ (bending N-H), 2931-2865 cm⁻¹ (stretching C-H), 1450 cm⁻¹ (bending of C-H) and 1410 cm⁻¹ (bending of Si-CH₂).
- **TG-DSC** (20 °C - 800 °C): 20 °C - 100 °C (endothermic peak - adsorbed water), 200 °C - 600 °C (propylamine groups).

4.2.6 Synthesis of MnTDCPPS-NH@MNPs

Compound **14** was prepared by two consecutive steps:

- a) metalation of **4** following the method of DMF/metallic salt;
- b) immobilization of MnTDCPPSO₂Cl (**13**) in **14**.

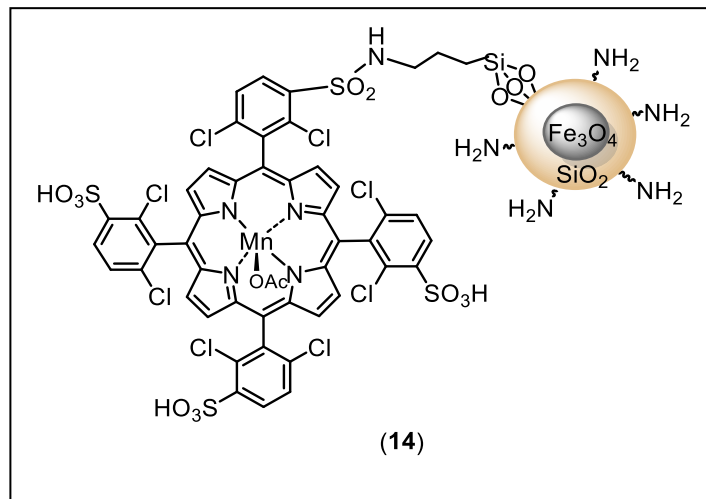
5,10,15,20-*tetrakis*(2,6-dichloro-3-chlorosulfonylphenyl)porphyrin (**4**) (240 mg; 0.19 mmol) and 7 equivalents of manganese (II) acetate tetrahydrate (637 mg; 1.3 mmol) was placed in a round bottom flask. Dry DMF (10 mL) was added, and the reaction was stirred for 4 h at 140 °C. The DMF was removed by rotary evaporation and MnTDCPPSO₂Cl (**13**) was precipitated by adding diethyl ether after leaving on the fridge overnight. The precipitate was washed with isopropyl alcohol to remove the

metal-free porphyrin **4**, so the desired MnTDCPPSO₂Cl (**13**) was obtained. Mn (II) metalation was checked by UV-Vis:

-**UV-Vis:** 465 nm

(Soret band).

Subsequently, in a round bottom flask, a solution of MnTDCPPSO₂Cl (**13**) (307 mg, 0.22 mmol) and cesium carbonate (310 mg, 0.95 mmol) in 50 mL of dry 1,2-dimethoxyethane was placed. Then, 1 g of **12** was added and the mixture was left



under stirring at 85 °C for 24 h. Afterwards, the material was collected with an external magnet and consecutively washed with acetonitrile (2×), ethyl acetate (2×) and dichloromethane (2×). Finally, magnetic compound **14**, was dried under vacuum.

The compound **14** was characterized by UV-Vis, TG-DSC and ICP:

- **UV-Vis:** 464 nm (Soret band);

- **ICP:** 0.095% of Mn;

- **TG-DSC** (25 °C - 800 °C): 50 °C - 200 °C (absorbed water), 200 °C - 800 °C (organic decomposition);

- **Immobilization yield:** 2% (0.018 mmol of porphyrin **13** per gram of functionalized silica).

4.2.7 Synthesis of hybrid catalyst MnTDCPPS@SiO₂

3-Aminopropyl functionalized silica (1 mmol of NH₂ per gram) (230 mg, 0.23 mmol NH₂) was placed in a 100 mL round bottom flask. Dry DMF (20 mL) and dry triethylamine (5 mL) were added. Then, porphyrin **4** (281 mg, 0.22 mmol), dissolved in 5 mL of dry DMF, was added dropwise with stirring, over 10 min. The reaction was further stirred for 24 h, at room temperature. At this point, manganese (II) acetate tetrahydrate (290 mg, 1.2 mmol) and sodium acetate (65 mg,

0.79 mmol) were consecutively added and the mixture was brought to 120 °C and left for another 24 h. After cooling, the reaction was centrifuged.

Compound **16** was collected and suspended in 15 mL distilled water. After stirring for 10 min, it was again centrifuged, and the solvent removed by decantation.

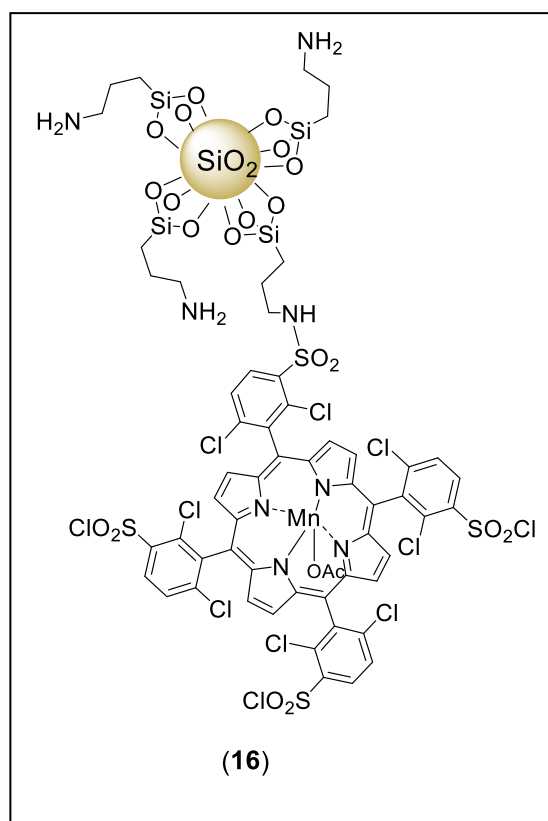
- **UV-Vis**: 466 nm for the Soret band;

- **FT-IR**: 3500 and 3350 cm^{-1} (stretching Si-OH), 1635 cm^{-1} (bending N-H), 2932 cm^{-1} (stretching C-H), 1082 cm^{-1} (bending of C-H), 804 cm^{-1} (bending Si-CH₂);

- **Immobilization yield**: 37%
(3.7×10^{-4} mol of porphyrin **4** per gram of functionalized silica);

- **ICP-OES**: 3.7 %;

- **TG-DSC** (25 °C - 900 °C): 25 °C - 100 °C (endothermic peak - adsorbed water), 200 °C - 450 °C (organic moiety), 500 °C - 900 °C (aminopropylsilyl groups).



4.2.8 Trimethoprim homogeneous degradation

In a typical experiment, a stock solution was prepared for each porphyrin (5.0×10^{-9} mol). In a 50 mL round bottom flask, trimethoprim (TMP) (1.3 mg, 4.5×10^{-6} mol) and a volume of porphyrin's stock solution (0.27 mL for **7**, 0.33 mL for **8**, 0.31 mL for **9**) were added. Then, a volume of distilled water was also added to achieve a final volume of 20 mL. The mixture was then stirred at room temperature. The UV-Vis spectrum of the initial mixture was registered before starting the reaction. The reaction started by adding the first aliquot of 30 μL hydrogen peroxide (30% w/v) and consecutive additions were made each 15 minutes, until a final volume of 300 μL (150 min) was achieved. Before each addition of peroxide, a sample was taken to analyze by HPLC.

4.2.9 Trimethoprim heterogeneous degradation

In a typical experiment (e.g. TMP: Cat = 500:1), TMP (13 mg, 4.5×10^{-5} mol) and the hybrid catalyst **16** (0.14 mg, 9.0×10^{-8} mol) were dissolved in 100 mL water in a 25 mL round bottom flask, with stirring. The UV-Vis spectrum of the mixture was recorded before starting the degradation reaction. The reaction started by adding the first 30 μ L of hydrogen peroxide (30% w/v) and consecutive 30 μ L additions of oxidant agent were then carried out every 15 minutes, until a final volume added of 300 μ L. Aliquots were taken before each addition to analyze by HPLC. Reaction times and substrate/catalyst proportions were changed accordingly.

4.2.10 Catalyst reutilization studies

Catalyst reutilization studies were performed using the optimized experimental conditions described above (TMP:Cat = 500; H_2O_2 = 2.6 mmol). After each catalytic cycle, the catalyst **16** was separated from the reaction medium by centrifugation and washed consecutively with distilled water, ethanol and acetonitrile, with centrifugation after each washing. After this process, the catalyst was dried for 16 h in the oven at 60 °C. The solvents collected through decantation were combined and a UV-Vis spectra was recorded. Catalyst **16** was reutilized for five consecutive cycles.

4.2.11 Ecotoxicity assay

The ecotoxicity studies were performed thanks to our collaboration with the Centre for Functional Ecology, Department of Life Sciences at University of Coimbra. Software PriProbit 1.63 was used to analyze the data and to calculate the EC_{20} and EC_{50} [10].

The intrinsic toxicity of a saturated TMP solution (494.4 mg L^{-1} in distilled water) and the resulting degradation products solution were tested toward three selected species: the bacteria *V. fischeri*, the microalgae *R. subcapitata* and the rotifer *B. calyciflorus*. Firstly, the TMP solution was diluted in a standard artificial moderately hard freshwater (pH = 7.25, conductivity = 325 $\mu\text{S}/\text{cm}$; ASTM 2002) [9] until concentrations of 225 mg L^{-1} for the bacteria and the rotifer and 285 mg L^{-1} for the

microalgae. Starting from these concentrations, six diluted solutions, with a diluted factor of 2 for bacteria and 1.75 for the other two species, were prepared.

A suspension of *V. fischeri* was obtained lyophilizing the preserved bacteria using a purchased reconstitution solution and the test protocol (Azur Environmental, Carlsbad, CA, USA). The TMP solution was diluted six times with a gradient of 5.76, 11.52, 22.95, 46.08, 92.14, 184.3 mg L⁻¹ and the degradation products solution was diluted nine times with a gradient of 0.320%, 0.639%, 1.28%, 2.56%, 5.12%, 10.24%, 20.48%, 40.95% and 81.90%. Then, the values of EC₅₀ were calculated after 5 minutes of exposure according to the Microtox 81.9% basic test protocol for water samples and using the toxicity analyzer model 500 (Strategic Diagnosis, Newark, DE, USA).

The freshwater microalga *P. subcapitata* (Koršhikov; formerly *Selenastrum capricornutum* Printz; strain Nr. WW 15-2521; Carolina Biological Supply Company, Burlington, NC, USA) was preserved in 100 mL nonaxenic batch cultures using Woods Hole MBL growth medium, with a temperature between 19-21 °C under continuous cool-white fluorescent illumination with an intensity of 100 μE m⁻² s⁻¹. Six TMP diluted solutions were prepared 285.00, 162.86, 93.06, 53.18, 30.39 and 17.36 mg L⁻¹, whereas the degradation products solution was diluted with a gradient of 6.09%, 10.66%, 18.66%, 32.65%, 57.14% and 100%. A volume of 900 μL of replicate cultures was prepared and inoculated with 100 μL of algal inoculum, whereas the same quantity of nutrients was added into TMP solution and degradation products. The 72 h growth inhibition test was carried out following the OECD (2001) (<https://www.oecd.org/chemicalsafety/testing/34241659.pdf>) and EC (1992) guidelines [8, 10]. After 72 h of exposure, the mean specific growth rate per day, ErC (1/d), was calculated and final cell densities, EbC (cells mL⁻¹), were measured [23] by a microscope (× 400 magnification) using a Neubauer chamber (American Optical, Buffalo, NY, USA) [24].

B. calyciflorus organisms were hatched from cysts, exposed to six 0.3 mL test solutions and incubated in darkness with a controlled temperature of 24 - 26 °C for 48 h. After 48 h, rotifers lethality alive or dead were counted. The test was performed following the Rotoxkit F standard operational procedure (www.microbiotests.com/wp-content/uploads/2019/07/freshwater-rotifer-toxicity-test_rotokit-f_standard-operating-procedure.pdf; conformed to the ISO standard 19827).

4.2.12 Synthesis of zinc (II) 5,10,15,20-tetrakis(2,6-dichloro-3-sulfonatophenyl)porphyrin

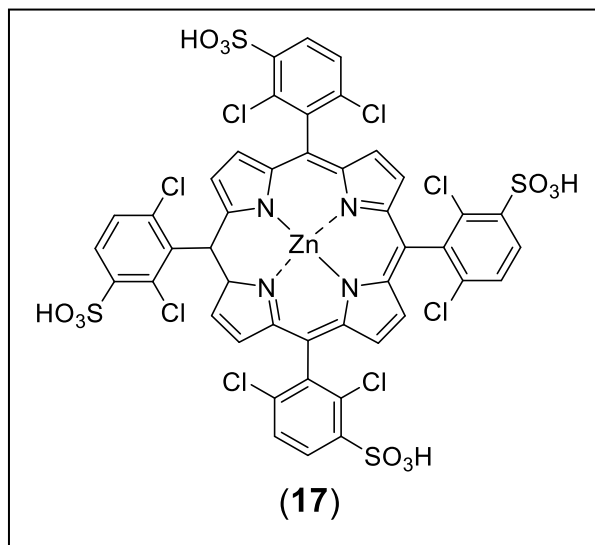
The $\text{CHCl}_3/\text{CH}_3\text{OH}$ metallic salts method was followed. 5,10,15,20-tetra(2,6-dichloro-3-sulfonatophenyl)porphyrin (594 mg, 0.49 mmol) was dissolved in 75 mL of chloroform and then, a solution of 10 equivalents of zinc(II) acetate dihydrate (1.0 g; 4.9 mmol) in 40 mL of methanol was added. The reaction was left for 3 h, at 60 °C with stirring. The desired metalloporphyrin was purified by silica gel chromatographic column using dichloromethane as eluent.

Yield (%): 90% (562 mg).

^1H NMR (400 MHz, CD_3OD), δ , ppm
= 9.0-8.68 (m, 8H, β -H), 8.53-8.52 (d, $J=8.4$ Hz, 4H, Ar-H), 8.03-8.01 (d, $J=8.4$ Hz, 4H, Ar-H).

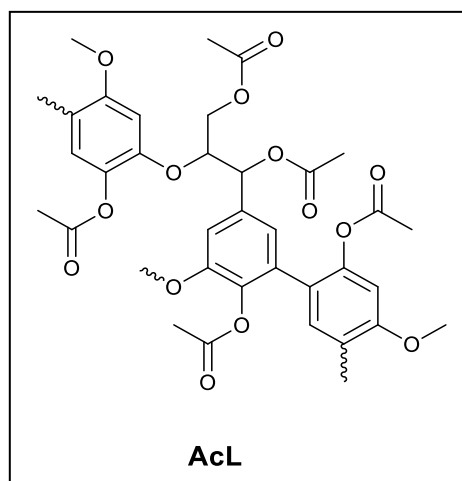
UV-Vis ($\text{H}_2\text{O}/\text{PBS}$), $\lambda_{\text{max}}/\text{nm}$

($\epsilon/\text{M}^{-1}\text{cm}^{-1}$): 420 (1.4×10^5), 550 (5.6×10^3), 589 (1.2×10^3) (data is in good agreement with literature) [19].



4.2.13 Synthesis of acetylated lignin (AcL)

The synthesis of acetylated lignin was performed following the Marchand' method [25]. The Kraft lignin (100 mg) was dissolved in 2 mL of pyridine-acetic anhydride (1/1, v/v) and the reaction was stirred for 24 h at room temperature, under argon atmosphere. After that, ethanol (25 mL) was added and the mixture was stirred for further 30 minutes, after which the solvents were removed by evaporation. This process was further repeated 8 times, in order to fully remove the pyridine and acetic anhydride. The material was additional purified by co-



precipitation with chloroform (2 mL) and diethyl ether (100 mL), added dropwise, under stirring. The precipitated compound was separated by centrifugation and washed with diethyl ether. Finally, the compound was dried under vacuum with KOH and P₂O₅.

4.2.14 Encapsulation of porphyrins inside acetylated lignin nanoparticles (Por@AcL)

The encapsulation of porphyrins (**Por**) inside acetylated lignin nanoparticles was carried out following previous reports [26].

General procedure for the preparation of Por@AcL. A solution of **Por** (2 mg) was prepared in acetone (10 mL), under stirring. Subsequently, AcL (20 mg) was added and stirred until complete dissolution. Meanwhile, a dialysis membrane was hydrated in distilled water for around 20 minutes. The solution was carefully introduced into a dialysis bag by a 10 mL syringe and then immersed in excess of deionized water, which was periodically replaced. After 24 hours, the nanoparticles were recovered by centrifugation (10.000 × g) for 1 h, at room temperature. The precipitate was separated from the liquid and re-suspended in distilled water, for further centrifugation. Then, the supernatant was collected and finally re-suspended in 5 mL of distilled water.

Quantification of porphyrin inside AcL

The quantification of porphyrin inside nanoparticles was obtained by UV-Vis spectroscopy [27].

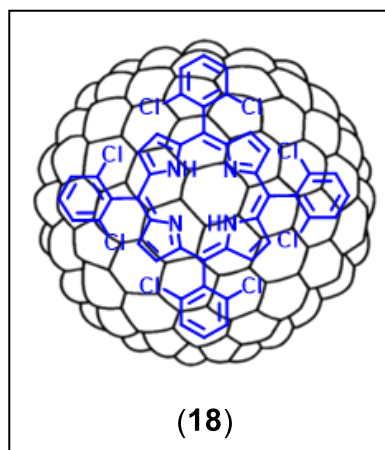
General procedure. In triplicate, 950 μL of acetone were placed in a glass tube (Solution A), and 50 μL of **Por@AcL** nanoparticles were added. In a second glass tube (Solution B) 4.745 mL of solvent were placed and 250 μL of Solution A were added, to obtain a dilution of 400 times. Acetone was used as control to register the UV-Vis spectra. The wavelength was calibrated between 800 and 350 nm and the individual amount of porphyrin encapsulated on nanoparticles suspension was calculated following the formula:

$$\text{Concentration}(\mu\text{M}) = \left(\frac{\text{Abs}_{\text{Soret}}}{\varepsilon} \right) \times 10^6 \times \text{dil. } F_{\text{SolutionA}} \times \text{dil. } F_{\text{SolutionB}}$$

Where Abs corresponds to the absorbance of the Soret band, ε corresponds to the absorption coefficient of the porphyrin under analysis and $dil.F$ corresponds to the dilution factor of each solution.

Preparation of TDCPP@AcL (18)

TDCPP, **2**, (2 mg) was used as porphyrin and AcL (20 mg) were completely dissolved in acetone (10 mL) under stirring. The concentration of **2** inside the nanoparticles was 504.5 μM .



4.2.15 Trimethoprim photodegradation under homogeneous conditions

General procedure. In a typical experiment, 1 L of 10^{-4} M TMP stock solution was prepared (30 mg, 1.0×10^{-4} mol). In the photoreactor vessel, 100 mL of TMP stock solution was placed (1.0×10^{-5} mol) and 1.2 mL of stock solution of sulfonated porphyrin (1.6×10^{-5} M, 7.9×10^{-7} mol) was also added to obtain a ratio between substrate and catalyst of 500:1. The reaction was left in dark under stirring for 30 min (pre-incubation time) and an UV-Vis spectrum was recorded. Then, the mercury lamp was switched on and the reaction was carried for 24 hours. During this time, samples were collected each 30 min, to check reaction evolution by HPLC. All reactions (including controls) were performed in triplicate.

The experiment was performed using two sulfonated porphyrins: TDCPPS (**6**), ZnTDCPPS (**17**).

4.2.16 Antibiotics photodegradation using TDCPP@AcL

General procedure. In a typical experiment, 1 L of 10^{-4} M antibiotic stock solution was prepared (1.0×10^{-4} mol). Then, 100 mL of this stock solution (1.0×10^{-5} mol) and a volume of stock solution of TDCPP@AcL (48.60 μL ,

4×10^{-9} mol) were placed in the photoreactor vessel to obtain a ratio between substrate and catalyst of 500:1. The reaction was stirred in the dark for 30 min (pre-incubation time). Then the mercury lamp was switched on and the reaction was carried for 24 h. During this time, samples were collected each 30 min to check the reaction evolution by HPLC.

All reactions (including controls) were performed in triplicate.

For the antibiotics photodegradation reactions, each 10^{-4} M stock solution was prepared using:

- TMP: 30 mg, 1.0×10^{-4} mol.
- SMX: 25 mg, 1.0×10^{-4} mol.
- TMP/SMX mixture: 4.5 mg of TMP and 21.6 mg of SMX, 1.0×10^{-4} mol.

4.2.17 TDCPP@AcL reutilization studies

General procedure. After each photocatalytic reaction, reutilization studies were performed using 24 h reaction times. After each cycle, an amount of 1.0×10^{-5} mol of antibiotic was added to the photoreactor vessel. After a pre-incubation time of 30 min, the irradiation was re-started, and the reaction was carried out for more 24 hours. Reactions were checked by HPLC every 30 minutes and by UV-Vis after each cycle.

Particularly:

- TMP catalytic reutilization studies: in each reaction 2.9 mg of TMP (1.0×10^{-5} mol) were added and 10 cycles were performed;
- SMX catalytic reutilization studies: in each reaction 2.5 mg of SMX (1.0×10^{-5} mol) were added and 10 cycles were performed.

4.3 Experimental of Chapter 3

In this section, the methodologies and full characterization of compounds used in Chapter 3 are presented.

4.3.1 Development of new multicomponent solid-forms

The new solid-state forms were experimentally prepared by mechanochemistry, by liquid-assisted grinding (LAG), using 10 μ L of dry ethanol. TMP was chosen as active pharmaceutical ingredient (API), whereas co-formers among Generally Regarded As Safe substances (GRAS) were selected as well as other APIs. The mixtures were constituted by TMP and selected co-formers in different proportions.

In a typical LAG experiment, TMP and co-former were mixed in a proportion of 1:1. The two compounds were placed into grinding jars of stainless steel equipped with two balls (7 mm of diameter) of the same material. Typically, a total mass of ~ 70-80 mg was used and 10 μ L of dry ethanol was also added. The mixer mill was set to a frequency of 30 Hz and the grinding times varied between 30 and 60 min.

The grinding outcomes were characterized by FTIR, DSC and XPRD. The same experimental grinding procedure was applied to TMP and each of the co-formers. The pure components were characterized by the same experimental techniques before and after the grinding process.

4.3.2 Intrinsic dissolution rate tests

Dissolution rate tests were performed in collaboration with the Faculty of Pharmacy at University of Coimbra in the Pharmaceutical Quality Control Unit, UCQFarma.

The analysis was carried out for commercial TMP and the three selected solid-state forms with nicotic acid (TMP-NIC), paracetamol (TMP-PARA), and ibuprofen (TMP-IBU).

General procedure. In a typical experiment, 900 mL of a HCl 0.1 M solution were placed into each glass dissolution rate vessel and pre-heated to 37 °C. Then, the die was attached to a surface plate through the three threaded holes located on the base of die, providing the base for the pellet. After that, ~ 50 mg of each powder were measured and located in the die cavity between two metal rods to facilitate its removal. A steel punch was inserted in this cavity and the desired compound was compressed with a hydraulic press applying 1 ton for 30 s. So, tablets of 8 mm of diameter were prepared for each pure compound and for the multicomponent systems. After the tablet

preparation, each die was assembled with a steel shaft, so the pellet surface is exposed horizontally no less than 1 cm from the bottom of the glass dissolution vessel. Once the samples have been placed into the HCl solution the test was performed at 37 °C, with 50 rpm and for a total time of 45 min, accordingly to the USP TMP tablets Monograph reported in literature [28]. A sample from each dissolution vessel was taken off each 5 min and checked by HPLC. The HPLC method was adjusted for each of the three solid forms tested and the wavelength of maximum absorbance at 270 nm. A TMP calibration curve was used to determine the amount of TMP dissolved, and calibration curves were also prepared for the co-formers. The results were depicted in a graphic showing the TMP concentration as function of time.

4.3.3 Trimethoprim MIC determination

The MIC determination of TMP was performed for *E. coli* ATCC 8739 and *S. aureus* ATCC 29213 strains with two tests: the broth microdilution and the agar dilution. In both cases, the two bacteria were cultured overnight in MH agar at 37 °C along 16-24 hours. The inoculum preparation was carried out diluting isolated colonies into distilled water to adjust the cell density achieving a turbidity of 0.5 optical density on the McFarland standard scale. This value was checked by a densitometer (Biosan DEN-1B) and corresponds to a $\sim 1-2 \times 10^8$ colony-forming units (CFU) mL⁻¹ for each bacterium. Aqueous stock solutions of 10 mg of APIs and co-formers were prepared with 10% DMSO and distilled water, whereas the CIP stock solution was prepared using 10 mg of CIP dissolved in HCl (final pH of ~ 5).

General procedure for broth microdilution test. 100 μ L of MH broth were added in each well of a sterile microplate with 96 round-bottomed wells using a multichannel pipette. Then, a 1 mg mL⁻¹ antibiotic solution was prepared and 100 μ L were added to the first well of each line. A serial 2-fold dilution was performed across each line by pipetting 100 μ L of the antibiotic in culture medium solution and diluting in the 100 μ L of culture medium in the next well. The prepared inoculum suspension was diluted with a factor of 1:20 with distilled water and then 10 μ L of this diluted bacteria suspension were added into all wells, for a final inoculum density of $\sim 5 \times 10^5$ CFU mL⁻¹. Control experiments using only the formulations (10% - 20% DMSO or 10⁻⁵ M HCl) were carried out to ensure that these did not contribute to

bacterial growth inhibition. Finally, the 96-well plate was placed into the incubator at 37 °C overnight (16-20 h). After the incubation time, bacterial growth was determined in each well, through the visual detection of a white pellet or turbidity. The MIC values were determined based on the minimum antibiotic concentration required to inhibit bacterial growth. In the specific case of TMP, according to guidelines [29], the MIC is considered the minimum antibiotic concentration required to inhibit 80% of visible bacterial growth. The experiments were performed in triplicate and results were depicted in a graph.

General procedure for agar dilution test [30]. A sterile cotton swab was soaked in a freshly prepared bacterial inoculum in distilled water. Then, a 100 mm MH agar Petri plate was inoculated by streaking the swab over the agar surface four times, rotating the plate ~ 60° each time to obtain a complete and homogeneous inoculum distribution. Then, disks (a TMP control standard and sterile paper disks to put our new solid forms) were evenly placed on the inoculated agar surface, for a maximum of 4 disks per Petri plate. After adding the same mass amount of our solid form samples on the sterile disks as used in the TMP disc control (1.25 µg, which corresponds to 1.25 µL of each stock solution) the plates were inverted and placed in an incubator at 37 °C and left overnight (16-20 h). After the incubation time, the resulting inhibition zones were uniformly circular, and their diameters were measured with a ruler. The experiments were performed in triplicate.

4.4 References

- [1] H.D. Burrows, M.M. Pereira, Química - síntese e estrutura-uma abordagem prática, Escolar Editora, Lisbon, 2006.
- [2] W.L.F. Armarego, D.D. Perrin, Purification of laboratory chemicals, Butterworth Heinemann, Oxford, 1996.
- [3] J. Schindelin, I. Arganda-Carreras, E. Frise, V. Kaynig, M. Longair, T. Pietzsch, S. Preibisch, C. Rueden, S. Saalfeld, B. Schmid, J.-Y. Tinevez, D.J. White, V. Hartenstein, K. Eliceiri, P. Tomancak, A. Cardona, Fiji: an open-source platform for biological-image analysis, *Nature Methods*, 9 (2012) 676. <https://doi.org/10.1038/Nmeth.2019>
- [4] A.O.L. Évora, R.A.E. Castro, T.M.R. Maria, M.R. Silva, J. Canotilho, M.E.S. Eusébio, Lamotrigine: design and synthesis of new multicomponent solid forms, *European Journal of Pharmaceutical Sciences*, 129 (2019) 148. <https://doi.org/10.1016/j.ejps.2019.01.007>
- [5] European Standards_ BS EN 1484:1997_Water analysis. Guidelines for the determination of total organic carbon (TOC) and dissolved organic carbon (DOC), German Institute for Standardisation (Deutsches Institut für Normung), 1997. <https://www.en-standard.eu/bs-en-1484-1997-water-analysis-guidelines-for-the-determination-of-total-organic-carbon-toc-and-dissolved-organic-carbon-doc/>
- [6] J.R. Stein-Taylor, Handbook of phycological methods, Cambridge University Press, Cambridge, 1973.
- [7] OECD, Test No. 201: Freshwater alga and cyanobacteria, growth inhibition test, OECD guidelines for the testing of chemicals, section 2, OECD Publishing, Paris, 2011. <https://doi.org/10.1787/9789264069923-en> (last accessed on 08/10/2022)
- [8] G.o. CANADA, Biological test method: growth inhibition test using a freshwater alga, 2nd edition, 2007 - March. <https://www.canada.ca/en/environment-climate-change/services/wildlife-research-landscape-science/biological-test-method-publications/growth-inhibition-test-freshwater-alga.html> (last accessed on 08/10/2022)
- [9] Standard test methods for determining sediment concentration in water samples, ASTM D3977-97, ASTM International, West Conshohocken, PA, 2002.
- [10] OECD, Report of the OECD workshop on statistical analysis of aquatic toxicity data, 2002. <https://doi.org/10.1787/9789264078284-en>

- [11] Clinical and laboratory standards institute, performance standards for antimicrobial disk susceptibility tests; CLSI standard M02. 13th Edition ed.; Clinical and Laboratory Standards Institute: Wayne, PA, 2018.
- [12] European committee on antimicrobial susceptibility testing_routine and extended internal quality control for MIC determination and disk diffusion as recommended by EUCAST (Version 12.0, valid from 2022-01-01 https://aurosan.de/images/mediathek/servicematerial/EUCAST_RefStaemme_Sollwerte.pdf) (last accessed on 08/10/2022)
- [13] A.M.D.R. Gonsalves, J.M.T.B. Varejão, M.M. Pereira, Some new aspects related to the synthesis of meso-substituted porphyrins, *Journal of Heterocyclic Chemistry*, 28 (1991) 635. <https://doi.org/10.1002/jhet.5570280317>
- [14] H.D. Burrows, A.M.R. Gonsalves, M.L.P. Leitão, M. da G. Miguel, M.M. Pereira, Phase transitions and self-assembly in meso-tetrakis(undecyl)porphyrin, *Supramolecular Science*, 4 (1997) 241. [https://doi.org/10.1016/S0968-5677\(97\)00010-2](https://doi.org/10.1016/S0968-5677(97)00010-2)
- [15] A.M.D.R. Gonsalves, M.M. Pereira, A.C. Serra, R.A.W. Johnstone, M.L.P.G. Nunes, 5,10,15,20-tetrakisaryl- and 2,3,7,8,12,13,17, 18-octahalogeno-5,10,15,20-tetrakisarylporphyrins and their metal complexes as catalysts in hypochlorite epoxidations, *Journal of the Chemical Society, Perkin Transactions 1*, (1994) 2053. <https://doi.org/10.1039/P19940002053>
- [16] C.J.P. Monteiro, M.M. Pereira, S.M.A. Pinto, A.V.C. Simões, G.F.F. Sá, L.G. Arnaut, S.J. Formosinho, S. Simões, M.F. Wyatt, Synthesis of amphiphilic sulfonamide halogenated porphyrins: MALDI-TOFMS characterization and evaluation of 1-octanol/water partition coefficients, *Tetrahedron*, 64 (2008) 5132. <https://doi.org/10.1016/j.tet.2008.03.055>
- [17] J.M. Dąbrowski, M.M. Pereira, L.G. Arnaut, C.J.P. Monteiro, A.F. Peixoto, A. Karocki, K. Urbańska, G. Stochel, Synthesis, photophysical studies and anticancer activity of a new halogenated water-soluble porphyrin, *photochemistry and photobiology science*, 83 (2007) 897. <https://doi.org/10.1111/j.1751-1097.2007.00073.x>
- [18] A.M.D.R. Gonsalves, R.A.W. Johnstone, M.M. Pereira, A.M.P. deSantAna, A.C. Serra, A.J.F.N. Sobral, P.A. Stocks, New procedures for the synthesis and analysis of 5,10,15,20-tetrakis(sulphophenyl)porphyrins and derivatives through chlorosulphonation, *Heterocycles*, 43 (1996) 829. <https://doi.org/10.3987/COM-95-7372>

- [19] C.J.P. Monteiro, M.M. Pereira, M.E. Azenha, H.D. Burrows, C. Serpa, L.G. Arnaut, M.J. Tapia, M. Sarakha, P. Wong-Wah-Chung, S. Navaratnam, A comparative study of water soluble 5,10,15,20-tetrakis(2,6-dichloro-3-sulphophenyl)porphyrin and its metal complexes as efficient sensitizers for photodegradation of phenols, *Photochemical & Photobiological Sciences*, 4 (2005) 617. <https://doi.org/10.1039/b507597a>
- [20] H. Sugimoto, H. Ohshima, S. Inoue, Alternating copolymerization of carbon dioxide and epoxide by manganese porphyrin: the first example of polycarbonate synthesis from 1-atm carbon dioxide, *Journal of Polymer Science Part a-Polymer Chemistry*, 41 (2003) 3549. <https://doi.org/10.1002/pola.10835>
- [21] L.M. Rossi, L.L.R. Vono, F.P. Silva, P.K. Kiyohara, E.L. Duarte, J.R. Matos, A magnetically recoverable scavenger for palladium based on thiol-modified magnetite nanoparticles, *Applied Catalysis A: General*, 330 (2007) 139. <https://doi.org/10.1016/j.apcata.2007.07.018>
- [22] D.K. Yi, S.S. Lee, G.C. Papaefthymiou, J.Y. Ying, Nanoparticle architectures templated by SiO₂/Fe₂O₃ nanocomposites, *Chemistry of Materials*, 18 (2006) 614. <https://doi.org/10.1021/cm0512979>
- [23] R. Rosa, M. Moreira-Santos, I. Lopes, L. Silva, J. Rebola, E. Mendonça, A. Picado, R. Ribeiro, Comparison of a test battery for assessing the toxicity of a bleached-kraft pulp mill effluent before and after secondary treatment implementation, *Environmental Monitoring and Assessment*, 161 (2010) 439. <https://doi.org/10.1007/s10661-009-0759-2>
- [24] European Standards_Water analysis - Guidelines for the determination of total organic carbon (TOC) and dissolved organic carbon (DOC), DIN EN 1484:1997-08, German Institute for Standardisation (Deutsches Institut für Normung), 1997.
- [25] G. Marchand, C.A. Calliste, R.M. Williams, C. McLure, S. Leroy-Lhez, N. Villandier, Acetylated lignins: a potential bio-sourced photosensitizer, *Chemistry Select*, 3 (2018) 5512. <https://doi.org/10.1002/slct.201801039>
- [26] G. Marchand, G. Fabre, N. Maldonado-Carmona, N. Villandier, S. Leroy-Lhez, Acetylated lignin nanoparticles as a possible vehicle for photosensitizing molecules, *Nanoscale Advances*, 2 (2020) 5648. <https://doi.org/10.1039/D0NA00615G>
- [27] N. Maldonado-Carmona, G. Marchand, N. Villandier, T.S. Ouk, M.M. Pereira, M.J.F. Calvete, C.A. Calliste, A. Zak, M. Piksa, K.J. Pawlik, K. Matczyszyn, S. Leroy-Lhez, Porphyrin-loaded lignin nanoparticles against bacteria: a photodynamic

antimicrobial chemotherapy application, *Frontiers in Microbiology*, 11 (2020) 606185.

<https://doi.org/10.3389/fmicb.2020.606185>

[28] U.S. Pharmacopeia - USP Trimethoprim tablets. http://www.pharmacopeia.cn/v29240/usp29nf24s0_m85955.html (last accessed on 25/09/2022)

[29] M.P. Weinstein, J.B. Patel, C.-A. Burnham, S. Campeau, P.S. Conville, C. Doern, G.M. Eliopoulos, M.F. Galas, R.M. Humphries, S.G. Jenkins, S.M. Kircher, J.S. Lewis II, B. Limbago, A.J. Mathers, T. Mazzulli, S.D. Munro, M.O. Smith de Danies, R. Patel, S.S. Richter, M. Satlin, J.M. Swenson, A. Wong, W.F. Wang, B.L. Zimmer, CLSI.M07_Methods for dilution antimicrobial susceptibility tests for bacteria that grow aerobically, 11th Edition ed., Wayne, PA: Clinical and Laboratory Standards Institute 2018.

[30] F.R. Cockerill, M.A. Wikler, J. Alder, M.N. Dudley, G.M. Eliopoulos, M.J. Ferraro, D.J. Hardy, D.W. Hecht, J.A. Hindler, J.B. Patel, M. Powell, J.M. Swenson, R.B. Thomson Jr., M.M. Traczewski, J.D. Turnidge, M.P. Weinstein, B.L. Zimmer, Performance standards for antimicrobial disk susceptibility tests; approved standard—11th Edition Wayne, PA: Clinical and Laboratory Standards Institute 2012.